Developing Metrology for Nondestructive Characterization of Buried Polymer Interfaces in Situ

by

John N. Myers

A dissertation submitted in partial fulfillment
of the requirements for the degree of
Doctor of Philosophy
(Chemistry)
in The University of Michigan
2016

Doctoral Committee:

Professor Zhan Chen, Chair
Assistant Professor Julie Biteen
Professor L. Jay Guo
Professor Robert Kennedy

DEDICATION

To my wife and my parents

ACKNOWLEDGEMENT

I first want to thank my advisor, Professor Zhan Chen, for his generous support, guidance, and patience during my time at the University of Michigan. He helped me learn to never accept mediocrity, but to always strive to improve myself.

I also want to thank several members of the research group who helped me during my Ph. D. research. Dr. Xiaofeng Han and Dr. Pei Yang taught me how to use and maintain SFG spectrometers and provided valuable insight on SFG data analysis. Chi (Jesse) Zhang taught me SFG fundamentals, helped me transition into polymer research, and demonstrated how powerful a positive mindset can be. I am very thankful to have worked with Dr. Xiaoxian Zhang for several years. In addition to teaching me several surface analytical techniques, she always encouraged me when I was down and helped me see the forest for the trees when I was lost. I'm also thankful for working on various projects together with Josh Jasensky, Peipei Hu, Chuan Leng, Yaoxin Li, Nathan Ulrich, and Minyu Xiao. I had the opportunity to work with several visiting scholars who visited Professor Chen's lab. Dr. Jintao Yang taught my about polymer brush materials and Dr. Shuangying Wei taught my about polyurethane adhesives.

Most of my dissertation work would not have been possible without the extensive help and support of many collaborators. I want to especially thank Dr. Yuying Wei and Dr. Yonghao Xiu for their contributions to chapter 5, Jaimal Williamson for his contributions to chapters 4 and 5, Dr. Jeffery Bielefeld for his contributions to chapter 6, 7, and 8, Dr. Qinghuang Lin for his contributions to chapters 6 and 7, Dr. Alfred Grill for his contributions to chapter 9, and Dr.

Kang-Wook Lee for his contributions to chapter 4 and 5. Finally, I want to thank Dr. Julie Biteen, Dr. L. Jay Guo, and Dr. Robert Kennedy for their support and encouragement.

Chapter 2 was adapted with permission from Elsevier (*J. Colloid Interface Sci.,* **2014**, *423*, 60-66) who holds the copyright thereto. Chapter 3 was adapted with permission from Elsevier (*Chin. Chem. Lett.,* **2015**, *26*, 449-454) who holds the copyright thereto. Chapter 4 was adapted with permission from *Langmuir,* 2014, **30**,165–171. Copyright 2013 American Chemical Society. Chapter 5 was adapted, with permission, from Myers, J. N.; Zhang, X.; Xiu, Y.; Wei, Y.; Williamson, J. M.; Lee, K.-W.; Chen, Z. Nondestructive Characterization of Molecular Structures at Buried Copper/Epoxy Interfaces and Their Relationship to Locus of Failure Analysis. *IEEE Trans. Compon. Packag. Manuf. Technol.* **2015**, *5*, 1432-1440. Copyright 2015 IEEE. Chapter 6 was adapted with permission from *ACS Appl. Mater. Interfaces* **2014**, *6*, 18951-18961. Copyright 2014 American Chemical Society. Chapter 7 was adapted with permission from *J. Phys. Chem. B* **2015,** *119*, 1736-1746. Copyright 2015 American Chemical Society. Chapter 8 was adapted with permission from *J. Phys. Chem. C* **2015**, *119*, 22514–22525. Copyright 2015 American Chemical Society. Chapter 9 was adapted from *J. Appl. Phys.* **2016**, *119*, 084101 with the permission of AIP Publishing.

TABLE OF CONTENTS

LIST OF FIGURES

LIST OF TABLES

CHAPTER 1

INTRODUCTION

1.1 Goals

Interfacial properties are largely determined by molecular structures at buried interfaces. Structure-property relationships at buried polymer interfaces, however, are not well understood due to a lack of nondestructive interface sensitive analytical techniques. The overall goals of this thesis are to develop instrumental and data analysis methodologies that can be used to nondestructively characterize interfacial molecular structures at buried polymer interfaces in microelectronic devices and to elucidate the relationship between buried molecular structures and interfacial properties. This thesis focuses on the development of the nonlinear optical technique infrared-visible sum frequency generation (SFG) vibrational spectroscopy into a metrology tool for nondestructive characterization of molecular structures at buried polymer/polymer, metal/polymer, and semiconductor/polymer interfaces in situ. Improved understanding of structure-property relationships enables the rational design of interfaces with improved properties.

In this thesis, four specific aims were investigated. The first aim was to elucidate relationships between interfacial molecular structures at model adhesive polymer interfaces and macroscopic properties. The second specific aim was to extend the first aim by elucidating relationships between interfacial molecular structures at realistic adhesive interfaces in microelectronic packaging and macroscopic properties. The third specific aim was to elucidate

relationships between interfacial molecular structures at low dielectric constant polymer interfaces and macroscopic properties. Finally, the fourth aim was to quantitatively characterize the molecular structures at buried metal/polymer and semiconductor/polymer interfaces in situ.

1.2 Buried Interfaces

Polymer interface engineering has recently experienced a tremendous growth in research activity due to numerous applications of modified interfaces in adhesives, coatings, microelectronics, solar cells, biomedical devices, automotive components, and food packaging[1-5]. In microelectronic packaging applications, polymers must adhere to a variety of other materials (e.g. metals or other polymers) while maintaining specific bulk properties. For example, epoxy based flip-chip underfills need to maintain strong adhesion with organic substrates, solder bumps, and die passivation layers in flip-chip packages[6,7]. In addition, the bulk properties of the underfill (e.g. glass transition temperature, coefficient of thermal expansion, and modulus) need to be within specific ranges[7,8]. Designing epoxy based underfills or molding compounds with both strong adhesion and appropriate bulk properties has been very challenging, because modifying bulk resin properties can result in unfavorable interfacial, and therefore adhesive, changes. Consequently, altering epoxy interfaces without substantially affecting bulk adhesive properties through the use of plasma treatment or interfacial adhesion promoters has been a primary goal of adhesion research in packaging[9-13].

Interfacial properties such as adhesion are strongly dependent on the structure and molecular composition of interfaces[4]. The interfacial structure at polymer interfaces can be substantially different than the molecular structure of polymer bulk materials due to different molecular interactions at the interface compared to the bulk[14]. For example, at polymer/metal interfaces, entropic contributions and molecular interactions can alter the conformation of

polymer chains near the rigid metal surface and thus the properties near the metal interface such as adhesion strength[15-17]. Therefore, characterizing and understanding the structure of polymer interfaces is important for engineering interfaces with tunable properties.

Rationally designing polymer interfaces with targeted properties is very challenging because predictive interfacial structure-property relationships are not well understood. Interfacial properties such as adhesion strength can be measured, however the corresponding interfacial structures at buried polymer interfaces are difficult to study using conventional surface analytical techniques in situ without breaking the interfaces. In recent years, sum frequency generation (SFG) vibrational spectroscopy has been used to characterize polymer/solid interfaces[14,18-23]. Nondestructive characterization of buried polymer interfaces using SFG has led to more detailed understanding of hydrogen bonding, acid-base interactions, water structure, polymer chain conformations, diffusion, and adhesion at polymer interfaces[14,18,24-33]. Although interfacial structures at polymer/polymer interfaces have been studied using SFG, progress in the development of interfacial structure-property relationships has been limited by a lack of direct correlations between the studied interfacial structures and interfacial properties. Furthermore, there are few reports on using SFG to study buried polymer/metal interfacial structures. In this thesis, methodology is developed to elucidate the structure of buried polymer/polymer, polymer/metal and polymer/semiconductor interfaces that have been found to delaminate during microelectronic stress testing or fabrication steps due to weak interfacial adhesion. In addition, interfacial structures at adhesive interfaces are directly correlated to interfacial adhesion properties.

1.3 SFG Theory

In order to probe a polymer interface using infrared-visible SFG, pulsed visible and infrared laser input beams must be overlapped spatially and temporally at an interface. In this thesis, a visible beam with a fixed frequency ω_{VIS} and an infrared beam with a tunable frequency ω_{IR} were utilized for infrared-visible narrowband SFG spectroscopy. In the SFG process, a new beam (ω_{SFG}) is generated at the site where the two input beams overlap[14,19,34,35]. The SFG photons that compose the generated SFG signal beam have a frequency equal to the sum of the two input beam frequencies ($\omega_{SFG} = \omega_{VIS} + \omega_{IR}$).[34] The SFG beam lies in the same plane as the input beams and the output angle of the generated beam (θ_{SFG}) is determined by the input angles of the infrared (θ_{IR}) and visible (θ_{VIS}) beams based on phase matching conditions (Figure 1.1).

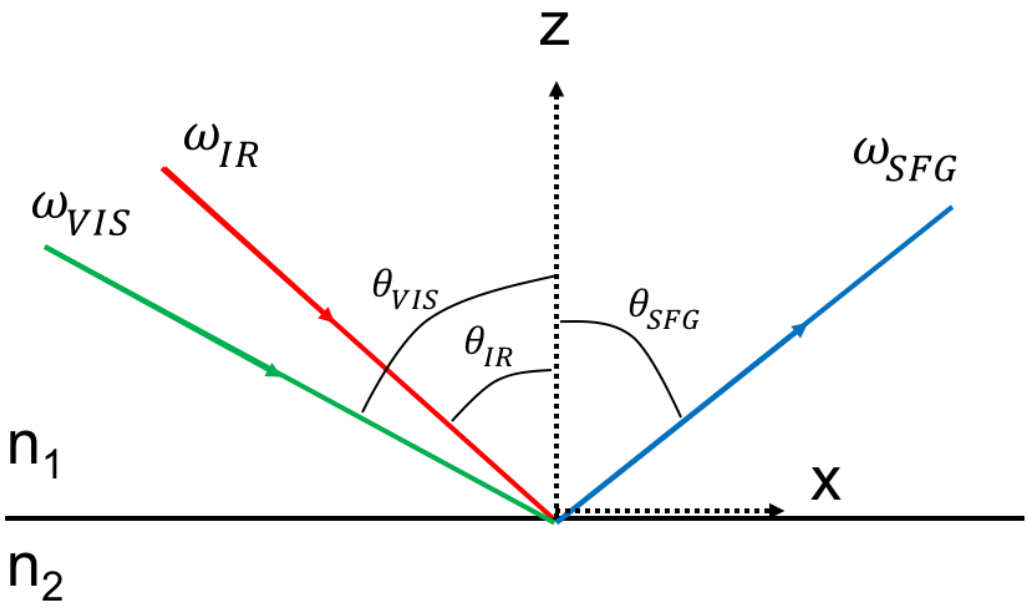

Figure 1.1. Co-propagating SFG experimental geometry showing the input angles θ_{IR} and θ_{VIS} and the output angle θ_{SFG}. The middle horizontal line shows the interface between two media with refractive index values of n_1 and n_2, respectively. The reflected and transmitted portions of the input beams are not shown for clarity. The transmitted SFG beam is not shown because this thesis focuses on the intensity of the reflected beam.

The intensity of the reflected SFG beam, I_{SFG}, generated at the interface between two media is proportional to the square of the second-order nonlinear optical susceptibility of the interface, $\chi^{(2)}_{IJK}$, and to the intensities of the incident visible (I_{VIS}) and infrared (I_{IR}) beams with frequencies of ω_{VIS} and ω_{IR}, respectively[36-38], under the electric dipole approximation:

$$I_{SFG}(\omega_{SFG}) \propto \left|\chi^{(2)}_{eff}\right|^2 \propto \left|\sum_{i,j,k} L_{ii}(\omega_{SFG})\chi^{(2)}_{ijk} L_{jj}(\omega_{VIS})L_{kk}(\omega_{IR})\right|^2 I_{VIS}I_{IR} \quad (1.1)$$

where i, j, k (=x, y, z) are the coordinate axes of the lab frame defined in Figure 1.1. $L_{ii}(\omega_{SFG})$, $L_{jj}(\omega_{VIS})$, and $L_{kk}(\omega_{IR})$ are the Fresnel factors or local field factors which adjust the magnitude of the input electric fields to the local electric fields present at the polarization sheet (i.e. at the interface). The intensity of the generated SFG beam is enhanced when the frequency of the input infrared beam matches a molecular vibrational frequency[14,34]. In a typical SFG spectrum, the intensity of the generated SFG beam is plotted against the frequency of the input infrared beam (in wavenumbers) which provides a vibrational spectrum of the interface.

The second-order nonlinear susceptibility, $\chi^{(2)}$, which is a property of materials, is a third rank tensor that changes sign under the inversion operation: $\chi^{(2)}$ (r) = -$\chi^{(2)}$ (-r). In a uniform material that has inversion symmetry, the value of $\chi^{(2)}$ should be constant at two areas in the material related by an inversion operation at locations r and –r : $\chi^{(2)}$ (r) = $\chi^{(2)}$ (-r). Considering both of these relations, $\chi^{(2)}$ (r) = 0. Therefore, under the electric dipole approximation, no SFG signal will be generated in the bulk of materials that have inversion symmetry[19,34,39,40]. Most bulk polymer materials have inversion symmetry and should not generate SFG signal. At polymer interfaces, the inversion symmetry present in the bulk is broken and $\chi^{(2)}$ (r) does not necessarily equal $\chi^{(2)}$ (-r), so the SFG process is allowed. The polymer materials studied in this thesis have bulk inversion symmetry, so detected SFG signal intensity should be solely contributed by

functional groups or molecules at polymer surfaces and interfaces and any contribution from the polymer bulk can be neglected.

If the interface between media 1 and 2 in Figure 1.1 is isotropic in the x-y plane, only four of the 27 tensor components of $\chi_{ijk}^{(2)}$ will be independent and nonzero[34]. With the lab coordinates defined in Figure 1.1, the nonvanishing components of $\chi^{(2)}$ at the azimuthally isotropic interface are χ_{zzz}, χ_{xxz} (= χ_{yyz}), χ_{xzx} (= χ_{yzy}), and χ_{zxx} (= χ_{zyy}). When the SSP polarization combination is applied ('SSP' indicates s-polarized SFG signal is detected, the visible input beam is s- polarized, and the input IR beam is p-polarized), only χ_{yyz} will be probed[34], so the intensity of the reflected SFG beam in the co-propagating incident beam geometry can be expressed as[36,37]:

$$I_{SFG,SSP}(\omega_{SFG}) \propto \left|-L_{yy}^{I}(\omega_{SFG})L_{yy}^{I}(\omega_{VIS})L_{zz}^{I}(\omega_{IR})sin\theta_{IR}\chi_{yyz}^{(2),I}\right|^2 I_{VIS}I_{IR} \quad (1.2)$$

where θ_{IR} is the infrared beam incident angle in medium 1. The PPP polarization combination will probe all four nonvanishing components of $\chi_{ijk}^{(2)}$, so the intensity of the reflected SFG beam in the co-propagating incident beam geometry can be expressed as[36,37]:

$$\begin{aligned} I_{SFG,PPP}(\omega_{SFG}) \\ &\propto \left|-L_{xx}^{I}(\omega_{SFG})L_{xx}^{I}(\omega_{VIS})L_{zz}^{I}(\omega_{IR})cos\theta_{SFG}cos\theta_{VIS}sin\theta_{IR}\chi_{xxz}^{(2),I}\right. \\ &- L_{xx}^{I}(\omega_{SFG})L_{zz}^{I}(\omega_{VIS})L_{xx}^{I}(\omega_{IR})cos\theta_{SFG}sin\theta_{VIS}cos\theta_{IR}\chi_{xzx}^{(2),I} \\ &+ L_{zz}^{I}(\omega_{SFG})L_{xx}^{I}(\omega_{VIS})L_{xx}^{I}(\omega_{IR})sin\theta_{SFG}cos\theta_{VIS}cos\theta_{IR}\chi_{zxx}^{(2),I} \\ &\left.+ L_{zz}^{I}(\omega_{SFG})L_{zz}^{I}(\omega_{VIS})L_{zz}^{I}(\omega_{IR})sin\theta_{SFG}sin\theta_{VIS}sin\theta_{IR}\chi_{zzz}^{(2),I}\right|^2 I_{VIS}I_{IR} \end{aligned} \quad (1.3)$$

where θ_{SFG} is the reflected angle of the SFG beam in medium 1.

As shown in equation 1.1, both local field factors and $\chi^{(2)}$ affect the intensity of generated SFG beams. In order to determine the magnitude of the second-order nonlinear susceptibility, which contains molecular structural information about interfaces, the contribution of local field factors to the detected SFG intensity needs to be determined. In equation 1.1, the local field factors for the reflected SFG beam generated at the interface between media 1 and 2 can be expressed as[36]:

$$L_{xx}^{I}(\omega) = 1 - r_{12}^{p} \tag{1.4}$$

$$L_{yy}^{I}(\omega) = 1 + r_{12}^{s} \tag{1.5}$$

$$L_{zz}^{I}(\omega) = (1 + r_{12}^{p})(\frac{n_1}{n_m})^2 \tag{1.6}$$

where n_1 and n_2 are the refractive index values for media 1 and 2, respectively, and n_m is the refractive index of the interfacial layer. The linear reflection and transmission coefficients for s- and p-polarized light at the plane boundary separating media i and j are given by[41]:

$$r_{ij}^{p} = \frac{n_j \cos(\theta_i) - n_i \cos(\theta_j)}{n_j \cos(\theta_i) + n_i \cos(\theta_j)} \tag{1.7}$$

$$r_{ij}^{s} = \frac{n_i \cos(\theta_i) - n_j \cos(\theta_j)}{n_i \cos(\theta_i) + n_j \cos(\theta_j)} \tag{1.8}$$

$$t_{ij}^{p} = \frac{2n_i \cos(\theta_i)}{n_j \cos(\theta_i) + n_i \cos(\theta_j)} \tag{1.9}$$

$$t_{ij}^{s} = \frac{2n_i \cos(\theta_i)}{n_i \cos(\theta_i) + n_j \cos(\theta_j)} \tag{1.10}$$

where n_i and n_j are the refractive indices of media i and j, respectively, and θ_i and θ_j are the incident angle in medium i and the transmitted angle into medium j, respectively.

The second-order nonlinear susceptibility of the interface has contributions from resonant and nonresonant terms[34]:

$$\chi_{ijk}^{(2)} = \chi_{NR,ijk}^{(2)} + \sum_q \chi_{R,ijk,q}^{(2)} \tag{1.11}$$

where $\chi^{(2)}_{NR,ijk}$ and $\chi^{(2)}_{R,ijk,q}$ are the nonresonant and resonant terms, respectively. The nonresonant term contributes to a nonresonant background in SFG spectra and does not typically show a dependence on the input infrared frequency. For most polymer materials (e.g. epoxies and low-k dielectrics) and bulk dielectric materials with inversion symmetry used as optical substrates in this thesis (e.g. fused silica and calcium fluoride), the nonresonant term can be neglected and does not contribute to the measured SFG intensity. The nonlinear susceptibilities of metal and semiconductor substrates (e.g. copper and silicon), however, have a relatively large nonresonant term which contributes to measured SFG intensities[34]. The resonant term of $\chi^{(2)}$ is dependent on the molecular structure of interfaces. The resonant component of the macroscopic susceptibility of the interface in the lab frame can be related to the microscopic (molecular) hyperpolarizability ($\beta^{(2)}_{i'j'k'}$) of interfacial molecules or functional groups in the molecular frame (i' j' k') through a cartesian coordinate transformation:[18,34,42]

$$\chi^{(2)}_{ijk,q} = N_s \sum_{i'j'k'=a,b,c} \langle R_{ii'} R_{jj'} R_{kk'} \rangle \beta^{(2)}_{i'j'k',q} \tag{1.12}$$

where R is a direction cosine matrix that projects the microscopic hyperpolarizability onto the lab frame, N_s is the interfacial molecular number density, and the $\langle\ \rangle$ operator indicates a molecular orientational average for interfacial molecules or functional groups. Therefore, $\chi^{(2)}$ is dependent on the microscopic hyperpolarizability of molecules or functional groups at interfaces projected to the lab frame. Consequently, $\chi^{(2)}$ is directly related to the orientation angle of interfacial molecules or functional groups relative to the lab frame, as discussed below.

When both ω_{VIS} and ω_{SFG} are far from an allowed electronic resonance, the microscopic hyperpolarizability of interfacial molecules can be expressed as[43]

$$\beta^{(2)}_{i'j'k'} = \frac{\beta_{q,i'j'k'}}{\omega_{IR} - \omega_q + i\Gamma_q} \tag{1.13}$$

where $\beta_{q,i'j'k'}$, ω_q, and Γ_q are the magnitude, resonant frequency, and damping coefficient of the vibrational mode q. The magnitude of the resonant component of the microscopic hyperpolarizability of molecules or functional groups at interfaces ($\beta^{(2)}_{i'j'k'}$) is related to the vibrational mode q by:

$$\beta^{(2)}_{i'j'k',q} \propto \frac{\partial \alpha^*_{i'j'}}{\partial Q_q}\frac{\partial u_{k'}}{\partial Q_q} \tag{1.14}$$

where Q_q is the normal coordinate, $\frac{\partial \alpha^*_{i'j'}}{\partial Q_q}$ is the Raman polarizability derivative of the vibrational mode q, $\frac{\partial u_{k'}}{\partial Q_q}$ is the infrared dipole moment derivative of the vibrational mode q, and the "*" indicates the complex conjugate[34,36]. Therefore, molecular vibrational modes detected in SFG spectroscopy must be both infrared and Raman active.

The dependence of the macroscopic resonant susceptibility on the input infrared frequency and the resonant frequency of the vibrational mode q can then be expressed as[34]

$$\chi^{(2)}_{ijk} = \chi^{(2)}_{NR,ijk} + N_s \sum_q \frac{\langle R_{Ii'} R_{Jj'} R_{Kk'}\rangle \beta_{q,i'j'k'}}{\omega_{IR} - \omega_q + i\Gamma_q} \tag{1.15}$$

As the infrared beam frequency is scanned across the resonant frequency of the vibrational mode q (as ω_{IR} approaches ω_q) , the second term of equation 1.15 will change in magnitude, resulting in a change in the intensity of the generated SFG beam (equation 1.1) that appears as a feature in SFG spectra.

In this thesis, the orientation of methyl groups, phenyl groups, and imide rings at buried interfaces is discussed. In each case, the relationship between $\chi^{(2)}_{ijk,q}$ and $\beta^{(2)}_{i'j'k',q}$ for the detected vibrational modes had been previously derived using eq 1.12 and each relationship is discussed as necessary. In this thesis, methyl groups are assumed to have C_{3v} symmetry and the second order nonlinear resonant susceptibilities of the methyl symmetric stretching vibrational mode can

be expressed as[34,36]:

$$\chi_{zzz}^{(2)} = N_s\beta_{ccc}^{(2)}[R\langle cos\theta\rangle + \langle cos^3\theta\rangle(1-R)] \quad (1.16)$$

$$\chi_{xxz}^{(2)} = \chi_{yyz}^{(2)} = \frac{1}{2}N_s\beta_{ccc}^{(2)}[\langle cos\theta\rangle(1+R) - \langle cos^3\theta\rangle(1-R)] \quad (1.17)$$

$$\chi_{xzx}^{(2)} = \chi_{yzy}^{(2)} = \chi_{zxx}^{(2)} = \chi_{zyy}^{(2)} = \frac{1}{2}N_s\beta_{ccc}^{(2)}(1-R)[\langle cos\theta\rangle - \langle cos^3\theta\rangle] \quad (1.18)$$

The second order nonlinear susceptibilities of the methyl asymmetric stretching vibrational mode can be expressed as[34,36]:

$$\chi_{zzz}^{(2)} = 2N_s\beta_{aca}^{(2)}[\langle cos\theta\rangle - \langle cos^3\theta\rangle] \quad (1.19)$$

$$\chi_{xxz}^{(2)} = \chi_{yyz}^{(2)} = -N_s\beta_{aca}^{(2)}[\langle cos\theta\rangle - \langle cos^3\theta\rangle] \quad (1.20)$$

$$\chi_{xzx}^{(2)} = \chi_{yzy}^{(2)} = \chi_{zxx}^{(2)} = \chi_{zyy}^{(2)} = N_s\beta_{aca}^{(2)}\langle cos^3\theta\rangle \quad (1.21)$$

Resonant line shapes in SFG spectra depend on the modulus and phase of the resonant and non-resonant susceptibilities of the effective nonlinear susceptibility[34]

$$I_{SFG} \propto \left|\chi_{eff}^{(2)}\right|^2 \propto \left|\left|\chi_{NR,ijk}^{(2)}\right|e^{i\varepsilon} + \left|\chi_{R,ijk}^{(2)}\right|e^{i\delta}\right|^2 \propto$$

$$\left|\chi_{NR,ijk}^{(2)}\right|^2 + \left|\chi_{R,ijk}^{(2)}\right|^2 + 2\left|\chi_{NR,ijk}^{(2)}\right|\left|\chi_{R,ijk}^{(2)}\right|\cos[\varepsilon - \delta] \quad (1.22)$$

$\chi_{NR,ijk}^{(2)}$ and $\chi_{R,ijk}^{(2)}$ are the non-resonant and resonant susceptibility components of $\chi_{eff}^{(2)}$, respectively, and ε and δ are the phases of the non-resonant and resonant susceptibilities, respectively[66]. When $|\chi_{NR}| \geq |\chi_R|$, the phase difference between the non-resonant and resonant susceptibilities in the third term of equation 1.22 significantly influences the SFG intensity and peak shape. Consequently, when $\chi_{NR,ijk}^{(2)} \sim 0$ (e.g. at polymer/polymer interfaces), SFG features will appear as positive peaks in SFG spectra. When $|\chi_{NR}| \geq |\chi_R|$ (e.g. SFG spectra acquired from thin epoxy films on copper or low-k dielectric films on silicon), SFG features may appear as

positive peaks or negative dips. It should be emphasized that the peak centers of SFG features found by fitting SFG spectra are the same regardless of the peak shape. This enables different SFG geometries to be used for the identification of functional groups at interfaces based on unique resonance frequencies that are both infrared and Raman active.

For one contributing interface, the effective second-order nonlinear susceptibility can be obtained from experimental SFG spectra by fitting using equation 1.23:[18]

$$I_{SFG}(\omega) \propto \left|\chi_{eff}^{(2)}\right|^2 \propto \left|\chi_{NR}e^{i\phi} + \sum_q \frac{A_q}{\omega_{IR}-\omega_q+i\Gamma_q}\right|^2 \quad (1.23)$$

where ϕ is the phase difference between the resonant and non-resonant susceptibility and A_q is the amplitude of the vibrational mode q. To obtain interfacial molecular structure information about polymer interfaces when only one interface contributed to the detected SFG signal, SFG spectra were collected from polymer interfaces using the SSP and PPP polarization combinations. The value of $\chi_{R,ijk}^{(2)}$ was then obtained using the relation $\chi_{ijk,q}^{(2)} = \frac{A_{ijk,q}}{\Gamma_{ijk,q}}$.[18]

When a thin film is located between two media as shown in Figure 1.2b, SFG signal can be generated at interfaces I and II because the centrosymmetry of medium 2 is broken at each interface.

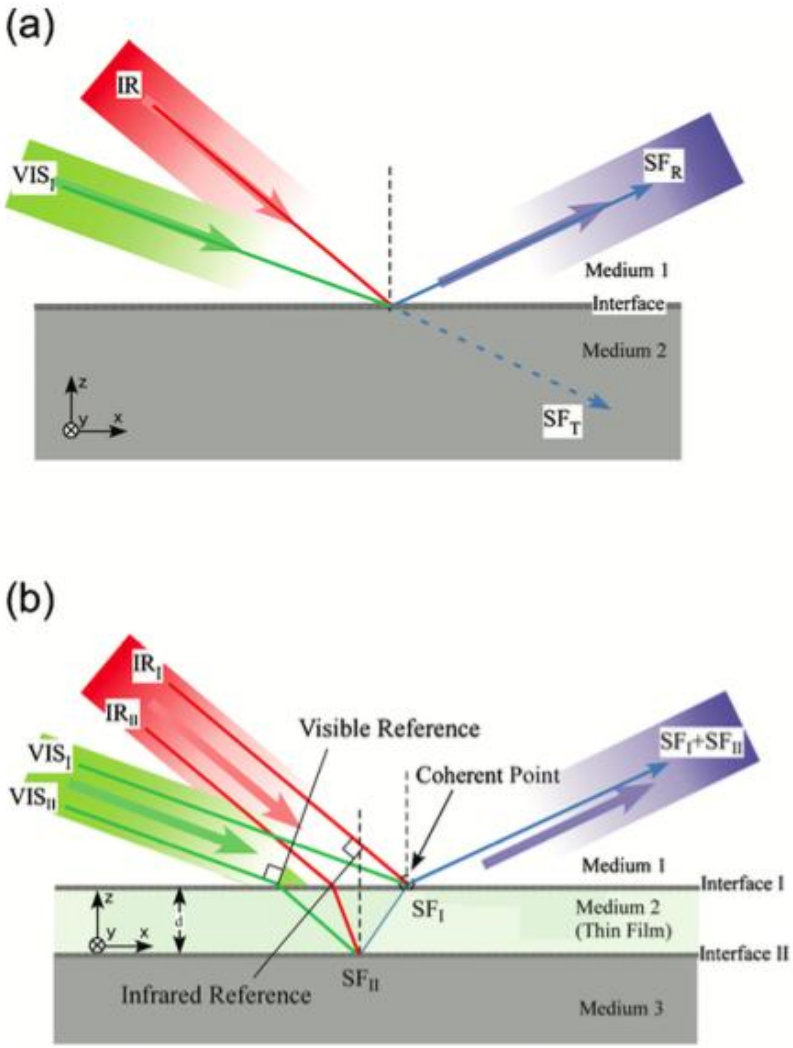

Figure 1.2. (a) SFG signal contributed from one interface between media 1 and 2. (b) SFG signal contributed from two interfaces at the surface (Interface I) and buried interface (Interface II) of a supported thin film. Adapted from reference 34 with permission.

The intensity of the reflected SFG beam will then be proportional to the sum of the SFG signal contributions from the two interfaces[36,37]

$$I_{SFG}(\omega_{SFG}) \propto \left|\sum_{i,j,k} L_{ii}^{I}(\omega_{SFG})\chi_{ijk}^{(2),I} L_{jj}^{I}(\omega_{VIS})L_{kk}^{I}(\omega_{IR}) + \sum_{i,j,k} L_{ii}^{II}(\omega_{SFG})\chi_{ijk}^{(2),II} L_{jj}^{II}(\omega_{VIS})L_{kk}^{II}(\omega_{IR})\right|^2 \quad (1.24)$$

Multiple reflections of the input and generated beams within medium 2 lead to film thickness dependent interference of the reflected SFG beam. When the SSP polarization combination is applied to probe χ_{yyz}, the intensity of the reflected SFG beam in the co-propagating incident beam geometry can be expressed as

$$I_{SFG,SSP}(\omega_{SFG}) \propto \left| \begin{matrix} -L_{yy}^{I}(\omega_{SFG})L_{yy}^{I}(\omega_{VIS})L_{zz}^{I}(\omega_{IR})sin\theta_{IR}\chi_{yyz}^{(2),I} \\ -L_{yy}^{II}(\omega_{SFG})L_{yy}^{II}(\omega_{VIS})L_{zz}^{II}(\omega_{IR})sin\theta_{IR}\chi_{yyz}^{(2),II} \end{matrix} \right|^2 I_{VIS}I_{IR} \quad (1.25)$$

where θ_{IR} is the infrared beam incident angle in medium 1.[36,37] The PPP polarization combination will probe all four nonvanishing components of $\chi_{ijk}^{(2)}$, so the intensity of the reflected SFG beam in the co-propagating incident beam geometry can be expressed as:

$$\begin{aligned} & I_{SFG,PPP}(\omega_{SFG}) \\ & \propto \left| -L_{xx}^{I}(\omega_{SFG})L_{xx}^{I}(\omega_{VIS})L_{zz}^{I}(\omega_{IR})cos\theta_{SFG}cos\theta_{VIS}sin\theta_{IR}\chi_{xxz}^{(2),I} \right. \\ & - L_{xx}^{I}(\omega_{SFG})L_{zz}^{I}(\omega_{VIS})L_{xx}^{I}(\omega_{IR})cos\theta_{SFG}sin\theta_{VIS}cos\theta_{IR}\chi_{xzx}^{(2),I} \\ & + L_{zz}^{I}(\omega_{SFG})L_{xx}^{I}(\omega_{VIS})L_{xx}^{I}(\omega_{IR})sin\theta_{SFG}cos\theta_{VIS}cos\theta_{IR}\chi_{zxx}^{(2),I} \\ & + L_{zz}^{I}(\omega_{SFG})L_{zz}^{I}(\omega_{VIS})L_{zz}^{I}(\omega_{IR})sin\theta_{SFG}sin\theta_{VIS}sin\theta_{IR}\chi_{zzz}^{(2),I} \\ & - L_{xx}^{II}(\omega_{SFG})L_{xx}^{II}(\omega_{VIS})L_{zz}^{II}(\omega_{IR})cos\theta_{SFG}cos\theta_{VIS}sin\theta_{IR}\chi_{xxz}^{(2),II} \\ & - L_{xx}^{II}(\omega_{SFG})L_{zz}^{II}(\omega_{VIS})L_{xx}^{II}(\omega_{IR})cos\theta_{SFG}sin\theta_{VIS}cos\theta_{IR}\chi_{xzx}^{(2),II} \\ & + L_{zz}^{II}(\omega_{SFG})L_{xx}^{II}(\omega_{VIS})L_{xx}^{II}(\omega_{IR})sin\theta_{SFG}cos\theta_{VIS}cos\theta_{IR}\chi_{zxx}^{(2),II} \\ & \left. + L_{zz}^{II}(\omega_{SFG})L_{zz}^{II}(\omega_{VIS})L_{zz}^{II}(\omega_{IR})sin\theta_{SFG}sin\theta_{VIS}sin\theta_{IR}\chi_{zzz}^{(2),II} \right|^2 I_{VIS}I_{IR} \end{aligned} \quad (1.26)$$

where θ_{SFG} is the reflected angle of the SFG beam in medium 1.[36,37]

The local field factors (L factors) at interface I are given by[36,37]:

$$L_{xx}^{I}(\omega) = \frac{t_{12}^{p}}{1+r_{12}^{p}r_{23}^{p}e^{2i\beta}}(1 - r_{23}^{p}e^{2i\beta})\frac{cos\theta_2}{cos\theta_1} \quad (1.27)$$

$$L_{yy}^{I}(\omega) = \frac{t_{12}^{s}}{1+r_{12}^{s}r_{23}^{s}e^{2i\beta}}(1 + r_{23}^{s}e^{2i\beta}) \quad (1.28)$$

$$L_{zz}^{I}(\omega) = \frac{t_{12}^{p}}{1+r_{12}^{p}r_{23}^{p}e^{2i\beta}}(1 + r_{23}^{p}e^{2i\beta})\frac{n_1 n_2}{n_{m,12}^{2}} \quad (1.29)$$

$$\beta = \frac{2\pi}{\lambda}n_2 d cos\theta_2 \quad (1.30)$$

where λ is the wavelength of the beam in nm, ω is the beam frequency, and θ_1 and θ_2 are the beam incident angles in medium 1 and medium 2, respectively. In this thesis, the unit of thickness of the film (d) is nm and $n_{m,12}$ is the refractive index of the interface. The local field factors at interface II are given by[36,37]:

$$L_{xx}^{II}(\omega) = e^{i\Delta}\frac{t_{12}^{p}}{1+r_{12}^{p}r_{23}^{p}e^{2i\beta}}(1 - r_{23}^{p}e^{2i\beta})\frac{cos\theta_2}{cos\theta_1} \quad (1.31)$$

$$L_{yy}^{II}(\omega) = e^{i\Delta}\frac{t_{12}^{s}}{1+r_{12}^{s}r_{23}^{s}e^{2i\beta}}(1 + r_{23}^{s}) \quad (1.32)$$

$$L_{zz}^{II}(\omega) = e^{i\Delta}\frac{t_{12}^{p}}{1+r_{12}^{p}r_{23}^{p}e^{2i\beta}}(1 + r_{23}^{p}e^{2i\beta})\frac{n_1 n_2}{n_{m,23}^{2}} \quad (1.33)$$

where

$$\Delta_{SFG} = \frac{2\pi n_{2,SFG} d}{\lambda_{SFG} cos\theta_{2,SFG}} \quad (1.34)$$

$$\Delta_{VIS} = \frac{2\pi n_{2,VIS} d}{\lambda_{VIS} cos\theta_{2,VIS}} - \frac{2\pi n_{1,VIS} d}{\lambda_{VIS}}(tan\theta_{2,VIS} + tan\theta_{2,SFG})sin\theta_{1,VIS} \quad (1.35)$$

$$\Delta_{IR} = \frac{2\pi n_{2,IR} d}{\lambda_{IR} cos\theta_{2,IR}} - \frac{2\pi n_{1,IR} d}{\lambda_{VIS}}(tan\theta_{2,IR} + tan\theta_{2,SFG})sin\theta_{1,IR} \quad (1.36)$$

In this thesis, SFG spectra are acquired from thin polymer films where two interfaces contribute to the detected SFG signal intensity. At each interface, both the local field factors and the interfacial molecular structure contribute to the intensity of the measured SFG signal. Analytical expressions for the local field factors allow their contribution to the signal to be deduced. After the local field factor contributions are known, measured SFG intensities can be

directly related to $\chi^{(2)}$, and thus to interfacial molecular structures. More details about the separation of local field factors and $\chi^{(2)}$ to detected SFG intensities will be discussed in later chapters.

1.4 SFG Instrumentation

In this thesis, all SFG spectra were acquired using a commercial SFG spectrometer purchased from EKSPLA (Vilnius, Lithuania). The SFG system was pumped with a picosecond Nd:YAG laser to generate the input visible and infrared beams. The fundamental output from the Nd:YAG laser was a 1064 nm beam with a 50 Hz repetition rate and a ~30 picosecond pulse duration. The fixed frequency input visible beam was generated by frequency-doubling the fundamental output from the Nd:YAG laser. The frequency tunable infrared beam was generated using an optical parametric generation (OPG)/optical parametric amplification (OPA)/difference frequency generation (DFG) system, referred to as the 'optical parametric generator' in Figure 1.3. The fixed frequency 532 nm visible input beam and frequency tunable infrared beam (2.3 – 10.0 μm) were overlapped spatially and temporally at various polymer interfaces (located in the "Sample stage" in Figure 1.3. The input angles and beam energies for the visible and infrared beams are reported in each chapter. Both beam diameters were approximately 500 μm at the interfaces. The reflected SFG beam was directed through a monochromator after which the beam intensity was measured using a photomultiplier tube (PMT) (Hamamatsu Corp.). All SFG spectra were collected in the SSP (s-polarized SFG signal, s-polarized input visible, and p-polarized input infrared) and PPP polarization combinations by scanning the infrared beam frequency in 5 cm^{-1} steps while the monochromator was tuned automatically.

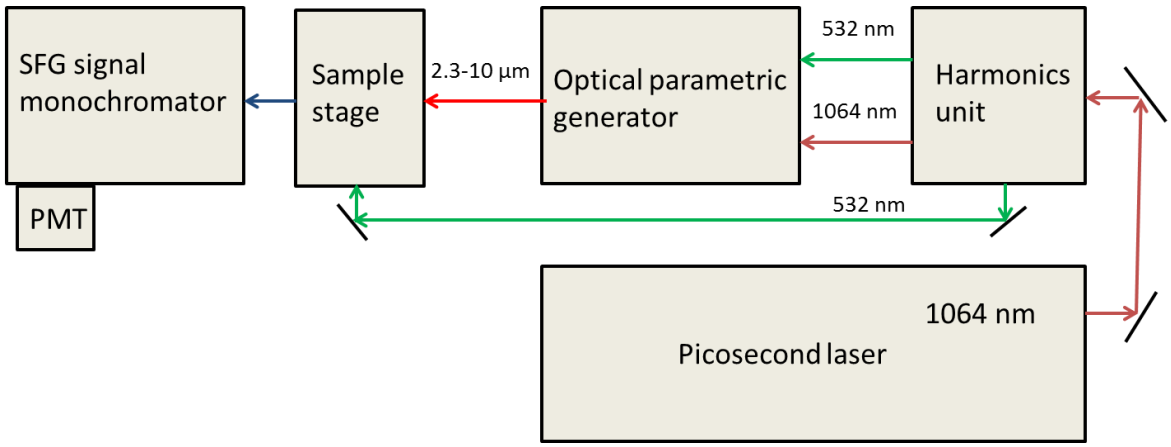

Figure 1.3. Diagram of the commercial EKSPLA SFG spectrometer used in this thesis.

1.5 SFG Analysis of Buried Polymer Interfaces

As discussed above, a typical SFG spectrum displays the intensity of a generated SFG beam plotted against the frequency of the input infrared beam which provides a vibrational spectrum of the interface. Analysis of SFG spectra enables quantitative and qualitative characterization of molecular structures at interfaces[18,34]. The peak centers of SFG signals enable selective identification of functional groups present at interfaces based on characteristic functional group vibrational frequencies. The intensity of SFG peaks can provide quantitative information about the spatial configuration of the detected functional groups such as orientation, orientation distribution, and surface coverage.

In a typical SFG experiment used to probe the surface of a polymer film or a buried polymer/polymer interface, a thin polymer film is first deposited onto a dielectric optical substrate that is transparent in the visible and mid infrared spectral regions such as fused silica or calcium fluoride. Next, the input laser beams are directed through the substrate and are overlapped at the polymer surface or buried interface, referred to as a 'face down' geometry (Figure 1.4a). An SFG spectrum is then acquired by measuring the intensity of the reflected SFG

beam plotted against the input infrared frequency in wavenumbers. Previous studies in the Chen lab have demonstrated that when a face down geometry is used to acquire SFG spectra from thin polymer films on optical substrates, the measured SFG intensity is dominated by signal contributed by the polymer/air interface for many common polymers such as poly methyl methacrylate[18]. Therefore, the face down geometry is frequently used to selectively characterize the molecular structure of polymer/air interfaces. To probe buried polymer/polymer interfaces, a thin (hundreds of nanometers) film is first deposited on an optical substrate after which a thick (>10 μm) polymer film is deposited on the first film (Figure 1.4b). The thickness of the second layer would attenuate the mid-IR beam and would thus prevent SFG signal generation at the thick polymer/air interface. If the SFG signal contributed from the substrate/thin polymer interface is negligible (discussed in chapter 3) then the detected SFG intensity is selectively contributed by signal from the buried polymer/polymer interface.

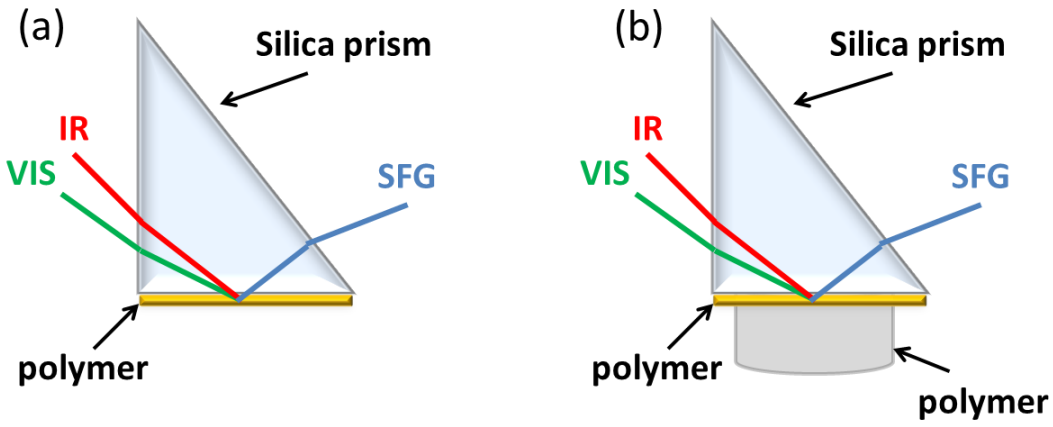

Figure 1.4. Diagram showing the face down SFG experimental geometry used to acquire SFG spectra from (a) polymer surfaces and (b) buried polymer/polymer interfaces.

To probe a buried polymer/metal interface using SFG, it is necessary to ensure that the two input laser beams can reach the buried interface to generate SFG signal. Metal substrates are usually not transparent to either visible or mid IR beams, therefore the visible and IR input beams should reach the interface from the polymer side (Figure 1.2b). If the polymer sample is thick, it would attenuate the mid-IR beam. Therefore, an appropriate sample geometry to probe buried polymer/metal interfaces is a polymer film on metal, where the polymer film is thin and its absorption of the mid IR laser is negligible. However, for a thin polymer film on a metal surface, SFG signal can be generated from both the buried polymer/metal interface as well as the polymer surface in air. Because the polymer film is thin, it is difficult to physically separate these two signal beams. To deconvolute the signal contributed from the buried interface, our group has successfully developed several methods to selectively probe the buried polymer film/metal interface using SFG.

In one of the first reports on using SFG to probe metal/polymer interfaces, SFG ssp spectra were collected from a series of poly(methyl methacrylate) (PMMA) films with varied thicknesses[44]. Because the film thickness is varied, the SFG signals collected from the surface in air and the buried polymer/metal interface interfere with each other differently. By carefully fitting the spectra using the surface contribution and the interfacial contribution as a function of film thickness, the SFG signal contributed from the buried PMMA/metal interface was successfully deconvoluted to deduce the buried interface structure[41].

Later, methodology was developed to minimize signal contributed by the polymer surface by placing a "cap" on top of a thin polymer film deposited on metal. Particularly, a fused silica window was placed on top of the polymer. Because the polymer is disordered at the silica/polymer interface, no SFG signal could be generated from the buried polymer/fused silica

interface. Therefore, the detected SFG signal was solely contributed from the polymer/metal interface[45].

As an extension of the previously developed methodology, SFG spectra collected from a thin polymer film deposited on a metal using ppp (all the input and output signals are in p-polarization) polarization combination was found to be dominantly contributed from the buried polymer/metal interface. Therefore, the buried polymer/metal interface could be directly probed by collecting SFG ppp spectra from a polymer film on metal in air[46]. Prior to the application of SFG to study a buried interface, the buried interface had to be separated and the two exposed surfaces were studied, which likely would alter the original interfacial interactions and the results obtained might not accurately reflect the interfacial structure. Differently, SFG could probe buried polymer/metal interfaces in situ.

However, each of the above three methods can have disadvantages: The preparation of a series of polymer samples with different thicknesses, the accurate measurement of the film thickness, and the spectral fitting for all the spectra using the same set of fitting parameters are tedious and labor intensive. The application of a "cap" may not be general; for certain polymers a suitable cap may not be available. SFG ppp spectra probe four tensor components of the second order nonlinear optical susceptibility, so the data analysis is not straightforward. Therefore, for different polymer/metal or polymer/semiconductor interfaces, it is necessary to choose the most appropriate method to probe the buried interfacial structure, which will be explored in this dissertation.

1.6 Presented Research

The first half of this thesis describes the development of methodology for nondestructive characterization of molecular structures at buried polymer/epoxy and metal/epoxy interfaces.

The second half describes methodology for the characterization of silicon/low-k dielectric interfaces in situ. In chapter 2, we report that the surface molecular structure of spin cast homopolymers which contain phenyl groups is influenced by the solvent aromaticity. In chapter 3, we elucidated the molecular structure at buried polymer/epoxy interfaces before and after plasma treatment. In chapter 4, molecular structural changes at buried polymer/epoxy interfaces are related to changes in macroscopic adhesion strength. In chapter 5, we extended previous research on metal/polymer interfaces by developing methodology to nondestructively characterize the molecular structure at buried copper/epoxy interfaces in situ. In chapter 6, methodology is developed to achieve in situ observation of water structure and water-induced structure changes at low-k dielectric surfaces and the buried interfaces at the molecular level by combining SFG vibrational spectroscopic and Fourier transform infrared (FTIR) spectroscopic studies. In chapter 7, in situ nondestructive methodology is developed to simultaneously characterize the molecular structure at the surface and buried interface of silicon-supported low-k dielectric thin films. In chapter 8, the methodology developed in chapter 7 is applied to characterize the effects of plasma on low-k interfaces with different porosities provided by Intel. In chapter 9, the methodology described in chapter 7 and 8 was used to characterize real industrial low-k films before and after manufacturing scale processing steps performed at IBM. The impacts of the research will be explicitly presented at the end of each chapter and will not be repeated here.

1.7 References

(1) Ho, P. K.; Kim, J. S.; Burroughes, J. H.; Becker, H.; Li, S. F.; Brown, T. M.; Cacialli, F.; Friend, R. H. Molecular-scale interface engineering for polymer light-emitting diodes. *Nature* **2000**, *404*, 481.

(2) Ma, H.; Yip, H. L.; Huang, F.; Jen, A. K. Y. Interface engineering for organic electronics. *Adv. Funct. Mater.* **2010**, *20*, 1371.

(3) Ma, Z.; Mao, Z.; Gao, C. Surface modification and property analysis of biomedical polymers used for tissue engineering. *Colloids and surfaces. B, Biointerfaces* **2007**, *60*, 137.

(4) Awaja, F.; Gilbert, M.; Kelly, G.; Fox, B.; Pigram, P. J. Adhesion of polymers. *Prog. Polym. Sci.* **2009**, *34*, 948.

(5) Goddard, J. M.; Hotchkiss, J. H. Polymer surface modification for the attachment of bioactive compounds. *Prog. Polym. Sci.* **2007**, *32*, 698.

(6) Paquet, M.-C.; Gaynes, M.; Duchesne, E.; Questad, D.; Belanger, L.; Sylvestre, J. Underfill Selection Strategy for Pb-Free, Low-K and Fine Pitch Organic Flip Chip Applications. Electronic Components and Technology Conference, 2006. Proceedings. 56th. IEEE, 2006; pp 1595–1603.

(7) Zhang, Z. Q.; Wong, C. P. Recent advances in flip-chip underfill: materials, process, and reliability. *IEEE T. Adv. Packaging* **2004**, *27*, 515.

(8) Ong, Y. Y.; Ho, S. W.; Sekhar, V. N.; Ong, X. F.; Ong, J.; Zhang, X. W.; Vaidyanathan, K.; Yoon, S. U.; Lau, J. H.; Kheng, L. Y.; Yeo, D.; Chan, K. C.; Zhang, Y. F.; Tan, J. B.; Sohn, D. K. Underfill Selection, Characterization, and Reliability Study for Fine-Pitch, Large Die Cu/Low-K Flip Chip Package. *IEEE T. Comp. Pack. Man.* **2011**, *1*, 279.

(9) Shin, D. K.; Lee, H. S.; Im, J. Chemical and Mechanical Analysis of PCB Surface Treated by Argon Plasma to Enhance Interfacial Adhesion. *IEEE T. Electron. Pack.* **2009**, *32*, 281.

(10) Sham, M. L. I.; Kim, J. K. Improved underfill adhesion in flip-chip packages by means of ultraviolet light/ozone treatment. *IEEE T. Adv. Packaging* **2004**, *27*, 179.

(11) Luo, S.; Wong, C. P. Influence of Temperature and Humidity on Adhesion of Underfills for Flip Chip Packaging. *IEEE Transactions on Components and Packaging Technologies* **2005**, *28* (1), 88–94.

(12) Song, S. M.; Cho, K.; Park, C. E.; Yun, H. K.; Oh, S. Y. Synthesis and characterization of water-soluble polymeric adhesion promoter for epoxy resin/copper joints. *J. Appl. Polym. Sci.* **2002**, *85*, 2202.

(13) Wong, C. K. Y.; Yuen, M. M. F.; Xu, B. Thiol-based self-assembly nanostructures in promoting interfacial adhesion for copper-epoxy joint. *Appl. Phys. Lett.* **2009**, *94*.

(14) Chen, Z. Investigating buried polymer interfaces using sum frequency generation vibrational spectroscopy. *Prog. Polym. Sci.* **2010**, *35*, 1376.

(15) Delle Site, L.; Abrams, C. F.; Alavi, A.; Kremer, K. Polymers near Metal Surfaces: Selective Adsorption and Global Conformations. *Physical review letters* **2002**, *89*, 156103.

(16) Abrams, C. F.; Delle Site, L.; Kremer, K. Dual-resolution coarse-grained simulation of the bisphenol-a-polycarbonate/nickel interface. *Physical review. E, Statistical, nonlinear, and soft matter physics* **2003**, *67*, 021807.

(17) Delle Site, L.; Leon, S.; Kremer, K. BPA-PC on a Ni (111) surface: The interplay between adsorption energy and conformational entropy for different chain-end modifications. *J. Am. Chem. Soc.* **2004**, *126*, 2944.

(18) Zhang, C.; Myers, J. N.; Chen, Z. Elucidation of molecular structures at buried polymer interfaces and biological interfaces using sum frequency generation vibrational spectroscopy. *Soft Matter* **2013**, *9*, 4738.

(19) Ye, S.; Tong, Y. J.; Ge, A. M.; Qiao, L.; Davies, P. B. Interfacial Structure of Soft Matter Probed by SFG Spectroscopy. *Chem. Rec.* **2014**, *14*, 791.

(20) Kearns, P. M.; O'Brien, D. B.; Massari, A. M. Optical Interference Enhances Nonlinear Spectroscopic Sensitivity: When Light Gives You Lemons, Model Lemonade. *J. Phys. Chem. Lett.* **2016**, *7*, 62.

(21) Zhang, C.; Shephard, N. E.; Rhodes, S. M.; Chen, Z. Headgroup Effect on Silane Structures at Buried Polymer/Silane and Polymer/Polymer Interfaces and Their Relations to Adhesion. *Langmuir* **2012**, *28*, 6052.

(22) Zhang, C.; Chen, Z. Quantitative Molecular Level Understanding of Ethoxysilane at Poly(dimethylsiloxane)/Polymer Interfaces. *Langmuir* **2013**, *29*, 610.

(23) Zhang, C.; Chen, Z. Probing Molecular Structures of Poly(dimethylsiloxane) at Buried Interfaces *in Situ*. *J. Phys. Chem. C* **2013**, *117*, 3903.

(24) Zhu, H.; Dhopatkar, N.; Dhinojwala, A. Effect of Acid–Base Interactions on Conformation of Adsorbed Polymer Chains. *ACS Macro Lett.* **2016**, *5*, 45.

(25) Zhou, J.; Anim-Danso, E.; Zhang, Y.; Zhou, Y.; Dhinojwala, A. Interfacial Water at Polyurethane–Sapphire Interface. *Langmuir* **2015**, *31*, 12401.

(26) Myers, J. N.; Zhang, C.; Lee, K. W.; Williamson, J.; Chen, Z. Hygrothermal aging effects on buried molecular structures at epoxy interfaces. *Langmuir* **2014**, *30*, 165.

(27) Chen, C. Y.; Wang, J.; Loch, C. L.; Ahn, D.; Chen, Z. Demonstrating the Feasibility of Monitoring the Molecular-Level Structures of Moving Polymer/Silane Interfaces during Silane Diffusion Using SFG. *J. Am. Chem. Soc.* **2004**, *126*, 1174.

(28) Loch, C. L.; Ahn, D. C.; Chen, C. Y.; Chen, Z. Polymer-silane interactions probed by sum frequency generation vibrational spectroscopy. *J. Adhesion* **2005**, *81*, 319.

(29) Loch, C. L.; Ahn, D.; Chen, Z. Sum Frequency Generation Vibrational Spectroscopic Studies on a Silane Adhesion-Promoting Mixture at a Polymer Interface. *J. Phys. Chem. B* **2006**, *110*, 914.

(30) Loch, C. L.; Ahn, D. C.; Vazquez, A. V.; Chen, Z. Diffusion of one or more components of a silane adhesion-promoting mixture into poly (methyl methacrylate). *J Colloid Interf. Sci.* **2007**, *308*, 170.

(31) Vazquez, A. V.; Shephard, N. E.; Steinecker, C. L.; Ahn, D.; Spanninga, S.; Chen, Z. Understanding molecular structures of silanes at buried polymer interfaces using sum frequency generation vibrational spectroscopy and relating interfacial structures to polymer adhesion. *J. Colloid Interf. Sci.* **2009**, *331*, 408.

(32) Vazquez, A. V.; Boughton, A. P.; Shephard, N. E.; Rhodes, S. M.; Chen, Z. Molecular Structures of the Buried Interfaces between Silicone Elastomer and Silane Adhesion Promoters Probed by Sum Frequency Generation Vibrational Spectroscopy and Molecular Dynamics Simulations. *ACS Appl. Mater. Inter.* **2010**, *2*, 96.

(33) Vazquez, A. V.; Holden, B.; Kristalyn, C.; Fuller, M.; Wilkerson, B.; Chen, Z. Surface and Buried Interfacial Structures of Epoxy Resins Used as Underfills Studied by Sum Frequency Generation Vibrational Spectroscopy. *ACS Appl. Mater. Inter.* **2011**, *3*, 1640.

(34) Lambert, A. G.; Davies, P. B.; Neivandt, D. Implementing the theory of sum frequency generation vibrational spectroscopy: a tutorial review. J. *Appl. Spectrosc. Rev.* **2005**, *40*, 103.

(35) Yan, E. C. Y.; Fu, L.; Wang, Z. G.; Liu, W. Biological macromolecules at interfaces probed by chiral vibrational sum frequency generation spectroscopy. *Chem. Rev.* **2014**, *114*, 8471.

(36) Tong, Y.; Zhao, Y.; Li, N.; Osawa, M.; Davies, P. B.; Ye, S. Interference Effects in the Sum Frequency Generation Spectra of Thin Organic Films. I. Theoretical Modeling and Simulation. *J. Chem. Phys.* **2010**, *133*, 034704.

(37) Backus, E. H. G.; Garcia-Araez, N.; Bonn, M.; Bakker, H. J. On the Role of Fresnel Factors in Sum-Frequency Generation Spectroscopy of Metal–Water and Metal-Oxide–Water Interfaces. *J. Phys. Chem. C* **2012**, *116*, 23351–23361.

(38) Lu, X.; Clarke, M. L.; Li, D.; Wang, X.; Xue, G.; Chen, Z. A Sum Frequency Generation Vibrational Study of the Interference Effect in Poly(*n* -Butyl Methacrylate) Thin Films Sandwiched between Silica and Water. *J. Phys. Chem. C* **2011**, *115*, 13759–13767.

(39) Chen, Z.; Shen, Y. R.; Somorjai, G. A. Studies of polymer surfaces by sum frequency generation vibrational spectroscopy. *Annu. Rev. Phys. Chem.* **2002**, *53*, 437.

(40) Shen, Y. R. Basic Theory of Surface Sum-Frequency Generation. *J. Phys. Chem. C* **2012**, *116*, 15505.

(41) Fowles, G. R. *Introduction to Modern Optics*; 2nd ed., Dover ed.; Dover Publications: New York, 1989.

(42) Roy, S.; Hung, K.-K.; Stege, U.; Hore, D. K. Rotations, projects, direction cosines, and vibrational spectra. *Appl. Spectrosc. Rev.* **2013,** *49*, 233.

(43) Gan, W.; Wu, D.; Zhang, Z.; Feng, R.; Wang, H. Polarization and Experimental Configuration Analyses of Sum Frequency Generation Vibrational Spectra, Structure, and Orientational Motion of the Air/water Interface. *J. Chem. Phys.* **2006**, *124*, 114705.

(44) Lu, X.; Shephard, N.; Han, J; Xue, G.; Chen, Z. Probing molecular structures of polymer/metal interfaces by sum frequency generation vibrational spectroscopy. *Macromolecules* **2008**, *41*, 8770.

(45) Lu, X; Li, D. W.; Kristalyn, C. B.; Han, J. L.; Shephard, N.; Rhodes, S.; Xue, G.; Chen, Z. Directly probing molecular ordering at the buried polymer/metal interface. *Macromolecules* **2009**, *42*, 9052.

(46) Lu, X.; Xue, G.; Wang, X.; Han, J.; Han, X.; Hankett, J.; Li, D.; Chen, Z. Directly probing molecular ordering at the buried polymer/metal interface 2: Using P-polarized input beams. *Macromolecules* **2012**, *45*, 6087.

CHAPTER 2

INFLUENCE OF CASTING SOLVENT ON PHENYL ORDERING AT THE SURFACE OF SPIN CAST POLYMER THIN FILMS

2.1 Introduction

Polymer thin film surface structures influence many important surface properties such as wettability, adhesive strength, lubricity, and biocompatibility.[1] Engineering polymer films with defined surface properties thus requires an understanding of how thin film deposition methods and post-deposition processing affect polymer surface structures at the molecular level. Although recent reviews have highlighted advances in the fabrication of patterned polymeric surfaces,[2] polymer surface plasma treatment,[3] and the effect of solvent on surface segregation in copolymer and polymer blend films,[4] the detailed relationship between polymer thin film deposition methods and the resulting surface molecular structure remains poorly understood.

One of the most frequently used methods of depositing thin polymer films is spin coating polymer solutions onto flat substrates. Spin speed, solvent selection, polymer concentration, and spin coating under a solvent-saturated atmosphere have been shown to affect film properties such as thickness, surface roughness, and bulk molecular order.[5] Rapid solvent evaporation during spin coating can trap non-equilibrium polymer chain conformations within cast films,[6,7] resulting in residual stress[8] and a smaller degree of entanglement than at equilibrium.[9] The trapped polymer chain conformations have been shown to resemble their solution conformation[10,11] which is dependent on the solvent quality.[12]

The role of solvent used for spin casting organic conjugated polymers has been extensively studied due to the relationship between a conjugated polymer's bulk morphology and its optical and electronic properties.[13-15] Shi et al. reported a correlation between the aggregation state of poly[2-methoxy-5-(2′-ethylhexyloxy)-1,4-phenylene vinylene (MEH-PPV) in solution and the quantum efficiency of the spin cast polymer film.[16] Aromatic solvents were hypothesized to preferentially solvate the aromatic backbone which led to aggregation of the alkyl side chains in the solution while non-aromatic solvents were hypothesized to expose the alkyl side chains to the solvent. Spin casting with non-aromatic solvents resulted in more polar polymer film surfaces than when aromatic solvents were used. The decrease in surface polarity when an aromatic spin casting solvent was used was likely due to the benzene ring lying perpendicular to the surface which decreased the surface concentration of polar methoxy groups.[16] However, there was no direct molecular level experimental evidence to confirm the conclusion.

The objective of this work was to investigate whether there is a correlation between the aromaticity of the solvent used for spin casting and the orientation of phenyl functional groups on spin cast polymer surfaces. In order to investigate the surface molecular structure of the films, the surface sensitive nonlinear optical laser technique sum frequency generation (SFG) vibrational spectroscopy was used. As introduced in the previous chapter, SFG vibrational spectroscopy is a second order nonlinear optical technique that can provide a vibrational spectrum of surfaces and buried interfaces.[17-29]

In this study, SFG spectra were collected from the surfaces of poly (phenyl methacrylate) (PPM), poly(benzyl methacrylate) (PBM), poly(methylphenylsiloxane) (PMPS) polysulfone (PSF), and poly(bisphenol A carbonate) (PBAC) films spin cast from aromatic and non-aromatic solvents. These polymers contain both aromatic and aliphatic functionalities with aromatic

groups either in the side chains or in backbones. Chlorobenzene and chloroform, both of which dissolve many polymers used in organic solar cells and microelectronic packaging, were selected to compare a completely aromatic solvent to a non-aromatic solvent. Surface molecular structures were then correlated with different polymer chain conformations at the solution/air interface, preferential solvation of functional groups during evaporation, and migration of bulky side groups to the polymer film/air interface.

2.2 Materials and Methods

2.2.1 Materials

Poly(phenyl methacrylate) (PPM) (M_w 100,000) was obtained from Scientific Polymer Products, Inc. poly(benzyl methacrylate) (PBM) (M_w 70,000), polysulfone (PSF) (Mw 35,000), and poly(bisphenol A carbonate) (PBAC) (M_w 64,000) were obtained from Sigma Aldrich, Inc. Poly(methylphenylsiloxane) (PMPS) (M_w 6,000) was obtained from Gelest, Inc. To ensure that no spectral confusion could occur from the solvent, deuterated solvents were used in this study. Chloroform-d ($CDCl_3$) and chlorobenzene-d_5 (clb-d_5) were obtained from Sigma Aldrich, Inc. The molecular structures of the polymers and the solvents used in the research are plotted in Figure 2.1 and the glass transition temperatures of the polymers are listed in Table 2.1.

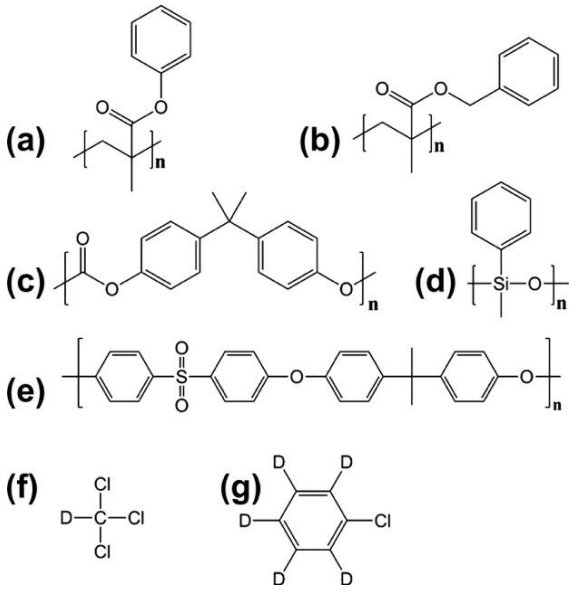

Figure 2.1. Molecular structures of: (a) poly(phenyl methacrylate) (PPM), (b) poly(benzyl methacrylate) (PBM), (c) poly(bisphenol A carbonate) (PBAC), (d) poly(methylphenylsiloxane) (PMPS), (e) polysulfone (PSF), (f) chloroform-d ($CDCl_3$), and (g) chlorobenzene-d_5.

Polymer	Glass transition temperature (℃)
Poly(methylphenylsiloxane)	−50
Poly(benzyl methacrylate)	54
Poly(phenyl methacrylate)	110
Poly(bisphenol A carbonate)	147
Polysulfone	185

Table 2.1. Glass transition temperatures of the polymers used in this study.

2.2.2 Preparation of polymer thin films

Polymer samples were dissolved in solvents to form 2.0 wt% solutions. Calcium fluoride windows (ESCO Products, Inc.) were used for all SFG measurements and were cleaned in an oxygen plasma (PE-50, Plasma Etch) prior to sample preparation. A Speedline Technologies P-

6000 spin coater was used to spin cast polymer solutions for 30 s onto the substrates. All films were held under vacuum overnight prior to measurements to remove any residual solvent.

2.2.3 Sum frequency generation vibrational spectroscopy measurements

The details of SFG theory and our SFG setup have been reported in the previous chapter.[30-32] The visible and IR beams passed through the back side of the window substrate and through the polymer film in a "face down" window geometry. The incident angles of the visible and IR input beams were 60 ° and 55 ° with respect to the substrate surface normal, respectively. The pulse energies of the visible and IR beams at the sample stage were approximately 150 and 100 μJ, respectively. SFG spectra were collected using the ssp and ppp polarization combinations in the frequency range between 2700 and 3200 cm^{-1}.

2.2.3 SFG spectral fitting

All SFG spectra were fit using equation 1.23.

2.3 Results and discussion

2.3.1 Molecular structure at the poly(phenyl methacrylate)/air interface

We first investigated the effect of using aromatic and non-aromatic solvents for spin casting polymers that contain phenyl groups as part of flexible side groups. SFG spectra were collected from the polymer/air interface of PPM films that were spin cast using chloroform-d, 3:1 (w/w) chloroform-d/chlorobenzene-d_5 (25%), 1:1 (w/w) chloroform-d/chlorobenzene-d_5 (50%), and chlorobenzene-d_5 (Fig. 2.2a). The aromatic group in PPM is connected to the backbone through a carboxyl group and the glass transition temperature is ~110 ℃ (Fig. 2.1 and Table 2.1).

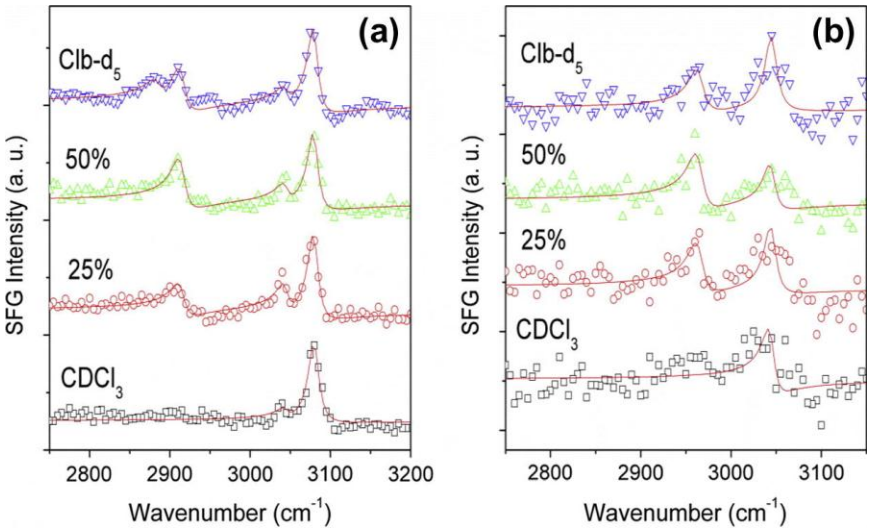

Figure 2.2. SFG (a) SSP and (b) PPP spectra collected from the surface of PPM spin cast in $CDCl_3$, 25% (3:1 (w/w) chloroform-d/chlorobenzene-d_5), 50% (1:1 (w/w) chloroform-d/chlorobenzene-d_5), and chlorobenzene-d_5 solvents.

The SSP SFG spectrum collected from the polymer/air interface of PPM cast with chloroform-d had SFG signals near 3045 and 3080 cm^{-1} which can be assigned to the ν_{7a} and ν_{20a} vibrational modes of the phenyl ring.[33,34] When 25% solvent was used, phenyl features were again observed near 3045 and 3080 cm^{-1} as well as a new feature near 2915 cm^{-1} which can be assigned to the backbone methylene. As the percentage of chlorobenzene-d_5 increased to 50%, the SFG spectrum closely resembled the spectrum collected from the film cast from a 25% solution, however the 2915 cm^{-1} feature was more clearly resolved. Similarly, the PPP spectrum collected when $CDCl_3$ was used as the casting solvent had one feature near 3045 cm^{-1} while an additional feature near 2965 cm^{-1} from the backbone methyl was only observed when 25% and 50% solvents were used.

We then collected SFG spectra from the surface of PPM films cast with chlorobenzene-d5 to investigate how a completely aromatic casting solvent affected the surface phenyl structure. The SSP SFG spectra collected from the polymer/air interface of PPM cast with clb-d5 had features near 2885, 2915, 3045, and 3080 cm^{-1}, respectively. The feature near 2885 cm^{-1} can be

assigned to the backbone methyl group. The PPP spectra had features near 2965 cm^{-1} and 3045 cm^{-1} which confirmed that both methyl groups on the backbone and side chain phenyl groups were present at the film surface.

The surface molecular structure of polystyrene phenyl groups has been extensively characterized in several SFG studies. Five vibrational modes have been observed from polystyrene aromatic C–H stretches with resonant frequencies near 3084, 3069, 3057, 3036, and 3024 cm^{-1} which can be assigned to the phenyl ν_{20a}, ν_2, ν_{7b}, ν_{7a}, and ν_{20b} modes (Fig. 2.3), respectively. [33,34] The irreducible representation of the ν_{20a}, ν_2, and ν_{7a} vibrational modes is totally symmetric A1 while the ν_{7b} and ν_{20b} vibrational modes belong to the B1 irreducible representation. Mono-substituted phenyl ring vibrational modes which belong to the A1 or B1 irreducible representations of the C_{2v} point group are both IR- and Raman-active, therefore all five modes are SFG active. However, only the ν_2, ν_{20b}, and ν_{7a} modes have a large hyperpolarizability product,[35] so they are the only vibrational modes predicted to have strong SFG signal.

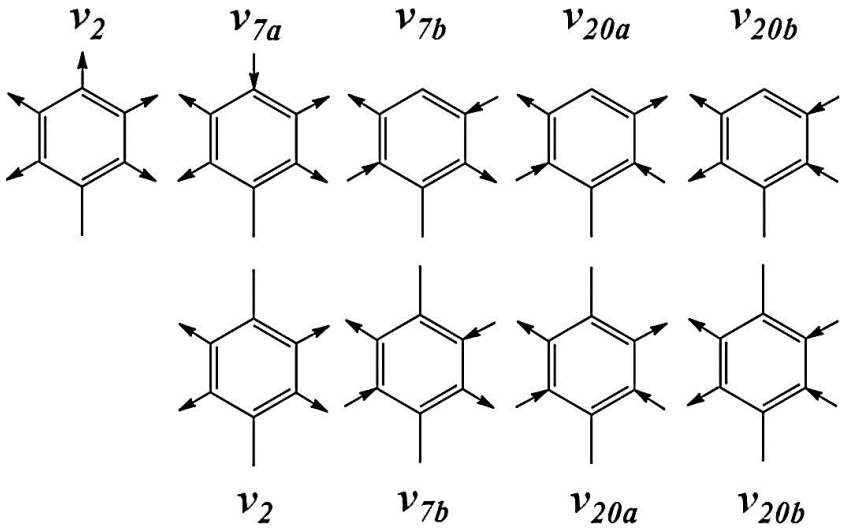

Figure 2.3. Mono-substituted (top) and para-substituted (bottom) phenyl ring C–H stretching normal modes.

Strong SFG signal intensity can be measured in the SSP polarization combination when a vibrational mode of a functional group has a vibrational dipole component perpendicular to the surface and a polarizability tensor component parallel to the surface. An estimate of the phenyl tilt angle relative to the surface normal can be obtained by calculating the ratio of the oscillator strengths of a B1 vibrational mode to an A1 vibrational mode measured in the SSP polarization combination:

$$\boldsymbol{R} = \left|\frac{A_{q,B_1}}{A_{q,A_1}}\right| = \left|\left(\frac{\beta_{caa,B_1}}{\beta_{aac,A_1}}\right)\left(\frac{2(\langle\cos 3\theta\rangle - \langle\cos\theta\rangle)}{(7+2r)\langle cos\theta\rangle + (1-2r)\langle cos3\theta\rangle}\right)\right| \tag{2.3}$$

where A is the oscillator strength, β is the hyperpolarizability, and R is the βccc/βaac for the A1 vibrational mode. As the phenyl tilt angle increases (tilting more toward the surface), Eq. (2.3) predicts that the value of R would increase (Fig. 2.4), meaning that the SFG SSP intensity for the A1 vibrational mode would decrease relative to the intensity of the B1 mode. Qualitatively, if monosubstituted phenyl rings were isotropically distributed perpendicular to the surface (θ = 0), only A1 vibrational modes would be observed in the SFG SSP spectrum. On the other hand, if the phenyl rings were isotropically oriented parallel to the surface (θ = 90), no signal would be detected in the SSP spectrum.

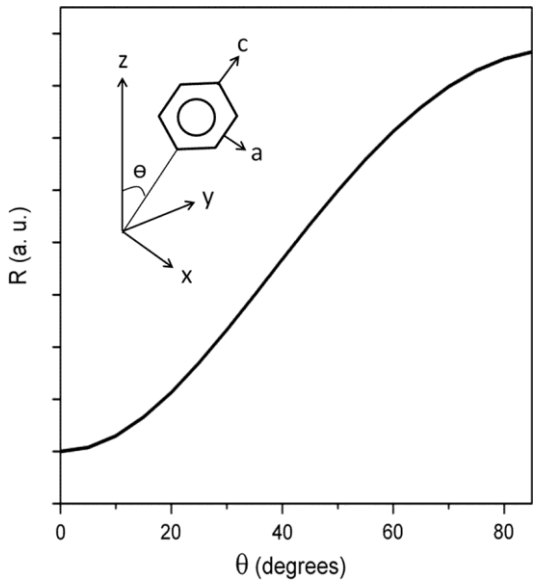

Figure 2.4. Eq. (2.3) plotted as a function of tilt angle. The inset shows the laboratory-fixed and molecular-fixed coordinate system for a mono-substituted phenyl ring.

Phenyl A1 vibrational modes dominated the PPM SSP spectrum regardless of the casting solvent used which suggests that phenyl rings were likely oriented nearly perpendicular to the film surface. The bulky side chains of PPM likely migrated to the polymer/air interface to minimize the interfacial free energy regardless of the casting solvent. Backbone structures, however, were affected by the casting solvent because methyl and methylene features were only observed when 25%, 50%, and Clb-d_8 solvents were used.

Polymer chains will assume a conformation in a particular solvent that results in a free energy minimum. Aromatic solvents are expected to solvate the phenyl group of the PPM side chain better than the backbone whereas non-aromatic solvents are expected to solvate the backbone better than the ester or phenyl group of the side chain.[16,36] Even though the glass transition temperature of PPM is higher than room temperature, the glass transition temperature usually characterizes the mobility of the backbones. Side chain groups can be mobile at temperatures much lower than the glass transition temperature, so the side chains can restructure

at the surface at room temperature after spin-casting. These observations are in agreement with previous reports that showed that the surfaces of poly(ethyl methacrylate) and poly(ethyl acrylate) are mainly covered by their side chains.[37]

The different backbone structures observed at the polymer/air interface when the polymers were cast in aromatic and non-aromatic solvents could be due to different molecular structures present at the solvent/air interface during spin casting. The relationship between the surface structure of spin cast polymer films and the casting solvent has been extensively investigated for a series of end-group fluorinated methacrylates.[38-40] When the fluorinated endgroups of the polymer chains were present at the solvent/air interface, the surface of the spin cast film was found to be dominated by fluorine groups.[40] However, when the fluorine moieties were trapped inside of a micelle within the solution, few fluorine moieties were present at the solvent/air interface which resulted in few fluorine groups present at the surface of the spin cast film. At the chlorobenzene/air interface, the PPM phenyl side groups likely remain preferentially solvated by the solvent while the backbone methyl and methylene groups are exposed to the air.

Ordered methyl groups at the chlorobenzene/air interface were likely carried over to the spin cast film surface. At the chloroform/air interface, however, the methyl and methylene groups on the backbone likely remained solvated, and phenyl groups exposed to air and were ordered. As the chloroform solvent evaporated, the backbone likely maintained some of its solvated structure. Solvated surface methyl and methylene groups would be more randomly ordered compared to their ordered structure in air.[41] The lack of backbone SFG signal when chloroform was used as the casting solvent can then be explained by randomly ordered surface methyl and methylene groups in chloroform which were transferred to the film surface.

Regardless of the solvents, the phenyl groups were ordered on the spin casted film surface because they are flexible with a lower surface free energy.

2.3.2 Molecular structure at the poly(benzyl methacrylate)/air interface

The SSP SFG spectra collected from PBM spin cast in chloroform-d (Fig. 2.5a) had features near 3055 and 3070 cm^{-1} which can be assigned to the phenyl ν_{7b} and ν_2 vibrational modes, respectively. It is worth noting that the phenyl signals from PPM and PBM were different which suggests that the phenyl groups on the side chains of PPM and PBM have different orientations at the film/air interface. This is due to the surface presence of the methylene group in PBM, which may alter the phenyl surface orientation.

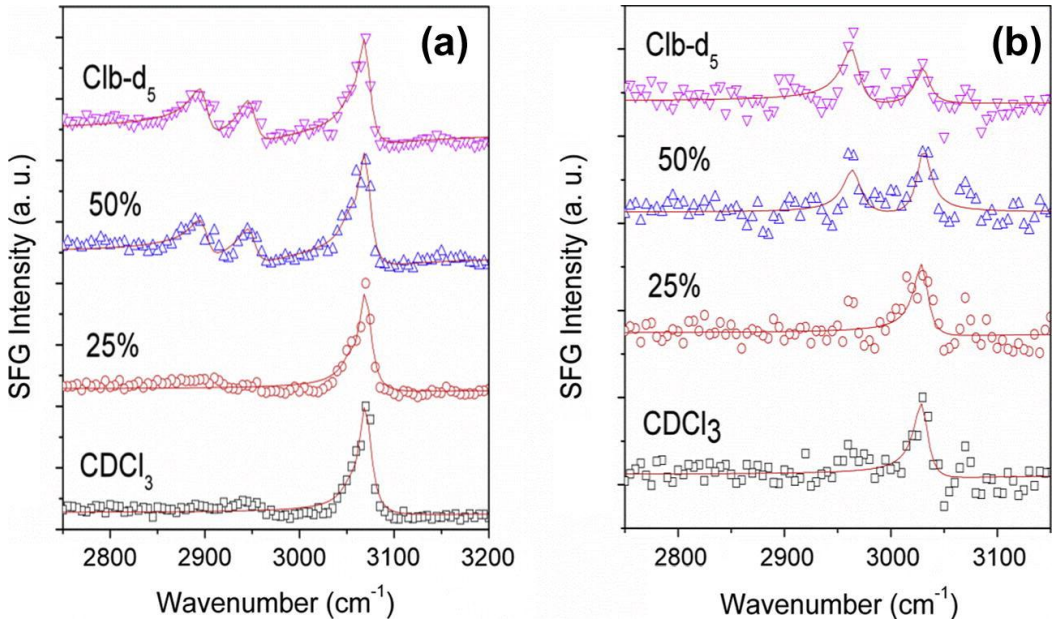

Figure 2.5. SFG (a) SSP and (b) PPP spectra collected from the surface of PBM spin cast in $CDCl_3$, 25%, 50%, and chlorobenzene-d_5 solvents.

The results from PBM surfaces are well correlated to those from PPM surfaces presented above. When chloroform was used, it is more compatible with the alkyl groups, therefore the random solvation at the solvent/air interface was carried over to the film and only aromatic C–H

stretching signal from phenyl groups which had migrated to the film/air interface after spin casting was observed. Again, the incompatible alkyl groups were not ordered on the surface, as in the PPM case when chloroform-d was used for spin-coating. The SSP SFG spectra collected from PBM prepared using Clb-d_5 and 50% were very similar, and very similar to those from PPM prepared using the same solvents, except an additional signal at ~2950 cm^{-1} (The ~2950 cm^{-1} signal may come from the methylene group on the side chain). Therefore, as with PPM, because the alkyl groups are not compatible with Clb-d_5, they were likely ordered at the chlorobenzene/air interface and their net ordering at the interface was carried to the film surface (evidenced by the 2900 cm^{-1} signal) along with the lower surface energy phenyl component. The PPP SFG spectra collected from PBM spin cast in chloroform-d (Fig. 2.5b) and 25% had one feature near 3030 cm^{-1} which can be assigned to the phenyl ν_{7a}. When 50% and chlorobenzene-d_5 solvents were used, an additional feature near 2965 cm^{-1} was observed which confirmed that backbone methyl groups were only ordered at the air interface when aromatic solvents were used.

2.3.3 Molecular structure at the poly(methylphenylsiloxane)/air interface

We then collected SFG spectra from PMPS films spin cast using solutions of chloroform-d, 25%, 50%, and clb-d_5 to study how casting solvent aromaticity affects surface phenyl rings directly linked to a polymer chain backbone. The SSP SFG spectra of spin cast PMPS (Fig. 2.6a) contained peaks at 2910, 2965, and 3058 cm^{-1}, which can be assigned to the Si–CH_3 symmetric stretch,[42] the Si–CH_3 antisymmetric stretch,[42] and the phenyl ν_{7b} mode. The SFG spectra show that the PMPS surface is covered by both the phenyl group and the methyl group connected to the backbone Si.

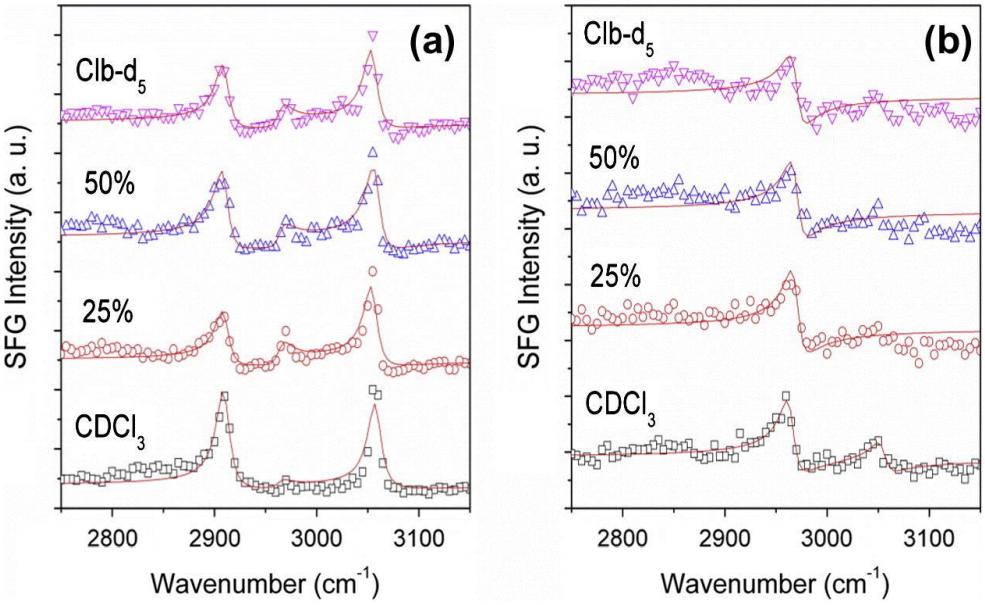

Figure 2.6. SFG (a) SSP and (b) PPP spectra collected from the surface of PMPS films cast in $CDCl_3$, 25%, 50%, and chlorobenzene-d_5 solvents.

PMPS has one phenyl and one methyl group directly attached to the backbone. Aromatic solvents are again expected to preferentially solvate the phenyl group more than the methyl group. Therefore methyl C–H signal may be observed from the sample prepared by using 50% or clb-d_5 solvents. However this was not the case; all the SFG spectra were more or less the same. The T_g of PMPS is −50 ℃ which is far below room temperature so the surface structure should have more or less relaxed to equilibrium after spin casting regardless of which solvent was used. The similar SFG spectra suggest that similar surface molecular structures were stable when aromatic or non-aromatic solvents were used for spin casting. Also, any solvent induced surface ordering of the phenyl groups should order the connected methyl group and thus affect the 2910 cm^{-1} signal.

Only small differences were observed among different spectra. The SSP SFG spectra of PMPS show that the Si–CH_3 symmetric stretch is stronger than the asymmetric stretch. The films spin cast from 25%, 50%, and clb-d_5 had a slightly lower symmetric to antisymmetric ratio than

the films cast from chloroform-d which suggests that the methyl groups were oriented closer to the surface normal on the chloroform-d casted film surface.[42]

As we discussed above, for PBM and PPM prepared using clb-d_5, both the phenyl side chain and the alkyl backbone were ordered at the surface whereas only phenyl groups were detected when chloroform was used. However, because the glass transition temperature is low and/or the methyl and phenyl are next to each other, this is not true for PMPS, where both methyl and phenyl signals were observed regardless of the solvent. In our previous study, we also showed that for PDMS-co-PS block copolymer and PDMS-co-poly(diphenyl siloxane) (PDPS) block copolymer, when spin coated using toluene, both methyl and phenyl signals can be observed.[42] In the later cases, the methyl and phenyl groups are not connected to each other. They both can be observed because the PDMS segment is very flexible and the methyl groups can be present on the surface, similar to the PPM and PBM cases.

2.3.4 Molecular structure at the polysulfone/air and poly(bisphenol A carbonate)/air interfaces

To study how spin casting solvent affects low flexibility phenyl groups that are part of a polymer chain backbone, PSF was spin cast in chloroform-d, 25%, 50%, and clb-d_5. The SFG spectrum collected at the PSF/air interface when chloroform-d solvent was used (Fig. 2.7) exhibited a very small feature near 3080 cm^{-1}, but no aliphatic C–H stretching signal. This is again similar to the PPM and PBM cases, even though PPM and PBM have phenyl in side chains but PSF has phenyl in the backbone. This is because the methyl group is compatible with chloroform-d, so they will not be ordered on the surface. Different from PPM and PBM, though, the polymer chain does not have flexible phenyl side groups which can stand up more or less at the polymer/air interface. Therefore, only very weak phenyl signal was observed.

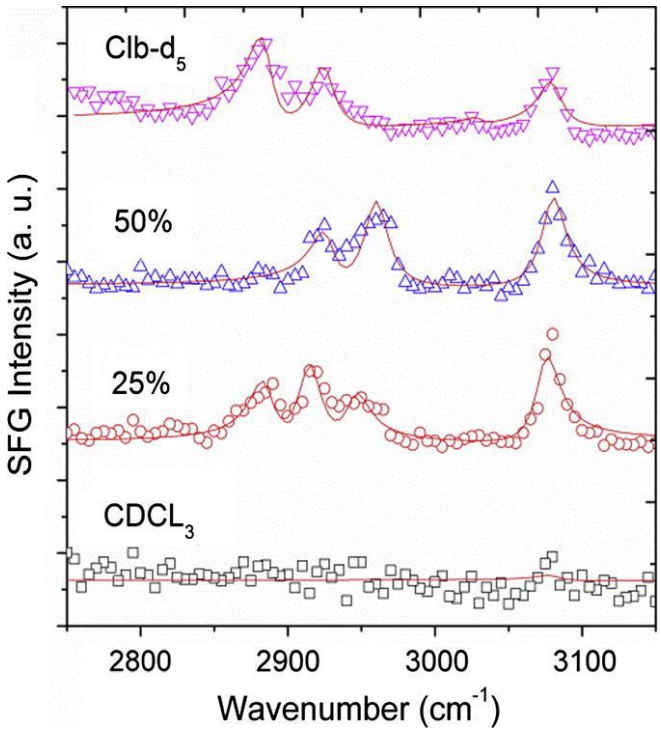

Figure 2.7. SFG SSP spectra from PSF films spin cast in $CDCl_3$, 25%, 50%, and chlorobenzene-d_5 solvents.

When 25% solvent was used, signals were observed near 2885, 2925, 2945, and 3080 cm^{-1}. Peaks at 2885 and 2945 cm^{-1} can be assigned to the methyl symmetric and Fermi resonance, respectively. This again is well correlated to the PPM and PBM data. Now Clb-d_5 is not compatible with the methyl groups, therefore methyl groups can be ordered on the surface and methyl SFG signal can be observed. Since the methyl groups are very close to the phenyl backbone, the ordering of surface methyl groups also induced surface order of lower surface energy phenyl groups. Therefore, phenyl signals were also detected. The Hildebrand solubility parameters of chloroform and chlorobenzene are 18.9 and 19.5,[43] respectively, which shows that small changes in solvent interaction can lead to significant changes in the surface molecular structures of spin cast polymer films without side chains.

The lack of strong phenyl signal in the SSP SFG spectra collected when $CDCl_3$ was used suggests that the surface phenyl groups were either quite randomly oriented (but not completely randomly oriented) or that they were oriented more or less parallel to the film surface (not completely lie down). The increase in the 3080 cm^{-1} signal after clb-d_5 was present in the solvent mixture suggests that the phenyl groups were ordered and oriented closer to the film surface normal (Table 2.2). These results are consistent with the behavior of MEH-PPV where the backbone phenyl was hypothesized to lie parallel to the spin cast film surface when non-aromatic casting solvent was used and perpendicular to the film when aromatic solvents were used.[1]

Polymer									
PPM		**$CDCl_3$**		**25%**		**50%**		**Clb-d_5**	
ω (cm^{-1})	**Assignment**	**$A_{q,ssp}$**	**Γ_q (cm^{-1})**	**$A_{q,ssp}$**	**Γ_q (cm^{-1})**	**$A_{q,ssp}$**	**Γ_q (cm^{-1})**	**$A_{q,ssp}$**	**Γ_q (cm^{-1})**
2885	methyl							1.7 ± 0.3	10.0
2915	methylene			4.0 ± 0.3	10.0	5.6 ± 0.3	10.0	5.1 ± 0.2	10.0
3045	ν_{7a}	1.1 ± 0.4	8.0	2.3 ± 0.3	8.0	1.6 ± 0.4	8.0	1.3 ± 0.3	8.0
3080	ν_{20a}	6.9 ± 0.2	8.0	6.8 ± 0.2	8.0	6.4 ± 0.2	8.0	6.7 ± 0.2	8.0
		$A_{q,ppp}$		**$A_{q,ppp}$**		**$A_{q,ppp}$**		**$A_{q,ppp}$**	
2965	methyl			4.1 ± 0.5	10.0	4.2 ± 0.4	10.0	3.9 ± 0.5	10.0
3045	ν_{7a}	3.6 ± 0.4	8.0	4.4 ± 0.4	8.0	3.4 ± 0.3	8.0	4.8 ± 0.3	8.0
PBM									
ω (cm^{-1})	**Assignment**	**$A_{q,ssp}$**	**Γ_q (cm^{-1})**	**$A_{q,ssp}$**	**Γ_q (cm^{-1})**	**$A_{q,ssp}$**	**Γ_q (cm^{-1})**	**$A_{q,ssp}$**	**Γ_q (cm^{-1})**
2900	methylene					3.4 ± 0.3	10.0	3.9 ± 0.3	10.0
2950	methyl					3.8 ± 0.4	10.0	4.3 ± 0.3	10.0
3055	ν_{7b}	1.0 ± 0.4	8.0	1.2 ± 0.4	8.0	1.3 ± 0.4	8.0	0.9 ± 0.4	8.0
3070	ν_2	7.3 ± 0.2	8.0	6.8 ± 0.2	8.0	7.1 ± 0.2	8.0	6.8 ± 0.2	8.0
		$A_{q,ppp}$	**Γ_q**	**$A_{q,ppp}$**	**Γ_q**	**$A_{q,ppp}$**	**Γ_q**	**$A_{q,ppp}$**	**Γ_q**
2965	methyl					4.7 ± 0.4	10.0	5.2 ± 0.4	10.0
3030	ν_{7a}	5.0 ± 0.3	8.0	5.0 ± 0.3	8.0	4.6 ± 0.3	8.0	3.5 ± 0.4	8.0
PMPS									
ω (cm^{-1})	**Assignment**	**$A_{q,ssp}$**	**Γ_q (cm^{-1})**	**$A_{q,ssp}$**	**Γ_q (cm^{-1})**	**$A_{q,ssp}$**	**Γ_q (cm^{-1})**	**$A_{q,ssp}$**	**Γ_q (cm^{-1})**
2910	methyl	7.0 ± 0.2	8.0	5.0 ± 0.2	8.0	5.7 ± 0.2	8.0	5.4 ± 0.2	8.0
2965	methyl	-2.0 ± 0.2	8.0	-3.0 ± 0.2	8.0	-2.5 ± 0.2	8.0	-3.0 ± 0.2	8.0
3058	ν_{7b}	6.6 ± 0.2	8.0	6.1 ± 0.2	8.0	5.9 ± 0.2	8.0	6.1 ± 0.2	8.0
		$A_{q,ppp}$	**Γ_q**	**$A_{q,ppp}$**	**Γ_q**	**$A_{q,ppp}$**	**Γ_q**	**$A_{q,ppp}$**	**Γ_q**
2965	methyl	4.8 ± 0.2	8.0	4.5 ± 0.5	8.0	3.7 ± 0.6	8.0	2.6 ± 0.3	8.0
3058	ν_{7b}	2.6 ± 0.3	8.0						
PSF									
ω (cm^{-1})	**Assignment**	**$A_{q,ssp}$**	**Γ_q (cm^{-1})**	**$A_{q,ssp}$**	**Γ_q (cm^{-1})**	**Aq,ssp**	**Γ_q (cm^{-1})**	**Aq,ssp**	**Γ_q (cm^{-1})**
2885	methyl			4.9 ± 0.4	10.0			6.2 ± 0.4	10.0
2925				6.3 ± 0.3	10.0	4.5 ± 0.4	10.0	5.9 ± 0.4	10.0
2945	methyl			4.2 ± 0.5	10.0				
2960	methyl					7.2 ± 0.2	10.0		
3080	ν_{20a}	1.7 ± 1.4	10.0	7.3 ± 0.3	10.0	7.7 ± 0.2	10.0	5.3 ± 0.4	10.0
PBAC									
ω (cm^{-1})	**Assignment**	**$A_{q,ssp}$**	**Γ_q (cm^{-1})**	**$A_{q,ssp}$**	**Γ_q (cm^{-1})**	**$A_{q,ssp}$**	**Γ_q (cm^{-1})**		
2870	methyl	6.1 ± 0.2	8.0	6.7 ± 0.2	8.0	5.8 ± 0.2	8.0		
2910		3.5 ± 0.3	8.0	4.8 ± 0.3	8.0	6.8 ± 0.2	8.0		
2960	methyl					5.0 ± 0.2	10.0		
3070	ν_2	2.7 ± 0.5	8.0	4.4 ± 0.3	8.0	4.4 ± 0.3	8.0		

Table 2.2. Fitting Results for the SFG spectra of PPM, PBM, PMPS, PSF, and PBAC Polymer Films.

SFG spectra were then collected from another polymer with phenyl groups in a rigid backbone, PBAC (Fig. 2.8). Different from PPM, PBM, and PSF, but similar to PMPS, both methyl and phenyl signals were observed near 2870, 2910, and 3070 cm^{-1} when $CDCl_3$ was used as the solvent, but the 3070 cm^{-1} peak was still weak. This is because the PBAC structure is quite rigid, so even the slightly ordered phenyl structure will induce ordered methyl groups on or near the surface, therefore both signals were observed. When 25% and 50% Clb-d_5 were used, signals from both methyl and phenyl groups again were observed, as the PPM, PBM, and PSF cases. The addition of clb-d_5 to the $CHCl_3$ solution again resulted in an increase in the SSP signal for aliphatic C–H stretching signals, indicating more ordered methyl groups on the surface (because methyl groups are more ordered at the solvent/air interface). Because PBAC structure is very rigid, the ordered methyl groups lead to more ordered phenyl groups orienting more toward the surface normal, increasing the signal at 3080 cm^{-1}. Another factor which may affect phenyl orientation is the dipole–dipole interaction[44] between the carbonate ester group on PBAC and the dipole moment of the solvent molecules. Chlorobenzene has a higher dipole moment than chloroform, so the stronger interaction with the polar portion of the PBAC backbone may induce more ordered carbonate ester groups which in turn lead to more phenyl ordering from chain rigidity. The increase in the phenyl SSP signal again suggests that spin casting with aromatic solvents resulted in the surface phenyl rings more ordered and oriented close to the surface normal while the phenyl rings were less ordered and oriented more parallel to the surface when non-aromatic solvents were used.

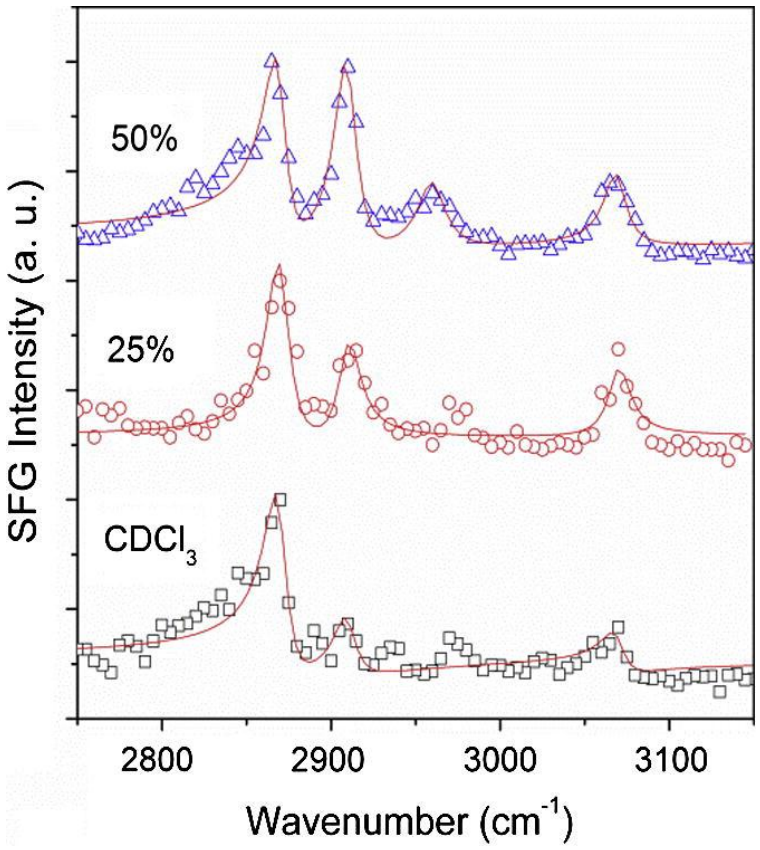

Figure 2.8. SFG SSP spectra from PBAC films spin cast in $CDCl_3$, 25%, and 50% solvents.

2.4 Conclusions

In conclusion, we have demonstrated that spin casting homopolymers that contain phenyl groups either in the side chains or backbones in aromatic or non-aromatic solvents can affect the resulting surface molecular structure. The mobility of phenyl groups in the investigated polymers likely determined whether the groups are ordered on the surface uniformly or remained locked into structural conformations induced by rapid solvent loss during spin casting. When the phenyl was part of a mobile side chain, the groups covered the polymer surface regardless of casting solvent and more or less stand up on the surface. However, when the phenyl was part of a rigid backbone and had low mobility, the phenyl groups tended to lie perpendicular to the film surface when aromatic solvent was used but tended to lie parallel to the film or were randomly oriented

when non-aromatic solvent was used. Backbone methyl and methylene structures were typically more ordered at the polymer/air interface when aromatic solvents were used which suggests that ordered backbone molecular structures at the solution/air interface were carried over to the spin cast film surface.

Future studies will correlate the molecular structure of polymer chains at the solvent/air interface determined using molecular dynamics simulations to that obtained from SFG studies to gain further insight into how solvent/air molecular structures are correlated to the surface molecular structure of spin cast films. Further studies will focus on the effect of polymer chain molecular weight on the surface structure of spin cast films as well as the consequences and applications of different polymer film surface structures induced by spin casting in aromatic and non-aromatic solvents.

2.5. Impact

In this chapter, general methodology was developed to elucidate relationships between thin film deposition methods and resulting film surface molecular structures. This general methodology can be applied to study a variety of thin films deposited using other methods (e.g. chemical or physical vapor deposition) by correlating deposition parameters to resulting surface structures and properties. Using this methodology, we found that the mobility of polymer side chains can determine whether the side chains migrate to the surface or remain buried in the polymer. We also found that molecular structures at solution/air interfaces could be carried over to spin cast film surfaces. This relationship provides a useful guideline for solvent selection when a specific polymer film surface structure in required for a particular application. The studies reported in this chapter can be used to help elucidate how functional group orientation influences contact angle measurements, how different polymer surfaces physically age, and how

different surface structures affect the formation buried interfaces, More generally, this methodology can be combined with surface property studies to elucidate polymer film surface structure-property relationships, which can be used in the design of film surfaces with optimized properties for many important applications such as microelectronic packaging, solar cells, and biomedical devices.

2.6 References

(1) Chen, Z.; Shen, Y. R.; Somorjai, G. A. Studies of Polymer Surfaces by Sum Frequency Generation Vibrational Spectroscopy. *Annu. Rev. Phys. Chem.* **2002**, *53*, 437–465.

(2) del Campo, A.; Arzt, E. Fabrication Approaches for Generating Complex Micro- and Nanopatterns on Polymeric Surfaces. *Chem. Rev.* **2008**, *108*, 911–945.

(3) Denes, F. Macromolecular Plasma-Chemistry: An Emerging Field of Polymer Science. *Prog. Polym. Sci.* **2004**, *29*, 815–885.

(4) Chen, J.; Zhuang, H.; Zhao, J.; Gardella, J. A. Solvent Effects on Polymer Surface Structure. *Surf. Interface Anal.* **2001**, *31*, 713–720.

(5) Norrman, K.; Ghanbari-Siahkali, A.; Larsen, N. B. 6 Studies of Spin-coated Polymer Films. *Annu. Rep. Sect. C Phys. Chem.* **2005**, *101*, 174.

(6) Thomas, K. R.; Chenneviere, A.; Reiter, G.; Steiner, U. Nonequilibrium Behavior of Thin Polymer Films. *Phys. Rev. E* **2011**, *83*.

(7) Raegen, A.; Chowdhury, M.; Calers, C.; Schmatulla, A.; Steiner, U.; Reiter, G. Aging of Thin Polymer Films Cast from a Near-Theta Solvent. *Phys. Rev. Lett.* **2010**, *105*.

(8) Reiter, G.; Hamieh, M.; Damman, P.; Sclavons, S.; Gabriele, S.; Vilmin, T.; Raphaël, E. Residual Stresses in Thin Polymer Films Cause Rupture and Dominate Early Stages of Dewetting. *Nat. Mater.* **2005**, *4*, 754–758.

(9) Barbero, D. R.; Steiner, U. Nonequilibrium Polymer Rheology in Spin-Cast Films. *Phys. Rev. Lett.* **2009**, *102*.

(10) Nguyen, T.-Q.; Doan, V.; Schwartz, B. J. Conjugated Polymer Aggregates in Solution: Control of Interchain Interactions. *J. Chem. Phys.* **1999**, *110*, 4068.

(11) Huser, T.; Yan, M.; Rothberg, L. J. Single Chain Spectroscopy of Conformational Dependence of Conjugated Polymer Photophysics. *Proc. Natl. Acad. Sci.* **2000**, *97*, 11187–11191.

(12) Li, R. N.; Clough, A.; Yang, Z.; Tsui, O. K. C. Equilibration of Polymer Films Cast from Solutions with Different Solvent Qualities. *Macromolecules* **2012**, *45*, 1085–1089.

(13) Geens, W.; Shaheen, S. E.; Wessling, B.; Brabec, C. J.; Poortmans, J.; Serdar Sariciftci, N. Dependence of Field-effect Hole Mobility of PPV-based Polymer Films on the Spin-casting Solvent. *Org. Electron.* **2002**, *3*, 105–110.

(14) Rispens, M. T.; Meetsma, A.; Rittberger, R.; Brabec, C. J.; Sariciftci, N. S.; Hummelen, J. C. Influence of the Solvent on the Crystal Structure of PCBM and the Efficiency of MDMO-PPV:PCBM 'plastic' Solar Cells. *Chem. Commun.* **2003**, 2116.

(15) Zhang, F.; Jespersen, K. G.; Björström, C.; Svensson, M.; Andersson, M. R.; Sundström, V.; Magnusson, K.; Moons, E.; Yartsev, A.; Inganäs, O. Influence of Solvent Mixing on the Morphology and Performance of Solar Cells Based on Polyfluorene Copolymer/Fullerene Blends. *Adv. Funct. Mater.* **2006**, *16*, 667–674.

(16) Shi, Y.; Liu, J.; Yang, Y. Device Performance and Polymer Morphology in Polymer Light Emitting Diodes: The Control of Thin Film Morphology and Device Quantum Efficiency. *J. Appl. Phys.* **2000**, *87*, 4254-4263.

(17) Shen, Y. R. Surface Properties Probed by Second-harmonic and Sum-frequency Generation. *Nature* **1989**, *337*, 519–525.

(18) Miyamae, T.; Nozoye, H. Poly(ethylene Terephthalate) Surface and Alumina/poly(ethylene Terephthalate) Interface Studied Using Sum-frequency Generation Spectroscopy. *Surf. Sci.* **2005**, *587*, 142–149.

(19) Miyamae, T.; Takada, N.; Tsutsui, T. Probing Buried Organic Layers in Organic Light-emitting Diodes Under Operation by Electric-field-induced Doubly Resonant Sum-frequency Generation Spectroscopy. *Appl. Phys. Lett.* **2012**, *101*, 073304.

(20) Miyamae, T.; Ito, E.; Noguchi, Y.; Ishii, H. Characterization of the Interactions Between Alq_3 Thin Films and Al Probed by Two-Color Sum-Frequency Generation Spectroscopy. *J. Phys. Chem. C* **2011**, *115*, 9551–9560.

(21) Ye, H.; Gu, Z.; Gracias, D. H. Kinetics of Ultraviolet and Plasma Surface Modification of Poly(dimethylsiloxane) Probed by Sum Frequency Vibrational Spectroscopy. *Langmuir* **2006**, *22*, 1863–1868.

(22) Li, Q.; Hua, R.; Chou, K. C. Electronic and Conformational Properties of the Conjugated Polymer MEH-PPV at a Buried Film/Solid Interface Investigated by Two-Dimensional IR−Visible Sum Frequency Generation. *J. Phys. Chem. B* **2008**, *112*, 2315–2318.

(23) Li, Q.; Kuo, C. W.; Yang, Z.; Chen, P.; Chou, K. C. Surface-enhanced IR–visible Sum Frequency Generation Vibrational Spectroscopy. *Phys. Chem. Chem. Phys.* **2009**, *11*, 3436.

(24) Hu, D.; Yang, Z.; Chou, K. C. Interactions of Polyelectrolytes with Water and Ions at Air/Water Interfaces Studied by Phase-Sensitive Sum Frequency Generation Vibrational Spectroscopy. *J. Phys. Chem. C* **2013**, *117*, 15698–15703.

(25) Kliewer, C. J.; Aliaga, C.; Bieri, M.; Huang, W.; Tsung, C.-K.; Wood, J. B.; Komvopoulos, K.; Somorjai, G. A. Furan Hydrogenation over Pt(111) and Pt(100) Single-Crystal Surfaces and Pt Nanoparticles from 1 to 7 Nm: A Kinetic and Sum Frequency Generation Vibrational Spectroscopy Study. *J. Am. Chem. Soc.* **2010**, *132*, 13088–13095.

(26) Baker, L. R.; Kennedy, G.; Van Spronsen, M.; Hervier, A.; Cai, X.; Chen, S.; Wang, L.-W.; Somorjai, G. A. Furfuraldehyde Hydrogenation on Titanium Oxide-Supported Platinum Nanoparticles Studied by Sum Frequency Generation Vibrational Spectroscopy: Acid–Base Catalysis Explains the Molecular Origin of Strong Metal–Support Interactions. *J. Am. Chem. Soc.* **2012**, *134*, 14208–14216.

(27) Krier, J. M.; Michalak, W. D.; Baker, L. R.; An, K.; Komvopoulos, K.; Somorjai, G. A. Sum Frequency Generation Vibrational Spectroscopy of Colloidal Platinum Nanoparticle Catalysts: Disordering Versus Removal of Organic Capping. *J. Phys. Chem. C* **2012**, *116*, 17540–17546.

(28) Li, B.; Zhou, J.; Xu, X.; Yu, J.; Shao, W.; Fang, Y.; Lu, X. Solvent Quality Affects Chain Conformational Order at the Polymer Surface Revealed by Sum Frequency Generation Vibrational Spectroscopy. *Polymer* **2013**, *54*, 1853–1859.

(29) Chen, Z. Investigating Buried Polymer Interfaces Using Sum Frequency Generation Vibrational Spectroscopy. *Prog. Polym. Sci.* **2010**, *35*, 1376–1402.

(30) Shen, Y. R. *The Principles of Nonlinear Optics*; Wiley classics library; Wiley classics library ed.; Wiley-Interscience: Hoboken, N.J, 2003.

(31) Wang, J.; Woodcock, S. E.; Buck, S. M.; Chen, C.; Chen, Z. Different Surface-Restructuring Behaviors of Poly(methacrylate)s Detected by SFG in Water. *J. Am. Chem. Soc.* **2001**, *123*, 9470–9471.

(32) Wang, J.; Chen, C.; Buck, S. M.; Chen, Z. Molecular Chemical Structure on Poly(methyl Methacrylate) (PMMA) Surface Studied by Sum Frequency Generation (SFG) Vibrational Spectroscopy. *J. Phys. Chem. B* **2001**, *105*, 12118–12125.

(33) Gautam, K.; Schwab, A.; Dhinojwala, A.; Zhang, D.; Dougal, S.; Yeganeh, M. Molecular Structure of Polystyrene at Air/Polymer and Solid/Polymer Interfaces. *Phys. Rev. Lett.* **2000**, *85*, 3854–3857.

(34) Oh-e, M.; Hong, S.-C.; Shen, Y. R. Orientations of Phenyl Sidegroups and Liquid Crystal Molecules on a Rubbed Polystyrene Surface. *Appl. Phys. Lett.* **2002**, *80*, 784.

(35) Curtis, A. D.; Calchera, A. R.; Asplund, M. C.; Patterson, J. E. Observation of Sub-surface Phenyl Rings in Polystyrene with Vibrationally Resonant Sum-frequency Generation. *Vib. Spectrosc.* **2013**, *68*, 71–81.

(36) Liu, J.; Shi, Y.; Yang, Y. Solvation-Induced Morphology Effects on the Performance of Polymer-Based Photovoltaic Devices. *Adv. Funct. Mater.* **2001**, *11*, 420.

(37) Chen, C.; Clarke, M. L.; Wang, J.; Chen, Z. Comparison of Surface Structures of Poly(ethyl Methacrylate) and Poly(ethyl Acrylate) in Different Chemical Environments. *Phys. Chem. Chem. Phys.* **2005**, *7*, 2357.

(38) Wang, X.; Ni, H.; Xue, D.; Wang, X.; Feng, R.; Wang, H. Solvent Effect on the Film Formation and the Stability of the Surface Properties of Poly(methyl Methacrylate) End-capped with Fluorinated Units. *J. Colloid Interface Sci.* **2008**, *321*, 373–383.

(39) Ye, X.; Zuo, B.; Deng, M.; Hei, Y.; Ni, H.; Lu, X.; Wang, X. Surface Segregation of Fluorinated Moieties on Poly(methyl Methacrylate-ran-2-perfluorooctylethyl Methacrylate) Films During Film Formation: Entropic or Enthalpic Influences. *J. Colloid Interface Sci.* **2010**, *349*, 205–214.

(40) Ni, H.; Li, X.; Hu, Y.; Zuo, B.; Zhao, Z.; Yang, J.; Yuan, D.; Ye, X.; Wang, X. Surface Structure of Spin-Coated Fluorinated Polymers Films Dominated by Corresponding Film-Formation Solution/Air Interface Structure. *J. Phys. Chem. C* **2012**, *116*, 24151–24160.

(41) Opdahl, A.; Somorjai, G. A. Solvent Vapor Induced Ordering and Disordering of Phenyl Side Branches at the Air/Polystyrene Interface Studied by SFG. *Langmuir* **2002**, *18*, 9409–9412.

(42) Chen, C.; Wang, J.; Chen, Z. Surface Restructuring Behavior of Various Types of Poly(dimethylsiloxane) in Water Detected by SFG. *Langmuir* **2004**, *20*, 10186–10193.

(43) Eastman, M. P.; Hughes, R. C.; Yelton, G.; Ricco, A. J.; Patel, S. V.; Jenkins, M. W. Application of the Solubility Parameter Concept to the Design of Chemiresistor Arrays. *J. Electrochem. Soc.* **1999**, *146*, 3907-3913.

(44) Bormashenko, E.; Chaniel, G.; Grynyov, R. Towards Understanding Hydrophobic Recovery of Plasma Treated Polymers: Storing in High Polarity Liquids Suppresses Hydrophobic Recovery. *Appl. Surf. Sci.* **2013**, *273*, 549-553.

CHAPTER 3

SURFACE PLASMA TREATMENT EFFECTS ON THE MOLECULAR STRUCTURE AT POLYIMIDE/AIR AND BURIED POLYIMIDE/EPOXY INTERFACES

3.1 Introduction

Durable adhesion between polymeric adhesives and microelectronic package components is important for long-term microelectronic package reliability.[1] Weak adhesion between epoxy adhesives and the chip passivation or organic substrate in flip chip packages can result in interfacial delamination at the adhesive interface during accelerated stress testing.[2] In particular, poor adhesion between polyimide and epoxy adhesives in flip chip packages can lead to crack propagation, interfacial moisture diffusion, and corrosion of metallized interconnections.[2-4] Although polyimides typically have poor adhesion to epoxy, they are widely used as chip passivation layers and organic substrates in microelectronic packaging due to their excellent chemical resistance, high glass transition temperature, high tensile strength, and low dielectric constant.[1]

Plasma treatment of polymer surfaces is commonly used to modify the surface energy and morphology of polymer surfaces which can increase the adhesion strength of polymers to other materials.[5] Although plasma treatment typically improves the adhesion strength at polymer/polymer and polymer/metal interfaces, the mechanisms by which the adhesion is improved are not well understood.[5] Interfacial adhesion properties and mechanisms are dependent on the molecular structure of buried interfaces.[5,6] However, nondestructive in situ characterization of such buried polymer interfaces is challenging using conventional surface

analytical techniques. Consequently, structure–property relationships at buried polymer interfaces are not well understood.

Among the many surface analytical techniques used to characterize polymer interfaces, sum frequency generation (SFG) vibrational spectroscopy has recently been utilized to non-destructively characterize molecular structures at buried polymer interfaces in situ.[6-8] SFG has recently been applied to correlate molecular structures at buried polymer interfaces to interfacial properties such as adhesion, interfacial water transport, and interfacial interaction energy.[9-18] In this chapter, we utilized infrared-visible SFG vibrational spectroscopy to study the effects of polyimide plasma treatment on the molecular structure at buried polyimide/epoxy interfaces. The molecular structure of a polyimide surface was first characterized in air and then at buried polyimide/epoxy interfaces. The effect of polyimide surface plasma treatment was studied by exposing the polyimide surface to plasma prior to forming the polyimide/epoxy interface. The molecular structure at the plasma treated polyimide/epoxy interface was then compared to the molecular structure at the untreated polyimide/epoxy interface to deduce the molecular level effects of the plasma treatment. Analysis of SFG spectra collected in different polarization combinations enabled the possible tilt and twist angles of the polyimide backbone at the buried polyimide/epoxy interface to be determined before and after plasma treatment of the polyimide surface.

3.2 Experimental

3.2.1 Materials

N-Methyl-2-pyrrolidone (NMP), bisphenol A diglycidyl ether, and 4,4′-diaminodiphenylmethane were purchased from Sigma–Aldrich. Poly(pyromellitic dianhydride-co-4,4′-oxydianiline) amic acid solution (polyamic acid) was purchased from Sigma-Aldrich as a

~13 wt% solution in solvent. Calcium fluoride (CaF_2) right-angle prisms were ordered from Altos Photonics, Inc. and CaF_2 windows were ordered from ESCO Products, Inc.

3.2.2 Sample Preparation

Poly(pyromellitic dianhydride-co-4,4′-oxydianiline) solution was diluted 1:3 by weight in NMP. Polyimide thin films were deposited by spin casting (Speedline Technologies P-6000) the diluted poly(pyromellitic dianhydride-co-4,4′-oxydianiline) solution on CaF_2 prisms or CaF_2 windows at 3000 RPM for 30 s. Cross-linked polyimide films were prepared by curing the poly(pyromellitic dianhydride-co-4,4′-oxydianiline) film in a vacuum furnace (STT-1200C-6-12 High Temperature Tube Furnace, Sentro Tech Corp.) at 260 ℃ for 60 min. The thickness of the cured polyimide films was ~50 nm based on profilometry measurements (DekTak 6 Profilometer). Epoxy precursor blends were prepared by mixing a stoichometric ratio of bisphenol A diglycidyl ether and 4,4′-diaminodiphenylmethane. Polyimide/epoxy interfaces were prepared by depositing the epoxy precursor blend on the polyimide film followed by curing of the epoxy precursor blend for 1 h at 50 ℃, 45 min at 75 ℃, and 30 min at 110 ℃.[19] Plasma treated interfaces were prepared by exposing cured polyimide films to oxygen or argon plasma for 10 s (Plasma Etch, Inc., PE-50), after which the plasma treated polyimide/epoxy interface was prepared following the same procedure used to prepare untreated polyimide/epoxy interfaces.

3.2.3 Instrumentation

Fourier transform infrared vibrational spectroscopy: Infrared spectra were collected using a Thermo Scientific Nicolet 6700 Fourier transform infrared (FTIR) spectrometer. IR spectra were collected under a nitrogen atmosphere in the 1000–2000 cm^{-1} range with a resolution of 4 cm^{-1} from poly(pyromellitic dianhydride-co-4,4′-oxydianiline) thin films on CaF_2 windows. Prior to collection of the IR spectrum, the spin cast poly(pyromellitic dianhydride-co-4,4′-

oxydianiline) thin film was cured at ~85 ℃ for 10 min to remove residual solvent. IR spectra were collected by averaging 32 scans before and after curing the poly(pyromellitic dianhydride-co-4,4′-oxydianiline) thin film to monitor the thermal imidization process.

Sum frequency generation vibrational spectroscopy: SFG has been extensively applied to study molecular structures at surfaces and buried interfaces as discussed in chapter 1.[20-31] SFG spectra were collected from polyimide/air and polyimide/epoxy interfaces of polyimide films on CaF_2 prisms. The input angles of the visible and infrared beams were 60 ° and 54 ° at the sample stage, respectively, and the pulse energies of the input visible and infrared beams were ~20 μJ and ~100 μJ, respectively. SFG spectra were collected in the SSP and PPP polarization combinations at ambient temperature and humidity (~20 ℃ and 40% relative humidity, respectively).

3.3 Results and Discussion

3.3.1 Polyimide imidization

The curing of the poly(pyromellitic dianhydride-co-4,4′-oxydianiline) thin film (Fig. 3.1a) was monitored by collecting IR spectra of the film before and after thermal curing (Fig. 3.1b). IR spectra collected from the uncured film contained peaks near 1230, 1408, 1500, 1540, 1654, and 1726 cm^{-1}. Peaks near 1409, 1500, 1538, 1654, and 1725 cm^{-1} can be assigned to the carboxylic acid -OH, the phenyl ring, -CNH amide II, C=O amide I, and carboxylic acid C=O stretches, respectively.[32,33] IR spectra collected from the cured film contained peaks near 1244, 1375, 1500, 1723, and 1777 cm^{-1}.

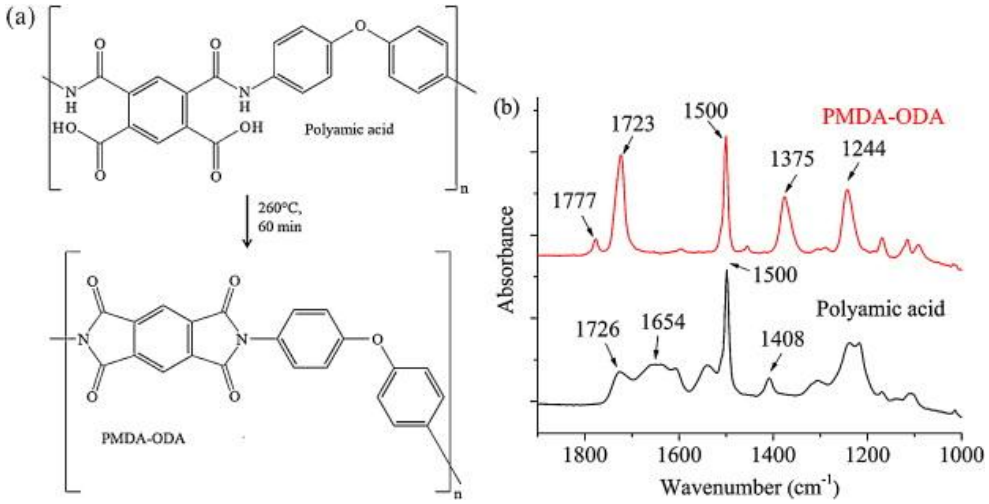

Figure 3.1 (a) Polyamic acid cross-link reaction and (b) FTIR before (polyamic acid) and after (PMDA-ODA) thermal cure of polyamic acid. The FTIR spectra in (b) were offset vertically for clarity.

Peaks near 1244, 1375, 1500, 1723, and 1777 cm^{-1} can be assigned to COC, CNC, phenyl ring, imide I coupled C=O asymmetric, and imide I coupled C=O symmetric stretches, respectively.[32,33] The detection of a strong axial-imide II peak near 1375 cm^{-1} together with a lack of a carboxylic acid -OH feature near 1409 cm^{-1} in the IR spectrum collected from the cured film indicates that the imidization reaction was nearly complete after the thermal cure.

3.3.2 Polyimide/air and polyimide/epoxy interfaces

SFG spectra were collected in the 1650–1850 cm^{-1} range (of the input infrared beam) from the surface of cured polyimide films to characterize the molecular structure of the cured polyimide/air interface. Two peaks near 1733 and 1773 cm^{-1} were detected in the SFG SSP spectrum collected from the polyimide/air interface which can be assigned to the asymmetric (as) and symmetric (s) stretch of the coupled C=O groups on the imide ring (Fig. 3.2a).[34-37]

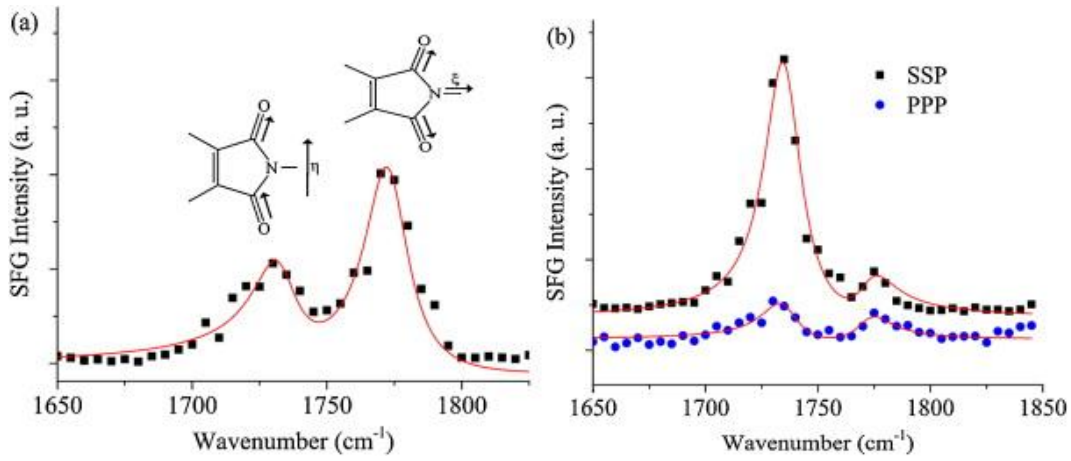

Figure 3.2. SFG SSP spectrum collected from the (a) polyimide/air interface and SFG SSP and PPP spectra collected from the (b) buried polyimide/epoxy interface. The SFG spectra in (b) were offset vertically for clarity.

Strong SFG signal detected in the SSP polarization combination indicates that the infrared dipole moment of the detected vibrational mode had a dipole component perpendicular to the surface[38] Therefore, based on the axis of infrared excitation of the asymmetric and symmetric vibrational modes shown in Fig. 3.2a, the symmetric peak in the SSP polarization combination will probe the tilt angle of the imide ring relative to the polyimide surface normal while the asymmetric peak will probe the twist angle of the coupled carbonyl groups in the plane of the imide backbone (Fig. 3.3). The strong symmetric and weak asymmetric peaks observed in the SFG spectra collected from the polyimide/air interface suggest that the imide backbone was tilted from the surface normal and that the imide ring had a relatively high twist angle.

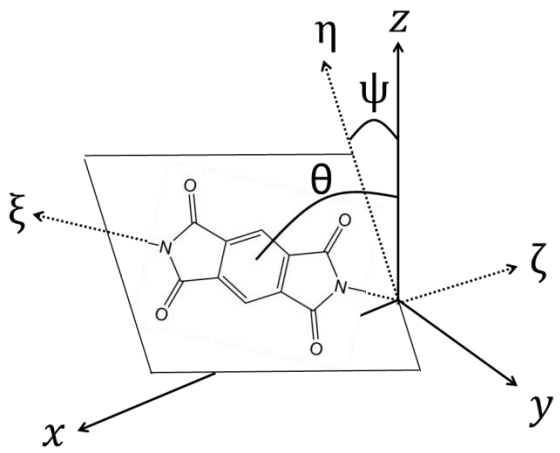

Fig. 3.3. Laboratory frame coordinate system (*x, y, z*) and molecular coordinate system (ξ,η,ζ) for the imide backbone of PMDA-ODA where *z* is the surface normal. The tilt angle θ is defined as the angle between the z axis and the ξ axis. The twist angle ψ is defined as the angle between the z axis and the η axis.

3.3.3 Polyimide Orientation Analysis

The detection of SFG signal contributed by the imide ring indicates that the functional groups are ordered and oriented with respect to the polyimide film surface normal. Collecting SFG spectra in both the SSP and PPP polarization combinations enabled the possible tilt and twist angles of the imide core to be deduced. The SSP polarization combination will solely probe the χ_{yyz} nonlinear susceptibility component while the PPP polarization in the near total reflection geometry will probe the χ_{zzz} susceptibility. No SFG signal was detected in SFG spectra collected from the interface between a CaF_2 prism and a thick, drop cast polyimide film. Therefore, SFG signals detected in CaF_2/polyimide/epoxy systems were believed to be generated at the polyimide/epoxy interface.

Previous studies have reported that the portion of the imide ring protruding from the film surface could be assigned C_{2v} symmetry. When the polyimide core is oriented nearly parallel to

the film surface (θ = 60-90 °), the second-order nonlinear optical susceptibility components of the imide ring probed by the SSP and PPP polarization combinations can then be expressed as:[35,36]

$$\chi_{yyz,as} = -N_s(a_{as})_{\xi\xi\eta}\langle sin^3\theta\rangle\langle cos\psi\rangle - (a_{as})_{\eta\eta\eta}(\langle sin\theta\rangle\langle sin^2\psi cos\psi\rangle + \langle sin\theta cos^2\theta\rangle\langle cos^3\psi\rangle) \quad (3.1)$$

$$\chi_{yyz,s} = -N_s(a_s)_{\xi\xi\eta}\langle sin^3\theta\rangle\langle cos\psi\rangle - (a_s)_{\eta\eta\eta}(\langle sin\theta\rangle\langle sin^2\psi cos\psi\rangle + \langle sin\theta cos^2\theta\rangle\langle cos^3\psi\rangle) \quad (3.2)$$

$$\chi_{zzz,as} = -2N_s(a_{as})_{\xi\xi\eta}\langle sin\theta cos^2\theta\rangle\langle cos\psi\rangle - 2(a_{as})_{\eta\eta\eta}(\langle sin^3\theta\rangle\langle cos^3\psi\rangle) \quad (3.3)$$

where $(a_{as})_{\eta\eta\eta}$ / $(a_{as})_{\xi\xi\eta}$ ≈ 1.13 and $(a_s)_{\eta\eta\eta}$ / $(a_s)_{\xi\xi\eta}$ ≈ 1.25.[35,36]

When the polyimide core is tilted with respect to the polyimide surface (θ = 0-60 °), the second-order nonlinear optical susceptibility components of the imide ring probed by the SSP polarization combination can then be expressed as:[35,36]

$$\chi_{yyz,as} = N_s\{(a_{as})_{\xi\eta\eta}\langle sin^2\theta cos\theta\rangle\langle cos^2\psi\rangle\} \quad (3.4)$$

$$\chi_{yyz,ss} = \frac{N_s}{2}\{(a_s)_{\xi\xi\xi}\langle sin^2\theta cos\theta\rangle + (a_s)_{\eta\eta\xi}(\langle cos\theta\rangle\langle sin^2\psi\rangle + \langle cos^3\theta\rangle\langle cos^2\psi\rangle)\} \quad (3.5)$$

where $(a_s)_{\eta\eta\xi}$ / $(a_s)_{\xi\xi\xi}$ ≈ 2.2 and $(a_{as})_{\xi\eta\eta}/(a_s)_{\xi\xi\xi}$ ≈ 1.3.[35,36]

The intensity of the SFG signal generated in the SSP and PPP polarization combinations can then be expressed as:

$$I_{SFG,SSP}(\omega_{SFG}) \propto \left|\chi^{(2)}_{eff,ssp}\right|^2 \propto \left|L_{yy}(\omega_{SFG})L_{yy}(\omega_{VIS})L_{zz}(\omega_{IR})sin\theta_{IR}\chi^{(2)}_{yyz}\right|^2 I_{VIS}I_{IR}$$
$$= \left|F_{yyz}\chi^{(2)}_{yyz}\right|^2 I_{VIS}I_{IR} \quad (3.6)$$

$$I_{SFG,PPP}(\omega_{SFG}) \propto \left|\chi^{(2)}_{eff,ppp}\right|^2 \propto$$

$$\left|L_{zz}(\omega_{SFG})L_{zz}(\omega_{VIS})L_{zz}(\omega_{IR})sin\theta_{SFG}sin\theta_{VIS}sin\theta_{IR}\chi^{(2)}_{zzz}\right|^2 I_{VIS}I_{IR} = \left|F_{zzz}\chi^{(2)}_{zzz}\right|^2 I_{VIS}I_{IR} \quad (3.7)$$

, respectively, where L_{yy} and L_{zz} are interfacial local field factors and θ_{IR} is the input angle of beam at the interface. Transmission of the input beams into the CaF_2 prism (t_{10} interface) and transmission of the SFG beam out of the prism (t_{01} interface) were taken into account in the local field factors at the polyimide/air and polyimide/epoxy interface

$$F_{yyz} = t^s_{10,SFG}L_{yy}(\omega_{SFG})t^s_{01,VIS}L_{yy}(\omega_{VIS})t^p_{01,IR}L_{zz}(\omega_{IR})sin\theta_{IR}$$

$$F_{zzz} = t^p_{10,SFG}L_{zz}(\omega_{SFG})t^p_{01,VIS}L_{zz}(\omega_{VIS})t^p_{01,IR}L_{zz}(\omega_{IR})sin\theta_{SFG}sin\theta_{VIS}sin\theta_{IR}$$

where t_{01} and t_{10} are the linear transmission coefficients for light entering and exiting the CaF_2 prism, respectively. The $\left|F_{zzz}/F_{yyz}\right|$ ratio was approximately 0.75 based on the thin film model discussed in chapter 1 using near total internal reflection prism geometry. Tilt and twist angles (θ, ψ), as defined in Figure 3.3, were then deduced by plotting $\chi^{(2)}_{eff,yyz,as}/\chi^{(2)}_{eff,yyz,ss}$ or $\chi^{(2)}_{eff,zzz,as}/\chi^{(2)}_{eff,yyz,as}$ and comparing experimentally determined susceptibility ratios to the calculated ratios.

SFG spectra were then collected from the buried polyimide/epoxy interface to investigate how interactions between the epoxy and the polyimide influenced the polyimide molecular structure (Fig. 3.2b). Two peaks near 1735 and 1773 cm^{-1} were detected in the SFG SSP spectrum collected from the buried polyimide/epoxy interface, similar to the spectrum collected from the polyimide/air interface. However, the intensity of the asymmetric peak was much larger than the intensity of the symmetric peak. The high asymmetric to symmetric peak intensity ratio indicates that that imide backbone was lying nearly parallel to the polyimide/epoxy interface and

that the carbonyl groups were oriented with a low twist angle. Carbonyl groups oriented with a low twist angle indicate that one of the carbonyl groups on the imide chain was directed toward the epoxy bulk, different from the behavior at the polyimide/air interface where the carbonyl groups were oriented more parallel to the polyimide surface.

Different SFG spectra at the polyimide/air and polyimide/epoxy interfaces indicate that the molecular structure at the two interfaces was different. The strong asymmetric peak in the SFG spectra collected from the buried polyimide/epoxy interface suggests that the carbonyl groups on the imide backbone reoriented due to chemical interactions with the epoxy. Furthermore, the strong asymmetric peak suggests that the imide carbonyl group was oriented with a lower twist angle, i.e. the carbonyl was directed more toward the epoxy bulk, compared to the orientation at the polyimide/air interface. Polar interactions between the polyimide carbonyl and polar functional groups in the cross-linked epoxy may have caused the reorientation of the carbonyl group.

3.3.4 Polyimide plasma treatment

SFG spectra were first collected from the polyimide surface before and after plasma treatment to investigate whether ordered polyimide rings were present at the film surface after plasma treatment. The intensities of the peaks in the SFG SSP spectrum collected from the oxygen plasma treated polyimide/air interface were higher than at the original interface (Fig. 3.4a). In addition, more peaks were observed after the plasma treatment or the widths of the imide ring peaks increased. The higher signal intensities after oxygen plasma treatment could be due to new carbonyl groups generated by reactions between the polyimide surface and the oxygen plasma. Oxygen plasma treatment of polyimide has been reported to oxidize the imide rings and phenyl groups at the surface of the film.[39-41] Consequently, plasma treatment is

commonly used to increase the surface hydrophilicity and surface energy of polyimide films.[42] Therefore, the additional carbonyl stretching signals observed after oxygen plasma treatment may have been contributed by carbonyl groups formed by oxidation of the imide ring or phenyl group by the oxygen plasma. Since this research is focused on the investigation of the buried polyimide interface using SFG as presented below, and plasma treatment of polyimide has been studied using other techniques,[39-41] here we only characterized the polyimide surface after plasma treatment using SFG.

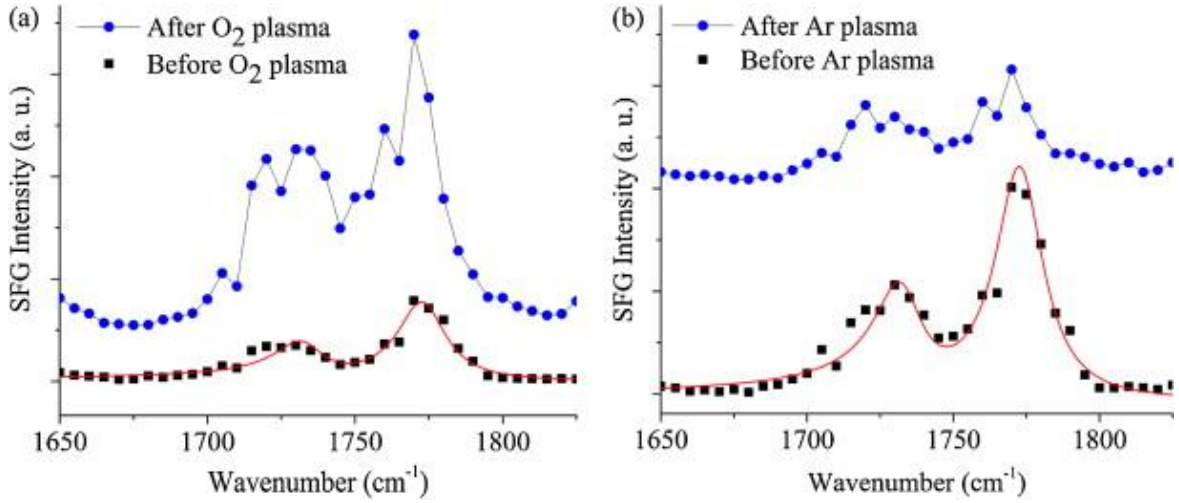

Figure 3.4. SFG spectra collected from the polyimide/air interface before and after (a) oxygen and (b) argon plasma treatment. The SFG spectra in (a) and (b) were offset vertically for clarity. The solid red curves are the fitting results. The lines connecting the data points are a guide to the eye.

The spectral features of the SFG spectrum collected from the argon plasma treated polyimide/air interface (Fig. 3.4b) were similar to the features of the SFG spectrum collected from the untreated polyimide/air interface. Similar spectral features before and after plasma treatment indicate that the orientation of the polyimide rings at the polyimide/air interface was not largely affected by the plasma treatment. However, unlike the oxygen plasma treated polyimide/air

interface, the intensities of the peaks in the spectrum collected from the argon plasma treated polyimide/air interface were lower than at the original interface. The decrease in the SFG intensity could be due to decreased ordering of the polyimide rings or to reactions between the ring and the argon plasma.[41]

After characterizing the effects of plasma treatment on the molecular structure at the polyimide/air interface, SFG spectra were collected from buried polyimide/epoxy interfaces before and after plasma treatment of the polyimide film to characterize the effect of polyimide plasma treatment on the molecular structure of corresponding polyimide/epoxy interfaces. The SFG spectrum collected from the oxygen plasma treated polyimide/epoxy interface (Fig. 3.5a) was similar to the SFG spectra collected from the untreated polyimide/epoxy interface. However, the asymmetric to symmetric peak intensity ratio was lower than the intensity ratio at the untreated polyimide/epoxy interface which indicates that plasma treatment permanently altered the orientation of the imide backbone at the buried interface. The detection of SFG peaks contributed by imide ring vibrational modes at the plasma treated polyimide/epoxy interface indicates that ordered imide rings were present at the buried interface.

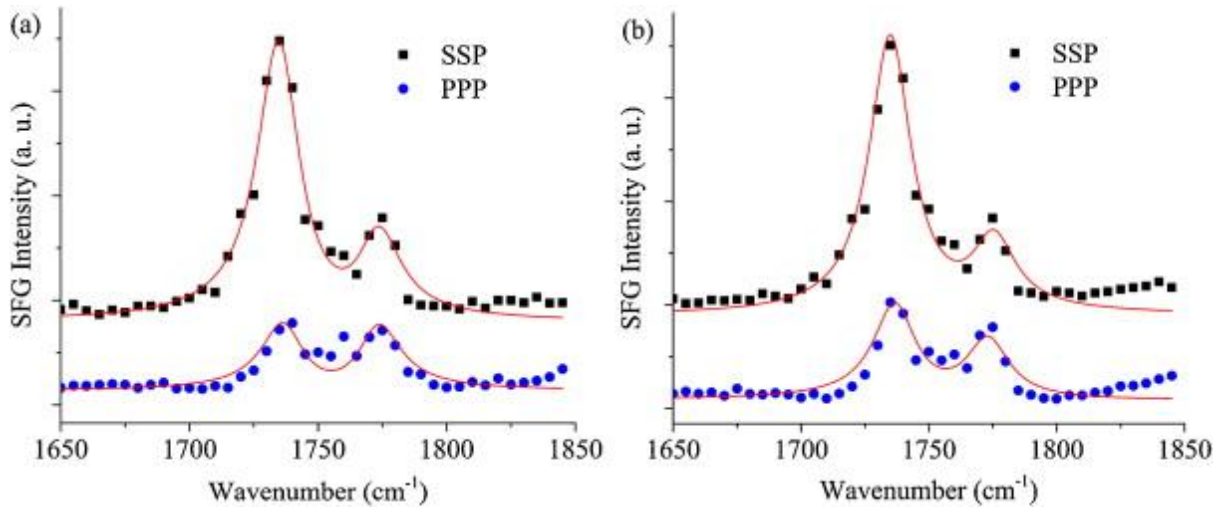

Figure 3.5. SFG spectra collected from (a) oxygen and (b) argon plasma treated polyimide/epoxy interface. The SFG spectra in (a) and (b) were offset vertically for clarity.

SFG SSP spectra collected from the argon plasma treated polyimide/epoxy interface (Fig. 3.5b) were similar to SFG spectra collected from the oxygen plasma treated polyimide/epoxy interface. The asymmetric to symmetric peak intensity ratio was again lower than the intensity ratio at the untreated polyimide/epoxy interface. To further characterize the effects of plasma treatment on the molecular structure at buried polyimide/epoxy interfaces, the possible orientations of the imide ring were determined before and after plasma treatment at the polyimide/air and polyimide/epoxy interfaces.

3.3.5 Orientation analysis

The orientation of the imide ring at the polyimide/air interface was estimated by assuming that the tilt angle was low ($\theta \approx 0$–$60°$) based on the strong symmetric peak in the corresponding SFG spectrum. The experimentally determined $\chi_{yyz,as}/\chi_{yyz,s}$ value at the untreated polyimide/air interface was ~0.49 (Table 3.1) which indicates that the imide ring had a tilt angle in the range of 35–60 ° and a twist angle in the range of ~0 ° to 42 ° (Fig. 3.6). The orientation of the imide ring

was not estimated after oxygen and argon plasma treatment due to possible overlap between signals contributed by carbonyl groups and the imide ring.

Polyimide/air									
ω (cm^{-1})	**$A_{q,ssp}$**	**Γ_q (cm^{-1})**							
1733	11.0	10.0	χ_{NR}	-1.5					
1773	22.5	10.0	φ	-1.1					
Polyimide/epoxy									
ω (cm^{-1})	**$A_{q,ssp}$**	**Γ_q (cm^{-1})**			**ω (cm^{-1})**	**$A_{q,ppp}$**	**Γ_q (cm^{-1})**		
1735	37.1	10.0	χ_{NR}	-1.5	1735.0	17.5	10.0	χ_{NR}	-0.6
1773	-35.4	10.0	φ	-0.8	1773.0	-15.2	10.0	φ	-0.1
O_2 treated Polyimide/epoxy									
ω (cm^{-1})	**$A_{q,ssp}$**	**Γ_q (cm^{-1})**			**ω (cm^{-1})**	**$A_{q,ppp}$**	**Γ_q (cm^{-1})**		
1735	36.6	10.0	χ_{NR}	-1.1	1737.0	21.5	10.0	χ_{NR}	-0.6
1773	-34.5	10.0	φ	-0.6	1773.0	-22.0	10.0	φ	-0.1
Ar treated Polyimide/epoxy									
ω (cm^{-1})	**$A_{q,ssp}$**	**Γ_q (cm^{-1})**			**ω (cm^{-1})**	**$A_{q,ppp}$**	**Γ_q (cm^{-1})**		
1735	37.4	10.0	χ_{NR}	-1.3	1737.0	27.4	10.0	χ_{NR}	-0.6
1775	-38.6	10.0	φ	-0.9	1773.0	-23.6	10.0	φ	-0.1

Table 3.1 SFG fitting results for Figures 3.2 and 3.5.

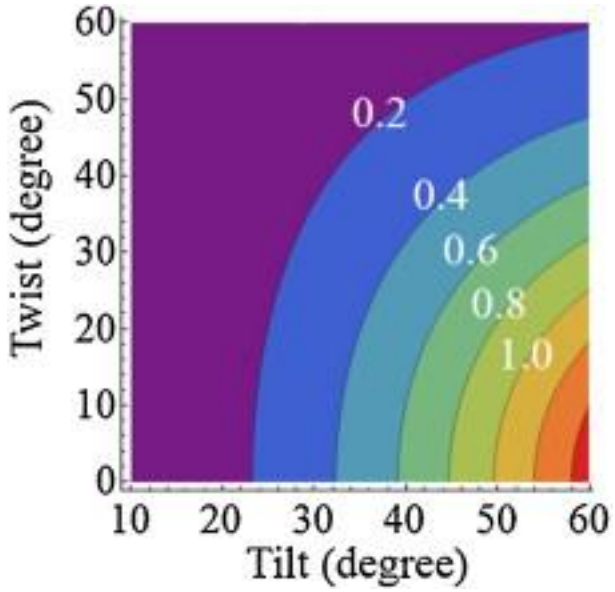

Figure 3.6. Contour plot of $\chi_{yyz,as}/\chi_{yyz,s}$ as a function of tilt (θ) and twist (ψ) angles when the tilt angle is between 0 and 60 °.

We then assumed that the tilt angle of the imide ring at the buried polyimide/epoxy interface was almost parallel to polyimide surface ($\theta \approx 60–90$ °) based on the weak symmetric peak in the corresponding SFG spectrum. The $\chi_{yyz,as}/\chi_{yyz,s}$ ratio was not sensitive to changes in twist angle at high tilt angles (Fig. 3.7a), so the $\chi_{zzz,as}/\chi_{yyz,as}$ ratio was used to determine the twist angle of the imide ring at the buried polyimide/epoxy interface. The experimentally determined $\chi_{zzz,as}/\chi_{yyz,as}$ value at the untreated polyimide/epoxy interface was ~0.47 which indicates that the imide ring had a twist angle of ~48 ° (Fig. 3.7b) at large tilt angles. After oxygen and argon plasma treatment, the imide ring twist angles at the buried polyimide/epoxy interface were ~43 ° and ~38 °, respectively.

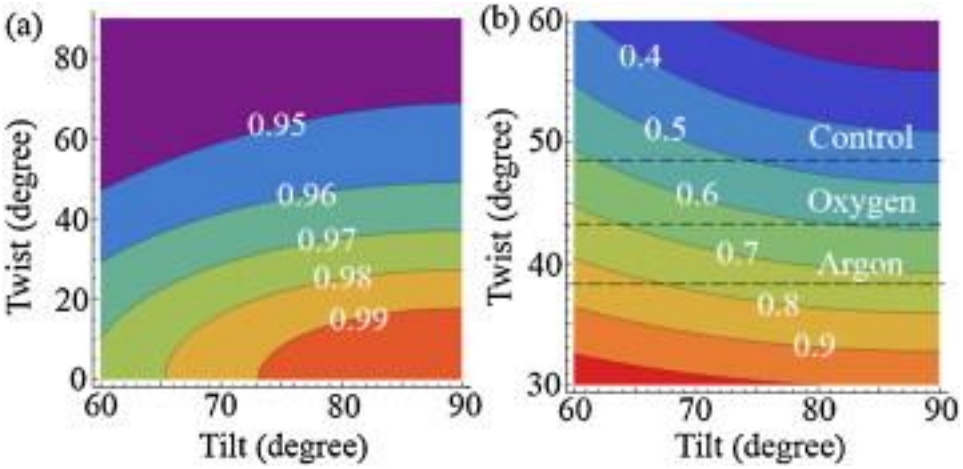

Figure 3.7. Contour plots of (a) $\chi_{yyz,as}/\chi_{yyz,s}$ and (b) $\chi_{zzz,as}/\chi_{yyz,as}$ as a function of tilt (θ) and twist (ψ) angles when the tilt angle is between 60 and 90°.

SFG orientation analysis suggests that plasma treatment resulted in a slight decrease in the twist angles of the imide ring at the buried polyimide/epoxy interface. The lower tilt angle of the imide ring after plasma treatment indicates that the carbonyl groups were directed slightly more into the epoxy bulk at the buried interface. If polymer chain scission occurred during the oxygen plasma treatment, entanglement loss could occur at the polyimide/air interface. Therefore, the different orientations of the imide ring at the polyimide/epoxy and plasma treated polyimide/epoxy interfaces may be due to greater flexibility of surface polyimide chains after plasma treatment.

3.4 Conclusion

In summary, we have demonstrated that plasma treatment of polyimide surfaces altered the molecular structure of corresponding polyimide/air and buried polyimide/epoxy interfaces. SFG results indicated that the polyimide backbone was tilted at the polyimide/air interface but was nearly lying down at the buried polyimide/epoxy interface. Furthermore, the twist angle of

the imide backbone carbonyl groups at the buried polyimide/epoxy interface was slightly decreased after plasma treatment.

3.5. Impact

Delamination at polyimide/epoxy interfaces due to weak interfacial adhesion continues to be reliability concern in microelectronic packaging. If predicative structure-property relationships at such buried adhesive interfaces were known, the interfaces could be rationally designed to withstand harsh reliability testing and products could be brought to market faster. In this chapter, we used SFG to directly probe polyimide surface molecular structures after plasma treatment. We found that different plasma treatments can lead to different surface molecular structures. In addition, we demonstrated that SFG can be used to directly probe molecular structures at buried adhesive interface *in situ*. By characterizing buried interfaces nondestructively, the effects of plasma treatments on molecular structures at buried interfaces could be directly characterized. This general approach can be applied to study a variety of different adhesive interfaces before and after many different surface processing or modification steps to elucidate how the steps affect molecular structures, and hence interfacial properties, at downstream buried interfaces. More generally, these results indicate that plasma treatment of polymer surfaces not only increases the polymer surface energy, increases surface roughness, and changes the surface elemental structure, but can also influence the molecular structure at corresponding buried interfaces prepared using the plasma treated surfaces. Different molecular structures at the polyimide/air, polyimide/epoxy, and plasma treated polyimide/epoxy interfaces provide insight on the molecular level effects of plasma treatment on adhesion strength, which can be used to address the previous lack of clear correlation between surface energy calculations

and interfacial adhesion strength measurements.[43] This research suggests that buried interfacial molecule structures can be affected by plasma treatment on the surfaces used to prepare the interfaces, which should be considered in adhesion mechanisms and such structures should be correlated to adhesion strength measurements. Such knowledge can then be used to predict adhesion properties in the design of new adhesive interfaces in microelectronic packages that can withstand harsh qualification tests.

3.6 References

(1) V.K. Khanna. Adhesion-delamination phenomena at the surfaces and interfaces in microelectronics and MEMS structures and packaged devices. *J. Phys. Appl. Phys.* **2011**, *44*, 034004.

(2) S. Luo, C.P. Wong. Influence of temperature and humidity on adhesion of underfills for flip chip packaging. *IEEE Trans. Compon. Packag. Technol*. **2005**, *28*, 88-94.

(3) S.J. Luo, C.P. Wong. Effect of UV/ozone treatment on surface tension and adhesion in electronic packaging. *IEEE Trans. Compon. Packag. Technol.* **2001**, *24*, 43-49.

(4) P. Hoontrakul, L.H. Sperling, R.A. Pearson. Understanding the strength of epoxy-polyimide interfaces for flip-chip packages. *IEEE Trans. Device Mater. Reliab.* **2003**, *3*, 159-166.

(5) F. Awaja, M. Gilbert, G. Kelly, B. Fox, P.J. Pigram. Adhesion of polymers. *Prog. Polym. Sci.* **2009**, *34*, 948-968.

(6) Z. Chen. Investigating buried polymer interfaces using sum frequency generation vibrational spectroscopy. *Prog. Polym. Sci.* **2010**, *35*, 1376-1402.

(7) C. Zhang, J.N. Myers, Z. Chen. Elucidation of molecular structures at buried polymer interfaces and biological interfaces using sum frequency generation vibrational spectroscopy. *Soft Matter*, **2013,** *9*, 4738-4761.

(8) J.M. Hankett, Y.W. Liu, X.X. Zhang, C. Zhang, Z. Chen. Molecular level studies of polymer behaviors at the water interface using sum frequency generation vibrational spectroscopy. *J. Polym. Sci. Part B Polym. Phys.* **2013,** *51*, 311-328.

(9) K. Nanjundiah, P.Y. Hsu, A. Dhinojwala. Understanding rubber friction in the presence of water using sum-frequency generation spectroscopy, J. Chem. Phys. **2009**, *130*, 024702.

(10) C.L. Loch, D. Ahn, Z. Chen, Sum frequency generation vibrational spectroscopic studies on a silane adhesion-promoting mixture at a polymer interface. *J. Phys. Chem. B* **2006**, *110*, 914-918.

(11) C.L. Loch, D. Ahn, A.V. Vázquez, Z. Chen. Diffusion of one or more components of a silane Adhesion-promoting mixture into poly(methyl Methacrylate). *J. Colloid Interface Sci.* **2007**, *308*, 170-175.

(12) A.V. Vázquez, A.P. Boughton, N.E. Shephard, S.M. Rhodes, Z. Chen. Molecular structures of the buried interfaces between silicone elastomer and silane adhesion promoters probed by sum frequency generation vibrational spectroscopy and molecular dynamics simulations. *ACS Appl. Mater. Interfaces* **2010**, *2*, 96-103.

(13) C. Zhang, J.N. Myers, Z. Chen. Molecular behavior at buried epoxy/poly(ethylene Terephthalate) interface. *Langmuir* **2014**, *30*, 12541-12550.

(14) C. Zhang, Z. Chen. Quantitative molecular level understanding of ethoxysilane at poly(dimethylsiloxane)/polymer interfaces. *Langmuir* **2013**, *29*, 610-619.

(15) J.N. Myers, C. Zhang, K.-W. Lee, J. Williamson, Z. Chen. Hygrothermal aging effects on buried molecular structures at epoxy interfaces. *Langmuir* **2014**, *30*, 165-171.

(16) X. Zhang, J.N. Myers, J.D. Bielefeld, Q. Lin, Z. Chen. *In situ* observation of water behavior at the surface and buried interface of a Low-K dielectric film. ACS Appl. Mater. Interfaces **2014**, *6*, 18951-18961.

(17) A. Kurian, S. Prasad, A. Dhinojwala. Direct measurement of Acid−base interaction energy at solid interfaces. *Langmuir* **2010**, *26*, 17804-17807.

(18) Y. Fang, B. Li, J. Yu, J. Zhou, X. Xu, W. Shao, X. Lu. Probing surface and interfacial molecular structures of a rubbery adhesion promoter using sum frequency generation vibrational spectroscopy. *Surf. Sci.* **2013**, *615*, 26-32.

(19) S. Onard, I. Martin, J.-F. Chailan, A. Crespy, P. Carriere. Nanostructuration in thin epoxy-amine films inducing controlled specific phase etherification: effect on the glass transition temperatures. *Macromolecules* **2011**, *44*, 3485-3493.

(20) W.-T. Liu, Y.R. Shen. *In situ* Sum-frequency vibrational spectroscopy of electrochemical interfaces with surface plasmon resonance. *Proc. Natl. Acad. Sci. USA* **2014**, *111*, 1293-1297.

(21) J. Sung, G.A. Waychunas, Y.R. Shen. Surface-induced anisotropic orientations of interfacial ethanol molecules at air/sapphire($1\bar{1}02$) and Ethanol/Sapphire($1\bar{1}02$) Interfaces. *J. Phys. Chem. Lett.* **2011**, *2*, 1831-1835.

(22) C.M. Thompson, L.M. Carl, G.A. Somorjai. Sum frequency generation study of the interfacial layer in liquid-phase heterogeneously catalyzed oxidation of 2-propanol on platinum: effect of the concentrations of water and 2-propanol at the interface. *J. Phys. Chem. C* **2013**, *117*, 26077-26083.

(23) H. Wang, A. Sapi, C.M. Thompson, et al. Dramatically different kinetics and mechanism at solid/liquid and solid/gas interfaces for catalytic isopropanol oxidation over Size-controlled platinum nanoparticles. *J. Am. Chem. Soc.* **2014**, *136*, 10515-10520.

(24) S.J. Ye, H.C. Li, W.L. Yang, Y. Luo. Accurate determination of interfacial protein secondary structure by combining interfacial-sensitive amide I and amide III spectral signals. *J. Am. Chem. Soc.* **2014**, *136*, 1206-1209.

(25) F. Wei, H.C. Li, S.J. Ye. Specific ion interaction dominates over hydrophobic matching effects in peptide–lipid bilayer interactions: The case of short peptide. *J. Phys. Chem. C* **2013**, *117*, 26190-26196.

(26) X. Lu, B.L. Li, P.Z. Zhu, G. Xue, D. Li. Illustrating consistency of different experimental approaches to probe the buried polymer/metal interface using sum frequency generation vibrational spectroscopy. *Soft Matter* **2014**, *10*, 5390-5397.

(27) X. Lu, J.N. Myers, Z. Chen. Molecular ordering of phenyl groups at the buried polystyrene/metal interface. *Langmuir* **2014**, *30*, 9418-9422.

(28) Q.F. Li, C.W. Kuo, Z. Yang, P.L. Chen, K.C. Chou. Surface-enhanced IR–visible sum frequency generation vibrational spectroscopy. *Phys. Chem. Chem. Phys.* **2009**, *11*, 3436-3442.

(29) Q.F. Li, R. Hua, K.C. Chou. Electronic and conformational properties of the conjugated polymer MEH-PPV at a buried film/solid interface investigated by Two-dimensional IR-visible sum frequency generation. *J. Phys. Chem. B* **2008**, *112*, 2315-2318.

(30) J.N. Myers, C. Zhang, C. Chen, Z. Chen, Influence of casting solvent on phenyl ordering at the surface of spin cast polymer thin films. *J. Colloid Interface Sci.* **2014**, *423*, 60-66.

(31) J. Wang, C. Chen, S.M. Buck, Z. Chen. Molecular chemical structure on poly(methyl Methacrylate) (PMMA) surface studied by Sum Frequency Generation (SFG) vibrational spectroscopy. *J. Phys. Chem. B* **2001**, *105*, 12118-12125.

(32) K. Ha, J.L. West. Studies on the Photodegradation of polarized UV-Exposed PMDA-ODA polyimide films. *J. Appl. Polym. Sci.* **2002**, *86*, 3072-3077.

(33) W.S. Li, Z.X. Shen, J.Z. Zheng, S.H. Tang. FT-IR study of the imidization process of photosensitive polyimide PMDA/ODA. *Appl. Spectrosc.* **1998**, *52*, 985-989.

(34) D. Kim, Y.R. Shen. Study of wet treatment of polyimide by sum-frequency vibrational spectroscopy. *Appl. Phys. Lett.* **1999**, *74*, 3314-3316.

(35) D. Kim, M. Oh-E, Y.R. Shen. Rubbed polyimide surface studied by Sum-frequency vibrational spectroscopy. *Macromolecules* **2001**, *34*, 9125-9129.

(36) J. Sung, D. Kim, C.N. Whang, M. Oh-E, H. Yokoyama. Sum-frequency vibrational spectroscopic study of polyimide surfaces made by spin coating and ionized cluster beam deposition. *J. Phys. Chem. B* **2004**, *108*, 10991-10996.

(37) M. Oh-E, H. Yokoyama, D. Kim. Mapping molecular conformation and orientation of polyimide surfaces for homeotropic liquid crystal alignment by nonlinear optical spectroscopy. *Phys. Rev. E* **2004**, *69*, 051705.

(38) A.G. Lambert, P.B. Davies, D.J. Neivandt. Implementing the theory of sum frequency generation vibrational spectroscopy: a tutorial review. *Appl. Spectrosc. Rev.* **2005**, *40*, 103-145.

(39) D. Wolany, T. Fladung, L. Duda, et al. Combined ToF-SIMS/XPS study of plasma modification and metallization of polyimide. *Surf. Interface Anal*. **1999**, *27*, 609-617.

(40) S.H. Kim, S.W. Na, N.-E. Lee, Y.W. Nam, Y.-H. Kim. Effect of surface roughness on the adhesion properties of Cu/Cr films on polyimide substrate treated by inductively coupled oxygen plasma. *Surf. Coat. Technol.* **2005**, *200*, 2072-2079.

(41) Y.-S. Lin, H.-M. Liu, H.-T. Chen. Surface modification of polyimide films by argon plasma for copper metallization on microelectronic flex substrates. *J. Appl. Polym. Sci*. **2006**, *99*, 744-755.

(42) K.W. Lee, S.P. Kowalczyk, J.M. Shaw. Surface modification of PMDA-oxydianiline polyimide. surface structure-adhesion relationship. Macromolecules **1990**, *23*, 2097-2100.

(43) P. Hoontrakul, R.A. Pearson. Surface reactivity of polyimide and its effect on adhesion to epoxy. *J. Adhes. Sci. Technol*. **2006**, *20*, 1905-1928.

CHAPTER 4

HYGROTHERMAL AGING EFFECTS ON BURIED MOLECULAR STRUCTURES AT EPOXY INTERFACES

4.1 Introduction

In last chapter we demonstrated that SFG is a powerful technique to probe the molecular structures of buried polymer/epoxy interfaces. We probed interfacial molecular structures at buried epoxy interfaces before and after plasma treatment of polyimide surfaces to investigate how the plasma treatment improved interfacial adhesion. Here we will further study buried interfaces between polymers and epoxy materials before and after simulated microelectronic package qualification testing to study how the stress testing weakened the interfacial adhesion.

Epoxy adhesives are widely used as underfill materials in flip chip microelectronic packaging. Although underfill increases flip chip solder joint reliability during thermal cycling tests,[1] package failure caused by delamination at underfill/silicon chip and underfill/organic substrate interfaces during hygrothermal aging stress testing continues to be a package reliability concern.[2] Hygrothermal aging of epoxy adhesive interfaces has been shown to cause a decrease in adhesion strength,[3] disrupt interfacial hydrogen bonds,[4] reduce the average molecular weight of polymer chains if chain scission occurs during hydrolysis reactions,[5] and generate stress and strain at interfaces if hygroscopic swelling of different interface materials occurs at different rates.[6] In addition, hygrothermal aging can alter bulk properties of epoxy such as the elastic modulus and glass-transition temperature.[7] Therefore, it is important to understand the

relationship between epoxy debonding mechanisms that occur during hygrothermal aging and the structure and properties of epoxy adhesive interfaces. Better understanding structure–property relationships will aid in the rational design of adhesive package interfaces that can withstand harsh stress testing conditions.

A majority of hygrothermal aging experimental studies on epoxy underfill adhesion in microelectronic packages have used bulk and surface analysis methods such as adhesion strength measurements,[8] moiré interferometry,[2] scanning acoustic microscopy (SAM),[9,10] thermogravimetric analysis,[11] Fourier transform infrared spectroscopy (FTIR),[3] scanning electron microscopy (SEM),[3,11] and X-ray photoelectron spectroscopy (XPS)[10] to analyze adhesion and delamination. Delamination at packaging interfaces is often directly imaged using SAM; however, acoustic imaging does not provide molecular-level information about delamination processes. Adhesion and delamination mechanisms, however, are largely determined by molecular structures and interactions at adhesive interfaces.[12] To develop a more complete understanding of how hygrothermal aging affects the molecular structure of epoxy interfaces and their debonding mechanisms, the molecular-level effects of exposing epoxy interfaces to high-temperature and high-humidity environments need to be studied. The purpose of this study was to investigate interfacial degradation that occurs at buried epoxy interfaces during hygrothermal aging in situ on the molecular level using SFG. As described in chapter 1, SFG can probe buried polymer/polymer interfaces[13-47] and our lab has used SFG to study molecular structures at epoxy interfaces and their relations to adhesion.[41-43]

In this study, SFG was applied to study how epoxy interfaces respond to prolonged exposure to high-temperature and high-humidity conditions. Specifically, we studied the SiO_2/epoxy, deuterated polystyrene (dPS)/epoxy, and deuterated poly(ethylene terephthalate)

(dPET)/epoxy buried interfaces. SFG and ATR-FTIR spectra of the interfaces collected during hygrothermal aging were compared to investigate the interfacial molecular structure. Lap shear adhesion tests were then performed to correlate macroscopic adhesion strength changes during hygrothermal aging to changes observed in SFG and ATR-FTIR spectra to understand the structure–property relationship of the buried epoxy interfaces.

4.2 Experimental Section

4.2.1 Materials

Right angle fused silica prism substrates (Altos Photonics, Inc.) were used in all SFG experiments as solid supports for polymer thin film deposition. Silica prisms were first cleaned in a concentrated sulfuric acid bath saturated with potassium dichromate followed by a deionized water rinse and then were dried under a flow of nitrogen. Following the acid cleaning, the substrates were exposed to oxygen plasma (PE-50, Plasma Etch) for 4 min prior to polymer film deposition. PET with a deuterated aliphatic chain (d_4-PET or dPET) and deuterated polystyrene (d_8-PS or dPS) were purchased from Polymer Science, Inc (Figure 4.1). dPET and dPS solutions (2.0 wt %) were prepared by dissolving the solid polymers in 2-chlorophenol (Sigma-Aldrich, >99%) and chloroform (Sigma-Aldrich, >99.8%), respectively. Polymer solutions were spin-cast on the fused silica substrates at 2500 rpm for 30 s using a P-6000 spin coater (Speedline Technologies). All polymer films were then held under vacuum to remove residual solvent. Commercial epoxy resin 3302 (CE3302) was obtained from Epoxies Etc. CE3302 base is primarily composed of bisphenol A-(epichlorohydrin) and small amounts of bis(1,2,2,6,6-pentamethyl-4 piperidinyl)-sebacate and 4-nonylphenol. The CE3302 hardener used was poly(oxypropylenediamine). Bisphenol A digylcidyl ether (BADGE) is produced in the curing process and then reacts with poly(oxypropylenediamine) to form a cross-linked structure.[41] The

mixing ratio for resin to hardener was 2:1 by mass. After mixing resin and hardener, the epoxy was cured on top of the spin-cast polymer films according to manufacturer specifications for 2 h at 52 ℃.[41] After epoxy curing, the samples were exposed to 85 ℃ and 100% relative humidity (RH) environmental conditions for defined periods of time by placing the samples above liquid water in a home-built, sealed container. Right angle silicon prisms were used in all ATR-FTIR experiments as solid supports and ATR elements. Silicon substrates were exposed to an oxygen plasma (PE-50, Plasma Etch) for 4 min, after which polymer film and epoxy deposition was performed using the same method that was used for the silica prisms.

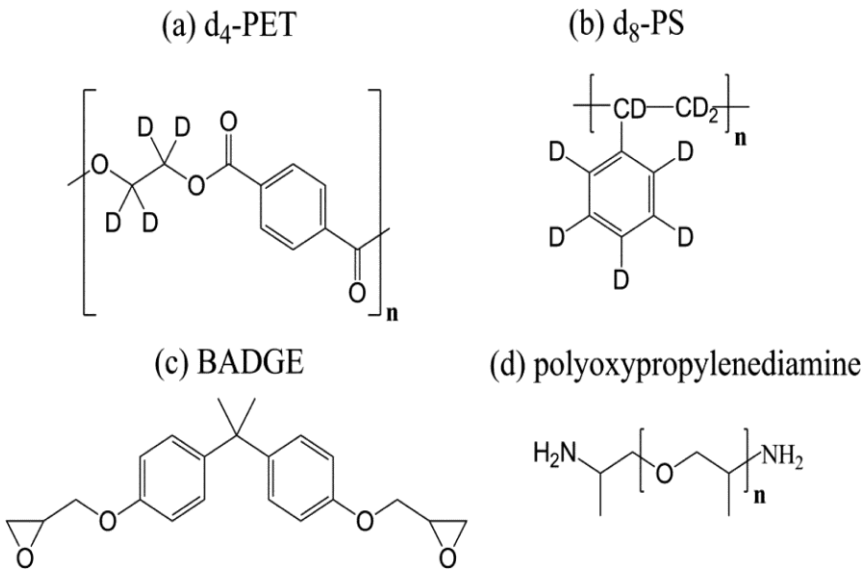

Figure 4.1. Molecular structures of (a) aliphatic-chain-deuterated poly(ethylene terephthalate) (d4-PET), (b) deuterated polystyrene (d8-PS), (c) bisphenol A diglycidyl ether (BADGE), and (d) poly(oxypropylenediamine).

4.2.2 SFG and ATR-FTIR

The SFG experimental geometry used to probe buried polymer/epoxy interfaces is shown in Figure 4.2. Single-bounce ATR-FTIR measurements (Figure 4.2) were performed using a Nicolet 6700 FT-IR spectrometer controlled by OMNIC software. The input angle was approximately 45 °. Single-bounce ATR-FTIR with a silicon prism internal reflection element (IRE) was used because of spectral transparency in the 1750–3600 cm^{-1} region and to facilitate cleaning of the IRE.

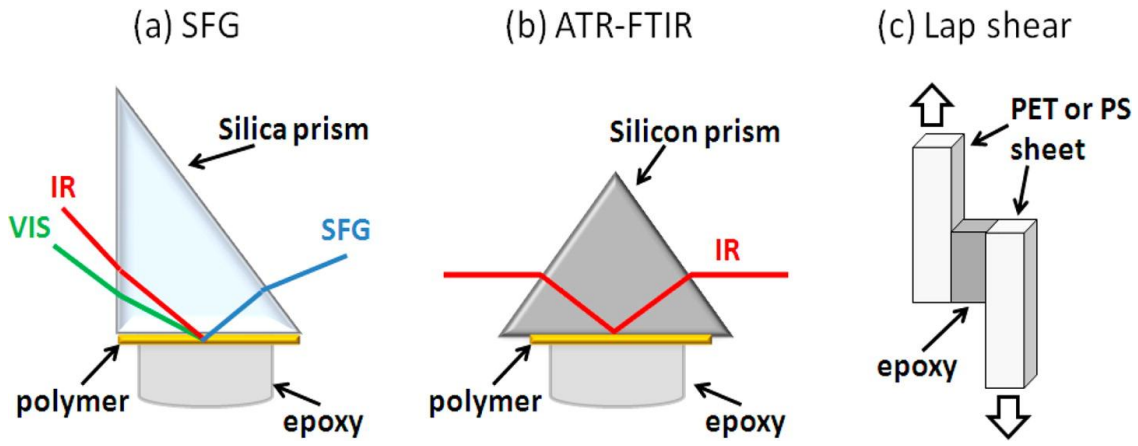

Figure 4.2. (a) SFG, (b) ATR-FTIR, and (c) lap shear experimental geometry used to study buried epoxy interfaces.

4.2.3 Adhesion Test

Adhesion tests were performed at room temperature after the specified hygrothermal aging time using a lap shear method based on ASTM D3163 (Figure 4.2). After the sheets were completely separated, a sudden drop in adhesion strength was observed. The maximum adhesion strength observed before the sudden drop was used for all reported adhesion strength measurements. All adhesion failures were primarily adhesive failure at the interface as determined by a visual comparison of the delaminated area and a control region that was not exposed to epoxy adhesive.

The interfacial molecular structures reported are therefore related to the interfacial adhesive properties.

4.3 Results and Discussion

4.3.1 Interface Between SiO_2 and Commercial Epoxy

The extent of adhesion strength degradation at epoxy interfaces during hygrothermal aging has been correlated to the hydrophobicity of the interface materials. It was previously reported that the die shear strengths of hydrophilic SiO_2/epoxy and Si_3N_4/epoxy interfaces decreased to almost zero after 24 h of exposure to a 121 ℃, 100% relative humidity (RH) environment.[8] However, relatively more hydrophobic interfaces such as benzocyclobutene/epoxy and polyimide/epoxy interfaces maintained about 32% and 21%, respectively, of their original adhesion strength after the same treatment.[8] The loss of adhesion strength at the hydrophilic interfaces was attributed to an increased number of interfacial water molecules that broke the original adhesive hydrogen bonds, dipole–dipole interactions, and covalent bonds between the epoxy underfill and the substrate; however, no molecular-level evidence was reported. Adhesion strength loss at the more hydrophobic interfaces was likely due to the moisture-induced degradation of the epoxy elastic modulus. Absorbed water can reduce the elastic modulus of epoxy by acting as a plasticizer and by hydrolyzing bonds.[48] Plasticization and hydrolysis reactions in epoxy can both result in molecular structural changes of the epoxy polymer chains, which in turn can alter the molecular structure of adhesive interfaces, so the interfacial and bulk effects of epoxy moisture uptake are often related.

In this study, we probed buried epoxy molecular structures at interfaces with varying degrees of hydrophobicity. We first collected SFG spectra from a hydrophilic SiO_2/commercial epoxy interface that was used as a model of the SiO_2-passivated silicon chip/epoxy interface. The

SFG spectrum of the untreated SiO_2/epoxy interface is shown in Figure 4.3a. One feature was observed near 2950 cm^{-1} and can be assigned to the Fermi resonance of the BADGE methyl group. The detection of the SFG signal originating from a methyl vibrational mode suggests that methyl groups were initially ordered at the SiO_2/epoxy interface. The ATR-FTIR spectrum of the untreated SiO_2/epoxy interfacial region is shown in Figure 4.3b. One broad feature was observed in the 2800–3000 cm^{-1} region with peaks near 2870, 2930, and 2965 cm^{-1} that can be assigned to methyl symmetric stretching, methylene asymmetric stretching, and methyl asymmetric stretching modes, respectively, in the epoxy bulk.[49]

The SFG spectrum collected from the SiO_2/epoxy interface after 24 h of hygrothermal aging is shown in Figure 4.3a. Two features near 2875 and 2935 cm^{-1} and one broad feature in the 3000–3400 cm^{-1} region were observed and can be assigned to the epoxy methyl symmetric stretch, epoxy methyl Fermi resonance, and water, respectively. New features in the spectrum suggest that molecular structural changes took place because of hygrothermal aging. After 24 h of hygrothermal aging, the lap shear adhesion strength of the SiO_2/epoxy interface decreased to nearly zero. The adhesion strength of untreated SiO_2/epoxy could not be quantitatively measured using the lap shear method because the adhesive strength was stronger than the cohesive strength of fused silica. However, the dramatic decrease in adhesion strength observed as a result of hygrothermal aging is consistent with previous reports that studied the interface between epoxy underfill and silicon dioxide passivation.[8] After 48 h of hygrothermal aging, the SFG spectrum again contained features near 2875 and 2935 cm^{-1} and a broad peak in the 3000–3500 cm^{-1} region with the center near 3175 cm^{-1}.

Interfacial SFG water signals with peak centers near 3200 cm^{-1} are contributed by strongly hydrogen bonded water or icelike water, as suggested in previous research.[39] The

presence of an SFG feature centered near 3200 cm^{-1} suggests that water diffused to hydrogen bonding sites at the SiO_2/epoxy interface. Although the presence of interfacial water has been correlated to low friction at buried sapphire/poly(dimethylsiloxane) (PDMS)[39] and quartz/poly(vinyl alcohol) (PVA)[40] interfaces in previous SFG studies, the effect of interfacial ordered water on the adhesion strength has not, to our knowledge, been reported. It is interesting that the ATR-FTIR spectra collected from the SiO_2/epoxy interface after 24 h of aging contained a broad peak from 2970 to 3700 cm^{-1} that is centered at 3400 cm^{-1}, as dominated by contributions from relatively weakly hydrogen bonded water. Such infrared features in the epoxy bulk have been attributed to water located in small pores within the epoxy bulk.[50] The broad feature of the IR signal indicates that some strongly hydrogen bonded water molecules were also present, which has been attributed to strong hydrogen bonding interactions between water and hydrophilic epoxy sites, leading to a red shift in the water OH oscillator vibrational frequency.[50]

The SFG signal is sensitive to the degree of ordering of functional groups. The SFG water signal collected from a buried interface thus suggests that ordered water is present at the interface. One of the driving forces for water ordering at the buried SiO_2/epoxy interface is the formation of hydrogen bonds. Ordered water detected at the buried interface likely replaced original adhesive hydrogen bonding sites between the terminal hydroxyl groups on the SiO_2 and polar functional groups on the epoxy that reduced the interfacial adhesive strength. The presence of strongly hydrogen bonded water at the SiO_2/epoxy interface suggests that hydrogen bonds are one of the primary contributors to adhesion because their disruption was directly correlated to an adhesion strength decrease to nearly zero. Furthermore, although both strongly hydrogen bonded water and relatively weakly hydrogen bonded water were detected in the epoxy bulk, only strongly hydrogen bonded water was detected at the buried interface.

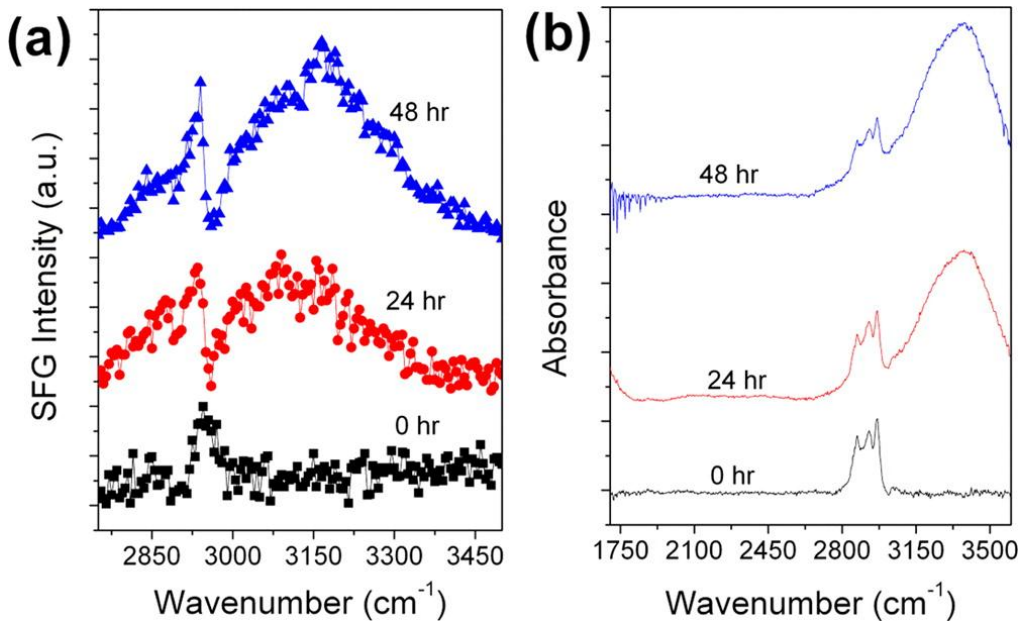

Figure 4.3. SFG and (b) ATR-FTIR spectra collected from the SiO_2/epoxy interface after hygrothermal aging time periods.

4.3.2 Interface between dPS and Commercial Epoxy

The effect of hygrothermal aging on a hydrophobic interface was examined by collecting the SFG spectrum from a dPS/epoxy interface (Figure 4.4a). Two peaks were observed in the SFG spectrum at 2870 and 2940 cm^{-1}, and they can be assigned to the symmetric stretching and Fermi resonance of epoxy methyl groups. SFG spectra collected from dPS/epoxy interfaces aged for 24 and 48 h again contained two peaks near 2870 and 2940 cm^{-1}. The 2870 to 2940 cm^{-1} peak intensity ratio increased slightly relative to the spectrum collected from the untreated interface, but overall the spectral features are more or less the same. We therefore believe that the interfacial structure did not substantially change after hygrothermal aging.

No water signal was observed in the SFG spectra collected from the dPS/epoxy interface after 24 or 48 h of hygrothermal aging. This suggests that no ordered water structure was present at the interface after the aging. To confirm that water diffused to the PS/epoxy interfacial region, ATR-FTIR was performed at a sufficient penetration depth to probe both the polymer film and the epoxy bulk. The penetration depth of the IR beam in the ATR-FTIR experiment was about 900 nm. The polymer thin film was about 100 nm; therefore, the ATR-FTIR can probe approximately 800 nm into the epoxy. Compared to the monolayer sensitivity of SFG, we referred to this region as epoxy bulk in the above discussion. ATR-FTIR spectra will thus be dominated by features from the dPS and epoxy bulk rather than their interfaces. The ATR-FTIR spectrum of the dPS/epoxy interfacial region (Figure 4.4b) contained three peaks in the epoxy methyl and methylene region near 2870, 2930, and 2965 cm^{-1} and three peaks near 2100, 2195, and 2270 cm^{-1} that can be assigned to the deuterated phenyl group. The presence of both the deuterated phenyl and the epoxy methyl signals verified that the penetration depth was sufficient to probe both the dPS and epoxy bulk. After 24 h, a broad peak was observed in the 2700 to 3700 cm^{-1} region with the peak center near 3400 cm^{-1} that can be assigned to the O–H stretching of relatively weakly hydrogen bonded water molecules in the epoxy bulk. After 48 h, the water absorbance from the bulk epoxy increased relative to the signal collected after 24 h. This suggests that water continued to diffuse into the epoxy bulk after 24 h of aging.

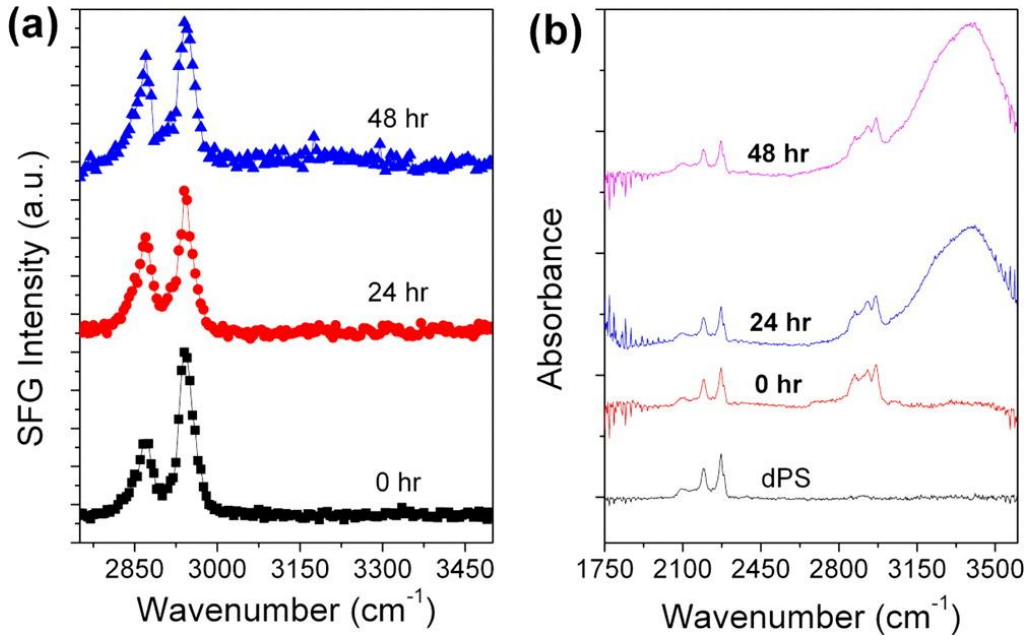

Figure 4.4. (a) SFG and (b) ATR-FTIR spectra collected from the dPS/epoxy interface after hygrothermal aging time periods.

Lap shear adhesion tests were then performed to relate the SFG and ATR-FTIR spectra to adhesion strength during hygrothermal aging. The adhesion strength of the dPS/epoxy samples decreased from 10.2 to 7.2 MPa after 24 h of hygrothermal aging (Figure 4.5). The decrease in adhesive strength is larger than what is typically observed for 85 ℃/85% RH aging at similar time scales but similar to aging at 121 ℃, 100% RH conditions. This observation is consistent with literature reports of large differences in the extent of adhesion loss when epoxy was aged under 85% versus 100% RH conditions.[51] These results are also consistent with the hygrothermal aging studies by Luo on interfaces between epoxy and hydrophobic polymers benzocyclobutene and polyimide that correlated the hydrophobicity of the interface to high resistance to hygrothermal degradation.[8] After hygrothermal aging, water signals were detected in the ATR-FTIR spectra collected from the epoxy bulk, but no ordered water was observed in the SFG spectra collected from the dPS/epoxy interface. At the dPS/epoxy interface, the dPS side does

not contain any hydrogen bonding sites in contrast to the epoxy side. Water can likely diffuse to the interface, but the lack of a water SFG signal from the buried interface suggests that no ordered water was present and thus no network of ordered hydrogen bonds was formed. If water was present at the buried interface, then the water molecules must have been randomly oriented. At the dPS/epoxy interface, no original hydrogen bonded network could be disrupted by the aging, so the relatively smaller decreased adhesion strength (compared to the SiO_2/epoxy interface) observed was likely a result of the minor change in the interface structure and bulk elastic modulus changes during the aging. This is different from the SiO_2/epoxy interface, at which the adhesion strength decrease after hygrothermal aging was solely due to the interfacial process.

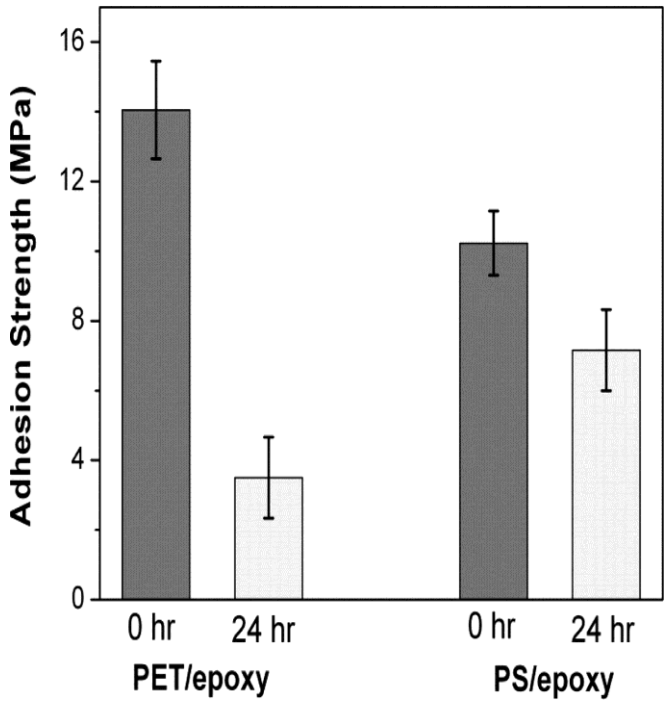

Figure 4.5. Adhesion strength of PET/epoxy and PS/epoxy interfaces before and after 24 h of hygrothermal aging.

4.3.3 Interface between dPET and Commercial Epoxy

The effect of hygrothermal aging on a slightly more hydrophilic interface was examined by collecting the SFG spectrum from a dPET/epoxy interface (Figure 4.6a) before and after hygrothermal aging. One feature near 2940 cm^{-1} was observed that can be assigned to the epoxy methyl group Fermi resonance. After 24 h of hygrothermal treatment, features near 2880 and 2940 cm^{-1} were observed and can be assigned to epoxy methyl groups in addition to a broad feature centered near 3150 cm^{-1} assigned to strongly hydrogen bonded interfacial water. The appearance of a new 2880 peak after 24 h of hygrothermal aging suggests that the interfacial methyl molecular structures were altered in the process, similar to the methyl structure behavior observed at the SiO_2/epoxy interface. After 48 h of hygrothermal aging, a small feature near 2940 cm^{-1} and a weak, broad peak centered near 3175 cm^{-1} were observed.

ATR-FTIR spectra collected from the untreated dPET/epoxy interfacial region (Figure 4.6b) displayed three peaks in the methyl and methylene region near 2870, 2930, and 2967 cm^{-1} and one peak near 1722 cm^{-1} that can be assigned to the dPET carbonyl group. After 24 h of hygrothermal aging, a broad peak was observed in the 2750 to 3700 cm^{-1} range centered near 3400 cm^{-1} that can be assigned to relatively weakly hydrogen-bonded water in the epoxy bulk and the intensity of the carbonyl peak decreased relative to that of the untreated carbonyl intensity. The loss of carbonyl intensity was likely due to hydrolysis reactions, which resulted in polymer chain scission and the conversion of carbonyl groups to carboxylic acid.[52]

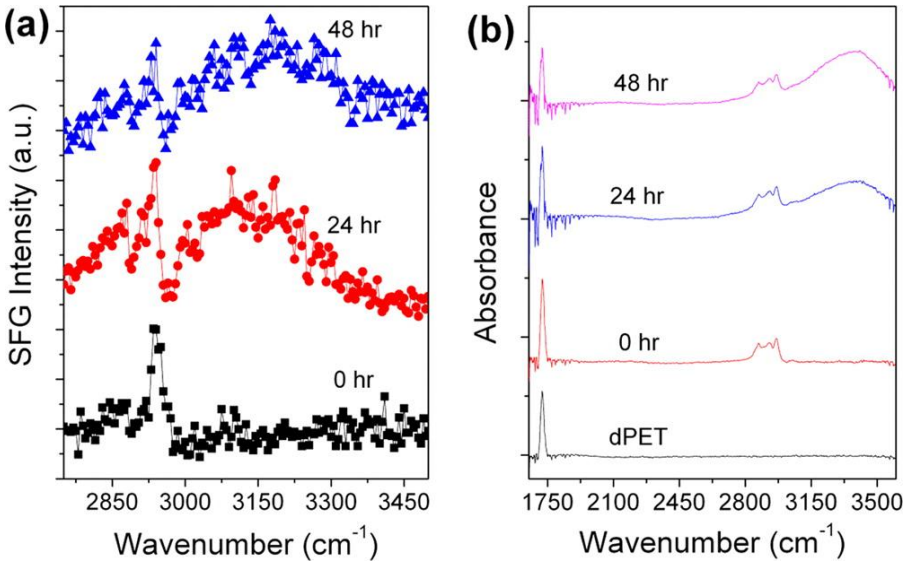

Figure 4.6. (a) SFG and (b) ATR-FTIR spectra of dPET/epoxy interfaces after hygrothermal aging time periods.

The lap shear adhesion strength of the PET/epoxy interface significantly decreased from 14.0 to 3.5 MPa after 24 h of hygrothermal aging (Figure 4.5). Water likely diffused to the interface and disrupted original interfacial hydrogen bonding because both the dPET and epoxy sides of the interface contain hydrogen bonding sites, different from the dPS/epoxy interface. Diffused water also likely hydrolyzed carbonyl groups in PET and the epoxy that reduced the elastic modulus of the bulk materials.

The changes observed in SFG spectra collected from the dPET/epoxy interface during hygrothermal aging could be due to the diffusion of polymer chains across the interface because the interface was held at 85 ℃ and the glass-transition temperature (T_g) of PET is ~80 ℃. If PET polymer chains diffused into the epoxy, then the SFG signal would likely decrease as the interphase formed.[37] SFG spectra collected from the PET/epoxy interface before and after thermal curing at 85 ℃ for 24 and 48 h (Figure 4.7) were nearly identical, which suggests that

little diffusion took place and that thermal curing alone was not responsible for the interfacial molecular structure changes induced by the hygrothermal aging.

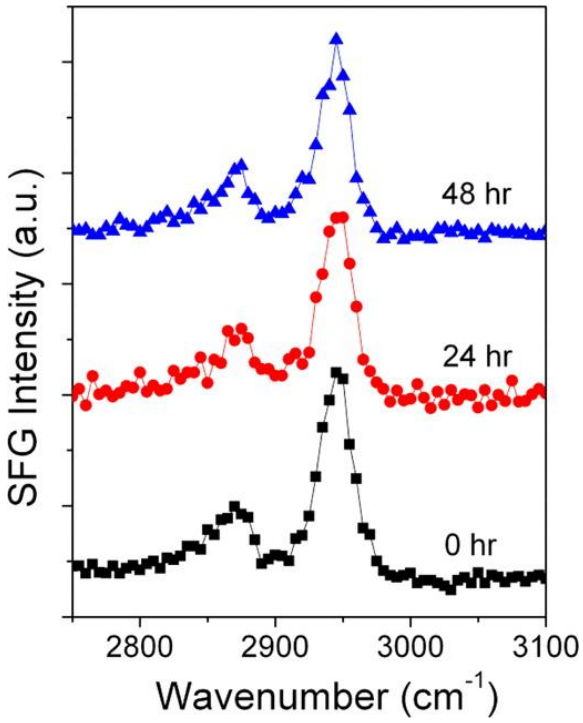

Figure 4.7. SFG spectra collected from the PET/epoxy interface after 0, 24, and 48 h of thermal annealing at 85 ℃.

4.4 Conclusions

In this study, molecular structures at buried epoxy interfaces were investigated in situ during hygrothermal aging using SFG and ATR-FTIR. SiO_2/epoxy, dPS/epoxy, and dPET/epoxy interfaces were examined to compare how molecular structures at interfaces with different hydrophobicity were affected by exposure to high temperature and humidity stress testing.

Ordered water was observed at the buried SiO_2/epoxy interface after 24 and 48 h of hygrothermal aging, which was correlated to a nearly complete loss of interfacial adhesion strength. Changes in methyl group molecular structures were also observed, which could be due to interfacial restructuring because of the hydrogen bond disruption or bulk changes in the epoxy

that affected the interfacial molecular structure. However, no ordered water was detected at the buried dPS/epoxy interface after the same hygrothermal aging treatment that was correlated to a minor decrease in the interfacial adhesion strength. Finally, hygrothermal aging was found to disrupt methyl structures at the dPET/epoxy interface as evidenced by the appearance of a new 2880 cm^{-1} peak after 24 h of hygrothermal aging. Similar to the SiO_2/epoxy interface, strongly hydrogen-bonded water was also detected at the dPET/epoxy interface. Such observations were correlated to a decrease in interfacial adhesion strength at the dPET/epoxy interface that was less than in the SiO_2/epoxy case but larger than in the dPS/epoxy case.

4.5 Impact

To our knowledge, this is the first report on molecular-level structural changes that occur at epoxy interfaces in situ during hygrothermal aging. Hydrophobic interfaces were found to maintain their adhesion strength during simulated qualification testing better than hydrophilic interfaces. The correlation of interfacial water at hydrophilic interfaces that appeared during hygrothermal aging to a substantial decrease in interfacial adhesion provides clear evidence that the adhesion failure occurred at the interface rather than in the bulk. This suggests that the failing interface should be engineered (e.g., made more hydrophobic) rather than modifying the bulk resin properties. The work in this chapter suggests that polymers with hydrophobic surface structures or polymers with surfaces modified to be more hydrophobic may be suitable replacements for polymers currently used as adhesives in microelectronic devices. Additionally, if no suitable polymer replacements can be found, this work suggests that by modifying the interface to be more hydrophobic (e.g. additives that segregate at the interface) may improve interfacial adhesion strength during hygrothermal aging qualification testing. More generally, understanding how hygrothermal aging affects molecular structures at buried polymer interfaces

in situ will contribute to the understanding of moisture-induced failure mechanisms in microelectronic packages and to the design and development of more robust adhesive polymers that can withstand accelerated stress testing.

4.6 References

(1) Chen, L; Zhang, Q.; Wang, G.; Xie, X.; Cheng, Z. The Effects of Underfill and its Material Models on Thermomechanical Behaviors of a Flip Chip Package. *IEEE T. Adv. Packaging* **2001**, *24*, 17–24.

(2) Park, J.-H.; Jang, K.-W.; Paik, K.-W.; Lee, S.-B. A Study of Hygrothermal Behavior of ACF Flip Chip Packages With Moiré Interferometry. *IEEE T. Compon. Pack. T.* **2010**, *33*, 215–221.

(3) Chiang, W. K.; Chan, Y. C.; Ralph, B.; Holland, A. Adhesive Strength of Flip Chip Packages. *Int. J. Adhes. Adhes.* **2008**, *28*, 109–119.

(4) Sharratt, B. M.; Wang, L. C.; Dauskardt, R. H. Anomalous Debonding Behavior of a Polymer/Inorganic Interface. *Acta Mater.* **2007**, *55*, 3601–3609.

(5) Lin, Y. C.; Chen, X.; Zhang, H. J.; Wang, Z. P. Effects of Hygrothermal Aging on Epoxy-Based Anisotropic Conductive Film. *Mater. Lett.* **2006**, *60*, 2958–2963.

(6) Shi, X. Q.; Zhang, Y. L.; Zhou, W.; Fan, X. J. Effect of Hygrothermal Aging on Interfacial Reliability of Silicon/Underfill/FR-4 Assembly. *IEEE T. Compon. Pack. T.* **2008**, *31*, 94–103.

(7) Choi, S.; Douglas, E. P. Complex Hygrothermal Effects on the Glass Transition of an Epoxy-Amine Thermoset. *ACS Appl. Mater. Interfaces* **2010**, *2*, 934–941.

(8) Luo, S.; Wong, C. P. Influence of Temperature and Humidity on Adhesion of Underfills for Flip Chip Packaging. *IEEE T. Compon. Pack. T.* **2005**, *28*, 88- 94.

(9) Buchwalter, S. L.; Brofman, P. J.; Feger, C.; Gaynes, M. A.; Lee, K.-W.; Matienzo, L. J.; Questad, D. L. Effects of mechanical stress and moisture on packaging interfaces. *IBM J. Res. Dev.* **2005**, *49*, 663–675.

(10) Lee, K.-W.; Gaynes, M. A.; Duchesne, E. Chip-Underfill Interfaces of Flip Chip Plastic Ball Grid Array Packages. *Electron. Mater. Lett.* **2006**, 2,171-174.

(11) Teh, L. K.; Teo, M.; Anto, E.; Wong, C. C.; Mhaisalkar, S. G.; Teo, P. S.; Wong, E. H. Moisture-Induced Failures of Adhesive Flip Chip Interconnects. *IEEE T. Compon. Pack.*

T. **2005**, *28*, 506–516.

(12) Awaja, F.; Gilbert, M.; Kelly, G.; Fox, B.; Pigram, P. J. Adhesion of Polymers. *Prog. Polym. Sci.* **2009**, *34*, 948–968.

(13) Lambert, A. G.; Davies, P. B.; Neivandt, D. J. Implementing the Theory of Sum Frequency Generation Vibrational Spectroscopy: A Tutorial Review. *Appl. Spectrosc. Rev.* **2005**, *40*, 103–145.

(14) Chen, Z.; Shen, Y. R.; Somorjai, G. A. Studies of Polymer Surfaces by Sum Frequency Generation Vibrational Spectroscopy. *Annu. Rev. Phys. Chem.* **2002**, *53*, 437–465.

(15) Mermut, O.; Phillips, D. C.; York, R. L.; McCrea, K. R.; Ward, R. S.; Somorjai, G. A. In Situ Adsorption Studies of a 14-Amino Acid Leucine-Lysine Peptide onto Hydrophobic Polystyrene and Hydrophilic Silica Surfaces Using Quartz Crystal Microbalance, Atomic Force Microscopy, and Sum Frequency Generation Vibrational Spectroscopy. *J. Am. Chem. Soc.* **2006**, *128*, 3598–3607.

(16) Stiopkin, I. V.; Jayathilake, H. D.; Bordenyuk, A. N.; Benderskii, A. V. Heterodyne-Detected Vibrational Sum Frequency Generation Spectroscopy. *J. Am. Chem. Soc.* **2008**, *130*, 2271–2275.

(17) Malyk, S.; Shalhout, F. Y.; O'Leary, L. E.; Lewis, N. S.; Benderskii, A. V. Vibrational Sum Frequency Spectroscopic Investigation of the Azimuthal Anisotropy and Rotational Dynamics of Methyl-Terminated Silicon(111) Surfaces. *J. Phys. Chem. C* **2013**, *117*, 935–944.

(18) Hu, D.; Yang, Z.; Chou, K. C. Interactions of Polyelectrolytes with Water and Ions at Air/Water Interfaces Studied by Phase-Sensitive Sum Frequency Generation Vibrational Spectroscopy. *J. Phys. Chem. C* **2013**, *117*, 15698–15703.

(19) Nihonyanagi, S.; Miyamoto, D.; Idojiri, S.; Uosaki, K. Evidence for Epitaxial Arrangement and High Conformational Order of an Organic Monolayer on Si(111) by Sum Frequency Generation Spectroscopy. *J. Am. Chem. Soc.* **2004**, *126*, 7034–7040.

(20) Rivera-Rubero, S.; Baldelli, S. Surface Characterization of 1-Butyl-3-methylimidazolium Br^-, I^-, PF_6^-, BF_4^-, $(CF_3SO_2)_2N^-$, SCN^-, $CH_3SO_3^-$, $CH_3SO_4^-$, and $(CN)_2N^-$ Ionic Liquids by Sum Frequency Generation. *J. Phys. Chem. B* 2006, *110*, 4756–4765.

(21) Santos, G. M.; Baldelli, S. Monitoring Localized Initial Atmospheric Corrosion of Alkanethiol-Covered Copper Using Sum Frequency Generation Imaging Microscopy: Relation between Monolayer Properties and Cu_2O Formation. *J. Phys. Chem. C* **2013**, *117*, 17591–17602.

(22) Ye, H.; Gu, Z.; Gracias, D. H. Kinetics of Ultraviolet and Plasma Surface Modification of Poly(dimethylsiloxane) Probed by Sum Frequency Vibrational Spectroscopy. *Langmuir* **2006**, *22*, 1863–1868.

(23) Li, Q.; Hua, R.; Chou, K. C. Electronic and Conformational Properties of the Conjugated Polymer MEH-PPV at a Buried Film/Solid Interface Investigated by Two-Dimensional IR−Visible Sum Frequency Generation. *J. Phys. Chem. B* **2008**, *112*, 2315–2318.

(24) Kweskin, S. J.; Komvopoulos, K.; Somorjai, G. A. Molecular Restructuring at Poly(*n*-butyl methacrylate) and Poly(methyl methacrylate) Surfaces Due to Compression by a Sapphire Prism Studied by Infrared−Visible Sum Frequency Generation Vibrational Spectroscopy. *Langmuir* **2005**, *21*, 3647–3652.

(25) Ye, H.; Abu-Akeel, A.; Huang, J.; Katz, H. E.; Gracias, D. H. Probing Organic Field Effect Transistors In Situ during Operation Using SFG. *J. Am. Chem. Soc.* **2006**, *128*, 6528–6529.

(26) Miyamae, T.; Nozoye, H. Poly(ethylene terephthalate) Surface and Alumina/Poly(ethylene terephthalate) Interface Studied using Sum-Frequency Generation Spectroscopy. *Surf. Sci.* **2005**, *587*, 142–149.

(27) Wilson, P. T.; Richter, L. J.; Wallace, W. E.; Briggman, K. A.; Stephenson, J. C. Correlation of Molecular Orientation with Adhesion at Polystyrene/Solid Interfaces. *Chem. Phys. Lett.* **2002**, *363*, 161–168.

(28) Harp, G. P.; Rangwalla, H.; Yeganeh, M. S.; Dhinojwala, A. Infrared-Visible Sum Frequency Generation Spectroscopic Study of Molecular Orientation at Polystyrene/Comb-Polymer Interfaces. *J. Am. Chem. Soc.* **2003**, *125*, 11283–11290.

(29) Harp, G. P.; Dhinojwala, A. Direct Probe of Interfacial Structure during Mechanical Contact between Two Polymer Films Using Infrared Visible Sum Frequency Generation Spectroscopy. *J. Adhesion* **2005**, *81*, 371–379.

(30) Fang, Y.; Li, B.; Yu, J.; Zhou, J.; Xu, X.; Shao, W.; Lu, X. Probing Surface and Interfacial Molecular Structures of a Rubbery Adhesion Promoter using Sum Frequency Generation Vibrational Spectroscopy. *Surf. Sci.* **2013**, *615*, 26–32.

(31) Anglin, T. C.; O'Brien, D. B.; Massari, A. M. Monitoring the Charge Accumulation Process in Polymeric Field-Effect Transistors via in Situ Sum Frequency Generation. *J. Phys. Chem. C* **2010**, *114*, 17629–17637.

(32) Ye, H.; Huang, J.; Park, J.-R.; Katz, H. E.; Gracias, D. H. Correlations between SFG Spectra and Electrical Properties of Organic Field Effect Transistors. *J. Phys. Chem. C* **2007**, *111*, 13250–13255.

(33) Chen, Z. Investigating Buried Polymer Interfaces Using Sum Frequency Generation Vibrational Spectroscopy. *Prog. Polym. Sci.* **2010**, *35*, 1376–1402.

(34) Zhang, C.; Myers, J. N.; Chen, Z. Elucidation of Molecular Structures at Buried Polymer Interfaces and Biological Interfaces using Sum Frequency Generation Vibrational Spectroscopy. *Soft Matter* **2013**, *9*, 4738- 4761.

(35) Loch, C. L.; Ahn, D.; Chen; Wang, J.; Chen, Z. Sum Frequency Generation Studies at Poly(ethylene terephthalate)/Silane Interfaces: Hydrogen Bond Formation and Molecular Conformation Determination. *Langmuir* **2004**, *20*, 5467–5473

(36) Kurian, A.; Prasad, S.; Dhinojwala, A. Direct Measurement of Acid−Base Interaction Energy at Solid Interfaces. *Langmuir* **2010**, *26*, 17804–17807.

(37) Chen, C.; Wang, J.; Loch, C. L.; Ahn, D.; Chen, Z. Demonstrating the Feasibility of Monitoring the Molecular-Level Structures of Moving Polymer/Silane Interfaces During Silane Diffusion Using SFG. *J. Am. Chem. Soc.* **2004**, *126*, 1174–1179.

(38) Loch, C. L.; Ahn, D.; Vázquez, A. V.; Chen, Z. Diffusion of One or More Components of a Silane Adhesion-Promoting Mixture into Poly(methyl methacrylate). *J. Colloid Interf. Sci.* **2007**, *308*, 170-175.

(39) Nanjundiah, K.; Hsu, P. Y.; Dhinojwala, A. Understanding Rubber Friction in the Presence of Water using Sum-Frequency Generation Spectroscopy. *J. Chem. Phys.* **2009**, *130*, 024702.

(40) Noguchi, H.; Hiroshi, M.; Tominaga, T.; Gong, J. P.; Osada, Y.; Uosaki, K. Interfacial Water Structure at Polymer Gel/Quartz Interfaces Investigated by Sum Frequency Generation Spectroscopy. *Phys. Chem. Chem. Phys.* **2008**, *10*, 4987-4993.

(41) Zhang, C.; Hankett, J.; Chen, Z. Molecular Level Understanding of Adhesion Mechanisms at the Epoxy/Polymer Interfaces. *ACS Appl. Mater. Interfaces* **2012**, *4*, 3730–3737.

(42) Vázquez, A. V.; Holden, B.; Kristalyn, C.; Fuller, M.; Wilkerson, B.; Chen, Z. Surface and Buried Interfacial Structures of Epoxy Resins Used as Underfills Studied by Sum Frequency Generation Vibrational Spectroscopy. *ACS Appl. Mater. Interfaces* **2011**, *3*, 1640–1651.

(43) Lu, X.; Han, J.; Shephard, N.; Rhodes, S.; Martin, A. D.; Li, D.; Xue, G.; Chen, Z. Phenolic Resin Surface Restructuring upon Exposure to Humid Air: A Sum Frequency Generation Vibrational Spectroscopic Study. *J. Phys. Chem. B* **2009**, *113*, 12944–12951.

(44) Shen, Y. R. Surface Properties Probed by Second-Harmonic and Sum-Frequency Generation. *Nature* **1989**, *337*, 519–525.

(45) Shen, Y. R. *The Principles of Nonlinear Optics*; Wiley classics library; Wiley classics library ed.; Wiley-Interscience: Hoboken, N.J, 2003

(46) Wang, J.; Chen, C.; Buck, S. M.; Chen, Z. Molecular Chemical Structure on Poly(methyl methacrylate) (PMMA) Surface Studied by Sum Frequency Generation (SFG) Vibrational Spectroscopy. *J. Phys. Chem. B* **2001**, *105*, 12118–12125.

(47) Wang, J.; Woodcock, S. E.; Buck, S. M.; Chen, C.; Chen, Z. Different Surface-Restructuring Behaviors of Poly(methacrylate)s Detected by SFG in Water. *J. Am. Chem. Soc* **2001**, *123*, 9470–9471.

(48) Ferguson, T. P.; Qu, J. The Effect of Moisture on the Adhesion and Fracture of Interfaces in Microelectronic Packaging. In *Micro- and Opto-Electronic Materials and Structures: Physics, Mechanics, Design, Reliability, Packaging*; Suhir, E.; Lee, Y. C.; Wong, C. P., Eds.; Springer US: Boston, MA; pp. B431–B471.

(49) Gonzlez, M.; Carlos, J.; Baselg, J. Applications of FTIR on Epoxy Resins - Identification, Monitoring the Curing Process, Phase Separation and Water Uptake. In *Infrared Spectroscopy - Materials Science, Engineering and Technology*; Theophile, T., Ed.; InTech, 2012.

(50) Liu, M.; Wu, P.; Ding, Y.; Chen, G.; Li, S. Two-Dimensional (2D) ATR−FTIR Spectroscopic Study on Water Diffusion in Cured Epoxy Resins. *Macromolecules* **2002**, *35*, 5500–5507.

(51) Wong, E. H.; Rajoo, R.; Lim, T. B.; Mai, Y.-W. Swelling and Time-Dependent Subcritical Debonding of Underfill During Temperature-Humidity Aging of Flip Chip Packages. *IEEE T. Compon. Pack. T.* **2005**, *28*, 862–868.

(52) Sammon, C.; Yarwood, J.; Everall, N. An FT–IR Study of the Effect of Hydrolytic Degradation on the Structure of Thin PET Films. *Polym. Degrad. Stabil.* **2000**, *67*, 149–158.

CHAPTER 5

NONDESTRUCTIVE CHARACTERIZATION OF MOLECULAR STRUCTURES AT BURIED COPPER/EPOXY INTERFACES AND THEIR RELATIONSHIP TO LOCUS OF FAILURE ANALYSIS

5.1 Introduction

In the last few chapters we presented SFG studies on polymer/air and polymer/epoxy interfaces. We will report our SFG studies on polymer/metal interfaces in this chapter. Epoxy-based thermoset polymers are widely used in microelectronic packaging as flip chip underfills, electrically conductive adhesives, die-attach adhesives, and molded encapsulants. Weak adhesion between epoxy adhesives and certain package components such as chip passivation layers, solder joints, and copper leadframes continues to be a package reliability concern because delamination at heterogeneous adhesive interfaces can lead to electrical failure. In particular, delamination at the interface between copper and epoxy molding compounds has been found to occur during reliability testing due to low interfacial adhesion strength and low moisture resistance.[1]

Although adhesion at metal/polymer and copper/epoxy interfaces has been extensively studied, adhesion and delamination mechanisms at buried metal/polymer interfaces are not well understood.[2] Adhesion at polymer/metal interfaces is typically studied by relating bulk interfacial adhesion strength to the exposed surface structures of a mechanically separated interface.[3] The structure of the exposed surfaces can be significantly different than the initial metal surface or the polymer bulk due to the presence of an interphase region between the metal and the polymer.[4] Metal-catalyzed chemical reactions and preferential adsorption of thermoset

components at the metal interface during thermoset curing can lead to a local molecular structure near the metal interface that has a chemical composition and network structure different from that of the bulk polymer.[5] The structures of the exposed surfaces, however, might not resemble the structure of the buried interface if polymer chain scission or restructuring of the cross-linked network occurred during the mechanical separation.

Interfacial properties such as adhesion, delamination, and wetting are largely determined by molecular structures at buried interfaces.[3,6] Accurate characterization of adhesion and delamination mechanisms at metal/polymer interfaces therefore requires in situ characterization of the molecular structure at the buried interface. In this chapter, methodology was developed to nondestructively characterize the molecular structure at buried copper/epoxy interfaces in situ using SFG. The developed methodology was then applied by correlating molecular structure at the buried copper/epoxy interface with the locus of failure analysis. Here, we utilized a recently developed sandwich experimental geometry that has been shown to selectively measure SFG signal generated from buried metal/polymer interfaces.[14,15] The interface between a thermoset epoxy and copper was characterized with and without silane adhesion promoter doped into the epoxy. Exposed surfaces from copper/epoxy interfaces which had been mechanically separated were characterized by SFG, scanning electron microscopy (SEM), energy dispersive X-ray spectroscopy (EDX), and X-ray photoelectron spectroscopy (XPS). Molecular structures at the buried copper/ epoxy interface were then correlated with the morphology, molecular structure, and elemental composition of the exposed surfaces in order to elucidate how adhesion promoters affected adhesion properties and the locus of failure.

5.2 Experimental Details

Bisphenol A diglycidyl ether (BADGE), 4,4'-Diamino-diphenylmethane (DDM) (≥97%), (3-Aminopropyl) trimethoxysilane (APTMS) (≥98%), (3-Glycidyloxypropyl) trimethoxysilane (γ-GPS) (≥98%), and toluene (≥99.5%) were obtained from Sigma-Aldrich (Figure 5.1). Fused silica windows (1-in diameter and 1/8-in thickness) were obtained from Esco Optics. Silicon (100) wafers were obtained from the Silicon Valley Microelectronics. Copper substrates for SFG measurements were prepared by depositing 200 nm of copper onto silicon wafers using E-beam evaporation at 10 $Å s^{-1}$ (Cooke evaporator and Cooke Vacuum Products). Copper sheets (C101 oxygen-free electronic copper, 99.99% Cu, and 0.02" thickness) were obtained from OnlineMetals.com and were used for all SEM, EDX, and XPS measurements.

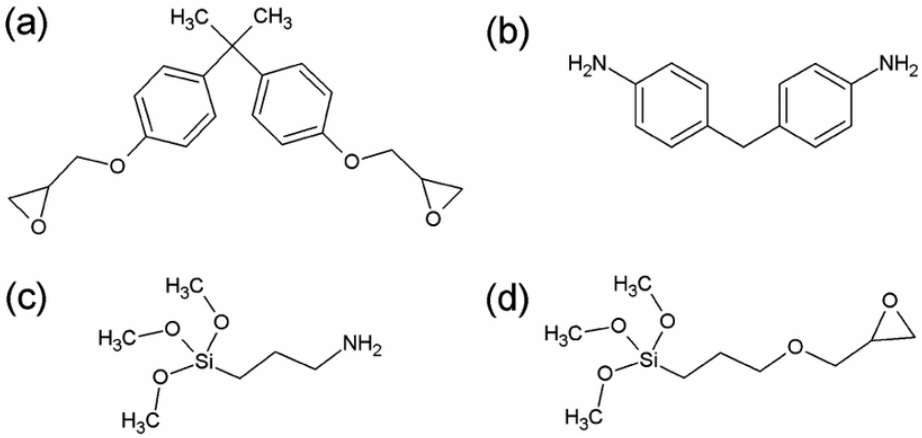

Figure 5.1. Molecular structures of (a) BADGE, (b) 4,4'-DDM, (c) 3-APTMS, and (d) (3-Glycidyloxypropyl)trimethoxysilane (γ-GPS).

Epoxy thin films were prepared by spin coating a toluene solution of BADGE and DDM on fused silica windows (Speedline Technologies P-6000). A stoichiometric mole ratio of two BADGE to one DDM was used. The solution concentration was ~60 gL^{-1}, which resulted in a

film thickness of approximately 200 nm.[16] Silane-doped films were prepared by dissolving 2% (by weight) silane adhesion promoter into the epoxy precursor solution prior to spin casting. Samples were initially cured at room temperature and pressure for 1 h after which they were held under vacuum to remove residual solvent. Following the vacuum treatment, the copper surface of a copper substrate was placed in contact with the epoxy film. All vapor deposited copper substrates were used within 24 h of copper deposition. Next, the samples were cured for 1 h at 50 ℃, 45 min at 75 ℃, and 30 min at 110 ℃.[16] The copper substrate was firmly adhered to the silica substrate by the epoxy after the cure cycle, which was suitable for SFG experiments (Figure 5.2).

SFG theory and descriptions of our infrared (IR) frequency scanning SFG system were presented in previous chapters. SFG spectra were collected in the 2750–3150 cm^{-1} wavenumber range (of the input IR beam) using the ppp polarization combination. All SFG spectra were fit using equation 1.23.

Copper sheets were cut into strips and were used without modification as substrates for XPS, SEM, and EDX measurements. Two copper sheets that were adhered together by epoxy were separated and immediately placed into the SEM or the XPS vacuum chamber for analysis. SEM secondary electrons were collected with a 15.0 kV acceleration voltage at a 10 cm working distance. XPS spectra were collected using an Al source. Survey and high-resolution XPS spectra were collected using pass energies of 160 and 20 eV, respectively.

5.3 Results and Discussion

5.3.1 Molecular Structure at the Interface Between Copper and Epoxy

SFG ppp spectra were first collected from the buried copper/undoped epoxy interface (Figure 5.3). SFG peaks were observed near 2855, 2875, and 2965 cm^{-1}, which can be assigned

to the methylene symmetric, methyl symmetric, and methyl asymmetric stretch vibrational modes, respectively.[28] DDM does not contain any methyl groups, therefore the detected methyl features in the SFG spectrum indicate that methyl groups on the BADGE were ordered at the copper/epoxy interface. Both BADGE and DDM contain methylene groups, thus the detected SFG peaks assigned to methylene groups indicate that the methylene groups on BADGE and/or DDM were ordered at the buried copper/undoped epoxy interface. In addition, no peaks were observed in the 3000–3100-cm^{-1} region, which suggests that no epoxide or phenyl groups were ordered at the buried interface.[28] The lack of epoxide signal indicates that all of the epoxide groups near the copper interface had undergone cross-linking ring-opening reactions or that the groups were randomly oriented. SFG spectra were then collected from the copper/epoxy interface where the epoxy was doped with APTMS adhesion promoter (the copper/APTMS doped cured epoxy interface is referred to as APTMS in Figure 5.3) prior to curing. APTMS has methoxy head groups and an amino end group (Figure 5.1). SFG peaks were observed near 2875 and 2970 cm^{-1}, which can be assigned to the methyl symmetric and methyl asymmetric stretches, respectively. The symmetric and asymmetric (or Fermi resonance) stretching frequencies of methyl groups on methoxy head groups of silane adhesion promoters have been observed near 2845 and 2945 cm^{-1}, respectively, in SFG spectra collected from buried poly(ethylene terephthalate)/poly (dimethylsiloxane) interfaces.[12] Therefore, the methyl features observed at the copper/APTMS doped epoxy interface indicate ordering of methyl groups on the BADGE at the buried interface. Although the APTMS was not directly detected, the SFG spectrum of the copper/APTMS doped epoxy interface did not contain any features contributed by methylene groups, different from the spectra at the undoped interface. The difference between spectra

collected from the copper/undoped epoxy and copper/APTMS doped epoxy indicates that the APTMS adhesion promoter modified the interfacial molecular structure.

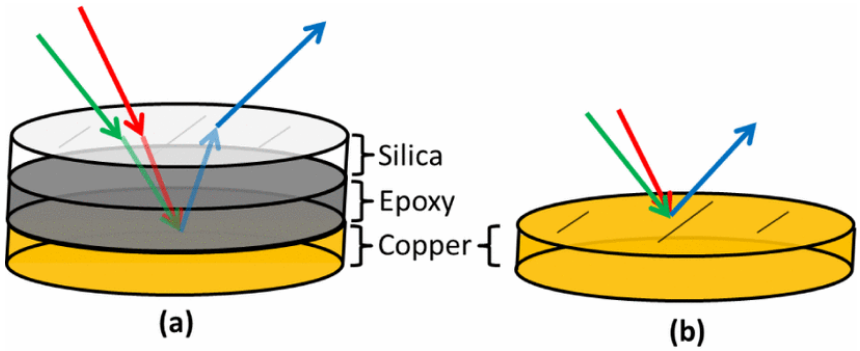

Figure 5.2 Schematic of the (a) sandwich and (b) face-up SFG experimental geometries.

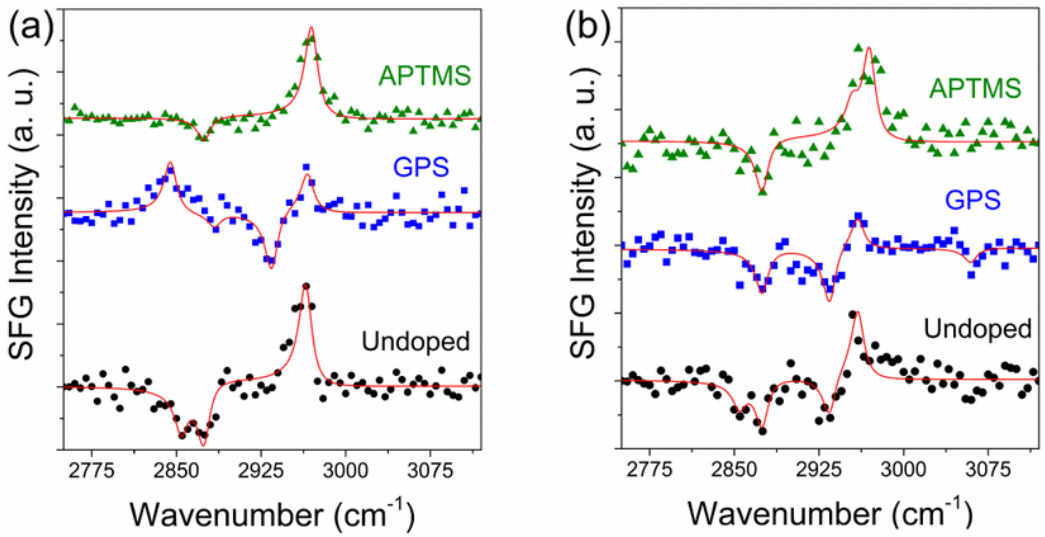

Figure 5.3. (a) SFG spectra collected from the undoped, GPS, and APTMS doped epoxy/copper interface. (b) SFG spectra collected from the exposed copper surface after undoped, Formula-GPS, and APTMS doped epoxy/copper interfaces were separated.

To compare how the silane end group affected the interfacial molecular structure, a SFG spectrum was collected from the copper/epoxy interface where the epoxy was doped with γ-GPS

adhesion promoter (the copper/γ-GPS doped cured epoxy interface is referred to as GPS in Figure 5.3) prior to curing. The γ-GPS molecule has methoxy head groups and an epoxide end group. SFG peaks were observed near 2845, 2884, 2935, and 2967 cm^{-1}, which can be assigned to the methoxy symmetric, methyl symmetric, methylene symmetric and/or methyl Fermi resonance, and methyl asymmetric stretches, respectively. The appearance of a feature near 2845 cm^{-1}, which may be assigned to the γ-GPS head group methoxy, when γ-GPS was doped into the epoxy suggests that the silane migrated to the copper interface and modified the interfacial molecular structure.

The SFG results indicate that both methyl and methylene groups on the epoxy network structure were ordered at the copper/undoped epoxy interface, which is in contrast to the expected random ordering of the groups in the epoxy bulk. Ordering of functional groups on polymer chains at metal/polymer (here copper/epoxy) interfaces has been predicted by molecular dynamics simulations based on preferential chemical interactions of certain functional groups with the metal surface.[29] Polymer chains at the metal interface will interact with both the metal and polymer chains in the bulk. Therefore, the molecular conformation of polymer chains near a metal interface can be different than the conformation of the chains in the bulk. Such differences in the conformation of the polymer chains thus affect the mechanical properties of the polymer near the metal interface. Similarly, for thermoset epoxies, functional groups on the cross-linked network may preferentially interact with the metal surface, different from the random conformation of the network in the bulk. In addition, certain components of the thermoset may preferentially adsorb at the metal interface during the cure reactions which would further affect the molecular structure of the network near the metal interface.[30]

Different molecular structures detected at the buried copper/epoxy interface due to doped silane adhesion promoters suggest that the silanes migrated to the interface and altered the interfacial molecular structure. The small weight percent of the silanes, however, is not expected to largely influence the bulk properties or structure of the epoxy. The differences observed between SFG spectra collected from the buried copper/APTMS doped epoxy and copper/GPS doped epoxy interfaces indicate that the end group of the silane affected how the silane altered the interfacial molecular structure. Both the adsorption of the silane at the copper interface and the chemical reactivity of the silane with the copper and the thermoset components will affect the interfacial behavior of the silane. Amine groups and the silane APTMS have been reported to adsorb on metal surfaces via the lone electron pair on the nitrogen atom.[30,31] Epoxide groups do not have a nitrogen atom and are not expected to strongly adsorb to the copper surface. Both γ-GPS and APTMS, however, can react with the metals to form Si–O–metal bonds. Furthermore, the amine and epoxide end groups are also expected to react differently with the epoxy thermoset components. For example, the terminal nitrogen of APTMS can react with the epoxide group on BADGE while the terminal epoxide of γ-GPS can react with the amino group on DDM.

The ordering of methoxy groups detected at the copper/γ-GPS doped epoxy interface may be due to preferential interaction of the γ-GPS methoxy head group with the copper surface which resulted in ordered methoxy groups at the interface. Also, the γ-GPS epoxide end group may have preferentially reacted with DDM in the epoxy bulk rather than the copper which resulted in the epoxide group being directed toward the bulk and the head group toward the copper.

Different from the γ-GPS doped interface, the lack of methoxy signal in the SFG spectrum collected from the copper/APTMS doped epoxy interface may be due to preferential

ordered adsorption of the amine group on the APTMS end group at the copper surface which resulted in the methoxy head group being directed into the epoxy bulk, away from the interface and more randomly oriented. The lack of methoxy signal could also be due to partial hydrolysis of ATPMS methoxy groups to silanol groups. Partially hydrolyzed APTMS molecules may preferentially interact with copper oxides on the copper surface through the silanol groups rather than through the amino group. Furthermore, the detection of γ-GPS methoxy groups may be related to different hydrolysis behaviors of γ-GPS and APTMS in the epoxy mixture. APTMS may have been susceptible to hydrolysis from moisture in the epoxy precursor mixture which converted its methoxy groups to silanol groups. Ordered methoxy groups detected at the copper/γ-GPS doped epoxy interface suggest that γ-GPS was less susceptible to hydrolysis in the epoxy precursor mixture.

To investigate how the adhesion promoters affected delamination, the copper/epoxy interface was mechanically separated and SFG spectra were collected from the exposed copper surfaces in a face-up geometry (Figure 5.2) immediately after separation. Figure 5.3 shows the SFG spectra collected from the exposed copper surface which had been adhered to undoped epoxy. SFG peaks were observed near 2855, 2875, 2935, and 2960 cm^{-1}, which can be assigned to the methylene symmetric, methyl symmetric, methylene asymmetric and/or methyl Fermi resonance, and methyl asymmetric stretches, respectively. SFG ppp spectra collected from thin polymer films on metal surfaces in the face-up geometry have been shown to selectively probe the buried polymer/metal interface and the spectra have been shown to be consistent with SFG spectra collected in the sandwich geometry.[15] The detection of methyl groups on the exposed copper surface indicates that some epoxy was adhered to the copper after the interface was separated and thus near-interface failure occurred. Furthermore, the SFG spectra of the buried

copper/undoped epoxy interface before and after delamination were similar except for the appearance of a feature near 2935 cm^{-1} and a slightly lower intensity of the methyl asymmetric peak at the exposed copper side relative to the buried interface. The similarity of the SFG spectra collected from the buried copper/epoxy interface before and after delamination suggests that the molecular structure at the buried copper/epoxy interface was not largely altered by delamination and that the molecular structure had low flexibility.

When γ-GPS was doped in the epoxy, SFG peaks were observed near 2875, 2935, 2960, and 3060 cm^{-1} in the spectra collected from the exposed copper surface, which can be assigned to the methyl symmetric, methylene asymmetric and/or methyl Fermi resonance, methyl asymmetric, and phenyl stretches, respectively. The SFG spectra collected from the exposed copper surfaces of the buried copper/epoxy and copper/γ-GPS doped epoxy interfaces were similar, unlike the spectra collected from the respective buried interfaces, except that a methylene feature was detected at the interface from the undoped epoxy. In addition, no methoxy features were detected, which indicates that the silane molecules were not ordered at the copper surface after delamination of the interface, in contrast to the buried interface. The spectral features, however, were similar before and after delamination, which indicates that the molecular structure was not largely altered.

When APTMS was doped in the epoxy, SFG peaks were observed near 2875, 2955, and 2970 cm^{-1} in the spectra collected from the exposed copper surface, which can be assigned to the methyl symmetric, methoxy asymmetric (or Fermi resonance), and CH_3 asymmetric stretches, respectively. The SFG spectrum collected from the exposed copper surface of the copper/APTMS doped epoxy interface was similar to the spectrum collected from the buried interface. The similarity may be due to Si–O–Cu bonds or adsorption of the amine end group to

the copper surface that withstood the effects of the applied shear force. As discussed above, the shear force slightly altered the molecular structure of the copper/undoped epoxy and copper/γ-GPS doped epoxy interfaces. Similar in all the three cases was the detection of epoxy components on the copper after delamination. The detection of ordered functional groups at the exposed copper surface indicates that the interfacial interactions that mediated the interfacial molecular ordering between the functional groups on the epoxy network and the copper surface were stronger than the applied shear force.

5.3.2 Methyl Group Orientation at the Buried Copper/Epoxy Interface

Features detected in SFG spectra collected from the copper/epoxy interfaces indicate that methoxy groups on the γ-GPS, methyl groups on the BADGE, and methylene groups on the BADGE and/or DDM were ordered at the buried interface. The orientation of methyl groups at the buried copper/epoxy interface was estimated by calculating the modulus of the ratio of the effective nonlinear susceptibilities for the methyl asymmetric and symmetric stretching vibrational modes[15]

$$\left|\frac{\chi_{eff,ppp,as}}{\chi_{eff,ppp,ss}}\right| \approx \left|\frac{-F_{xxz}\chi_{xxz,as}+F_{zzz}\chi_{zzz,as}}{-F_{xxz}\chi_{xxz,ss}+F_{zzz}\chi_{zzz,ss}}\right| \quad (5.1)$$

Local field factors at the copper/epoxy interface, $F_{zzz} = 0.94 - 0.56i$ and $F_{xxz} = -0.51 - 0.23i$, were calculated using previously established models for SFG signal generation in a silica/polymer/metal three layer sandwich geometry.[14] As shown in Figure 5.4, eq. 4.1 will increase in magnitude as the methyl tilt angle (with respect to the copper surface normal) increases. The orientation of methyl groups at the copper/undoped epoxy interface was determined to be ~67° relative to the copper surface. The high tilt angle observed is similar to

previous reports on the orientation of methyl groups at buried silver/poly(ethyl methacrylate) interfaces and phenyl groups at the buried silver/polystyrene interface.[15,32] Similar to silver/poly(ethyl methacrylate) interfaces, the high methyl tilt angle at the copper/epoxy interface may be due to attractive interactions between the electronegative oxygen and nitrogen atoms or the phenyl group with the copper which induced a high tilt angle of the methyl groups due to the rigidity of the cross-linked network structure. In addition, preferential interactions between polar functional groups on the epoxy and the copper surface are consistent with the detection of ordered functional groups at the copper/epoxy interface.

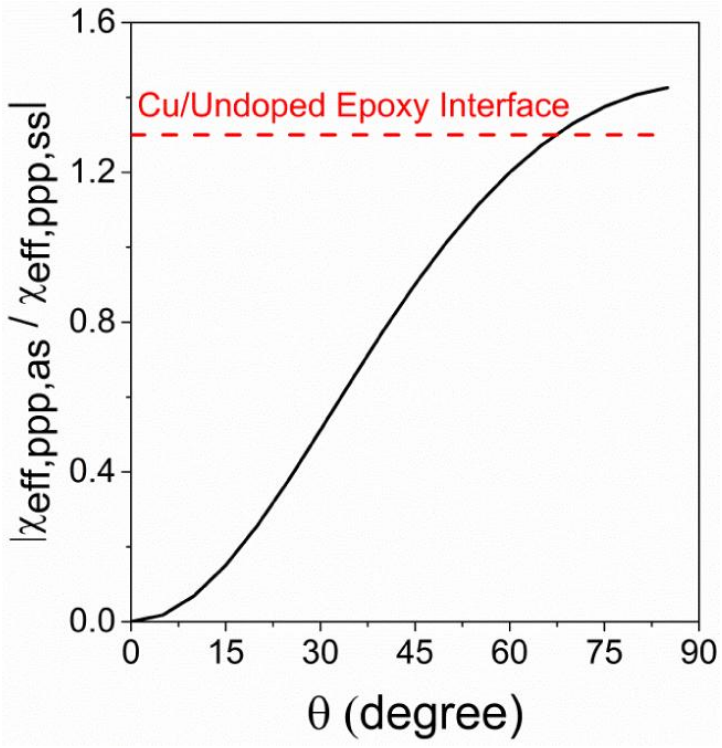

Figure 5.4 Plot of Formula as a function of tilt angle with respect to the copper surface normal.

The orientation of methyl groups at the exposed copper surfaces could not be estimated due to possible overlap between signals contributed by the methyl asymmetric and methoxy asymmetric (or Fermi resonance) vibrational modes. Qualitatively, however, the strength of the methyl asymmetric peaks were approximately equal to or greater than the symmetric peaks which suggests that the groups were oriented at a high tilt angle, similar to the behavior at the copper/undoped epoxy interface. In addition, the high tilt angle of the methyl groups on the exposed copper surface suggests that the attractive polar interactions at the copper interface that mediated the interfacial molecular ordering resulted in residual ordered epoxy components adhered to the copper after delamination. To correlate the molecular structure at the buried copper/epoxy interfaces with the locus of failure, the morphology and elemental composition of the epoxy and copper sides were characterized using SEM and XPS.

5.3.3 Morphology of Exposed Surfaces

SEM images were collected from the exposed surfaces to characterize the surface morphology. A typical optical and SEM image of the surfaces formed after separation of the copper/epoxy interfaces is shown in Figure 5.5. The surface morphology of one exposed surface closely resembled the morphology of the pure copper substrate (copper side), while the other side displayed a continuous film on top of the copper substrate (epoxy side). The absence of a distinct film on one of the exposed surfaces suggests that failure occurred near the copper interface.

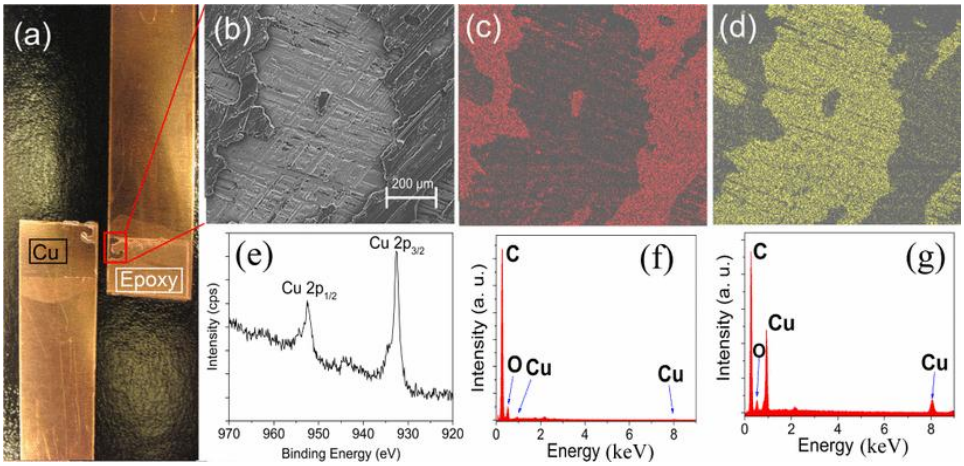

Figure 5.5. (a) Optical image and (b) SEM image of a peeled copper/epoxy interface. EDX mapping images of (c) carbon and (d) copper from the SEM image displayed in (b). (e) Typical XPS spectrum collected from the bare copper substrate surface. A typical EDX spectrum collected from the (f) exposed epoxy surface and (g) copper delaminated region.

EDX spectra were then collected from the copper and epoxy sides to characterize the elemental composition of the exposed surfaces. Strong carbon and copper peaks were detected in the EDX spectra collected from the copper side (Figure 5.5) which suggests that epoxy remained on the copper side after delamination. EDX carbon and copper mapping images collected from an exposed surface region that contained both the copper and epoxy sides indicate that carbon was continuously distributed throughout the exposed copper side which suggests near-interface failure occurred. Carbon signal detected on the copper side could also be contributed by amorphous carbon. The detection of nitrogen on the copper side would more accurately indicate residual epoxy, so XPS spectra were collected from the exposed copper and epoxy surfaces.

5.3.4 Elemental Composition of Exposed Surfaces

XPS survey and high resolution spectra were collected from the copper and epoxy exposed surfaces to characterize the elemental composition. First, an XPS spectrum was collected from the bare copper substrate surface [Figure 5.5(e)]. The XPS spectrum acquired

from the copper substrate surface was very similar to XPS spectra collected from pure copper surfaces that have been previously published.[33] Therefore, we believe that the surfaces of the two copper substrates used for SFG and XPS measurements are comparable. XPS survey spectra collected from the copper side of the copper/undoped epoxy interface displayed peaks near 950, 930, 532, 400, and 285 eV (Figure 5.6), which can be assigned to the copper 2p, oxygen 1s, nitrogen 1s, and carbon 1s transitions.[30] The presence of carbon and nitrogen peaks indicates that epoxy components remained on the copper side after the interface was separated, which is consistent with the SFG and EDX results. Furthermore, the presence of copper peaks together with carbon and nitrogen peaks indicate that all three elements were present within the penetration depth of the XPS measurement. The percentage atomic concentrations of the copper side were 24.8% Cu, 56.2% C, 14.8% O, and 4.2% N (Table 5.1). This suggests that about one fourth of the sample within the XPS penetration depth (~10 nm) was the copper substrate and thus that an epoxy film of less than or equal to approximately 10 nm thickness remained on top of the copper. The very small film thickness is consistent with the SEM image of the copper side where no obvious film was observed. XPS peaks near 950, 930, 532, 400, and 285 eV were detected on the epoxy side (Figure 5.6). The percentage atomic concentrations of the epoxy surface were 1.2% Cu, 82.6% C, 12.8% O, and 3.4% N. Small amounts of copper detected on the epoxy surface may be due to partial failure within the copper or to copper ions which had diffused through the epoxy film during curing.

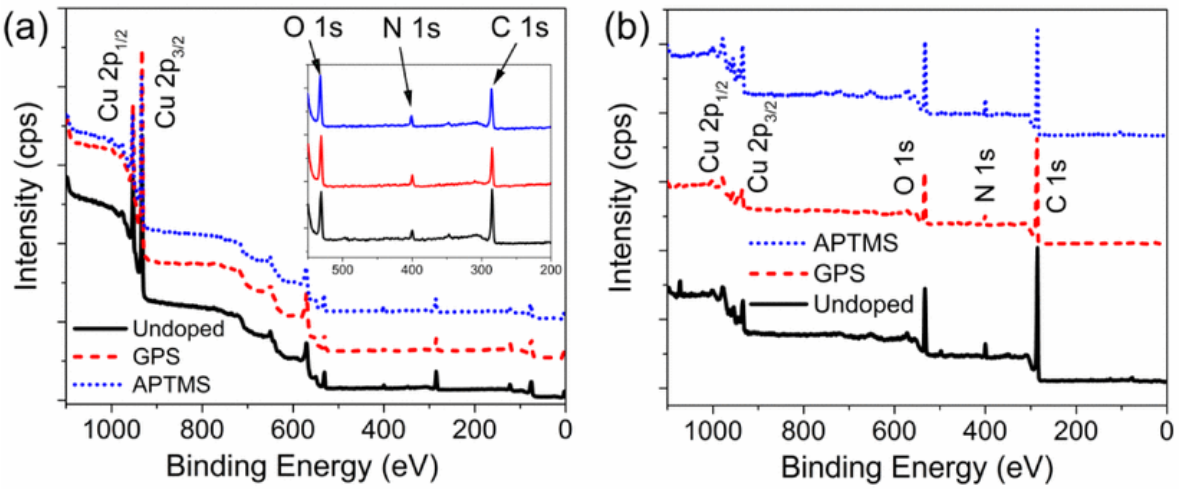

Figure 5.6. XPS survey scans of (a) copper and (b) epoxy sides of undoped, GPS, and APTMS doped epoxy/copper interfaces. Inset: in (a) shows the spectrum in the 600–200 eV range.

	Undoped		γ-GPS		APTMS	
	Cu Side	Epoxy Side	Cu Side	Epoxy Side	Cu Side	Epoxy Side
Cu	24.8	1.2	34.1	1.0	21.5	2.0
C	56.2	82.6	45.3	82.8	53.7	74.3
O	14.8	12.8	15.0	12.1	18.5	16.4
N	4.2	3.4	5.6	4.1	6.3	6.0
Si	-	-	-	-	-	1.3

Table 5.1. Atomic Percentages at the Copper and Epoxy Sides of Undoped, Formula-GPS, and APTMS Doped Epoxy/Copper Interfaces

Considering a mole ratio of two BADGE to one DDM, the expected nitrogen to carbon atomic ratio is 0.036. The nitrogen to carbon ratio at the copper and epoxy sides were 0.07 and 0.04, respectively. The ratio at the epoxy side is close to the expected value in the epoxy bulk which suggests that the epoxy side resembles the epoxy bulk. However, the ratio at the copper

side is higher than expected, which suggests that the DDM concentration near the copper interface was higher than in the bulk. An enrichment of DDM near the copper surface may be due to preferential adsorption of the component during the curing process.[30]

XPS survey spectra collected from the copper and epoxy sides of the copper/γ-GPS doped epoxy closely resembled the corresponding spectra collected from the copper/undoped epoxy interface which suggests that the locus of failure was similar in both cases. The nitrogen to carbon atomic ratio was 0.12 on the copper side and 0.05 on the epoxy side which again suggests that there was an enrichment of the curing agent near the copper interface and that the epoxy side resembled the epoxy bulk. Similarly, the nitrogen to carbon atomic ratios from the copper and epoxy sides of the copper/APTMS doped epoxy interface were 0.12 and 0.08. APTMS contains a nitrogen atom in the end group, therefore segregation of the silane near the copper interface would increase the nitrogen atomic ratio relative to the undoped epoxy case. The epoxy side of the copper/APTMS doped epoxy interface had the highest nitrogen atomic concentration of the three investigated epoxy sides which suggests that APTMS was present at the fractured epoxy side as well as enriched at the copper side. Therefore, the APTMS enrichment extended at least 10 nm from the copper surface toward the epoxy bulk.

High-resolution XPS scans of the carbon 1s region were then collected to characterize the chemical bonding environment of the carbon on the exposed surfaces (Figure 5.7). The carbon 1s peak detected in the spectra collected from the copper side of the copper/undoped epoxy interface was decomposed into constituent peaks at 285.0, 286.5, 288.0, 289.0–289.5, and 290–292 eV, which can be assigned to C–C, C–OH/C–O–C/C–N, C=O, O-C=O, and the π-π* shake up peak from the phenyl ring.[34] The C 1s peak detected in the spectra collected from the epoxy side of the copper/undoped epoxy interface, however, was dominated by the 285.0 and 286.5 eV

peaks, which indicates that the carbon species on the epoxy side surface were approximately 67% C–C groups and 33% C–O/C–N groups. This bond ratio is similar to the expected ratio within the cross-linked bulk.

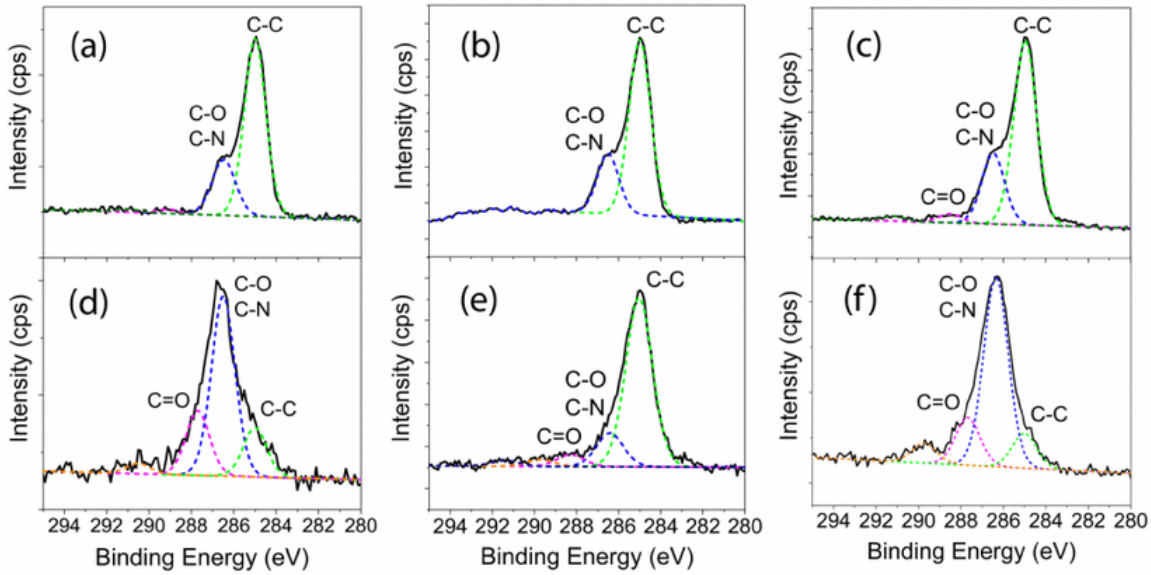

Figure 5.7. XPS high resolution scans collected from the epoxy [(a) undoped, (b) GPS, and (c) APTMS] and copper [(d) undoped, (e) GPS, and (f) APTMS] sides. The solid black line is the measured intensity and the dashed lines are the individual peaks used to fit the detected peak.

At the copper side, the carbon species were approximately 25% C–C groups, 50% C–O/C–N groups, and 25% C=O groups. Therefore, considering that the XPS measurement at the copper side probed the entire thickness of the residual epoxy film, the fracture occurred such that the epoxy on the copper side surface was primarily composed of polar C–O/C–N/C=O groups while the epoxy side surface more closely resembled the epoxy bulk. The higher percentage of polar groups detected at the copper side relative to the epoxy side is consistent with an enrichment of DDM, and hence C–N bonds, near the copper surface. Considering the high percentage of polar carbon bonds and the similarity between the molecular structure at the buried

copper/undoped epoxy interface before and after delamination, the residual epoxy film may have had low flexibility due to strong polar interactions and molecular ordering at the copper surface.

The C–C to C–O/C–N bond ratio at the epoxy side, which resembled the expected peak ratio of the stoichiometric mixture of BADGE to DDM, will be related to the different molecular structures of the cross-linked network near the copper surface and in the epoxy bulk. As discussed above, molecular ordering and amine enrichment near the copper surface will lead to a gradient in network structure from the copper surface toward the epoxy bulk. Although polymer/metal interphases have been reported to be micrometers in length,[5] molecular ordering is only expected at the solid copper surface and was directly observed by SFG measurements. The similarity of the C–C to C–O/C–N bond ratio detected at the epoxy side to the expected bond ratio for the cross-linked epoxy suggests that the network molecular structure had already approached the bulk structure at the epoxy side surface. The molecular structure at the copper surface was significantly different than the structure of the epoxy ~10–20 nm away from the copper surface into the epoxy bulk. Therefore, ordered methyl and methylene groups as well as preferential adsorption of amine species at the copper surface influenced the molecular structure of the cross-linked network at the copper interface, while the molecular structure of the epoxy bulk was increasingly determined by the BADGE to DDM ratio based on the distance away from the copper surface.

XPS C 1s scans were then collected from the copper and epoxy sides of the copper/γ-GPS doped epoxy interface to examine how γ-GPS influenced the interfacial delamination behavior. Although γ-GPS segregation and ordering at the copper surface was directly observed with SFG measurements, the effects of γ-GPS on the molecular structure of the cross-linked epoxy may

extend further into the epoxy bulk. The C 1s peak in the spectra collected from the epoxy side of the copper/γ-GPS doped epoxy interface (Figure 5.7) was dominated by peaks at 285.0 and 286.5 eV, which again indicates that the epoxy side surface resembled the cross-linked epoxy bulk. The carbon peak on the copper side was also dominated by the 285.0- and 286.5-eV peaks, contrary to the copper/undoped epoxy interface. Thus, both the copper and epoxy side surfaces were dominated by nonpolar C–C groups. SFG characterization of the buried copper/GPS doped epoxy interface indicated that γ-GPS was segregated at the copper surface and that the methoxy groups on γ-GPS were initially ordered at the copper interface but were disordered after delamination, likely due to a more flexible cross-linked structure relative to the APTMS case. Interface segregation of γ-GPS at the copper surface will increase the epoxide to amine ratio near the copper/epoxy interface closer to the epoxide to amine ratio in the epoxy bulk. The carbon bonding molecular structure of the residual epoxy at the copper side of the copper/γ-GPS doped epoxy interface, therefore, may more closely resemble the structure in the epoxy bulk which would result in similar XPS spectra at the copper and epoxy sides.

Interface segregation of APTMS at the copper/APTMS doped epoxy interface would decrease the epoxide to amine ratio near the copper/epoxy interface below the epoxide to amine ratio in the epoxy bulk. In addition, SFG characterization of the copper/ATPMS doped epoxy interface indicated that the molecular structure at the buried interface was not largely affected by the delamination. The similar interfacial molecular structure before and after delamination indicates that the interfacial molecular structure of the cross-linked epoxy may have been slightly less flexible than at the copper/γ-GPS doped epoxy interface. The C 1s spectra collected from the copper side of the copper/APTMS doped epoxy interface was dominated by the 286.5 eV peak, similar to the undoped epoxy interface. Different from undoped epoxy, the peak also had a

component near 289.5 eV which can be assigned to O–C=O species. Therefore, the fracture occurred such that the residual epoxy on the copper side surface was largely composed of polar carbon species while the epoxy side again resembled the bulk structure. As discussed above, the low epoxide to amine ratio near the copper interface would increase the density of polar C–O and C–N bonds. In addition, the similarity of the SFG spectra collected from the buried copper/epoxy interface before and after delamination indicated that the interfacial epoxy network had low flexibility which is also consistent with strong polar interactions and/or Si–O–Cu bonds at the copper/epoxy interface.

5.3.5 Locus of Failure Analysis

SFG and XPS results indicated that an epoxy film of ~10 nm or less remained on the copper substrate after copper/epoxy interfaces were separated. Higher than expected nitrogen-to-carbon ratios were measured at all of the copper interfaces which suggests that the local amine concentration near the copper was higher than the concentration in the epoxy bulk. In addition, molecular ordering of methyl and methylene groups was directly observed at the buried copper/epoxy interfaces. Molecular ordering as well as amine enrichment near the copper interface will result in a molecular structure gradient from the copper surface to the epoxy bulk. Different molecular structures near the metal interface and in the bulk will consequently result in a gradient of mechanical properties near the metal/polymer interface.

The thin epoxy layer remaining on the copper after interfacial separation suggests that fracture occurred along a weak planar region within the epoxy very near the copper interface where the cohesive strength was lower than the interfacial copper/epoxy strength and the cohesive strength of the epoxy. Considering the SFG and XPS analysis of the interfacial region, the fracture likely happened at the transition zone between the molecular structure of the epoxy

near the copper surface and the molecular structure of the epoxy ~10–20 nm into the bulk. Furthermore, silane adhesion promoters directly affected the transition region where failure occurred by modifying the molecular structure of the copper/epoxy interface and by affecting whether the exposed epoxy film on the copper side was dominated by polar or nonpolar carbon species. Therefore, the effect of adhesion promoters is not simply due to chemical bonding at the copper surface, but to how the silane influences the molecular ordering and molecular structure at and near the copper interface.

5.4 Conclusion

In this chapter, we showed another example of using SFG to nondestructively examine buried interfacial structures *in situ*. Different from the polymer/polymer interfacial structures in the previous chapters, here the molecular structure at buried copper/epoxy interfaces was nondestructively characterized *in situ* using SFG. Vibrational spectra of buried copper/epoxy interfaces were selectively measured in situ by utilizing an SFG sandwich geometry. Furthermore, the utilized sandwich geometry enabled SFG vibrational spectra to be collected from exposed copper surfaces after mechanical separation of copper/epoxy interfaces. SFG and locus of failure results suggest that delamination occurred at a weak zone within the epoxy that was caused by a local change in the epoxy network structure near the copper interface.

5.5 Impact

Delamination at copper/adhesive interfaces due to weak interfacial adhesion continues to be a reliability concern in microelectronic packaging. If such buried metal/adhesive interfaces could be rationally designed to withstand qualification testing using predictive structure-property relationships, microelectronic products could be brought to market faster and work more reliably. In this chapter, methodology was developed that can be applied to further investigate the

relationship between molecular structures at many buried polymer/metal interfaces and locus of failure analysis. We found that copper/epoxy interfaces delaminate near, but not exactly at, the metal/polymer interface in dry conditions and that silane adhesion promoters modify the interfacial region near the copper surface. This work suggests that the entire interfacial layer near copper needs to be modified rather than only modifying the copper surface or adding adhesion promoters. As common adhesion promoters aren't sufficient, this work suggests that a transition layer that replaces the weak zone could substantially improve adhesion at the copper/epoxy interface. The transition layer would need to have high cohesive strength, strong adhesion to copper and copper oxides, and sufficient thickness and composition to allow diffusion of the epoxy components into the layer such that sharp gradients in cohesive strength are not present in the layer. This work could be extended to study delamination at metal/polymer interfaces induced by Joint Electron Device Engineering Council qualification testing of microelectronic packaging (e.g. hygrothermal aging studies presented in chapter 4).

5.6 References

(1) Turunen, M. P. .; Marjamäki, P.; Paajanen, M.; Lahtinen, J.; Kivilahti, J. K. Pull-off Test in the Assessment of Adhesion at Printed Wiring Board Metallisation/epoxy Interface. *Microelectron. Reliab.* **2004**, *44* (6), 993–1007.

(2) Grundmeier, G.; Stratmann, M. Adhesion and De-Adhesion Mechanisms at Polymer/Metal Interfaces: Mechanistic Understanding Based on In Situ Studies of Buried Interfaces. *Annu. Rev. Mater. Res.* **2005**, *35* (1), 571–615.

(3) Awaja, F.; Gilbert, M.; Kelly, G.; Fox, B.; Pigram, P. J. Adhesion of Polymers. *Prog. Polym. Sci.* **2009**, *34* (9), 948–968.

(4) Lee, L.-H. Molecular Bonding and Adhesion at Polymer-Metal Interphases. *J. Adhes.* **1994**, *46* (1-4), 15–38.

(5) Roche, A. .; Bouchet, J.; Bentadjine, S. Formation of Epoxy-Diamine/metal Interphases. *Int. J. Adhes. Adhes.* **2002**, *22* (6), 431–441.

(6) Chen, Z. Investigating Buried Polymer Interfaces Using Sum Frequency Generation Vibrational Spectroscopy. *Prog. Polym. Sci.* **2010**, *35* (11), 1376–1402.

(7) Hankett, J. M.; Liu, Y.; Zhang, X.; Zhang, C.; Chen, Z. Molecular Level Studies of Polymer Behaviors at the Water Interface Using Sum Frequency Generation Vibrational Spectroscopy. *Journal of Polymer Science Part B: Polymer Physics* **2013**, *51* (5), 311–328.

(8) Zhang, C.; Myers, J. N.; Chen, Z. Elucidation of Molecular Structures at Buried Polymer Interfaces and Biological Interfaces Using Sum Frequency Generation Vibrational Spectroscopy. *Soft Matter* **2013**, *9* (19), 4738.

(9) Geiger, F. M. Second Harmonic Generation, Sum Frequency Generation, and $\chi^{(3)}$: Dissecting Environmental Interfaces with a Nonlinear Optical Swiss Army Knife. *Annual Review of Physical Chemistry* **2009**, *60* (1), 61–83.

(10) Zhang, C.; Hankett, J.; Chen, Z. Molecular Level Understanding of Adhesion Mechanisms at the Epoxy/Polymer Interfaces. *ACS Applied Materials & Interfaces* **2012**, *4* (7), 3730–3737.

(11) Myers, J. N.; Zhang, C.; Lee, K.-W.; Williamson, J.; Chen, Z. Hygrothermal Aging Effects on Buried Molecular Structures at Epoxy Interfaces. *Langmuir* **2014**, *30* (1), 165–171.

(12) Zhang, C.; Shephard, N. E.; Rhodes, S. M.; Chen, Z. Headgroup Effect on Silane Structures at Buried Polymer/Silane and Polymer/Polymer Interfaces and Their Relations to Adhesion. *Langmuir* **2012**, *28* (14), 6052–6059.

(13) Fang, Y.; Li, B.; Yu, J.; Zhou, J.; Xu, X.; Shao, W.; Lu, X. Probing Surface and Interfacial Molecular Structures of a Rubbery Adhesion Promoter Using Sum Frequency Generation Vibrational Spectroscopy. *Surface Science* **2013**, *615*, 26–32.

(14) Lu, X.; Li, D.; Kristalyn, C. B.; Han, J.; Shephard, N.; Rhodes, S.; Xue, G.; Chen, Z. Directly Probing Molecular Ordering at the Buried Polymer/Metal Interface. *Macromolecules* **2009**, *42* (22), 9052–9057.

(15) Lu, X.; Li, B.; Zhu, P.; Xue, G.; Li, D. Illustrating Consistency of Different Experimental Approaches to Probe the Buried Polymer/metal Interface Using Sum Frequency Generation Vibrational Spectroscopy. *Soft Matter* **2014**, *10* (29), 5390.

(16) Onard, S.; Martin, I.; Chailan, J.-F.; Crespy, A.; Carriere, P. Nanostructuration in Thin Epoxy−Amine Films Inducing Controlled Specific Phase Etherification: Effect on the Glass Transition Temperatures. *Macromolecules* **2011**, *44* (9), 3485–3493.

(17) Wang, J.; Chen, C.; Buck, S. M.; Chen, Z. Molecular Chemical Structure on Poly(methyl Methacrylate) (PMMA) Surface Studied by Sum Frequency Generation (SFG)

Vibrational Spectroscopy. *The Journal of Physical Chemistry B* **2001**, *105* (48), 12118–12125.

(18) Stiopkin, I. V.; Jayathilake, H. D.; Bordenyuk, A. N.; Benderskii, A. V. Heterodyne-Detected Vibrational Sum Frequency Generation Spectroscopy. *Journal of the American Chemical Society* **2008**, *130* (7), 2271–2275.

(19) Malyk, S.; Shalhout, F. Y.; O'Leary, L. E.; Lewis, N. S.; Benderskii, A. V. Vibrational Sum Frequency Spectroscopic Investigation of the Azimuthal Anisotropy and Rotational Dynamics of Methyl-Terminated Silicon(111) Surfaces. *The Journal of Physical Chemistry C* **2013**, *117* (2), 935–944.

(20) Miyamae, T.; Ito, E.; Noguchi, Y.; Ishii, H. Characterization of the Interactions between Alq_3 Thin Films and Al Probed by Two-Color Sum-Frequency Generation Spectroscopy. *The Journal of Physical Chemistry C* **2011**, *115* (19), 9551–9560.

(21) Achtyl, J. L.; Vlassiouk, I. V.; Dai, S.; Geiger, F. Interactions of Organic Solvents at Graphene/α-Al_2O_3 and Graphene Oxide/α-Al_2O_3 Interfaces Studied by Sum Frequency Generation. *The Journal of Physical Chemistry C* **2014**, *118* (31), 17745–17755.

(22) Buchbinder, A. M.; Gibbs-Davis, J. M.; Stokes, G. Y.; Peterson, M. D.; Weitz, E.; Geiger, F. M. Method for Evaluating Vibrational Mode Assignments in Surface-Bound Cyclic Hydrocarbons Using Sum-Frequency Generation. *The Journal of Physical Chemistry C* **2011**, *115* (37), 18284–18294.

(23) Ye, S.; Wei, F. An Approach to Compatible Multiple Nonlinear Vibrational Spectroscopy Measurements Using a Commercial Sum Frequency Generation System. *The Analyst* **2011**, *136* (12), 2489.

(24) Ye, S.; Li, H.; Yang, W.; Luo, Y. Accurate Determination of Interfacial Protein Secondary Structure by Combining Interfacial-Sensitive Amide I and Amide III Spectral Signals. *Journal of the American Chemical Society* **2014**, *136* (4), 1206–1209.

(25) Ye, H.; Gu, Z.; Gracias, D. H. Kinetics of Ultraviolet and Plasma Surface Modification of Poly(dimethylsiloxane) Probed by Sum Frequency Vibrational Spectroscopy. *Langmuir* **2006**, *22* (4), 1863–1868.

(26) Ye, H.; Abu-Akeel, A.; Huang, J.; Katz, H. E.; Gracias, D. H. Probing Organic Field Effect Transistors In Situ during Operation Using SFG. *Journal of the American Chemical Society* **2006**, *128* (20), 6528–6529.

(27) Miyamae, T.; Yamada, Y.; Uyama, H.; Nozoye, H. Molecular Orientation of Poly(ethylene Terephthalate) and Buried Interface Characterization of TiO2 Films on Poly(ethylene Terephthalate) by Using Infrared-Visible Sum-Frequency Generation. *Surface Science* **2001**, *493* (1-3), 314–318.

(28) Vázquez, A. V.; Holden, B.; Kristalyn, C.; Fuller, M.; Wilkerson, B.; Chen, Z. Surface and Buried Interfacial Structures of Epoxy Resins Used as Underfills Studied by Sum Frequency Generation Vibrational Spectroscopy. *ACS Applied Materials & Interfaces* **2011**, *3* (5), 1640–1651.

(29) Delle Site, L.; Abrams, C.; Alavi, A.; Kremer, K. Polymers near Metal Surfaces: Selective Adsorption and Global Conformations. *Physical Review Letters* **2002**, *89* (15).

(30) Marsh, J.; Minel, L.; Barthés-Labrousse, M. .; Gorse, D. Interaction of Epoxy Model Molecules with Aluminium, Anodised Titanium and Copper Surfaces: An XPS Study. *Applied Surface Science* **1998**, *133* (4), 270–286.

(31) Horner, M. R.; Boerio, F. J.; Clearfield, H. M. An XPS Investigation of the Adsorption of Aminosilanes onto Metal Substrates. *Journal of Adhesion Science and Technology* **1992**, *6* (1), 1–22.

(32) Lu, X.; Myers, J. N.; Chen, Z. Molecular Ordering of Phenyl Groups at the Buried Polystyrene/Metal Interface. *Langmuir* **2014**, *30* (31), 9418–9422.

(33) Platzman, I.; Brener, R.; Haick, H.; Tannenbaum, R. Oxidation of Polycrystalline Copper Thin Films at Ambient Conditions. *Journal of Physical Chemistry C* **2008**, *112* (4), 1101–1108.

(34) Gardella, J. A.; Ferguson, S. A.; Chin, R. L. $\pi^* \leftarrow \pi$ Shakeup Satellites for the Analysis of Structure and Bonding in Aromatic Polymers by X-Ray Photoelectron Spectroscopy. *Appl. Spectrosc.* **1986**, *40*, 224–232.

CHAPTER 6

IN SITU OBSERVATION OF WATER BEHAVIOR AT THE SURFACE AND BURIED INTERFACE OF A LOW-K DIELECTRIC FILM

6.1 Introduction

In the previous chapters, we mainly investigated molecular behaviors of polymer adhesives at buried interfaces. In the next few chapters, we will study the structures of low dielectric constant (or low-k) materials including low-k polymers at buried interfaces. Low-k materials and copper have been introduced to replace silicon dioxide and aluminum as interconnections in high performance integrated circuits to improve resistance-capacitance (RC) delay, minimize crosstalk-noise, enhance signal transmission, and reduce power dissipation.[1-3] SiCOH based porous low-k dielectric materials have been studied extensively as intrametal dielectrics in recent years.[3] Especially, silsesquioxane (SSQ) materials have a silica-like structure but with a fraction of the Si–O bonds replaced with other bonds, which have lower polarizability such as Si–CH_3, Si–C, and Si–F. The most common replacement is Si–CH_3 and the resultant materials are called methylsilsesquioxane (MSQ). Disruption of the silica structure with such groups increases the hydrophobicity of the resultant low-k material and reduces the relative dielectric constant to as low as 2.8.[3] Cage structures as well as nanopores were additionally introduced into the materials to further lower the overall dielectric constant to below 2.8, depending on the porosity of SSQ film.[1,4]

The integration of porous low-k dielectrics into large-scale microelectronic circuits, however, has been found to be extremely challenging. The introduction of high porosity has been

reported to degrade the mechanical properties and thermal stability of the materials as compared with SiO_2.[2,5,6] For instance, the poor mechanical strength of porous low-k dielectric films induced higher interfacial delamination and cohesive failure during chemical mechanical polish (CMP).[7] In addition, high porosity has been related to increased diffusion rates of molecular species and metal ions into low-k bulk and weaker dielectric breakdown strengths relative to SiO_2.

For porous dielectrics, there are additional concerns related to moisture uptake induced by processing steps such as resist removal, postetch cleaning, CMP, or post-CMP cleaning.[8-10] Previous reports showed that moisture could diffuse into the SSQ film stacks even though SSQ materials are usually hydrophobic.[11] Water uptake is detrimental to the performance and the reliability of integrated circuits. Increased water in the low-k materials can lead to significantly increased leakage current, lower breakdown electric fields, and shorter dielectric breakdown lifetimes because water could increase dielectric permittivity, accelerate fracture behavior, and degrade the adhesion between the low-k material and the capping layer.[8]

Recently, extensive research has been carried out to understand the impact of water on the properties and the reliability of low-k materials.[9,10,12,13] Many techniques, such as Fourier transform infrared (FTIR) spectroscopy, Raman vibrational spectroscopy, and thermal desorption spectroscopy (TDS) have been widely implemented to evaluate the influence of absorbed water on the low-k dielectric reliability and the bulk molecular structure of low-k materials.[4,12,14] For example, Li et al. suggested that there was more than one kind of possible water components in the low-k dielectric.[9] Physisorbed water could be easily removed by a low-temperature anneal which improved leakage current and time-dependent-dielectric-breakdown (TDDB) lifetime. Another type of water, referred to as chemisorbed, however, was only able to be desorbed after

annealing at temperatures as high as 400 ℃ and was thus thought to be the main reason for water related TDDB failure mechanism.[9] Nevertheless, there is still a lack of a direct measurement technique to reveal the dynamic moisture uptake process and the water adsorption mechanism at the molecular level. In particular, few studies have been done to elucidate the influence of different absorbed water components at the surface and the interface of low-k dielectrics on device performance.

Surfaces and buried interfaces play an increasingly important role as the porosity of low-k dielectrics increases and the size of the microelectronic devices continues to shrink. In the past few decades, both theoretical and experimental results have shown that water molecules at surfaces could behave differently than in the bulk.[15-22] Previous simulation results indicated that for certain low-k materials, ~0.4 vol % chemisorbed moisture found on the pore surface could induce a 17–23% increase of the dielectric constant.[23] Water diffusion along the interface of a low-k material has been observed experimentally with isotope tracer diffusion experiments combined with dynamic secondary ion mass spectroscopy (SIMS);[8] however, no molecular structural information about interfacial adsorbed water could be obtained. More importantly, the water uptake process may be influenced by high vacuum environments needed for conducting the analysis. For a porous low-k material, moreover, the inner surfaces of the pores form another important interface, which is challenging to characterize. For a low-k material with a high porosity, the total area of these low-k material/air surfaces could be much larger than that of the low-k/solid interface. Therefore, water adsorption at these low-k material/air surfaces cannot be ignored and these surfaces increasingly influence the film properties and reliability as the porosity of low-k film increases. The introduction of higher porosity into low-k dielectric is required in the near future to further lower the dielectric constant.

Herein, to address the problems above, we propose a simple and direct method using sum frequency generation vibrational spectroscopy (SFG), transmission FTIR, and attenuated total reflectance FTIR (ATR-FTIR) to investigate water behavior at the exposed surface and buried interface of low-k dielectrics as well as probe the dynamic water uptake process through low-k material *in situ* at the molecular level. SFG is a second order nonlinear optical technique that can selectively and nondestructively probe the molecular structures of polymers[24,25] and biomolecules[26] at surfaces and buried interface in situ with high surface selectivity due to its selection rules.[27-39] Here, water behavior at the low-k dielectric/air surface was first investigated at the molecular level to simulate water adsorption at the pore inner surfaces of porous low-k dielectrics. Subsequently, combining SFG, transmission FTIR, and ATR-FTIR, the water uptake was selectively investigated to trace preferential water uptake pathways directly. Various water molecular structures were compared at the low k material/SiO_2 buried interface and in the bulk to correlate the molecular structure changes to low-k properties. To emulate the molecular structures of low-k materials, we selected a caged SSQ and poly(methylsilsesquioxane) (PMSQ) as model low-k materials.

6.2 Materials and Methods

6.2.1 Materials

PSS-Octakis (dimethylsilyloxy) substituted (PSS) was purchased from Sigma-Aldrich (St. Louis, Mo) and poly(methyl silsesquioxane) (PMSQ) (≥99.5% purity) was purchased from Gelest. Tetrahydrofuran (THF; ≥ 99.9% purity) was obtained from Sigma-Aldrich (St. Louis, Mo) and used as received. Right angle fused silica prism substrates were obtained from Altos Photonics, Inc.

6.2.2 Sample Preparation

Both PSS and PMSQ were dissolved in THF to form 2 wt % solutions. Then, PSS and PMSQ thin films were prepared on silica windows by spin coating (3000 r/min, 30 s) using a P-6000 spin coater (Speedline Technologies). Drop-casting was used to prepare PMSQ thick film for buried interface investigation. Similar drop-cast thick films were deposited on Si prism for ATR-FTIR measurements. The samples were then placed in a vacuum chamber (200 mTorr) for about 12 h at room temperature to completely evaporate residual solvent. Notably, since almost no SFG signals were detected using a face-down window geometry when samples were in contact with water, fused silica prisms were also applied here to provide in situ surface structure information on PMSQ thin films in contact with water.[27-29,40] Film thicknesses were measured by a depth profilometer (Dektak 6 M Stylus Surface Profilometer, Veeco) and the average thicknesses of thin films and thick films were around 200 nm and 5 μm, respectively.

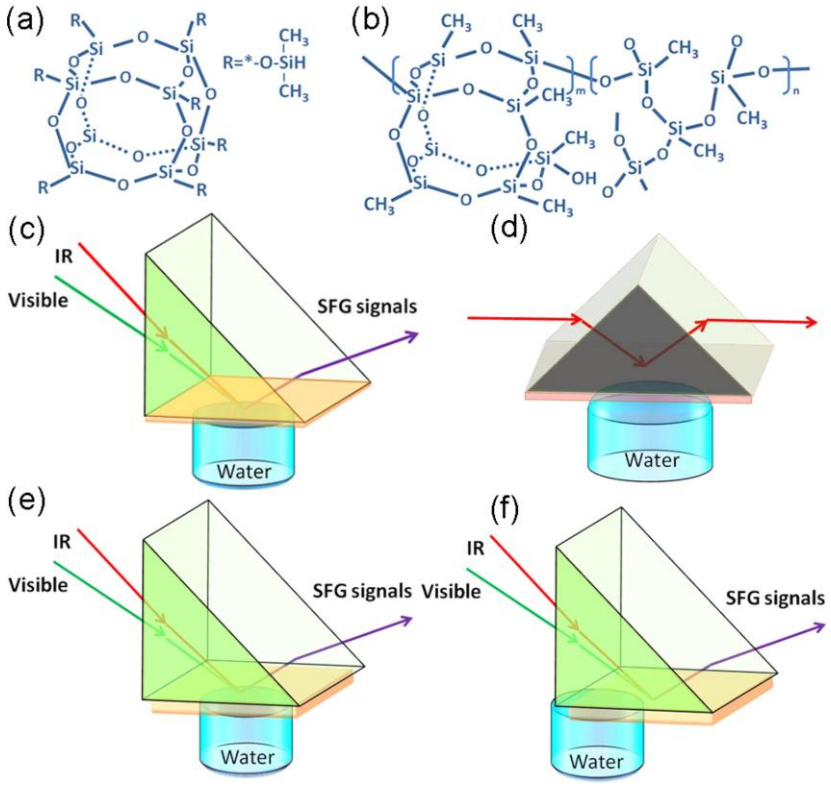

Figure 6.1. Chemical structures of monomer (a) PSS and (b) PMSQ. Experimental geometry of SFG experiment with a PMSQ thin film in contact with water (c), ATR-FTIR experiment with a PMSQ thick film in contact with water (d), SFG experiment with water in contact with PMSQ thick film at the middle of the film (method 1) (e) and at the edge of the film (method 2) (f).

6.2.3 SFG and FTIR Experimental

The SFG setup used in this research was a commercially available system purchased from EKSPLA. The optical setup has been described in chapter 1.[27-30,32] The SFG spectra were collected in the ssp polarization combination by using the face-down reflection geometry (Figure 6.1c, e, f). For each sample, spectra were collected at least at five different spots; for each spot, five spectra were detected to examine the film homogeneity. FTIR and ATR-FTIR measurements were performed using a Nicolet 6700 FTIR spectrometer controlled by OMNIC

software. The experimental setup for ATR-FTIR tests during water uptake process is illustrated in Figure 6.1d. The input angle was approximately 55 °.

6.3 Results and Discussion

6.3.1 SFG Study of the PSS Thin Film

First, PSS with high purity was selected as a simple model system for peak assignments. As shown in Figure 6.1a, PSS has a cage structure containing 8 silicon atoms and substituent R. Here, R, whose structure is shown in Figure 1a, contains Si-CH_3 and Si–H groups. The chemical structure of PSS is very similar to the widely used low-k material PMSQ and poly(hydrosilsesquioxane) (HSQ). Figure 6.2 shows ssp SFG spectra collected from a spin-coated PSS thin film on a silica window and a prism, respectively. Two pronounced peaks were observed near 2915 and 2970 cm^{-1}, which can be assigned to Si-CH_3 symmetric and asymmetric stretching modes, respectively (Figure 6.2a).[41] The intensity of the symmetric stretching signal was much stronger than that of the asymmetric stretching peak. According to a previous study,[42] for windows geometry, SFG signals in the C–H stretching frequency region from the polymer/hydrophilic substrate are usually quite weak, so ssp SFG spectrum collected from windows face-down geometry can be considered to be dominated by the SFG signals generated from polymer/air surface. Therefore, the SFG spectrum shown in Figure 6.2a indicates that Si-CH_3 functional groups cover the surface of the PSS film. Figure 6.2b exhibits the ssp SFG spectra collected from the PSS thin film coated on silica prism. Not surprisingly, very similar spectral features were observed around 2915 and 2970 cm^{-1} with a similar intensity ratio relative to the window geometry, which suggests that ssp SFG spectrum of PSS thin film using prism geometry can be considered to be dominated by PSS/air surface signals as well. The only difference is the peak intensities are substantially higher than those collected with window

geometry, which is reasonable because prism geometry has been shown to enhance SFG intensities.[43]

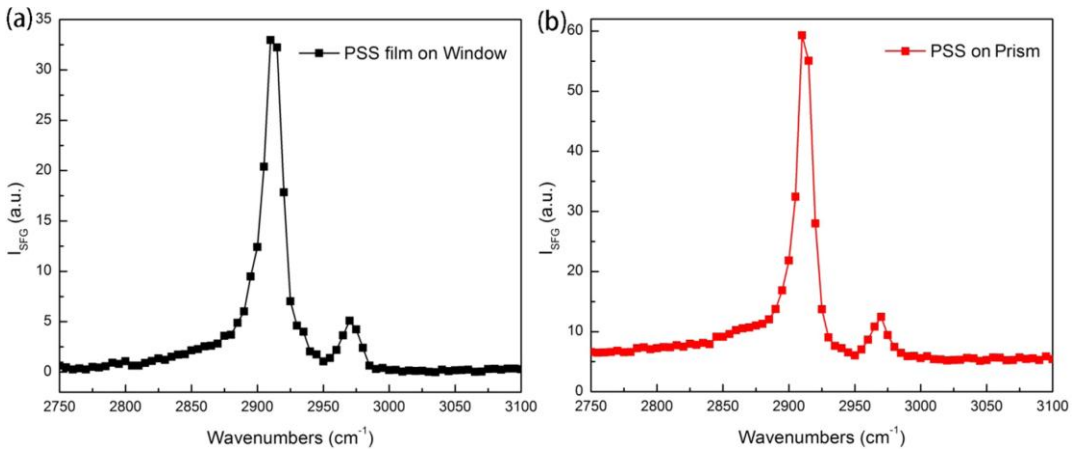

Figure 6.2. ssp SFG spectra of PSS on fused silica window (a) and prism (b).

6.3.2 SFG and FTIR Studies of the PMSQ Thin Film in Air

After using PSS to assign the peaks in ssp SFG spectra, SFG measurements were carried out on PMSQ thin film spin-coated on a silica window (Figure 6.3a) and prism (Figure 6.3b) as well. The molecular structure of PMSQ is shown in Figure 6.1b. Different from the monomer PSS, PMSQ consists of two kinds of Si–O structures, which are often referred to as "cage" and "network" structures. In addition to Si–O bonds, Si-CH_3 functional groups are also present in the PMSQ structure. Similar to the case of PSS, the ssp SFG spectrum collected from the PMSQ thin film using window geometry was dominated by two peaks near 2915 and 2970 cm^{-1}, indicating that the surface of PMSQ thin film is covered by Si-CH_3 groups as well. Despite the similar spectral features of PSS and PMSQ, the asymmetric peak (2970 cm^{-1}) strength is higher here, leading to slightly different orientation of Si-CH_3 groups at the surface of PMSQ film compared to the PSS film. Besides, the peak intensities observed in Figure 6.3a are lower than that of the PSS thin film, which could be interpreted by a less ordered surface or less coverage of Si-CH_3

groups at the surface of the PMSQ film. Considering the similar molecular structures of PSS and PMSQ, we believe the surface of PMSQ thin film was more disordered than that of PSS.

Similar SFG spectral features were again observed in the prism and window geometry (Figure 6.3b) for PMSQ thin films. As in the PSS case, the SFG intensity was enhanced in the prism geometry. However, the peak intensities detected here are still lower than that of the PSS film, implying less ordered surface of PMSQ compared to that of PSS. As expected, two pronounced peaks, 2915 and 2970 cm^{-1}, with similar peak ratio as the two peaks in the SFG spectra collected from PSS films, were observed in the ssp SFG spectrum of PMSQ thin film. These results imply that the molecular structures at the surfaces of PMSQ films deposited on window and prism resembled each other, both of which are covered by Si-CH_3 groups with similar orientations. As the SFG spectral features of PMSQ thin films collected using silica window and prism are very similar, the prism geometry was utilized below for water contact experiments.

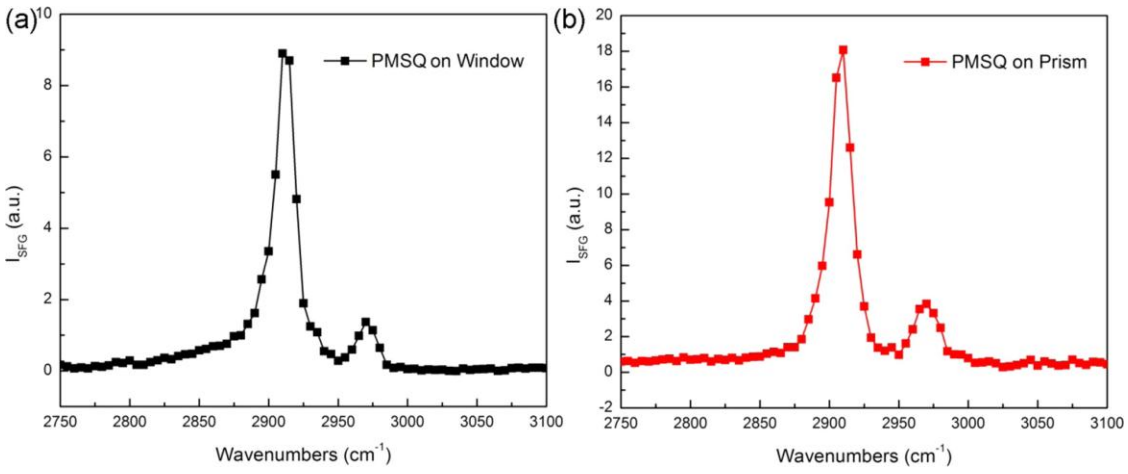

Figure 6.3. ssp SFG spectra of PMSQ on fused silica window (a) and prism (b).

To clarify the impact of the interference of SFG signals originating from the buried interface and the surface, the Fresnel coefficients in the PMSQ/silica buried interface and PMSQ/Medium (air/water) were calculated using the thin film model discussed in chapter 1, and the corresponding calculated Fresnel coefficients were plotted as a function of film thickness (Figure 6.4).

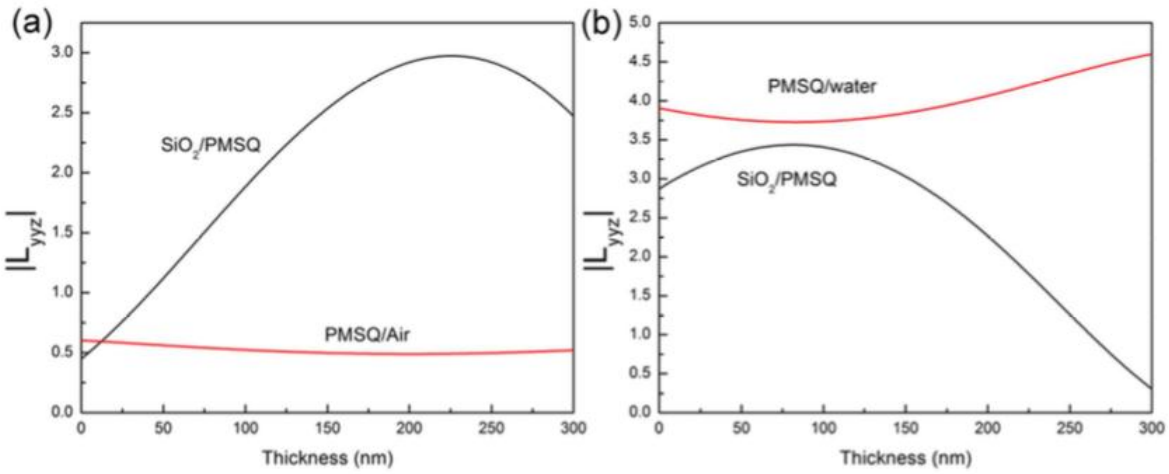

Figure 6.4. The calculated Fresnel coefficients for the PMSQ thin film deposited on prism (with face-down geometry) with air (a) and water (b) as the bottom contacting media.

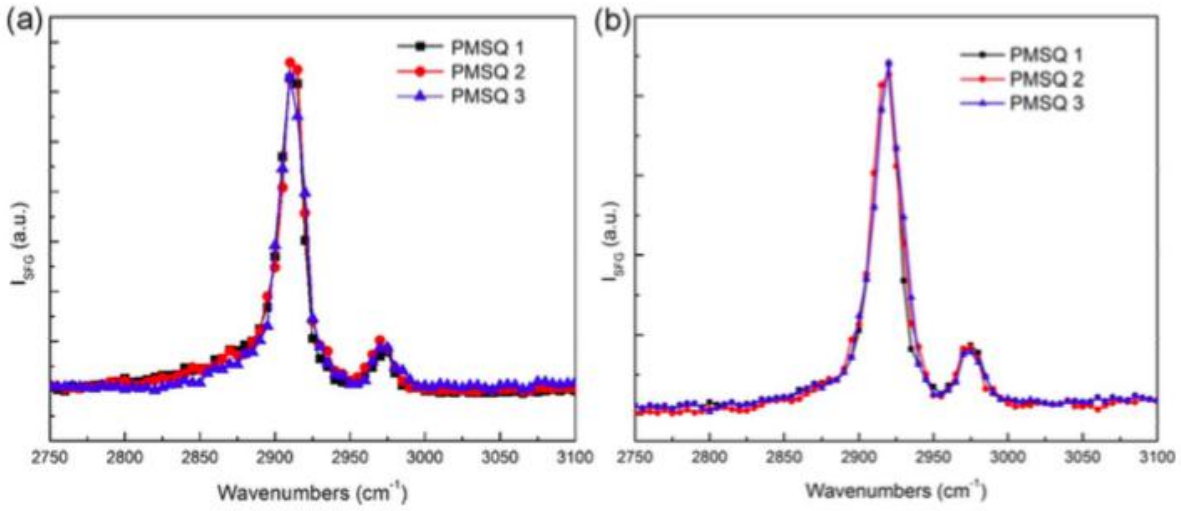

Figure 6.5. SFG ssp spectra of spin-on PMSQ thin films deposited on (a) fused silica windows, and (b) fused silica prisms with different thicknesses using the "face-down" geometry. For PMSQ 1-3, the thickness is ~120 nm, ~150 nm and ~200 nm respectively.

Besides, PMSQ thin films were spin-coated on the surfaces of silica windows and prism with different thicknesses to clarify that the origins of the ssp SFG signals collected from the PMSQ film using face-down window and prism geometry. The thickness dependent SFG spectra of PMSQ films deposited on fused silica windows and prisms are shown in Figure 6.5. For a thin PMSQ film on a silica substrate, SFG spectral signals from both the top (surface in air) and the bottom (the silica/PMSQ interface) of the film may be detected simultaneously, therefore it is important to clarify the origin of SFG signals detected from the PMSQ film on silica to understand the SFG results. For the case of PMSQ film in contact with water, the Fresnel coefficient of the PMSQ surface in water is larger than the SiO_2/PMSQ buried interface (for the thickness 200 nm: the Fresnel coefficients for surface and buried interface are ~4.06 and ~2.56 respectively). So the contribution from the buried interface is likely smaller for PMSQ in water. However, for the case of PMSQ in air, the Fresnel coefficient of the PMSQ surface in air is much

smaller than that of the SiO_2/PMSQ buried interface (for the thickness 200 nm we used here, the Fresnel coefficients for surface in air and buried interface are ~0.50 and ~2.93 respectively). This means that the collected ssp spectra from a PMSQ thin film using the prism geometry in air may have contributions from both the SiO_2/PMSQ buried interface and the PMSQ/air surface and perhaps, the buried interface signal is stronger.

It is reasonable if the ssp SFG signals generated from the PMSQ film on silica prism in air are contributed largely from the buried PMSQ/silica interface because the absolute Fresnel coefficient of the PMSQ/silica interface is ~2.93 and that of the PMSQ surface in air is much smaller, only ~0.497 (film thickness ~200 nm). However, the molecular structure at the buried interface may be weakly ordered which would result in a negligible contribution from the buried interface to the measured SFG signal intensity. To investigate ordering at the buried interface, we collected film thickness dependent SFG spectra from PMSQ on silica using both the window "face-down" geometry (Figure 6.5a) and the prism "face-down" geometry (Figure 6.5b). It was found that for both cases, the SFG spectra are independent of the film thickness. In addition, the SFG spectra collected using the two experimental geometries are similar. These results indicate that the SFG spectra shown here are dominated by surface signals. Otherwise, as the sample film thickness changed, the interferences between the surface and buried interface signals would be varied, altering the detected intensity in the SFG spectra. Since here the SFG spectral signatures collected from the prism geometry are very similar to those of the window geometry and are independent of the film thickness, we can conclude that the collected SFG spectra from the prism geometry must be dominated by the surface signals. This is because the Si-CH_3 groups at the buried interface are quite disordered. Since the SFG signals were not influenced as the thicknesses of PMSQ films varied for both windows and prism geometry, we believe that the ssp

SFG spectrum of PMSQ thin film is dominated by the SFG signals generated from polymer/air surface. Signals from the polymer/substrate buried interface were demonstrated to be extremely weak and should be able to be ignored.

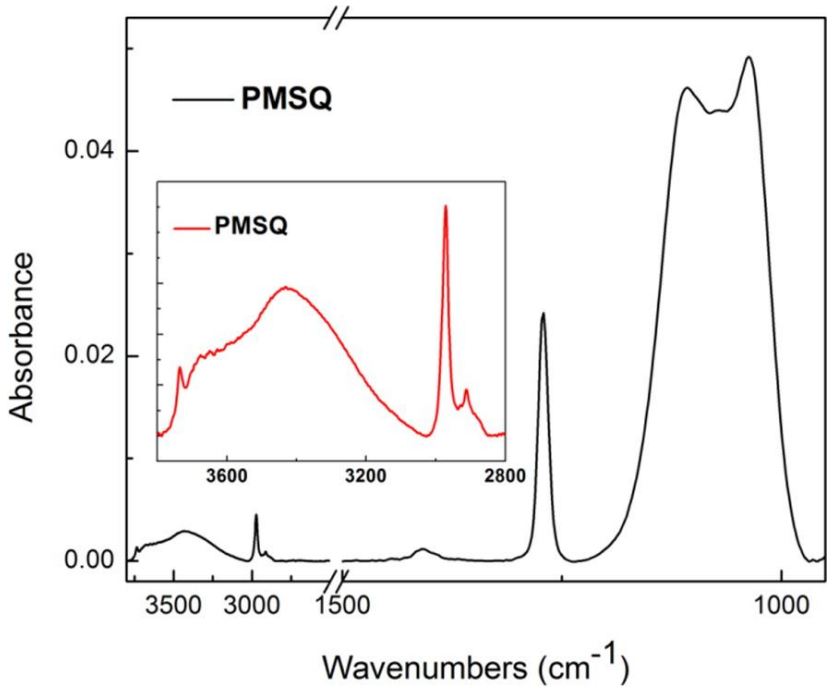

Figure 6.6. Transmission FTIR spectrum of PMSQ thin film spin coated on CaF_2 window, the inset is the enlarged spectrum in C–H and water region.

To compare the chemical structures of PMSQ bulk to that of PMSQ surface, FTIR measurement was performed on as-deposited PMSQ thin film to characterize the bulk structure. With regard to possible water components in low-k materials, Proost et al. reported that there may exist four types of water related chemical groups, which were attached to the skeleton for silica based dielectrics.[12,44] Li et al. pointed out that two of them, physisorbed (α) and chemisorbed (β) water, were found to degrade the dielectric reliability of integrated low-k materials and selective studies have elucidated the respective contributions of α water and β water to increased leakage current and TDDB failure.[9] The other two kinds of water present in

low-k dielectrics, γ1 and γ2, were not able to be desorbed by conventional anneal, which is compatible with low-k materials unless the anneal temperature was as high as 700 ℃. As a result, only the first two kinds of water will be considered for the water adsorption mechanism and the influence of different kinds of adsorbed water on low-k properties here. Figure 6.6 shows that the FTIR spectral features are very similar to most carbon-doped oxide low-k films.[1,4,13] In the fingerprint region, several clear peaks were observed. The peak around 1272 cm^{-1} can be assigned to Si-CH_3 and the two strong overlapped peaks around 1109 and 1035 cm^{-1} can be assigned to caged Si–O bond structure and network Si–O bond structure, respectively.[4] In the C–H stretching frequency region, only one weak CH_3 peak near 2971 cm^{-1} and a strong water peak from 2975 to 3800 cm^{-1} centered around 3400 cm^{-1} were detected. Such FTIR features have been attributed to weakly hydrogen bonded water located inside the PMSQ bulk, which suggests that most of water adsorbed in the bulk is physisorbed water.[12,19] Most of the water molecules (e.g., those that contribute to the signal centered at 3400 cm^{-1}) present in PMSQ bulk should be removed after annealing above 100 ℃. However, the broad peak feature ranging from 2975 to 3800 cm^{-1} implies that a small part of other water components, such as those with peak centered near 3200 cm^{-1} may also be present in the PMSQ bulk. This peak has been assigned to strongly hydrogen bonded water (e.g., those with strong hydrogen bonding interactions with hydrophilic sites within a polymer; they are often called chemisorbed water).[12,45] According to a previous study,[23] only a small amount of this type of water molecules exist in low-k materials. The previous FTIR characterization of the PMSQ bulk structure is consistent with this result. Note that after curing the PMSQ film under vacuum at 400 ℃ for 1 h, the water peak became almost undetectable by FTIR.[23]

6.3.3 Water Uptake at the Surface and Buried Interface of PMSQ Film

In order to reveal the water behavior at the PMSQ surface and correlate the water structures to low-k degradation, in situ SFG measurements were first performed on a spin-on PMSQ thin film deposited on silica prism. SFG studies on the surface of PMSQ thin film during contact with water and after water removal were subsequently performed. The experimental setup for in situ SFG investigation of PMSQ surface structures in contact with water was depicted in Figure 6.1c. To selectively detect the molecular structural changes in the C–H stretching frequency region, D_2O was applied in SFG experiments to remove the influence of H_2O on SFG signals in the C–H region. Figure 6.7 shows the ssp SFG spectra collected from the PMSQ surface before, during, and after water contact (Figure 6.7a–c). D_2O results are also shown in Figure 6.7d–f.

Figure 6.7a shows the original ssp SFG spectra of PMSQ thin film in the C–H and water O–H stretching frequency region (2750 cm^{-1} to 3500 cm^{-1}). Except for pronounced Si-CH_3 signals, no water peaks were detected, indicating that no ordered water structures were present at the PMSQ/air surface. It is interesting to see that water behaved very differently at the PMSQ surface than in the bulk (a broad water peak around 3400 cm^{-1} was detected by FTIR). Once the film was in contact with water, a broad water peak centered near 3150 cm^{-1} was observed in the SFG spectrum (Figure 6.7b). This means although PMSQ is quite hydrophobic, ordered water components can be present at the PMSQ/water interface. The water peak near 3200 cm^{-1} has been assigned to strongly hydrogen bonded water.[12,19,20] The presence of an SFG feature centered near 3150 cm^{-1}, which is shifted from the 3200 cm^{-1} peak to a lower wavenumber, suggests the formation of strong hydrogen bonded water at the PMSQ/water interface. Combining FTIR and SFG results above (Figure 5.6 and Figure 6.7), we can conclude that water tends to form strong

hydrogen bonds with PMSQ (~3150 cm^{-1}) at the PMSQ/water interface (evidenced by the SFG result). Whereas water molecules are more flexible in the bulk, that is, they prefer to stay in the bulk by forming weak hydrogen bonds (evidenced by FTIR result). Moreover, the intensity of the SFG water peak did not change much while contacting with water for a longer time, showing that formation of strongly hydrogen bonded water at the PMSQ surface is quite fast.

According to the previous studies, the chemisorbed water components are more difficult to be removed from the low-k network than physisorbed water.[9,12] However, detection of such water components at the pore inner surfaces is quite challenging because the amount of these water components is small. Here, we employed SFG measurements with high surface sensitivity to obtain direct evidence of chemisorption as water molecules reached the PMSQ surface. It is suggested that when water molecules reach the pore inner surfaces of porous low-k materials, they tend to form strong hydrogen bonds with the low-k material at the pore inner surfaces. Since these chemisorbed water components have been closely related to the TDDB failure mechanism of low-k materials,[9] we believe that the chemisorbed water molecules at the pore inner surfaces are mainly responsible for these negative effects on low-k material properties than the water components in the bulk (e.g., those inside the pores but not interacting with the pore surfaces).

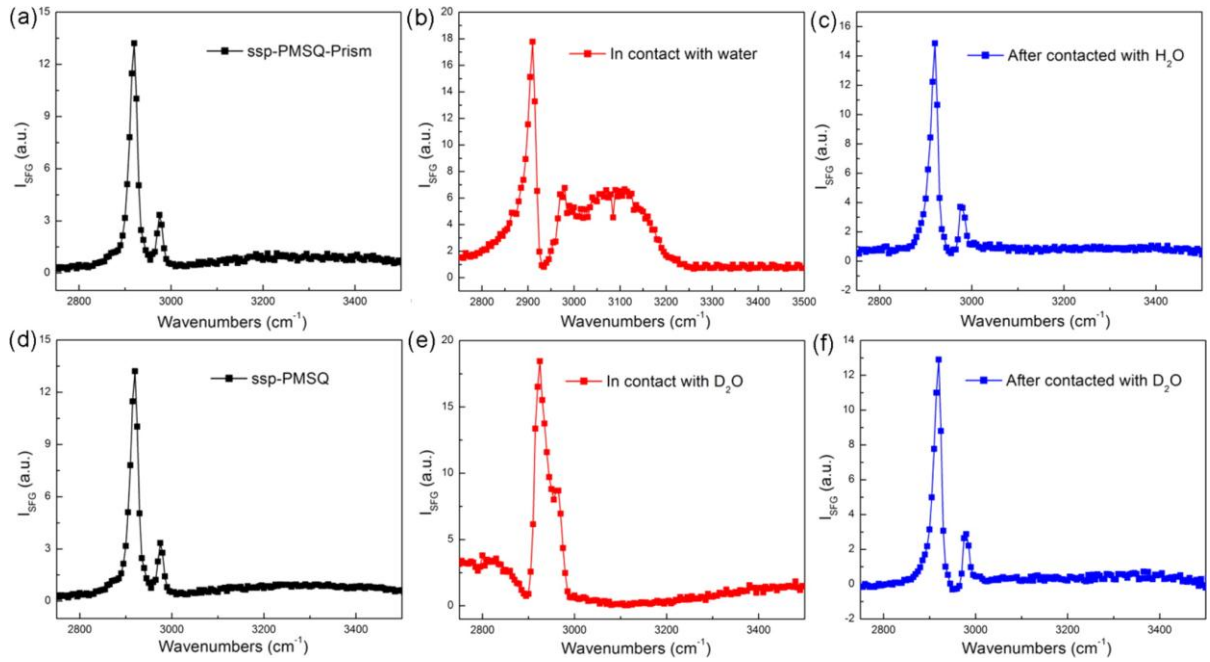

Figure 6.7. ssp SFG spectra collected from the PMSQ surface before, during, and after contacting with H_2O (a–c) and D_2O (d–f).

SFG signals in the C–H stretching frequency region were enhanced during contact with water. Considering the Fresnel coefficient change from the polymer/air surface to the polymer/water interface,[42] the normalized peak intensity of the methyl peaks (Figure 6.7b) should be higher. Compared to the peak in air (Figure 6.7a), the intensity of the symmetric Si-CH_3 stretch is slightly higher compared to the peak in air, indicating that Si-CH_3 groups were slightly more ordered at the PMSQ/water interface when water molecules formed strong hydrogen bonds with PMSQ. We speculate that the ordering of Si-CH_3 groups at the surface during contact with water is likely related closely to the formation of strong hydrogen bonds between water and PMSQ at the PMSQ surface. Therefore, the intermediate intensity of the water peak in Figure 6.5b should be attributed to the small amounts of ordered water components at the PMSQ surface rather than less ordering of water molecules. Additionally, after removing the PMSQ film from water, the surface of PMSQ thin film was found to dry immediately and the

molecular structure was also observed to recover to its original structure before water contact (Figure 6.7c). That is, no water peaks were observed at surface by SFG after drying, which could be ascribed to no ordered water components or no water molecules left at the surface. Considering the difficulty of breaking these strongly hydrogen bonds, it is most likely that ordered water structures formed at PMSQ surface under the water environment become disordered in air.

To avoid the influence of the water peak at 2900–3000 cm^{-1} in the C–H stretching frequency region, D_2O was also utilized to clarify the molecular structure changes of the PMSQ surface in contact with water. Parts e and f of Figure 6.7 show the ssp SFG spectra collected from the PMSQ/D_2O interface and the PMSQ/air surface after removal of D_2O, respectively. Similar to the observation when PMSQ was in contact with H_2O, stronger Si-CH_3 peaks around 2915 and 2970 cm^{-1} were detected during contacting with D_2O. The stronger intensities here suggest that Si-CH_3 groups become more ordered at the PMSQ surface during water contact. After removing D_2O, the SFG spectrum closely resembled the original one shown in Figure 6.7a. This implies that surface molecular structures were recovered after removing water. Therefore, the molecular structure of PMSQ at pore inner surfaces will not be permanently influenced by water for porous low-k materials.

SFG spectra were also collected from a cured PMSQ thin film before, during, and after contact with water and D_2O (Figure 6.8).

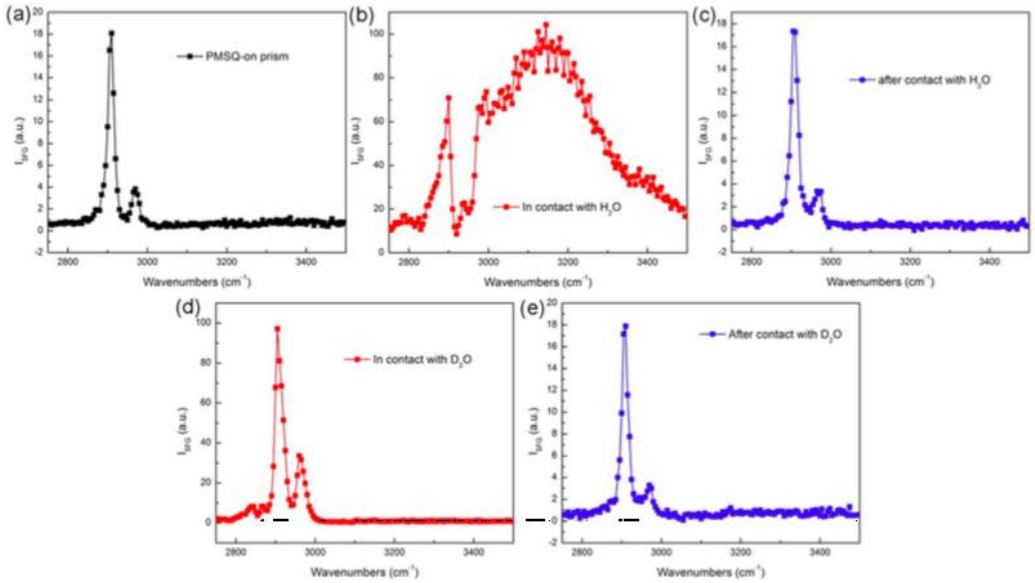

Figure 6.8. SFG ssp spectra collected from surface of cured PMSQ thin film before contact (a), during contact with H_2O (b) and D_2O (d) and after contact with H_2O (c) and D_2O (e).

The surface structures were found to be almost unchanged after curing at 400 ℃ for 1 h. However, during contact with water, water signals at the cured PMSQ surface were much stronger than those in spectra collected from the uncured film. A strong peak around 3150 cm^{-1} (chemisorbed water component) and a relatively weak peak near 3400 cm^{-1} (physisorbed water component) were detected in the SFG spectrum (Figure 6.8). According to previous studies, low-k material may be slightly more hydrophilic after curing because a portion of the C–H components might be removed during the curing process.[4] We believe the increased hydrophilicity after curing should be responsible for the enhancement of water signals at the cured PMSQ surface. Moreover, the D_2O experiments shown in Figure 6.8d and e demonstrate

that Si-CH_3 signals also become much higher during contact with D_2O. This trend is very consistent with the uncured results. Additionally, these results also support our hypothesis that the ordering of Si-CH_3 groups should be driven by the formation of strongly hydrogen bonded water at the PMSQ surface. These SFG observations on cured samples also demonstrate that the method developed here is general and can be applied to investigate the water behavior at low-k material interfaces after various treatments.

Subsequently, the water uptake process through PMSQ bulk or PMSQ/substrate buried interface was selectively investigated in situ by SFG measurements. Two experiments were designed to directly trace the preferential pathway of water uptake via combined FTIR and SFG measurements. Drop-cast PMSQ thick films were utilized here to block SFG signals from the PMSQ surface. The experimental setups for these two experiments are schematically illustrated in Figure 6.1e and f. At first, a water drop was placed in contact with the surface of the PMSQ thick film. Subsequently, in situ SFG and ATR-FTIR measurements were performed on and near the PMSQ/SiO_2 buried interface, respectively, to detect the changes of water signals. If water signals were found to gradually increase, the water uptake primarily occurred through the PMSQ bulk; we name this method as "method 1" (Figure 6.1e). As a contrast, as a water drop was placed in contact with the edge of the PMSQ thick film, SFG and ATR-FTIR measurements were conducted at the center of the thick film, so increased water signals would indicate water uptake along the buried interface (Figure 6.1f). We name this method as "method 2". Since the film thickness was around 5.0 μm, while the distance from film edge to film center was around 0.5 cm, it should be possible to trace the preferential water uptake pathway by comparing the water signals in ATR-FTIR and SFG spectra using "method 1" and "method 2".

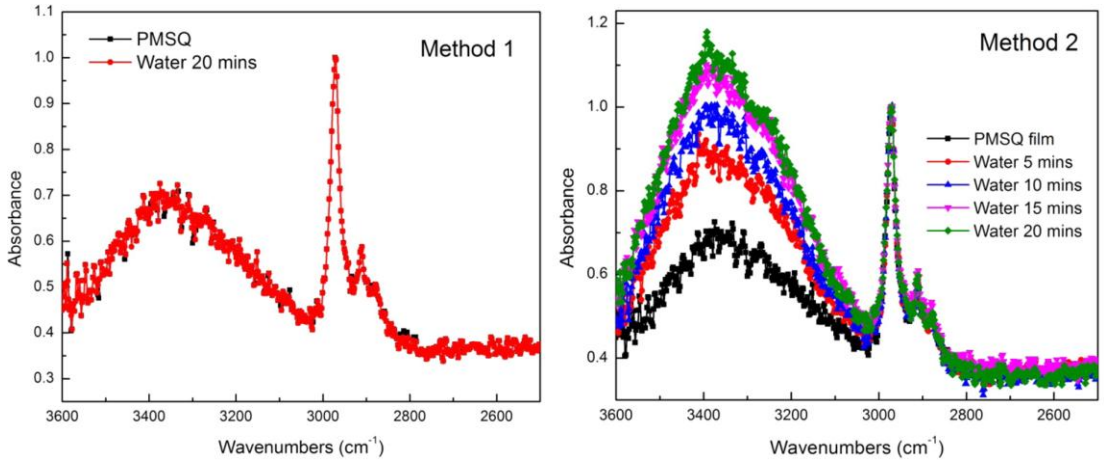

Figure 6.9. Series of ATR-FTIR spectra collected from PMSQ in contact with H_2O as a function of time (a) using "method 1" shown in Figure 1e and (b) "method 2" shown in Figure 1f.

In-situ ATR-FTIR measurements were implemented on PMSQ thick films drop-casted on Si prisms using "method 1" and "method 2", separately. Similar to the FTIR spectrum of PMSQ film shown in Figure 6.6, the original spectrum of PMSQ thick film detected by ATR-FTIR (Figure 6.9a) was dominated by a C–H stretching peak around 2970 cm^{-1} as well as a broad water O–H stretching peak centered at ~3390 cm^{-1}. It is noticeable that the water peak center is slightly blue-shifted, which could be due to a higher contribution of the chemisorbed water component near ~3200 cm^{-1} to the broad water peak at the buried interface. The ATR-FTIR penetration depth was approximately 500 nm, so the water peak characterizes molecular structure 500 nm near the PMSQ buried interface. However, following "method 1", no detectable increase of water signals were found in ATR-FTIR spectra even after contact with water for 20 min (Figure 6.9a), indicating that water uptake through the hydrophobic PMSQ film is relatively slow. As a contrast, using "method 2", the water peak around 3390 cm^{-1} was observed to gradually increase after water contact. The rate became slower as time increased, which may be

due to gradual saturation of water in the bulk near the buried interface. The corresponding ATR-FTIR spectra of PMSQ thick films were collected during contact with water after 5, 10, 15, and 20 min (shown in Figure 6.9b). The water signals were found to be unchanged after 20 min, which again may be due to the saturated water near the buried interface. These results indicate that water molecules transport through PMSQ/solid interface faster than through the bulk. These results are consistent with previous reports which utilized isotope-label tracer and SIMS.[8] It is notable that the small shoulder near 3200 cm^{-1} was more evident in the ATR-FTIR spectrum after contact with water for 20 min, which might be attributed to the formation of strongly hydrogen bonded water near the PMSQ/SiO_2 buried interface.

In order to further elucidate water behavior at the PMSQ/SiO_2 buried interface and correlate the molecular structure to the degradation of low-k properties, corresponding SFG measurements using "method 1" and "method 2" were conducted on the drop-cast PMSQ thick films on fused silica prism. First, we can see from Figure 5.10a that the ssp SFG spectrum collected from the PMSQ/SiO_2 buried interface was dominated by two Si-CH_3 peaks around 2915 and 2970 cm^{-1}, respectively. However, the asymmetric stretching peak (2970 cm^{-1}) was stronger than the symmetric stretching peak (2915 cm^{-1}). This result indicates that although the PMSQ/SiO_2 buried interface is also dominated by Si-CH_3 groups, the orientation of Si-CH_3 groups at buried interface is different from that of surface.[46] The strong asymmetric peak suggests that Si-CH_3 groups were oriented more parallel to the substrate at the buried interface, whereas at the surface the groups tended to orient more perpendicular to the substrate. In addition, no water peaks were detected at the buried interface, indicating that no water molecules were present at the buried interface or that the water molecules were randomly oriented. After contact with water, using "method 1", no water signals were detected by SFG from the

PMSQ/SiO_2 buried interface after contact with water after 20 min, which suggests that no ordered water was present at the buried interface. This is consistent with the corresponding ATR-FTIR results shown in Figure 6.9a. However, when using "method 2", two water peaks around 3200 and 3400 cm^{-1} appeared in SFG spectrum collected from the PMSQ/SiO_2 buried interface soon after contact with water. Different from the PMSQ surface, both chemisorbed (strongly hydrogen bonded) and physisorbed (weakly hydrogen bonded) water components formed at the PMSQ/SiO_2 buried interface. The possible mechanisms of various water behaviors at PMSQ surface and the PMSQ/SiO_2 buried interface will be discussed later. Here, we can see in Figure 6.10a that as the water contact time increased, these two water peaks continued to increase slowly. In particular, the intensity of 3200 cm^{-1} peak increased more quickly than that of 3400 cm^{-1} peak. Time-dependent SFG observations were also utilized to compare the kinetics of formation of these two water peaks at the buried interface during the water uptake process. The corresponding time-dependent SFG spectra are shown in Figure 6.11.

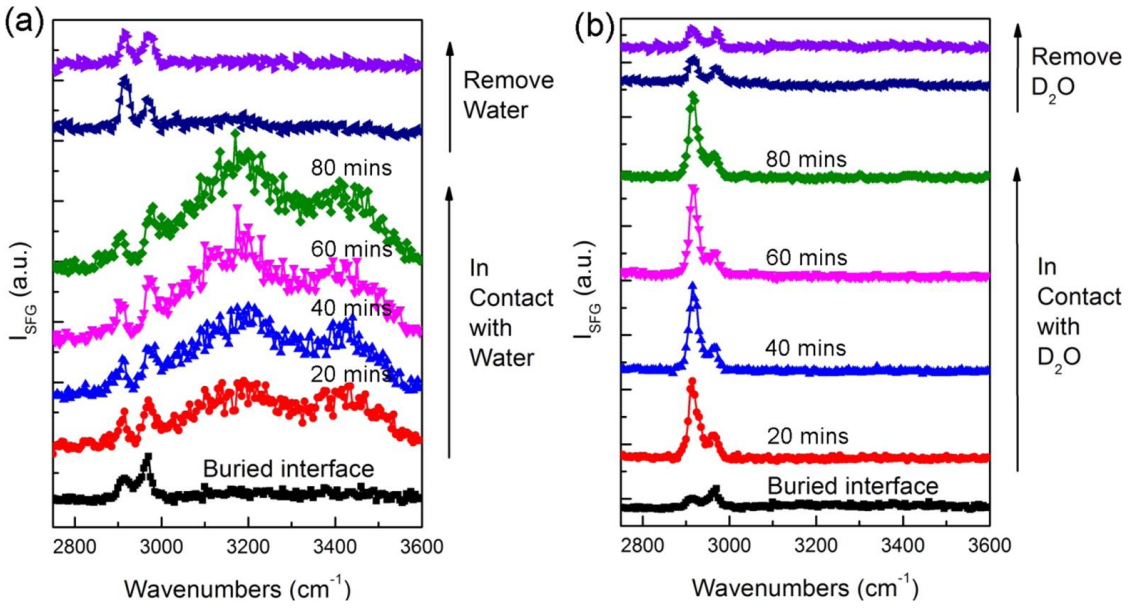

Figure 6.10. Series of ssp SFG spectra collected from the PMSQ/SiO_2 buried interface before and during contact with H_2O (a) and D_2O (b) as a function of time and then after water removal using "method 2" (Figure 1f).

According to in situ ATR-FTIR observation of adsorbed water molecules shown above, water in the bulk near the buried interface would be saturated after 20 min. Since every SFG spectrum shown here took about 20 min to collect, it is interesting to see that water signals, especially the water component located at ~3200 cm^{-1} at the buried interface, still gradually increased even after contact with water for ~80 min. It is surprising to see that both of the water peaks quickly appeared after contact with water, indicating that water uptake through the buried interface is much quicker than through the PMSQ bulk. Different from the PMSQ surface in contact with water, the intensities of two peaks around 3200 and 3400 cm^{-1} were both found to gradually increase and the rates of increase could both be fitted linearly after water arrived at the interface. This means that although relatively quick water uptake occurred through the PMSQ/SiO_2 buried interface, and the saturation of water molecules in the bulk near the buried interface occurred after 20 min, the formation of ordered water structures, especially strongly hydrogen bonded water, is a gradual process that continues to occur even after water saturation in the bulk near the buried interface. We can also see from Figure 6.10a that the Si-CH_3 signals at the buried interface were also influenced by water, so D_2O experiments were performed to clarify the impact of water on the orientation of Si-CH_3 groups at the buried interface, which will be discussed in more details later.

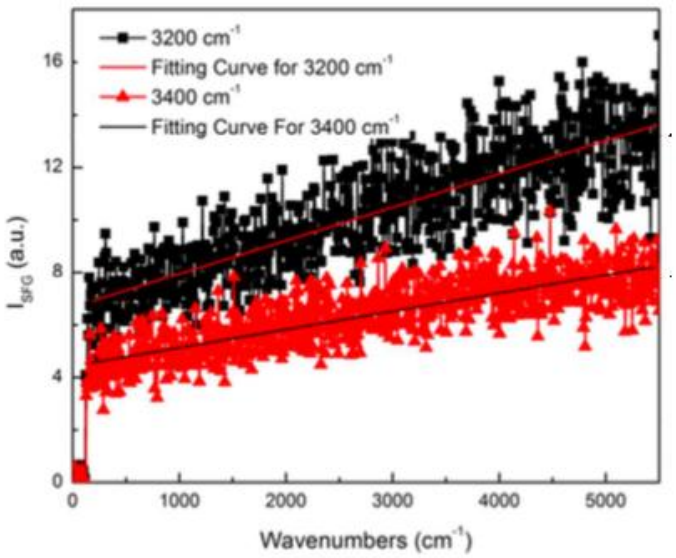

Figure 6.11. Time-dependent SFG signals and the fitting lines of chemisorbed water components at 3200 cm^{-1} and physisorbed water at 3400 cm^{-1} observed at the buried PMSQ/silica interface. The 3200 cm^{-1}peak increased faster as time increased while a slower increment was observed for the 3400 cm^{-1} peak.

Here, in addition to in situ observation of the water uptake process through the buried interface, Figure 6.10a also provides the ssp SFG spectra collected from the PMSQ/SiO_2 buried interface after water removal. Almost no water signals were detected immediately after removal of water from the PMSQ film surface; only a very small peak around 3200 cm^{-1} was observed in the SFG spectra. This peak was undetectable after collecting the second SFG spectrum. Based on our previous discussion, we believe that the disappearance of water peaks in the SFG spectrum after removing water is due to disordering of these water components rather than the absence of water at the PMSQ interface in air after removing the sample from water. In addition, the ratio of two Si-CH_3 peaks was also affected by removal of water from the buried interface (Figure 6.10a). The symmetric stretching peak became dominant at the buried interface after water removal then the intensities of the symmetric and asymmetric stretching peaks were very similar. These results

indicate that although no ordered water components were detected from the buried interface after water removal, the orientation of Si-CH_3 groups was permanently changed due to the formation of strongly hydrogen bonded water at the buried interface. This is very different from the PMSQ/air surface, which recovered when exposed to air again. According to previous studies,[9,12] in addition to the chemisorbed (β) and physorbed (α) water molecules, there might be two other water components present in low-k materials, γ1 (hydrogen-bonded to silanols) and γ2 (hydrogen-bonded to isolated silanols). Annealing temperature as high as 700 ℃ has been recommended to remove these two water components. We therefore did not study these two types of water by high temperature annealing in this research and such high temperatures are not compatible with semiconductor interconnects. The permanent changes of the orientation of Si-CH_3 groups after water uptake at the buried interface might be due to the less flexibility of the functional groups at the buried interface than that at the PMSQ surface.

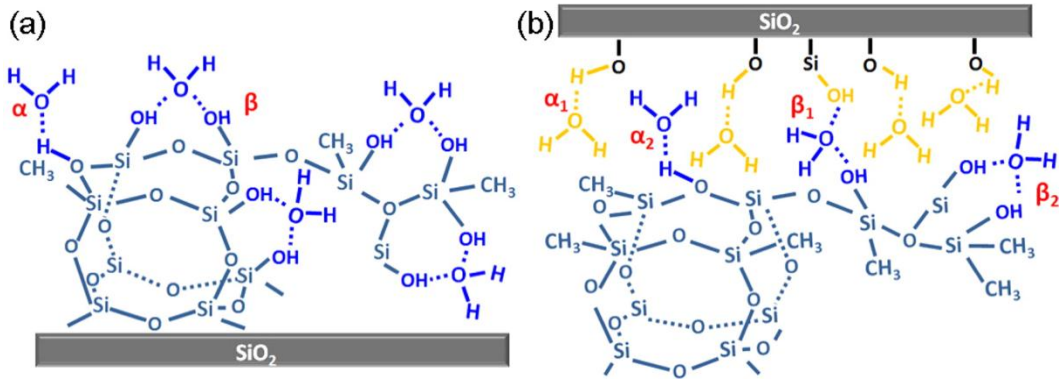

Figure 6.12. Schematic illustration of water structures at the PMSQ surface (a) and the buried interface (b) after water uptake.

As mentioned before, D_2O experiments were also performed to clarify the molecular structural changes in the C–H stretching frequency region at the buried interface during

contacting with water (Figure 6.10b). Similar to the H_2O case, strong Si-CH_3 signals were detected from the buried interface when the PMSQ thick film was in contact with D_2O. The enhanced peak intensities may be due to higher ordering or more coverage of reorientated Si-CH_3 groups at the PMSQ/SiO_2 buried interface. The symmetric Si-CH_3 peak (2915 cm^{-1}) was more pronounced than the asymmetric peak (2970 cm^{-1}), indicating that the Si-CH_3 groups at the buried interface tilted more toward the surface normal after water uptake. Just as we discussed before, we believe that the number of interfacial Si-CH_3 groups of PMSQ would not be changed due to water uptake, so the Si-CH_3 groups became more ordered as water molecules reached the buried interface and formed strong hydrogen bonds at the buried interface. Moreover, as the contact time increased, the peak intensities of symmetric and asymmetric Si-CH_3 peaks kept increasing with a relatively constant peak ratio. After removal of the D_2O, the SFG spectra collected from the PMSQ/SiO_2 buried interface were very similar to the H_2O results shown in Figure 6.10a.

Based on our in situ SFG and ATR-FTIR observations above, the possible water adsorption mechanisms at the PMSQ/water interface and PMSQ/SiO_2 buried interface are schematically illustrated in Figure 6.12. At the PMSQ/water surface, which resembles the inner surfaces of pores of low-k material, water tends to form strong hydrogen bonds (β) with PMSQ although there might still be some weakly bonded water elements (α) (shown in Figure 6.12a). At the PMSQ/SiO_2 buried interface (Figure 6.12b), water may also form hydrogen bonds with the SiO_2 substrate (α1 and β1 in Figure 6.12b).[47,48] Considering the dominant β water observed in SFG spectrum collected from PMSQ/water surface, we believe the ordered water components attached to PMSQ at the buried interface should still be dominated by chemisorbed water (α2 in Figure 6.12b) although both α2 and β2 should be present. It is suggested that these chemisorbed

water components present at pore inner surfaces and at the buried interface are more responsible for the TDDB failure in low-k dielectric reliability tests than the physisorbed water in the bulk.

6.4 Conclusion

In this study, a simple method was proposed and demonstrated to probe water molecular structures in situ at the PMSQ/water and PMSQ/substrate buried interfaces by combining SFG and FTIR measurements. First, selective in situ SFG observation of water uptake process provides direct evidence that water diffuses predominantly along the PMSQ/solid buried interface rather than through the porous low-k film and also that water uptake through the hydrophobic dense low-k film was slow. Moreover, in situ SFG measurements were conducted on the PMSQ/water interface to simulate water behavior at the pore inner surfaces for porous low-k materials. Most of the water molecules were found to be strongly bonded to the PMSQ surface. However, FTIR results showed that most of the water molecules were found to be weakly bonded to the bulk PMSQ. Meanwhile, Si-CH_3 groups at the PMSQ surface were observed to form ordered structures when water molecules were present, which may be driven by the formation of highly ordered water components at the surface. However, both strongly hydrogen bonded and weakly hydrogen bonded water were observed at the PMSQ/SiO_2 buried interface. Formation of both of these water components is influenced by the nature of the substrate. More importantly, the orientation of the Si-CH_3 groups at the buried interface was permanently changed due to water contact which might be due to the lower flexibility of Si-CH_3 groups at the buried interface. We also provided direct evidence that water molecules tend to form chemisorbed water components (strongly hydrogen bonded water) at two kinds of interfaces, that is, pore inner surfaces and low-k/solid interface of porous low-k materials, while weakly hydrogen bonded water components were detected in the bulk.

6.5 Impact

In this chapter, general methodology was developed to characterize water molecular structures at low-k dielectric surfaces and buried interfaces. This methodology can be applied to study water structures on a variety of polymer surfaces and buried interfaces. Better understanding of how polymer surfaces mediate interfacial water bonding is important in the design of surfaces that are engineered to repel or attract water in applications such as anti-icing coatings or nets for capturing water from fog.

The work in this chapter is also important for the design and development of new low-k dielectric materials and in the modification of existing low-k materials. We presented evidence that suggests that water at the low-k surfaces, rather than the bulk, should be more responsible for TBBD failure and chemisorbed water related degradation of the interconnection layer. This finding suggests that the structure of low-k pore surfaces and film surfaces should be modified to prevent chemisorbed water. Such a structure-property relationship could be developed using methodology developed in this chapter by correlating different low-k surface structures to the presence or absence of interfacial chemisorbed water detected in SFG spectra and to dielectric breakdown studies.

6.6 References

(1) Grill, A. Porous Psicoh Ultralow-K Dielectrics for Chip Interconnects Prepared by PECVD. *Annu. Rev. Mater. Res.* **2009**, *39*, 49−69.

(2) Shamiryan, D.; Abell, T.; Iacopi, F.; Maex, K. Low-k Dielectric Materials. *Mater. Today* **2004**, *7*, 34−39.

(3) Maex, K.; Baklanov, M.; Shamiryan, D.; Brongersma, S.; Yanovitskaya, Z. Low Dielectric Constant Materials for Micro-electronics. *J. Appl. Phys.* **2003**, *93*, 8793−8841.

(4) Grill, A. Plasma Enhanced Chemical Vapor Deposited Sicoh Dielectrics: From Low-K to Extreme Low-K Interconnect Materials. *J. Appl. Phys.* **2003**, *93*, 1785−1790.

(5) Li, Z.; Johnson, M. C.; Sun, M.; Ryan, E. T.; Earl, D. J.; Maichen, W.; Martin, J. I.; Li, S.; Lew, C. M.; Wang, J. Mechanical and Dielectric Properties of Pure-Silica-Zeolite Low-k Materials. *Angew. Chem., Int. Ed.* **2006**, *45*, 6329−6332.

(6) Bao, J.; Shi, H.; Liu, J.; Huang, H.; Ho, P.; Goodner, M.; Moinpour, M.; Kloster, G. Mechanistic Study of Plasma Damage of Low K Dielectric Surfaces. *J. Vac. Sci. Technol. B* **2008**, *26*, 219−226.

(7) Cheng, Y.-Y.; Kan, J. Y.; Lin, I. Adhesion Studies of Low-k Silsesquioxane. *Thin Solid Films* **2004**, *462*, 297−301.

(8) Li, H.; Tsui, T. Y.; Vlassak, J. J. Water Diffusion and Fracture Behavior in Nanoporous Low-K Dielectric Film Stacks. *J. Appl. Phys.* **2009**, *106*, 033503.

(9) Li, Y.; Ciofi, I.; Carbonell, L.; Heylen, N.; Van Aelst, J.; Baklanov, M. R.; Groeseneken, G.; Maex, K.; Tőkei, Z. Influence of Absorbed Water Components on SIOCH Low-K Reliability. *J. Appl. Phys.* **2008**, *104*, 034113.

(10) Michelon, J.; Hoofman, R. J. Moisture Influence on Porous Low-k Reliability. *IEEE Trans. Device Mater. Reliab.* **2006**, *6*, 169−174.

(11) Guyer, E. P.; Gantz, J.; Dauskardt, R. H. Aqueous Solution Diffusion in Hydrophobic Nanoporous Thin-Film Glasses. *J. Mater. Res.* **2007**, *22*, 710−718.

(12) Proost, J.; Baklanov, M.; Maex, K.; Delaey, L. Compensation Effect during Water Desorption from Siloxane-Based Spin-on Dielectric Thin Films. *J. Vac. Sci. Technol. B* **2000**, *18*, 303−306.

(13) Cheng, Y.-L.; Leon, K.-W.; Huang, J.-F.; Chang, W.-Y.; Chang, Y.-M.; Leu, J. Effect of Moisture on Electrical Properties and Reliability of Low Dielectric Constant Materials. *Microelectron. Eng.* **2014**, *114*, 12−16.

(14) Lam, J. C.; Huang, M. Y.; Tan, H.; Mo, Z.; Mai, Z.; Wong, C. P.; Sun, H.; Shen, Z. Vibrational Spectroscopy of Low-k/Ultra-low-k Dielectric Materials on Patterned Wafers. *J. Vac. Sci. Technol. A* **2011**, *29*, 051513.

(15) Du, Q.; Freysz, E.; Shen, Y. R. Vibrational Spectra of Water Molecules at Quartz/Water Interfaces. *Phys. Rev. Lett.* **1994**, *72*, 238− 241.

(16) Raghavan, K.; Foster, K.; Berkowitz, M. Comparison of The Structure and Dynamics of Water at The Pt (111) and Pt (100) Interfaces: Molecular Dynamics Study. *Chem. Phys. Lett.* **1991**, *177*, 426−432.

(17) Rose, D. A.; Benjamin, I. Adsorption of Na^+ and Cl^- at the Charged Water−Platinum Interface. *J. Chem. Phys.* **1993**, *98*, 2283− 2290.

(18) Lenk, R.; Bonzon, M.; Greppin, H. Dynamically Oriented Biological Water as Studied by NMR. *Chem. Phys. Lett.* **1980**, *76*, 175− 177.

(19) Nanjundiah, K.; Hsu, P. Y.; Dhinojwala, A. Understanding Rubber Friction in the Presence of Water Using Sum-Frequency Generation Spectroscopy. *J. Chem. Phys.* **2009**, *130*, 024702.

(20) Noguchi, H.; Hiroshi, M.; Tominaga, T.; Gong, J. P.; Osada, Y.; Uosaki, K. Interfacial Water Structure at Polymer Gel/Quartz Interfaces Investigated by Sum Frequency Generation Spectroscopy. *Phys. Chem. Chem. Phys.* **2008**, *10*, 4987−4993.

(21) Du, Q.; Freysz, E.; Shen, Y. R. Surface Vibrational Spectroscopic Studies of Hydrogen Bonding and Hydrophobicity. *Science* **1994**, *264*, 826−828.

(22) Baldelli, S.; Schnitzer, C.; Shultz, M. J.; Campbell, D. Sum Frequency Generation Investigation of Glycerol/Water Surfaces. *J. Phys. Chem. B* **1997**, *101*, 4607−4612.

(23) Che, M.-L.; Teng, J.-Y.; Lai, P.-C.; Leu, J. Moisture Uptake and Dielectric Property of Methylsilsesquioxane/High-Temperature Porogen Hybrids and Porous Low-K Films. *J. Mater. Res.* **2011**, *26*, 2987− 2995.

(24) Li, Q.; Hua, R.; Chou, K. C. Electronic and Conformational Properties of the Conjugated Polymer MEH-PPV at a Buried Film/ Solid Interface Investigated by Two-Dimensional IR-Visible Sum Frequency Generation. *J. Phys. Chem. B* **2008**, *112*, 2315−2318.

(25) Gautam, K. S.; Dhinojwala, A. Molecular Structure of Hydrophobic Alkyl Side Chains at Comb Polymer−Air Interface. *Macromolecules* **2001**, *34*, 1137−1139.

(26) Su, X.; Cremer, P. S.; Shen, Y. R.; Somorjai, G. A. Pressure Dependence (10^{-10}−700 Torr) of the Vibrational Spectra of Adsorbed CO on Pt (111) Studied by Sum Frequency Generation. *Phys. Rev. Lett.* **1996**, *77*, 3858−3860.

(27) Chen, Z. Understanding Surfaces and Buried Interfaces of Polymer Materials at The Molecular Level Using Sum Frequency Generation Vibrational Spectroscopy. *Polym. Int.* **2007**, *56*, 577−587.

(28) Chen, Z. Investigating Buried Polymer Interfaces Using Sum Frequency Generation Vibrational Spectroscopy. *Prog. Polym. Sci.* **2010**, *35*, 1376−1402.

(29) Chen, Z.; Shen, Y.; Somorjai, G. A. Studies of Polymer Surfaces by Sum Frequency Generation Vibrational Spectroscopy. *Annu. Rev. Phys. Chem.* **2002**, *53*, 437−465.

(30) Zhang, X.; Chen, Z. Observing Phthalate Leaching from Plasticized Polymer Films at the Molecular Level. *Langmuir* **2014**, *30*, 4933−4944.

(31) Zhang, C.; Shephard, N. E.; Rhodes, S. M.; Chen, Z. Headgroup Effect on Silane Structures at Buried Polymer/Silane and Polymer/ Polymer interfaces and Their Relations to Adhesion. *Langmuir* **2012**, *28*, 6052−6059.

(32) Zhang, X.; Zhang, C.; Hankett, J. M.; Chen, Z. Molecular Surface Structural Changes of Plasticized PVC Materials after Plasma Treatment. *Langmuir* **2013**, *29*, 4008−4018.

(33) Zhang, C.; Hankett, J.; Chen, Z. Molecular Level Understanding of Adhesion Mechanisms at the Epoxy/Polymer Interfaces. *ACS Appl. Mater. Interfaces* **2012**, *4*, 3730−3737.

(34) Zhang, C.; Myers, J. N.; Chen, Z. Elucidation of Molecular Structures at Buried Polymer Interfaces and Biological Interfaces Using Sum Frequency Generation Vibrational Spectroscopy. *Soft Matter* **2013**, *9*, 4738−4761.

(35) Myers, J. N.; Zhang, C.; Lee, K.-W.; Williamson, J. M.; Chen, Z. Hygrothermal Aging Effects on Buried Molecular Structures at Epoxy Interfaces. *Langmuir* **2014**, *30*, 165−171.

(36) Trudeau, T. G.; Jena, K. C.; Hore, D. K. Water Structure at Solid Surfaces of Varying Hydrophobicity. *J. Phys. Chem. C* **2009**, *113*, 20002−20008.

(37) Perry, A.; Neipert, C.; Space, B.; Moore, P. B. Theoretical Modeling of Interface Specific Vibrational Spectroscopy: Methods and Applications to Aqueous Interfaces. *Chem. Rev.* **2006**, *106*, 1234−1258.

(38) Eisenthal, K. Liquid Interfaces Probed by Second-Harmonic and Sum-Frequency Spectroscopy. *Chem. Rev.* **1996**, *96*, 1343−1360.

(39) Messmer, M. C.; Conboy, J. C.; Richmond, G. L. Observation of Molecular Ordering at the Liquid−Liquid Interface by Resonant Sum Frequency Generation. *J. Am. Chem. Soc.* **1995**, *117*, 8039−8040.

(40) Wang, J.; Woodcock, S. E.; Buck, S. M.; Chen, C.; Chen, Z. Different Surface-Restructuring Behaviors of Poly(methacrylate)s Detected by SFG in Water. *J. Am. Chem. Soc.* **2001**, *123*, 9470−9471.

(41) Ye, H.; Gu, Z.; Gracias, D. H. Kinetics of Ultraviolet and Plasma Surface Modification of Poly(dimethylsiloxane) Probed by Sum Frequency Vibrational Spectroscopy. *Langmuir* **2006**, *22*, 1863−1868.

(42) Hankett, J. M.; Lu, X. L.; Liu, Y. W.; Seeley, E.; Chen, Z. Interfacial Molecular Restructuring of Plasticized Polymers in Water. *Phys. Chem. Chem. Phys.* **2014**, *16*, 20097−20106.

(43) York, R. L.; Li, Y.; Holinga, G. J.; Somorjai, G. A. Sum Frequency Generation Vibrational Spectra: The Influence of Experimental Geometry for An Absorptive Medium or Media. *J. Phys. Chem. A* **2009**, *113*, 2768−2774.

(44) Proost, J.; Kondoh, E.; Vereecke, G.; Heyns, M.; Maex, K. Critical Role of Degassing for Hot Aluminum Filling. *J. Vac. Sci. Technol. B* **1998**, *16*, 2091−2098.

(45) Liu, M.; Wu, P.; Ding, Y.; Chen, G.; Li, S. Two-Dimensional (2D) ATR-FTIR Spectroscopic Study on Water Diffusion in Cured Epoxy Resins. *Macromolecules* **2002**, *35*, 5500−5507.

(46) Zhang, C.; Chen, Z. Probing Molecular Structures of Poly(dimethylsiloxane) at Buried Interfaces in situ. *J. Phys. Chem. C* **2013**, *117*, 3903−3914.

(47) Shen, Y. R.; Ostroverkhov, V. Sum-Frequency Vibrational Spectroscopy on Water Interfaces: Polar Orientation of Water Molecules at Interfaces. *Chem. Rev.* **2006**, *106*, 1140−1154.

(48) Ostroverkhov, V.; Waychunas, G. A.; Shen, Y. Vibrational Spectra of Water at Water/A-Quartz (0001) Interface. *Chem. Phys. Lett.* **2004**, *386*, 144−148.

CHAPTER 7

NONDESTRUCTIVE IN SITU CHARACTERIZATION OF MOLECULAR STRUCTURES AT THE SURFACE AND BURIED INTERFACE OF SILICON-SUPPORTED LOW-K DIELECTRIC FILMS

7.1 Introduction

Porous organosilicate (pSiCOH) materials are widely used as the low-k interlayer dielectric (ILD) materials for copper interconnect structures in advanced integrated circuits.[1-3] Low-k dielectrics with high volume percent porosity, however, typically have low Young's modulus and fracture toughness, which can lead to thin film cracking and delamination during chemical mechanical polishing and packaging.[4-7] Moreover, plasma treatment and wet chemical treatment during back-end of line processing have been found to degrade the dielectric properties of pSiCOH materials and the interconnect leakage current.[8-11]

As copper/low-k interconnects continue to shrink in dimension, the properties of the low-k dielectric materials will increasingly be determined by interfacial properties. Furthermore, in porous low-k materials, the inner pores constitute a polymer/air interface, which may have a surface area that exceeds the surface area of the outer interfaces. Interfacial properties are largely determined by molecular structures at interfaces.[12,13] Therefore, as the ILD thickness reaches ~100 nm or less for 20 nm technologies,[5] structure–property relationships of ILD materials will be increasingly determined by interfacial molecular structures. In particular, the effects of plasma treatment, wet chemical treatment, chemical mechanical polishing, and pore sealing on ILD properties have been related to the structure of ILD surfaces and inner pores.[11,14-16] Furthermore,

the ILD surface molecular structure has been found to influence the atomic layer deposition nucleation process.[17,18] The structure of buried low-k interfaces, for example, low-k/etch stop and low-k/barrier interfaces, has also been related to interfacial properties such as adhesion strength, moisture transport, and charge transport.[19-21] Structure–property relationships at ILD surfaces and buried interfaces, however, are not well understood. Therefore, nondestructive characterization of the molecular structure at low-k surfaces and buried interfaces is necessary for the development of understanding on interfacial structure–function relationships.

The structures of low-k dielectric materials can be characterized in terms of volume percent porosity, average pore size, pore size distribution, pore connectivity, elemental composition, and the molecular structure within the film.[3] Descriptions of analytical techniques capable of characterizing the porosity and elemental composition of low-k dielectrics can be found elsewhere.[2] Two of the most common techniques used to characterize the molecular structures of low-k dielectrics are Fourier transform infrared spectroscopy (FTIR) and nuclear magnetic resonance spectroscopy (NMR). FTIR has been utilized to identify functional groups within low-k dielectric materials and to investigate the molecular structure of disrupted silica networks.[22,23] For example, the ratio of absorbances of two asymmetric Si–O–Si stretch vibrational modes near 1050 and 1150 cm^{-1} can be used to estimate the ratio of cage-like to open network structures in poly(silsesquioxane) thin films.[24] Complementary structural information can be obtained with ^{29}Si solid-state NMR by identification of different chemical bonding environments of Si within low-k films in terms of organosilicate structures.[25-27] For example, comparison of the peak areas of different organosilicate structures has been used to estimate the relative fractions of the structures within low-k dielectric films.[3] Although FTIR and NMR have been used to characterize the bulk molecular structure of low-k dielectrics, the molecular

structure of low-k dielectric surfaces and buried interfaces has not been thoroughly characterized due to a lack of nondestructive, interface sensitive analytical techniques.

Previous work reported in the previous chapter has shown that SFG and attenuated total reflectance FTIR (ATR-FTIR) can be used to characterize the molecular structure of low-k dielectric surfaces and buried interfaces.[28] The methodology developed was utilized to elucidate the molecular structure of water at buried low-k/silica and low-k/air interfaces. The low-k/air interface was used as a model for inner pore surfaces within ILD materials, which enabled a direct comparison between water behavior at the surface and at the buried interface. However, the method required that the ILD material was deposited on a fused silica window or prism optical substrate.

Modern low-k ILD materials are commonly fabricated by plasma-enhanced chemical vapor deposition (PE-CVD).[1] PE-CVD methods for fabricating low-k ILD materials are commonly optimized for deposition on silicon substrates.[3,29] Furthermore, many developed microfabrication and thin film characterization methods (e.g., nanoindentation, X-ray diffraction, ellipsometry, Raman spectroscopy, leakage current) are extensively used with silicon-supported thin films. Therefore, nondestructive in situ characterization of the interfacial molecular structures of low-k dielectric materials requires analytical techniques that can probe the surface and buried interface of silicon-supported low-k materials.

In this chapter, we report that the interfacial molecular structures of silicon-supported low-k dielectric thin films can be characterized nondestructively *in situ* using SFG. SFG has recently been developed into an analytical technique that can characterize the molecular structure of surfaces and buried interfaces by selectively detecting molecular functional groups at interfaces and quantifying the interfacial orientation and orientation distribution of the detected

functional groups.[30-47] Here, we extend a previously developed method for characterizing molecular structure at buried polymer/metal interfaces to the characterization of the low-k/air and Si/low-k interfaces of a silicon-supported low-k dielectric thin film.[48-51]

7.2 Experimental Section

7.2.1 Materials

Poly(methylsilsesquioxane) (PMSQ) was obtained from Gelest, Inc. as a white powder, and tetrahydrofun (THF) (99%) was ordered from Sigma-Aldrich. Fused silica windows and right angle prisms were acquired from Esco Products, Inc. P-type silicon (100) wafers were purchased from Wafer World, Inc. Prior to film deposition, silicon wafers were exposed to oxygen plasma for 30 s (PE-50, Plasma Etch, Inc.). PMSQ solutions were prepared by dissolving PMSQ in THF. PMSQ thin films were deposited on silicon wafers and fused silica windows by spin-casting PMSQ solutions in THF at 3000 rpm for 30 s. Film thickness was controlled by varying the PMSQ weight percentage in the spin-casting solution. PMSQ thick films were deposited by drop casting a 2 wt % PMSQ solution on a silica right angle prism. All films were held under a vacuum prior to SFG measurements to remove residual solvent and to minimize moisture uptake in the thin film. Film thickness was measured using a Dektak 3 surface profilometer and ellipsometry.

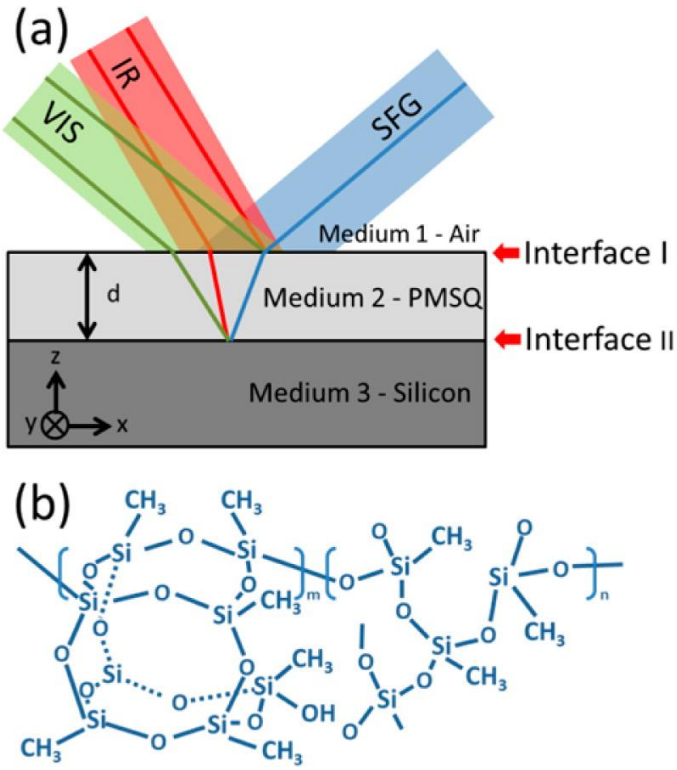

Figure 7.1. (a) Face-up SFG experimental geometry and (b) molecular structure of the low-k material PMSQ used in this study.

7.2.2 SFG Instrumentation

Basic SFG theory, data analysis, and our experimental setup have been described in chapter 1.[52-62] The visible and infrared input beams were overlapped at the surface of PMSQ films on silicon wafers with input angles of 60 ° and 51 ° versus the surface normal, respectively (Figure 7.1). The beam energies for the visible and infrared beams were ~9 and ~90 μJ, respectively. Both beam diameters were approximately 500 μm at the PMSQ film surface. All SFG spectra were collected in the SSP and PPP polarization combinations.

7.2.3 SFG Interference in a Three-Layer System

Theoretical frameworks for the analysis of SFG spectra collected from two and three-layer thin polymer film system have been described in chapter 1.[56,63-72] The effects of thin film interference on SFG spectra acquired from supported thin films were discussed in chapter 1. In this chapter, interface I and II refer to the PMSQ/air and Si/PMSQ interfaces, respectively.

7.3 Results and Discussion

7.3.1 Molecular Structure at the PMSQ/Air and Silica/PMSQ Interfaces

The molecular structure of the PMSQ/air interface was first characterized by collecting SFG SSP spectra from a ~100 nm thick PMSQ film on a silica window in the face-down geometry (Figure 7.2).

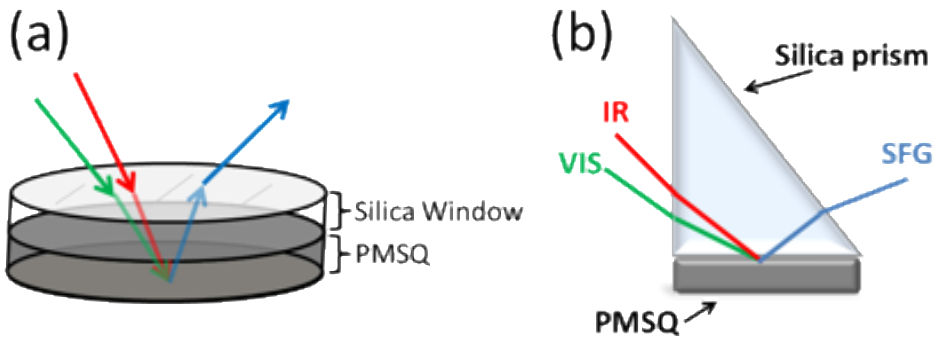

Figure 7.2 SFG (a) face down and (b) near critical angle reflection prism experimental geometries.

Two peaks were observed near 2920 and 2970 cm^{-1}, which can be assigned to the Si–CH_3 symmetric and asymmetric stretching vibrational modes, respectively.[73,74] The intensity of reflected SFG beams collected from thin polymer films in the face-down geometry has been

shown to be largely composed of SFG signal generated from the polymer/air interface with little contribution from the buried silica/polymer interface.[54]

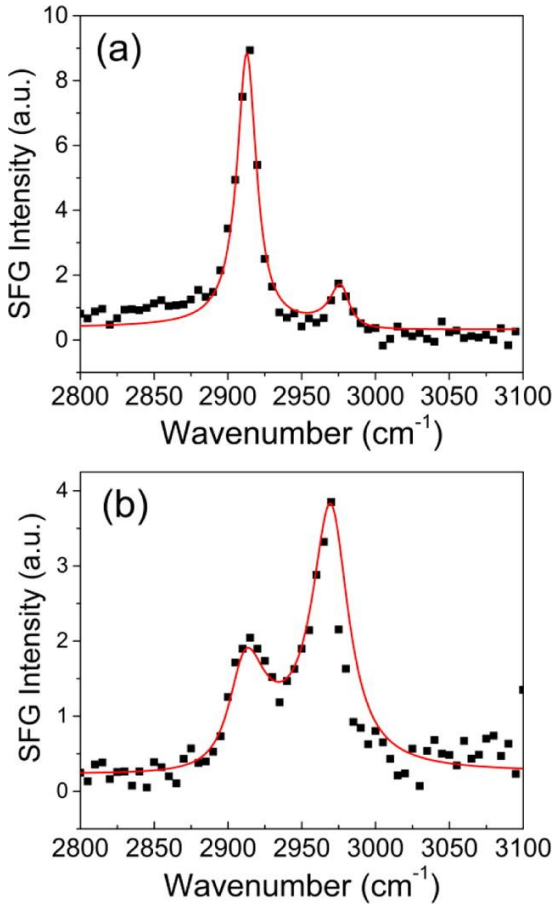

Figure 7.3. SFG SSP spectra collected from a (a) thin PMSQ on a silica window substrate and a (b) thick PMSQ on a silica prism in a near critical angle reflection geometry. In (a) and (b), the solid red curves connecting the data points are the fitting results.

The high methyl symmetric to asymmetric C–H stretching peak strength ratio indicates that the PMSQ/air interface is dominated by ordered methyl groups that are oriented close to the surface normal. The orientation of methyl groups at the PMSQ/air interface was calculated to be ~37 ° (Figure 7.4) based on the ratio of the methyl asymmetric susceptibility ($\chi_{yyz,as}$) to the

symmetric susceptibility ($\chi_{yyz,ss}$) (Table 7.1). By calculating the $\chi_{eff,yyz,as}/\chi_{eff,yyz,ss}$ ratio in the SSP polarization combination, the local field factors cancel and $\chi_{eff,yyz,as}/\chi_{eff,yyz,ss} = \chi_{yyz,as}/\chi_{yyz,ss}$:

$$\left|\frac{\chi^{(2)}_{yyz,as}}{\chi^{(2)}_{yyz,ss}}\right| = \left|\frac{-N_s\beta^{(2)}_{aca}[\langle cos\theta\rangle - \langle cos^3\theta\rangle]}{\frac{1}{2}N_s\beta^{(2)}_{ccc}[\langle cos\theta\rangle(1+R) - \langle cos^3\theta\rangle(1-R)]}\right| \quad (7.1)$$

Window			
ω (cm^{-1})	**Assignment**	**$A_{q,ssp}$**	**Γ_q (cm^{-1})**
2915	**Si-CH3 (ss)**	23.5 ± 1.0	8.0 ± 0.5
2975	**Si-CH3(as)**	-9.7 ± 0.8	8.0 ± 0.9
Prism			
2910	**Si-CH3 (ss)**	20.5 ± 1.1	15.0 ± 1.0
2970	**Si-CH3(as)**	-29.7 ± 0.9	15.0 ± 0.7
Wafer			
2921	**Si-CH3 (ss)**	19.8 ± 1.5	8.0 ± 0.8
2975	**Si-CH3(as)**	-8.7 ± 0.9	8.0 ± 0.9
ϕ	7.4 ± 0.1		
χ_{NR}	-7.0 ± 0.1		

Table 7.1. SFG SSP fitting results for Figures 7.3 and 7.5a.

The low tilt angle of the methyl groups on PMSQ is consistent with previous SFG studies, which reported that methyl groups on polymer chains at polymer/air interfaces tend to be oriented toward the air due to a reduction in surface free energy.[75,76]

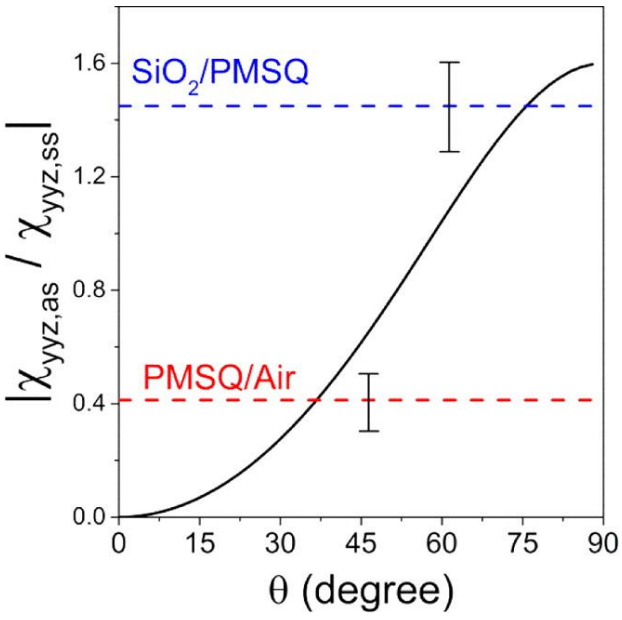

Figure 7.4. $|\chi_{yyz,as}/\chi_{yyz,ss}|$ plotted as a function of methyl tilt angle with respect to the PMSQ surface normal.

The molecular structure of the buried SiO_2/PMSQ interface was then characterized by collecting an SFG spectrum from a thick PMSQ film on a silica prism in a near critical angle reflection prism geometry (Figure 7.2).[77] In contrast to the SFG SSP spectra collected from the PMSQ/air interface, the methyl asymmetric C–H stretching peak was larger than the symmetric peak in the SFG SSP spectrum collected from the buried SiO_2/PMSQ interface (Figure 7.3b), which indicates that the methyl groups were oriented at a high tilt angle away from the surface normal. The orientation of methyl groups at the SiO_2/PMSQ interface was ~75 ° based on Figure 7.4 (Table 7.1). The high methyl C–H stretching asymmetric to symmetric ratio indicated that the $R = \beta_{aac}/\beta_{ccc}$ ratio was 4.0, which is within the commonly reported range of 1.6–4.2.[78,79] The high tilt angle observed at the buried SiO_2/PMSQ interface is similar to previous reports that methyl groups are oriented at high tilt angles at buried polymer/metal interfaces.[50,51] Attractive

interactions between electronegative atoms and the metal have been hypothesized to result in high methyl tilt angles due to the rigidity of the polymer chain conformation. Similarly, at the SiO_2/PMSQ interface, the oxygen atoms on the PMSQ network may preferentially interact with polar Si–OH groups on the silica, which induced the methyl groups to orient nearly parallel to the SiO_2 surface. Considering the SFG results above, the methyl groups on PMSQ are oriented near the PMSQ surface normal at the PMSQ/air interface and close to parallel to the SiO_2 surface at the buried SiO_2/PMSQ interface based on the interaction between the O–Si–CH_3 group and hydrophobic air or hydrophilic SiO_2, respectively.

7.3.2 SFG Spectra Collected from Silicon-Supported PMSQ Films

Thickness-dependent SFG SSP spectra were then collected from PMSQ films that had been spin coated on silicon wafers (Figure 7.5) in the face-up geometry (Figure 7.1). The polymer/air and polymer/substrate interfaces should both contribute to the intensity of the reflected SFG beam in the face-up geometry as discussed in chapter 1. Two peaks were observed near 2925 and 2975 cm^{-1} from PMSQ films of ~100 nm thickness, which again can be assigned to the Si–CH_3 C–H symmetric and asymmetric stretching vibrational modes, respectively. The methyl symmetric vibrational mode, however, appears as a dip in the spectrum, while the methyl asymmetric vibrational mode appears as a peak. Resonant signals will appear as dips or peaks based on the phase difference between the nonresonant susceptibility of the silicon substrate at the Si/PMSQ interface and the resonant susceptibility of the PMSQ. The nonresonant background contributed by silicon in second harmonic generation and sum frequency generation spectra has been extensively characterized in previous publications.[80-82] No substantial azimuthal angle dependence was detected in SFG SSP or PPP spectra collected from PMSQ/Si systems, so the azimuthal angle was not held constant.

The χ_{yyz} resonant susceptibilities of the methyl symmetric and asymmetric stretching vibrational modes have opposite signs, so for the case of resonant signal generated at one interface, one vibrational mode may appear as a peak while the other may appear as a dip based on the fixed phase of the nonresonant susceptibility of the silicon substrate. In addition, constructive or destructive interference will occur between the methyl resonant susceptibility and the silicon nonresonant susceptibility based on the absolute orientation of the methyl group at the interface. The absolute orientation of the methyl group with respect to the silicon substrate surface normal will be discussed later.

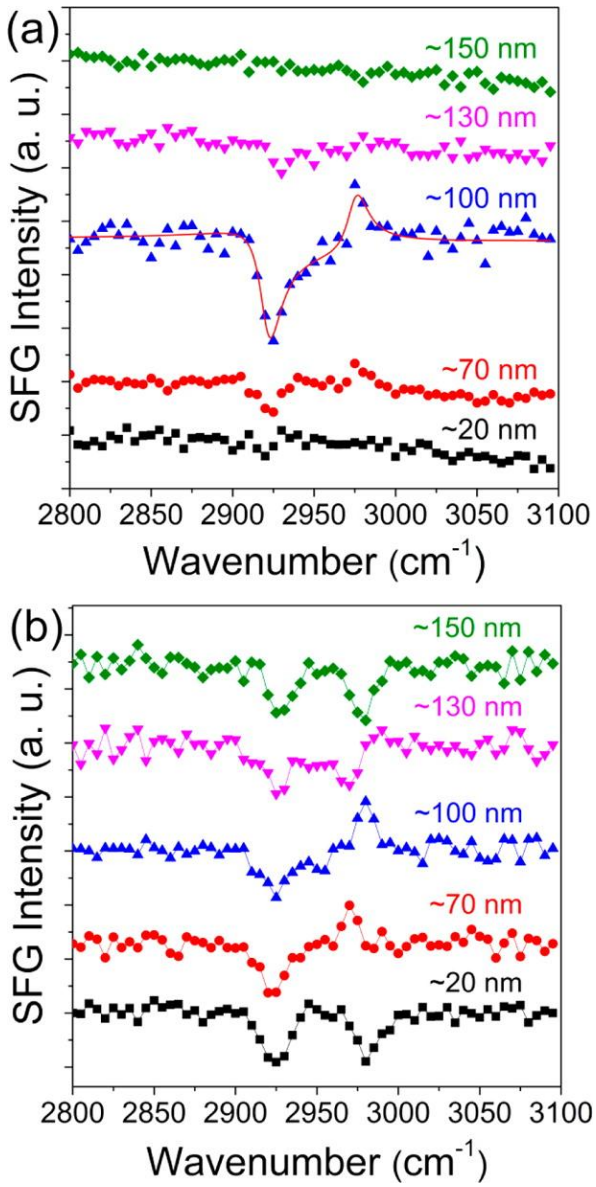

Figure 7.5. SFG (a) SSP and (b) PPP spectra collected from PMSQ films of different thicknesses on silicon substrates. In (a), the solid red curve is the fitting result. In (b), the solid curves connecting the data points are a guide to the eye.

The SFG SSP intensity was largely dependent on the thickness of the film. The largest intensity was observed from films of approximately 100 nm thickness. The spectral features, however, were similar at different film thicknesses. Film thickness-dependent SFG signal intensity suggests that the SFG signal was influenced by film thickness-dependent interference effects in the PMSQ film.

To take into account multiple reflections within the PMSQ film, local field factors were calculated for both the PMSQ/air and the PMSQ/Si interfaces for a three-layer system (Figure 7.6). The native oxide on the silicon wafer was <5 nm. Therefore, the effect of the refractive index of the silicon native oxide on the local field factors at the PMSQ/Si interface was assumed to be negligible. Furthermore, the local field factors were assumed to be dispersionless. More detailed studies including frequency-dependent complex refractive index[83] values will be performed in the future. The film thickness was below ~1 μm, so the effect of absorption of the infrared beam by the PMSQ film on the SFG intensity was assumed to be negligible.[34] The L_{yyz} ($L_{yyz} = L_{yy}(\omega_{SFG})L_{yy}(\omega_{VIS})L_{zz}(\omega_{IR}) \sin \theta_{IR}$) local field factor for the PMSQ/air interface clearly changes based on the thickness of the film, and the highest value occurs near 110 nm. Although the L_{yyz} local field factor for the PMSQ/Si interface is also highest near 110 nm, the value is approximately one order of magnitude lower than that of the PMSQ/air interface. The trend in SFG SSP signal intensity from films of different thickness follows the trend in the thickness dependence of the PMSQ/air L_{yyz} modulus, which suggests that the signal thickness dependence was due to the thickness dependence of the L_{yyz} local field factor of the PMSQ/air interface.

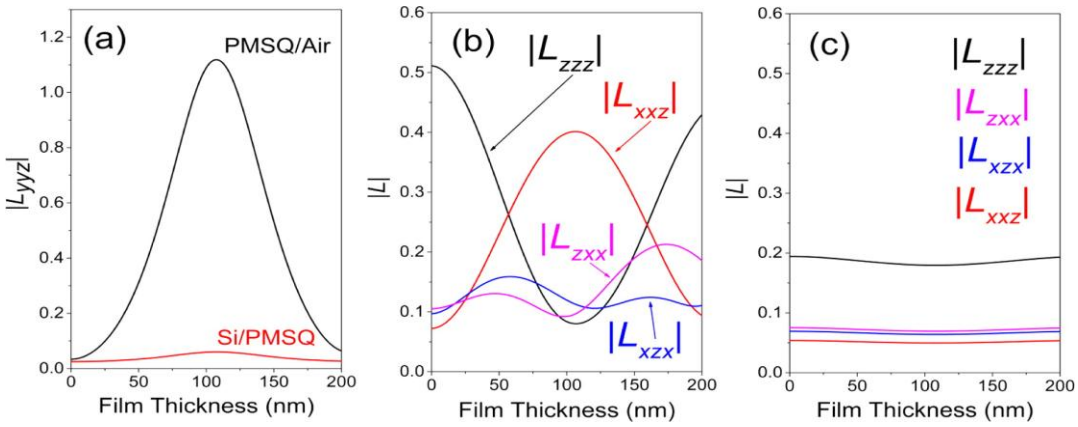

Figure 7.6. Local field factors at the Si/PMSQ and PMSQ/air interfaces plotted as a function of film thickness for the (a) SSP polarization combination. Local field factors at the (b) PMSQ/air and (c) Si/PMSQ interfaces plotted as a function of film thickness for the PPP polarization combination. In (c), the order of solid curves from the bottom to the top corresponds to the order of the L factors listed in the legend from the bottom to the top.

SFG SSP signal collected from films of approximately 100 nm thickness will thus be dominated by signal contributed by the PMSQ/air interface. Therefore, SFG in the SSP polarization can be used to selectively characterize the molecular structure of the PMSQ/air interface in situ from PMSQ films deposited on silicon wafers. The selectivity of the measurement also simplifies the calculation of methyl group orientation because the local field factor at the PMSQ/air interface is the same for the methyl symmetric and the asymmetric stretching vibrational modes and thus cancels when the asymmetric to symmetric ratio is calculated. As the SSP measurement selectively probed the PMSQ/air interface, the SFG SSP spectra collected from the ~100 nm thick film were fit using eq 1.23. The orientation of methyl groups at the PMSQ/air interface from films on silicon wafers was ~38 ° (Table 7.1, Figure 7.4), which is consistent with the orientation determined using the face-down geometry with a fused silica substrate. The consistency of the face-up and face-down orientation calculations supports the surface selectivity of the face-up measurement.

To characterize the molecular structure at the Si/PMSQ interface, SFG PPP spectra were collected from the PMSQ films. The moduli of the local field factors in the PPP polarization combination at the PMSQ/air and Si/PMSQ interfaces are on the same order of magnitude (Figure 7.6). Therefore, in contrast to the SSP polarization combination, both interfaces are expected to contribute to the detected SFG intensity. Furthermore, the modulus of each local field factor at the PMSQ/air interface is dependent on the film thickness. However, the moduli of the local field factors at the Si/PMSQ interface remain relatively constant at different film thicknesses. The thickness dependence of the local field factors at the PMSQ/air and the Si/PMSQ interfaces is similar to the thickness dependence of local field factors at polymer/air and metal/polymer interfaces.[50,51]

SFG PPP spectra collected from PMSQ films of different thicknesses are shown in Figure 7.5. Methyl C–H symmetric and asymmetric stretching peaks were observed near 2920 and 2975 cm^{-1}, and film thickness-dependent spectra were observed, which are similar to the spectra collected in the SSP polarization combination. However, unlike the SSP spectra, the intensity of the methyl symmetric and asymmetric peaks remained relatively constant at different thicknesses, while the peak shape (e.g., a peak or a dip) of the methyl asymmetric peak was dependent on the film thickness. For example, at 20 nm film thickness, the methyl asymmetric and symmetric stretching vibrational modes both appear as dips in the spectrum. At ~100 nm, the methyl symmetric and asymmetric stretching vibrational modes appear as a dip and a peak, respectively.

The intensity of the SFG signal generated in the PPP polarization combination can be expressed by eq 7.2. We believe that the nonresonant susceptibility of the silicon substrate will have the same susceptibility components and local field factors as $\chi_{R,ijk}^{(2),II}$. Therefore, χ_{zzz}, χ_{zzz}, χ_{zzz},

and χ_{zzz} contribute to the non-resonant susceptibility of the Si/PMSQ interface ($\chi^{(2),II}_{NR,ijk}$ i.e. the non-resonant background):[63]

$$I_{SFG,PPP}(\omega_{SFG}) \propto \left| \begin{matrix} -L^{I}_{xxz}\chi^{(2),I}_{xxz} - L^{I}_{xzx}\chi^{(2),I}_{xzx} + L^{I}_{zxx}\chi^{(2),I}_{zxx} + L^{I}_{zzz}\chi^{(2),I}_{zzz} \\ -L^{II}_{xxz}\chi^{(2),II}_{xxz} - L^{II}_{xzx}\chi^{(2),II}_{xzx} + L^{II}_{zxx}\chi^{(2),II}_{zxx} + L^{II}_{zzz}\chi^{(2),II}_{zzz} \\ -L^{II}_{xxz}\chi^{(2),II}_{NR,xxz} - L^{II}_{xzx}\chi^{(2),II}_{NR,xzx} + L^{II}_{zxx}\chi^{(2),II}_{NR,zxx} + L^{II}_{zzz}\chi^{(2),II}_{NR,zzz} \end{matrix} \right|^2 I_{VIS}I_{IR} \quad (7.2)$$

Following Tong et al., the local field factors at the buried Si/PMSQ interface influence the magnitude and phase of $\chi^{(2),II}_{NR,ijk}$.[63] Therefore, the detected SFG signal intensity is influenced by the modulus and phase of $\chi^{(2),I}_{eff,R,ijk}$, $\chi^{(2),II}_{eff,R,ijk}$, and $\chi^{(2),II}_{NR,ijk}$. Here the effective nonlinear resonant susceptibilities of the surface and buried interface are defined as

$$\chi^{(2),I}_{eff,R,ijk} = -L^{I}_{xxz}\chi^{(2),I}_{xxz} - L^{I}_{xzx}\chi^{(2),I}_{xzx} + L^{I}_{zxx}\chi^{(2),I}_{zxx} + L^{I}_{zzz}\chi^{(2),I}_{zzz} \quad (7.3)$$

$$\chi^{(2),II}_{eff,R,ijk} = -L^{II}_{xxz}\chi^{(2),II}_{xxz} - L^{II}_{xzx}\chi^{(2),II}_{xzx} + L^{II}_{zxx}\chi^{(2),II}_{zxx} + L^{II}_{zzz}\chi^{(2),II}_{zzz} \quad (7.4)$$

while the non-resonant background is defined as

$$\chi^{(2),II}_{NR,ijk} = -L^{II}_{xxz}\chi^{(2),II}_{NR,xxz} - L^{II}_{xzx}\chi^{(2),II}_{NR,xzx} + L^{II}_{zxx}\chi^{(2),II}_{NR,zxx} + L^{II}_{zzz}\chi^{(2),II}_{NR,zzz} \quad (7.5)$$

7.3.3 Simulated SFG Spectra

In order to elucidate the effect of the thickness dependence of the local field factors on the intensity of the SFG PPP signal, equation 7.2 was plotted as a function of ω_{IR}. The SFG spectra simulations follow the method developed by Tong et al.[63] Simulated spectra were plotted using Mathematica 9.0 software (Wolfram Research, Inc., Mathematica, Version 9.0, Champaign, IL (2012)). Complex local field factors were calculated based on previously developed theoretical modeling of interference effects in SFG spectra collected from a thin polymer film on a reflective substrate.[63-65] For convenience, expressions for the local field factors and the

nonlinear susceptibilities of the methyl symmetric and asymmetric stretching vibrational modes ($\chi^{(2)}_{IJK,ss}$ and $\chi^{(2)}_{IJK,as}$, respectively) can be found in chapter 1. The values of β_{aac}, β_{ccc}, and β_{aca} were set as β_{aac}:β_{ccc}:β_{aca} = 4:1:4 where $\beta_{aac} \approx \beta_{ccc}$ and β_{ccc} = 1.[37,84] The initial orientation of methyl groups at the surface and buried interface was 37 ° and 75 °, respectively, based on the interface selective SFG results discussed above (The silicon substrate has a native SiO_2 layer, therefore we believe that the methyl orientations at the PMSQ/silicon and PMSQ/fused silica interfaces are similar). In addition, the molecular densities at the PMSQ/air and Si/PMSQ interfaces were assumed to be equal. SFG spectra were then simulated by replacing $-L^{II}_{xxz}\chi^{(2),II}_{NR,xxz} - L^{II}_{xzx}\chi^{(2),II}_{NR,xzx} + L^{II}_{zxx}\chi^{(2),II}_{NR,zxx} + L^{II}_{zzz}\chi^{(2),II}_{NR,zzz}$ in equation 7.2 with a single complex number $\chi^{(2),II}_{NR,ijk} = \left|\chi^{(2),II}_{NR,ijk}\right|(cos\varphi + isin\varphi)$. The modulus of the non-resonant susceptibility was initially set as $\left|\chi^{(2),II}_{NR,ijk}\right| \approx \left|\chi^{(2),I}_{eff,R,ijk} + \chi^{(2),II}_{eff,R,ijk}\right|$ where $\left|\chi^{(2),I}_{eff,R,ijk} + \chi^{(2),II}_{eff,R,ijk}\right| \approx 0.1$. The modulus was then raised in small increments while varying the phase φ from 0-2π until the simulated spectra matched the observed SFG spectra. The modulus of the non-resonant susceptibility that provided the closest match to the experimental spectra was 0.15. In addition, $\left|\chi^{(2),II}_{NR,ijk}\right|$ was kept at a constant value at all simulated thicknesses due to the relatively constant modulus of the local field factors at the Si/PMSQ interface. The simulated peak width (Γ) was 8 cm^{-1} based on fitting of the experimental spectra.

Simulated SFG spectra for films of thickness 20, 70, 100, 130, and 150 nm are shown in Figure 7.7. The change of the asymmetric vibrational mode from a dip to a peak while the symmetric vibrational mode remained a dip was reproduced by changing φ. Furthermore, the best fit occurred when the methyl orientation at the buried interface was 70 ° and $\chi^{(2),I}_{R,ijk} =$

$-\chi_{R,ijk}^{(2),II}$, i.e. when the methyl groups at the PMSQ/air and Si/PMSQ interfaces had opposite absolute orientations.

Slight differences between the structure of the native oxide on a silicon wafer and the structure of fused silica may have influenced the optimized methyl orientation at the buried Si/SiO_2 interface relative to the fused silica interface. Different silica structures may have interacted differently with PMSQ which slightly altered the interfacial methyl orientation. In addition, the molecular structure of PMSQ at the interface between fused silica and a drop cast PMSQ film may be slightly different than at the interface between a silicon wafer with a native oxide layer and a thin PMSQ film. However, even considering these differences, the optimized orientation of methyl groups at the buried Si/SiO_2/PMSQ interface was very similar to the initially determined orientation of methyl groups at the fused silica/PMSQ interface.

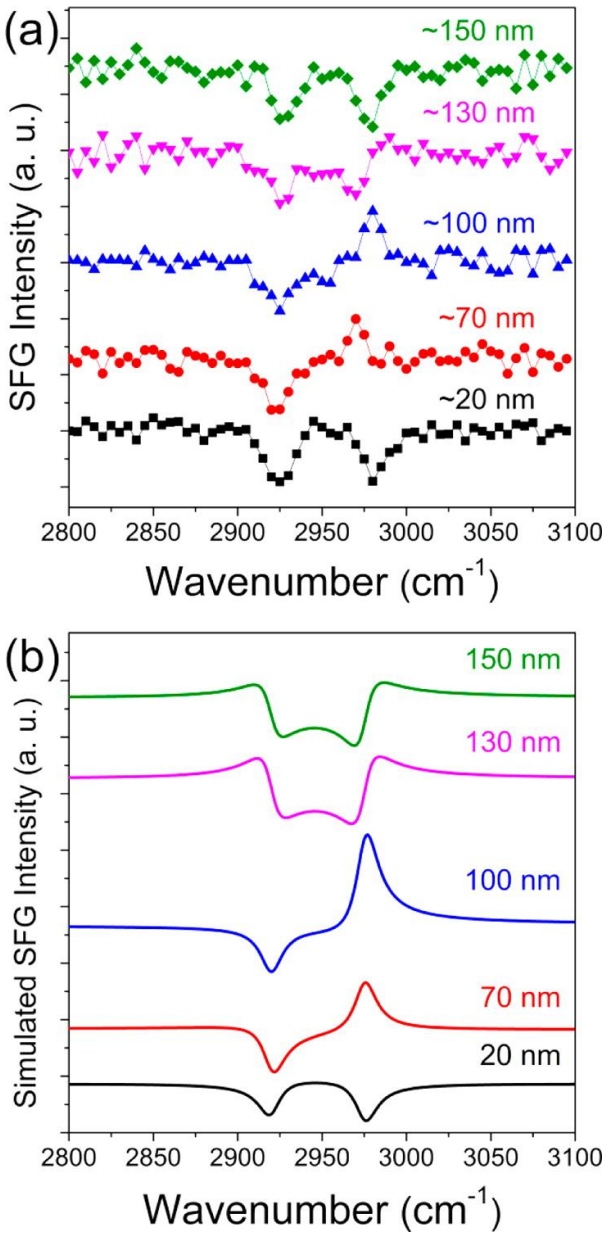

Figure 7.7. (a) Experimental and (b) simulated film thickness-dependent PPP SFG spectra collected from PMSQ films on silicon substrates.

The phase of $\chi^{(2),II}_{NR,ijk}$ is expected to be dependent on the film thickness due to the thickness dependence of the phase of the local field factors at the Si/PMSQ interface.[63] Each non-resonant susceptibility component of $\chi^{(2),II}_{NR,ijk}$ ($\chi^{(2),II}_{NR,xxz}$, $\chi^{(2),II}_{NR,xzx}$, $\chi^{(2),II}_{NR,zxx}$, $\chi^{(2),II}_{NR,zzz}$) was modeled as a constant complex number.[72,85] Therefore, the overall phase of $\chi^{(2),II}_{NR,ijk}$ will be determined by the linear combination of the four contributing effective non-resonant susceptibilities. Accurate determination of the non-resonant susceptibilities, however, would require the relationships between the four susceptibilities to be known.

In addition to showing a change of the asymmetric peak from a dip to a peak, the simulated spectra at different film thicknesses also show similar changes in peak positions as observed in the experimental spectra. For example, at 100 and 130 nm, the experimental peaks appear to occur at different peak centers even though both peaks centers were ~2975 cm^{-1}. The apparent shift in peak center is due to the interference between the resonant and non-resonant susceptibility components which determine the observed peak shape. The effect of the non-resonant susceptibility on the observed peak shape is similar to the effect at metal interfaces which has been reported[85,86]. However, unlike gold substrates where $L_{zzz}\chi^{(2),II}_{NR,zzz}$ dominates the non-resonant signal, the modulus and phase of all four non-resonant susceptibilities should contribute to the PPP non-resonant background from silicon substrates as discussed above.

The effect of $\chi^{(2),II}_{NR,ijk}$on the experimental spectra can be inferred by simulating the spectra from the surface and buried interface separately. Specifically, the surface, buried interface, and SFG signal can be simulated as:

$$I_{SFGI,PPP}(\omega_{SFG}) \propto \left|\chi^{(2),I}_{eff,R,ijk} + \chi^{(2),II}_{NR,ijk}\right|^2 \tag{7.6}$$

$$I_{SFGII,PPP}(\omega_{SFG}) \propto \left|\chi^{(2),II}_{eff,R,ijk} + \chi^{(2),II}_{NR,ijk}\right|^2 \tag{7.7}$$

$$I_{SFG,PPP}(\omega_{SFG}) \propto \left|\chi^{(2),I}_{eff,R,ijk} + \chi^{(2),II}_{eff,R,ijk} + \chi^{(2),II}_{NR,ijk}\right|^2 \quad (7.8)$$

respectively.

Parameter	Value	Parameter	Value	Parameter	Value
θ_{VIS}	60 °	$n_{2,VIS}$	1.42	$\left\|\chi^{(2),II}_{NR}\right\|$	0.15
θ_{IR}	51 °	$n_{2,IR}$	1.39	$n_{m2,3}$	1.42
λ_{VIS}	532 nm	$n_{2,SFG}$	1.42	$n_{m1,2}$	1.20
λ_{IR}	3367 nm	$n_{3,VIS}$[87]	4.150 + 0.044i	θ_I	37 °
λ_{SFG}	459 nm	$n_{3,IR}$[87]	3.433	θ_{II} initial	75 °
ω_{ss}	2920 cm^{-1}	$n_{3,SFG}$[87]	4.585 + 0.130i	θ_{II} optimized	70 °
ω_{as}	2975 cm^{-1}	Γ	8 cm^{-1}		

Table 7.2. List of Parameters and Values for Local Field Factor Calculations and Simulated SFG Spectra.

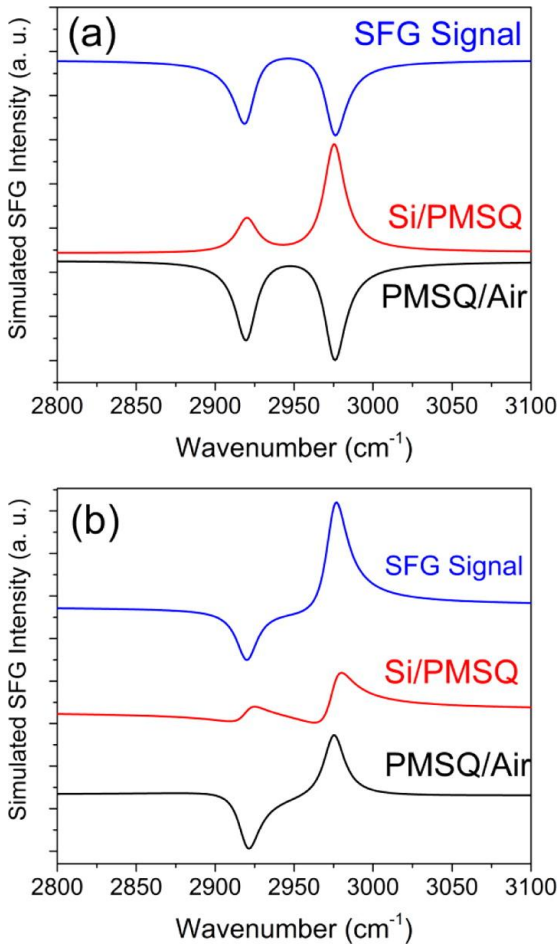

Figure 7.8. Simulated SFG spectra of (a) 20 and (b) 100 nm thick PMSQ films and contributions to the simulated SFG spectra from the surface and buried interface signal.

As shown in Figure 7.8, the opposite orientations of the methyl group at the surface and buried interface contributed to the peak shape and intensity at each interface. In addition, the high tilt angle of the methyl group at the buried interface resulted in the buried interface contributing more to the asymmetric stretching peak than to the symmetric stretching peak. The larger contribution of the buried interface to the asymmetric stretching peak than to the symmetric stretching peak is consistent with the experimental SFG spectra where the asymmetric stretching peak shape was affected by the film thickness while the symmetric peak was relatively constant. For example, Figure 7.8 shows that in the simulated SFG spectra of the PMSQ/air

interface of a 20 nm thick film the asymmetric stretching peak intensity is larger than the intensity of the symmetric stretching peak. However, in the SFG signal, the intensity of the asymmetric stretching peak is decreased due to a destructive contribution from the Si/PMSQ interface. Different from the 20 nm thick film, simulated SFG spectra of a 100 nm thick film show that the asymmetric stretching peak in the SFG signal is enhanced relative to the intensity at the PMSQ/air interface due to a constructive contribution from the Si/PMSQ interface. Furthermore, the simulated SFG spectra could not be approximated as the sum of the surface and buried interface signal (i.e. $\left|\chi^{(2),I}_{eff,R,ijk}+\chi^{(2),II}_{NR,ijk}\right|^2+\left|\chi^{(2),II}_{eff,R,ijk}+\chi^{(2),II}_{NR,ijk}\right|^2$) due to cross terms in the squared expression of equation 7.8.[71]

More generally, resonant and non-resonant contributions to the overall SFG signal were deduced by adjusting the phase of $\chi^{(2),II}_{NR,ijk}$ in thickness dependent simulated SFG spectra until the simulated spectra matched the experimental spectra. Separation of the resonant and non-resonant contributions to the SFG signal enabled the interfacial resonant susceptibilities to be obtained. The deduced interfacial resonant susceptibilities, which are determined by interfacial molecular structures, can then be used to characterize the molecular structure of the surface and buried interface.

7.4 Conclusion and Impact

In this work, we developed a general method to characterize the molecular structure at the surface and buried interface of silicon-supported low-k dielectric thin polymer films using SFG vibrational spectroscopy. The intensity of the reflected SFG beam in the SSP and PPP polarization combinations collected from PMSQ films on silicon wafers was dependent on the thickness of the film. Interference effects in the low-k film resulted in thickness-dependent local field factors at the PMSQ/air and Si/PMSQ interfaces, which in turn influenced the detected SFG

intensity. SFG measurements collected in the SSP polarization were found to selectively probe the PMSQ/air interface, while the PPP polarization combination probed both the surface and the buried Si/PMSQ interface.

The contributions of SFG signal generated at the surface and buried interface to the observed SFG spectra were determined by simulating SFG spectra generated from a three-layer system using known parameters. The contributions to the SFG signal from the PMSQ/air and Si/PMSQ interfaces were then deduced by simulating the SFG spectra generated from the respective interfaces. Deduced SFG spectra then provided characterization of the molecular structure of each interface in terms of molecular absolute orientation and molecular density. Although the molecular density was assumed to be equal at the PMSQ/air and Si/PMSQ interfaces, the method developed here could also be used to determine the molecular density ratio at the surface relative to the buried interface. For example, when the orientation and orientation distribution of methyl groups at each interface are known, expected ratios of methyl susceptibilities could be compared to experimentally determined susceptibility ratios to deduce N_s^I/N_s^{II}.

The method developed here is general and can be applied to characterize the surface and buried interfacial molecular structure of silicon-supported thin polymer or organic films. Therefore, the developed methodology can be directly incorporated into microelectronic packaging metrology. Molecular level characterization of the polymer or organic/air and silicon/organic or polymer interfaces can thus be obtained in the same sample geometry used in adhesion strength, leakage current, ellipsometry, and surface analytical techniques. In situ SFG characterization of organic or polymer thin films on silicon wafers should provide more direct

correlations between molecular structure and interfacial properties, which can be used in the development of interfacial structure function relationship.

7.5 References

(1) Grill, A.; Gates, S. M.; Ryan, T. E.; Nguyen, S. V.; Priyadarshini, D. Progress in the Development and Understanding of Advanced Low K and Ultralow K Dielectrics for Very Large-Scale Integrated interconnects—State of the Art. *Appl. Phys. Rev.* **2014**, *1*, 011306.

(2) *Dielectric Films for Advanced Microelectronics*; Baklanov, M.; Green, M.; Maex, K., Eds.; Wiley series in materials for electronic and optoelectronic applications; John Wiley & Sons: Chichester, England ; Hoboken, NJ, 2007.

(3) Grill, A. Porous pSiCOH Ultralow- *k* Dielectrics for Chip Interconnects Prepared by PECVD. *Annu. Rev. Mater. Res.* **2009**, *39*, 49–69.

(4) Taek-Soo Kim; Dauskardt, R. H. Integration Challenges of Nanoporous Low Dielectric Constant Materials. *IEEE Trans. Device Mater. Reliab.* **2009**, *9*, 509–515.

(5) Zhou, W.; Bailey, S.; Sooryakumar, R.; King, S.; Xu, G.; Mays, E.; Ege, C.; Bielefeld, J. Elastic Properties of Porous Low-K Dielectric Nano-Films. *J. Appl. Phys.* **2011**, *110*, 043520.

(6) Bailey, S.; Mays, E.; Michalak, D. J.; Chebiam, R.; King, S.; Sooryakumar, R. Mechanical Properties of High Porosity Low- *k* Dielectric Nano-Films Determined by Brillouin Light Scattering. *J. Phys. Appl. Phys.* **2013**, *46*, 045308.

(7) Guotao Wang; Merrill, C.; Jie-Hua Zhao; Groothuis, S. K.; Ho, P. S. Packaging Effects on Reliability of Cu/low-K Interconnects. *IEEE Trans. Device Mater. Reliab.* **2003**, *3*, 119–128.

(8) Bao, J.; Shi, H.; Liu, J.; Huang, H.; Ho, P. S.; Goodner, M. D.; Moinpour, M.; Kloster, G. M. Mechanistic Study of Plasma Damage of Low K Dielectric Surfaces. *J. Vac. Sci. Technol. B Microelectron. Nanometer Struct.* **2008**, *26*, 219.

(9) Shamiryan, D.; Baklanov, M. R.; Vanhaelemeersch, S.; Maex, K. Comparative Study of SiOCH Low-K Films with Varied Porosity Interacting with Etching and Cleaning Plasma. *J. Vac. Sci. Technol. B Microelectron. Nanometer Struct.* **2002**, *20*, 1923.

(10) Li, Y.; Ciofi, I.; Carbonell, L.; Heylen, N.; Van Aelst, J.; Baklanov, M. R.; Groeseneken, G.; Maex, K.; Tőkei, Z. Influence of Absorbed Water Components on SiOCH Low-K Reliability. *J. Appl. Phys.* **2008**, *104*, 034113.

(11) Baklanov, M. R.; de Marneffe, J.-F.; Shamiryan, D.; Urbanowicz, A. M.; Shi, H.; Rakhimova, T. V.; Huang, H.; Ho, P. S. Plasma Processing of Low-K Dielectrics. *J. Appl. Phys.* **2013**, *113*, 041101.

(12) Awaja, F.; Gilbert, M.; Kelly, G.; Fox, B.; Pigram, P. J. Adhesion of Polymers. *Prog. Polym. Sci.* **2009**, *34*, 948–968.

(13) Somorjai, G. A. *Introduction to Surface Chemistry and Catalysis*; 2nd ed.; Wiley: Hoboken, N.J, 2010.

(14) Sun, Y.; Krishtab, M.; Struyf, H.; Verdonck, P.; De Feyter, S.; Baklanov, M. R.; Armini, S. Impact of Plasma Pretreatment and Pore Size on the Sealing of Ultra-Low- *k* Dielectrics by Self-Assembled Monolayers. *Langmuir* **2014**, *30*, 3832–3844.

(15) Ishikawa, A.; Shishida, Y.; Yamanishi, T.; Hata, N.; Nakayama, T.; Fujii, N.; Tanaka, H.; Matsuo, H.; Kinoshita, K.; Kikkawa, T. Influence of CMP Chemicals on the Properties of Porous Silica Low-K Films. *J. Electrochem. Soc.* **2006**, *153*, G692.

(16) Armini, S.; Loyo Prado, J.; Krishtab, M.; Conard, T.; Meersschaut, J.; Le, Q. T.; Verdonck, P.; Baklanov, M. R. Study of Wet Surface Activation Routes to Enable the Deposition of Monomolecular Organic Thin Films on K 2.0 Porous Dielectrics. *ECS J. Solid State Sci. Technol.* **2014**, *3*, N3106–N3111.

(17) Liu, J.; Kim, W.; Bao, J.; Shi, H.; Baek, W.; Ho, P. S. Restoration and Pore Sealing of Plasma Damaged Porous Organosilicate Low K Dielectrics with Phenyl Containing Agents. *J. Vac. Sci. Technol. B Microelectron. Nanometer Struct.* **2007**, *25*, 906.

(18) Liu, J.; Bao, J.; Scharnberg, M.; Kim, W. C.; Ho, P. S.; Laxman, R. Effects of Surface Chemistry on ALD Ta_3N_5 Barrier Formation on Low-K Dielectrics. *J. Vac. Sci. Technol. Vac. Surf. Films* **2005**, *23*, 1107.

(19) Guo, X.; Jakes, J. E.; Nichols, M. T.; Banna, S.; Nishi, Y.; Shohet, J. L. The Effect of Water Uptake on the Mechanical Properties of Low-K Organosilicate Glass. *J. Appl. Phys.* **2013**, *114*, 084103.

(20) Guo, X.; Jakes, J. E.; Banna, S.; Nishi, Y.; Leon Shohet, J. Effect of Water Uptake on the Fracture Behavior of Low-K Organosilicate Glass. *J. Vac. Sci. Technol. Vac. Surf. Films* **2014**, *32*, 031512.

(21) Atkin, J. M.; Cartier, E.; Shaw, T. M.; Laibowitz, R. B.; Heinz, T. F. Charge Trapping at the Low-K Dielectric-Silicon Interface Probed by the Conductance and Capacitance Techniques. *Appl. Phys. Lett.* **2008**, *93*, 122902.

(22) Grill, A.; Neumayer, D. A. Structure of Low Dielectric Constant to Extreme Low Dielectric Constant SiCOH Films: Fourier Transform Infrared Spectroscopy Characterization. *J. Appl. Phys.* **2003**, *94*, 6697.

(23) King, S. W.; French, M.; Bielefeld, J.; Lanford, W. A. Fourier Transform Infrared Spectroscopy Investigation of Chemical Bonding in Low-K a-SiC:H Thin Films. *J. Non-Cryst. Solids* **2011**, *357*, 2970–2983.

(24) Park, E. S.; Ro, H. W.; Nguyen, C. V.; Jaffe, R. L.; Yoon, D. Y. Infrared Spectroscopy Study of Microstructures of Poly(silsesquioxane)s. *Chem. Mater.* **2008**, *20*, 1548–1554.

(25) Mabboux, P.-Y.; Gleason, K. K. Chemical Bonding Structure of Low Dielectric Constant Si:O:C:H Films Characterized by Solid-State NMR. *J. Electrochem. Soc.* **2005**, *152*, F7.

(26) Casserly, T. B.; Gleason, K. K. Density Functional Theory Calculation of ^{29} Si NMR Chemical Shifts of Organosiloxanes. *J. Phys. Chem. B* **2005**, *109*, 13605–13610.

(27) Gerbaud, G.; Hediger, S.; Bardet, M.; Favennec, L.; Zenasni, A.; Beynet, J.; Gourhant, O.; Jousseaume, V. Spin-Coated and PECVD Low Dielectric Constant Porous Organosilicate Films Studied by 1D and 2D Solid-State NMR. *Phys. Chem. Chem. Phys.* **2009**, *11*, 9729.

(28) Zhang, X.; Myers, J. N.; Bielefeld, J. D.; Lin, Q.; Chen, Z. In Situ Observation of Water Behavior at the Surface and Buried Interface of a Low-K Dielectric Film. *ACS Appl. Mater. Interfaces* **2014**, *6*, 18951–18961.

(29) Grill, A. Plasma Enhanced Chemical Vapor Deposited SiCOH Dielectrics: From Low-K to Extreme Low-K Interconnect Materials. *J. Appl. Phys.* **2003**, *93*, 1785.

(30) Hankett, J. M.; Liu, Y.; Zhang, X.; Zhang, C.; Chen, Z. Molecular Level Studies of Polymer Behaviors at the Water Interface Using Sum Frequency Generation Vibrational Spectroscopy. *J. Polym. Sci. Part B Polym. Phys.* **2013**, *51*, 311–328.

(31) Chen, Z. Investigating Buried Polymer Interfaces Using Sum Frequency Generation Vibrational Spectroscopy. *Prog. Polym. Sci.* **2010**, *35*, 1376–1402.

(32) Zhang, C.; Myers, J. N.; Chen, Z. Elucidation of Molecular Structures at Buried Polymer Interfaces and Biological Interfaces Using Sum Frequency Generation Vibrational Spectroscopy. *Soft Matter* **2013**, *9*, 4738.

(33) Ye, S.; Kathiravan, A.; Hayashi, H.; Tong, Y.; Infahsaeng, Y.; Chabera, P.; Pascher, T.; Yartsev, A. P.; Isoda, S.; Imahori, H.; et al. Role of Adsorption Structures of Zn-Porphyrin on TiO_2 in Dye-Sensitized Solar Cells Studied by Sum Frequency Generation Vibrational Spectroscopy and Ultrafast Spectroscopy. *J. Phys. Chem. C* **2013**, *117*, 6066–6080.

(34) Tong, Y.; Zhao, Y.; Li, N.; Ma, Y.; Osawa, M.; Davies, P. B.; Ye, S. Interference Effects in the Sum Frequency Generation Spectra of Thin Organic Films. II: Applications to Different Thin-Film Systems. *J. Chem. Phys.* **2010**, *133*, 034705.

(35) Zhang, C.; Hankett, J.; Chen, Z. Molecular Level Understanding of Adhesion Mechanisms at the Epoxy/Polymer Interfaces. *ACS Appl. Mater. Interfaces* **2012**, *4*, 3730–3737.

(36) Vázquez, A. V.; Holden, B.; Kristalyn, C.; Fuller, M.; Wilkerson, B.; Chen, Z. Surface and Buried Interfacial Structures of Epoxy Resins Used as Underfills Studied by Sum Frequency Generation Vibrational Spectroscopy. *ACS Appl. Mater. Interfaces* **2011**, *3*, 1640–1651.

(37) Zhang, C.; Chen, Z. Probing Molecular Structures of Poly(dimethylsiloxane) at Buried Interfaces *in Situ*. *J. Phys. Chem. C* **2013**, *117*, 3903–3914.

(38) Zhang, C.; Chen, Z. Quantitative Molecular Level Understanding of Ethoxysilane at Poly(dimethylsiloxane)/Polymer Interfaces. *Langmuir* **2013**, *29*, 610–619.

(39) Darwish, T. A.; Tong, Y.; James, M.; Hanley, T. L.; Peng, Q.; Ye, S. Characterizing the Photoinduced Switching Process of a Nitrospiropyran Self-Assembled Monolayer Using In Situ Sum Frequency Generation Spectroscopy. *Langmuir* **2012**, *28*, 13852–13860.

(40) Jena, K. C.; Hung, K.-K.; Schwantje, T. R.; Hore, D. K. Methyl Groups at Dielectric and Metal Surfaces Studied by Sum-Frequency Generation in Co- and Counter-Propagating Configurations. *J. Chem. Phys.* **2011**, *135*, 044704.

(41) Jena, K. C.; Covert, P. A.; Hall, S. A.; Hore, D. K. Absolute Orientation of Ester Side Chains on the PMMA Surface. *J. Phys. Chem. C* **2011**, *115*, 15570–15574.

(42) Sung, J.; Zhang, L.; Tian, C.; Waychunas, G. A.; Shen, Y. R. Surface Structure of Protonated R-Sapphire ($1\bar{1}02$) Studied by Sum-Frequency Vibrational Spectroscopy. *J. Am. Chem. Soc.* **2011**, *133*, 3846–3853.

(43) Liu, W.-T.; Shen, Y. R. In Situ Sum-Frequency Vibrational Spectroscopy of Electrochemical Interfaces with Surface Plasmon Resonance. *Proc. Natl. Acad. Sci.* **2014**, *111*, 1293–1297.

(44) Thompson, C. M.; Carl, L. M.; Somorjai, G. A. Sum Frequency Generation Study of the Interfacial Layer in Liquid-Phase Heterogeneously Catalyzed Oxidation of 2-Propanol on Platinum: Effect of the Concentrations of Water and 2-Propanol at the Interface. *J. Phys. Chem. C* **2013**, *117*, 26077–26083.

(45) Kennedy, G.; Baker, L. R.; Somorjai, G. A. Selective Amplification of C O Bond Hydrogenation on Pt/TiO $_2$: Catalytic Reaction and Sum-Frequency Generation Vibrational Spectroscopy Studies of Crotonaldehyde Hydrogenation. *Angew. Chem.* **2014**, *126*, 3473–3476.

(46) Wang, H.; Sapi, A.; Thompson, C. M.; Liu, F.; Zherebetskyy, D.; Krier, J. M.; Carl, L. M.; Cai, X.; Wang, L.-W.; Somorjai, G. A. Dramatically Different Kinetics and Mechanism at Solid/Liquid and Solid/Gas Interfaces for Catalytic Isopropanol Oxidation over Size-Controlled Platinum Nanoparticles. *J. Am. Chem. Soc.* **2014**, *136*, 10515–10520.

(47) Aliaga, C.; Park, J. Y.; Yamada, Y.; Lee, H. S.; Tsung, C.-K.; Yang, P.; Somorjai, G. A. Sum Frequency Generation and Catalytic Reaction Studies of the Removal of Organic Capping Agents from Pt Nanoparticles by UV−Ozone Treatment. *J. Phys. Chem. C* **2009**, *113*, 6150–6155.

(48) Lu, X.; Shephard, N.; Han, J.; Xue, G.; Chen, Z. Probing Molecular Structures of Polymer/Metal Interfaces by Sum Frequency Generation Vibrational Spectroscopy. *Macromolecules* **2008**, *41*, 8770–8777.

(49) Lu, X.; Li, D.; Kristalyn, C. B.; Han, J.; Shephard, N.; Rhodes, S.; Xue, G.; Chen, Z. Directly Probing Molecular Ordering at the Buried Polymer/Metal Interface. *Macromolecules* **2009**, *42*, 9052–9057.

(50) Lu, X.; Li, B.; Zhu, P.; Xue, G.; Li, D. Illustrating Consistency of Different Experimental Approaches to Probe the Buried Polymer/metal Interface Using Sum Frequency Generation Vibrational Spectroscopy. *Soft Matter* **2014**, *10*, 5390.

(51) Lu, X.; Xue, G.; Wang, X.; Han, J.; Han, X.; Hankett, J.; Li, D.; Chen, Z. Directly Probing Molecular Ordering at the Buried Polymer/Metal Interface 2: Using P-Polarized Input Beams. *Macromolecules* **2012**, *45*, 6087–6094.

(52) Boyd, R. W. *Nonlinear Optics*; 3rd ed.; Academic Press: Amsterdam ; Boston, 2008.

(53) Shen, Y. R. *The Principles of Nonlinear Optics*; Wiley classics library; Wiley classics library ed.; Wiley-Interscience: Hoboken, N.J, 2003.

(54) Wang, J.; Chen, C.; Buck, S. M.; Chen, Z. Molecular Chemical Structure on Poly(methyl Methacrylate) (PMMA) Surface Studied by Sum Frequency Generation (SFG) Vibrational Spectroscopy. *J. Phys. Chem. B* **2001**, *105*, 12118–12125.

(55) Hall, S. A.; Jena, K. C.; Covert, P. A.; Roy, S.; Trudeau, T. G.; Hore, D. K. Molecular-Level Surface Structure from Nonlinear Vibrational Spectroscopy Combined with Simulations. *J. Phys. Chem. B* **2014**, *118*, 5617–5636.

(56) Roy, S.; Hung, K.-K.; Stege, U.; Hore, D. K. Rotations, Projections, Direction Cosines, and Vibrational Spectra. *Appl. Spectrosc. Rev.* **2014**, *49*, 233–248.

(57) Covert, P. A.; FitzGerald, W. R.; Hore, D. K. Simultaneous Measurement of Magnitude and Phase in Interferometric Sum-Frequency Vibrational Spectroscopy. *J. Chem. Phys.* **2012**, *137*, 014201.

(58) Roy, S.; Post, J. S.; Hung, K.-K.; Stege, U.; Hore, D. K. 2D Correlation Analysis in Vibrational Sum-Frequency Generation Spectroscopy. *J. Mol. Struct.* **2014**, *1069*, 103–111.

(59) Shen, Y. R. Basic Theory of Surface Sum-Frequency Generation. *J. Phys. Chem. C* **2012**, *116*, 15505–15509.

(60) Shen, Y. R. Phase-Sensitive Sum-Frequency Spectroscopy. *Annu. Rev. Phys. Chem.* **2013**, *64*, 129–150.

(61) Ji, N.; Ostroverkhov, V.; Belkin, M.; Shiu, Y.-J.; Shen, Y.-R. Toward Chiral Sum-Frequency Spectroscopy. *J. Am. Chem. Soc.* **2006**, *128*, 8845–8848.

(62) McGuire, J. A.; Shen, Y. R. Signal and Noise in Fourier-Transform Sum-Frequency Surface Vibrational Spectroscopy with Femtosecond Lasers. *J. Opt. Soc. Am. B* **2006**, *23*, 363.

(63) Tong, Y.; Zhao, Y.; Li, N.; Osawa, M.; Davies, P. B.; Ye, S. Interference Effects in the Sum Frequency Generation Spectra of Thin Organic Films. I. Theoretical Modeling and Simulation. *J. Chem. Phys.* **2010**, *133*, 034704.

(64) Backus, E. H. G.; Garcia-Araez, N.; Bonn, M.; Bakker, H. J. On the Role of Fresnel Factors in Sum-Frequency Generation Spectroscopy of Metal–Water and Metal-Oxide–Water Interfaces. *J. Phys. Chem. C* **2012**, *116*, 23351–23361.

(65) Lu, X.; Clarke, M. L.; Li, D.; Wang, X.; Xue, G.; Chen, Z. A Sum Frequency Generation Vibrational Study of the Interference Effect in Poly(*n* -Butyl Methacrylate) Thin Films Sandwiched between Silica and Water. *J. Phys. Chem. C* **2011**, *115*, 13759–13767.

(66) Lambert, A. G.; Davies, P. B.; Neivandt, D. J. Implementing the Theory of Sum Frequency Generation Vibrational Spectroscopy: A Tutorial Review. *Appl. Spectrosc. Rev.* **2005**, *40*, 103–145.

(67) Wang, J.; Paszti, Z.; Even, M. A.; Chen, Z. Measuring Polymer Surface Ordering Differences in Air and Water by Sum Frequency Generation Vibrational Spectroscopy. *J. Am. Chem. Soc.* **2002**, *124*, 7016–7023.

(68) Gan, W.; Wu, D.; Zhang, Z.; Feng, R.; Wang, H. Polarization and Experimental Configuration Analyses of Sum Frequency Generation Vibrational Spectra, Structure, and Orientational Motion of the Air/water Interface. *J. Chem. Phys.* **2006**, *124*, 114705.

(69) O'Brien, D. B.; Massari, A. M. Modeling Multilayer Thin Film Interference Effects in Interface-Specific Coherent Nonlinear Optical Spectroscopies. *J. Opt. Soc. Am. B* **2013**, *30*, 1503.

(70) O'Brien, D. B.; Massari, A. M. Simulated Vibrational Sum Frequency Generation from a Multilayer Thin Film System with Two Active Interfaces. *J. Chem. Phys.* **2013**, *138*, 154708.

(71) Holman, J.; Davies, P. B.; Nishida, T.; Ye, S.; Neivandt, D. J. Sum Frequency Generation from Langmuir−Blodgett Multilayer Films on Metal and Dielectric Substrates. *J. Phys. Chem. B* **2005**, *109*, 18723–18732.

(72) Dreesen, L.; Humbert, C.; Celebi, M.; Lemaire, J. J.; Mani, A. A.; Thiry, P. A.; Peremans, A. Influence of the Metal Electronic Properties on the Sum-Frequency Generation Spectra of Dodecanethiol Self-Assembled Monolayers on Pt (111), Ag (111) and Au (111) Single Crystals. *Appl. Phys. B* **2002**, *74*, 621–625.

(73) Chen, C.; Wang, J.; Chen, Z. Surface Restructuring Behavior of Various Types of Poly(dimethylsiloxane) in Water Detected by SFG. *Langmuir* **2004**, *20*, 10186–10193.

(74) Zhang, D.; Ward, R. S.; Shen, Y. R.; Somorjai, G. A. Environment-Induced Surface Structural Changes of a Polymer: An *in Situ* IR + Visible Sum-Frequency Spectroscopic Study. *J. Phys. Chem. B* **1997**, *101*, 9060–9064.

(75) Opdahl, A.; Phillips, R. A.; Somorjai, G. A. Surface Segregation of Methyl Side Branches Monitored by Sum Frequency Generation (SFG) Vibrational Spectroscopy for a Series of Random Poly(ethylene- *co* -Propylene) Copolymers. *J. Phys. Chem. B* **2002**, *106*, 5212–5220.

(76) Kweskin, S. J.; Komvopoulos, K.; Somorjai, G. A. Molecular Restructuring at Poly(*n* -Butyl Methacrylate) and Poly(methyl Methacrylate) Surfaces Due to Compression by a Sapphire Prism Studied by Infrared−Visible Sum Frequency Generation Vibrational Spectroscopy. *Langmuir* **2005**, *21*, 3647–3652.

(77) Zhang, C.; Shephard, N. E.; Rhodes, S. M.; Chen, Z. Headgroup Effect on Silane Structures at Buried Polymer/Silane and Polymer/Polymer Interfaces and Their Relations to Adhesion. *Langmuir* **2012**, *28*, 6052–6059.

(78) Zhuang, X.; Miranda, P.; Kim, D.; Shen, Y. Mapping Molecular Orientation and Conformation at Interfaces by Surface Nonlinear Optics. *Phys. Rev. B* **1999**, *59*, 12632–12640.

(79) Watanabe, N.; Yamamoto, H.; Wada, A.; Domen, K.; Hirose, C.; Ohtake, T.; Mino, N. Vibrational Sum-Frequency Generation (VSFG) Spectra of N-Alkyltrichlorosilanes Chemisorbed on Quartz Plate. *Spectrochim. Acta Part Mol. Spectrosc.* **1994**, *50*, 1529–1537.

(80) Sipe, J.; Moss, D.; van Driel, H. Phenomenological Theory of Optical Second- and Third-Harmonic Generation from Cubic Centrosymmetric Crystals. *Phys. Rev. B* **1987**, *35*, 1129–1141.

(81) Tom, H.; Heinz, T.; Shen, Y. Second-Harmonic Reflection from Silicon Surfaces and Its Relation to Structural Symmetry. *Phys. Rev. Lett.* **1983**, *51*, 1983–1986.

(82) Malyk, S.; Shalhout, F. Y.; O'Leary, L. E.; Lewis, N. S.; Benderskii, A. V. Vibrational Sum Frequency Spectroscopic Investigation of the Azimuthal Anisotropy and Rotational Dynamics of Methyl-Terminated Silicon(111) Surfaces. *J. Phys. Chem. C* **2013**, *117*, 935–944.

(83) York, R. L.; Li, Y.; Holinga, G. J.; Somorjai, G. A. Sum Frequency Generation Vibrational Spectra: The Influence of Experimental Geometry for an Absorptive Medium or Media. *J. Phys. Chem. A* **2009**, *113*, 2768–2774.

(84) Hirose, C.; Akamatsu, N.; Domen, K. Formulas for the Analysis of Surface Sum-Frequency Generation Spectrum by CH Stretching Modes of Methyl and Methylene Groups. *J. Chem. Phys.* **1992**, *96*, 997.

(85) Braun, R.; Casson, B. D.; Bain, C. D.; van der Ham, E. W. M.; Vrehen, Q. H. F.; Eliel, E. R.; Briggs, A. M.; Davies, P. B. Sum-Frequency Generation from Thiophenol on Silver in the Mid and Far-IR. *J. Chem. Phys.* **1999**, *110*, 4634.

(86) Bain, C. D.; Davies, P. B.; Ong, T. H.; Ward, R. N.; Brown, M. A. Quantitative Analysis of Monolayer Composition by Sum-Frequency Vibrational Spectroscopy. *Langmuir* **1991**, *7*, 1563–1566.

(87) Palik, E. D.; Ghosh, G. *Handbook of Optical Constants of Solids*; Academic Press: Orlando, 1985.

Chapter 8

PLASMA TREATMENT EFFECTS ON MOLECULAR STRUCTURES AT DENSE AND POROUS LOW-K SICOH FILM SURFACES AND BURIED INTERFACES

8.1 Introduction

Porous organosilicate (pSiCOH) dielectrics with dielectric constants (k) lower than silica have been successfully integrated in modern integrated circuits as the interlayer dielectric (ILD) of copper interconnect structures.[1] As the dimensions of interconnects continue to decrease, the interfaces of the ILD material will constitute a larger portion of the ILD. Therefore, the interfacial properties of the ILD will increasingly determine the physical properties of the ILD. Consequently, many of the challenges of integrating low-k dielectrics in very large scale integrated chips have been related to ILD interfaces.[2-4]

One key reliability issue found in the integration of low-k dielectrics has been delamination that occurs at low-k interfaces during fabrication, reliability testing, or packaging due to weak interfacial adhesion strength.[5] In particular, the interface between low-k dielectrics and dielectric diffusion caps (e.g., SiCNH) has been reported to have weak adhesion strength.[6,7] Grill et al. reported that the weak adhesion strength at a SiCOH/SiCNH interface was caused by a thin layer of SiCOH near the SiCOH/SiCNH interface that had a weaker cohesive strength than the bulk SiCOH.[2] Failure analysis indicated that the elemental composition of a thin interfacial SiCOH layer had a higher percentage of carbon than the composition of the bulk SiCOH. To improve the interfacial adhesion strength, the elemental composition of the SiCOH near the dielectric cap interface was adjusted to more closely match the composition of the SiCOH bulk

through modification of the PECVD deposition parameters. After adjusting the interfacial molecular structure, the adhesion strength at the SiCOH/SiCNH interface increased to a value near the bulk cohesive strength of the SiCOH bulk. More generally, the results of this study indicate that the molecular structure at the SiCOH/SiCNH interface largely determined the interfacial adhesion strength. In addition to interfacial adhesion, several other ILD integration challenges have been found to occur at ILD interfaces such as low-k breakdown,[3] moisture diffusion,[7] and plasma-induced damage.[8] Further requirements and challenges for the successful integration of low-k dielectrics in very large-scale integrated interconnects which take into account the bulk properties of the ILD can be found elsewhere.[1,9]

The physical properties of an interface are strongly dependent on the interfacial molecular structure. Physical and chemical interactions at the interface between two materials (e.g., polymer/solid or polymer/air) can result in molecular restructuring of one or both of the materials at the interface.[10,11] Molecular restructuring near an interface can result in substantially different physical properties of the restructured material near the interface relative to the bulk properties. Therefore, to control the molecular structure and physical properties of low-k dielectric interfaces (e.g., SiCOH/air and SiCOH/SiCNH) for rational interface engineering, relationships between interfacial molecular structures and interfacial properties need to be elucidated. However, structure–property relationships at low-k/air and low-k/dielectric barrier interfaces are not well understood due to a lack of techniques that can nondestructively characterize molecular structures at low-k surfaces and buried interfaces.

In the last two chapters, we reported our studies on model low-k materials. In this research, we investigated low-k samples provided by our industrial collaborators. We utilized SFG to characterize the molecular structure at the low-k/air and Si/SiO_2/low-k interfaces of

silicon-supported low-k SiCOH films (provided by Intel) before and after plasma treatment. The effects of plasma treatment on the molecular structures at the interfaces were compared to the bulk damage by comparing SFG and Raman spectra collected from the films before and after plasma damage. In previous work, SFG and ATR-FTIR were used to elucidate the behavior of water at low-k surfaces and buried interfaces.[12] Here we applied the methodology developed in chapter 5 to separate contributions from the low-k/air and Si/SiO_2/low-k interfaces to SFG spectra collected from silicon-supported SiCOH films.[13] To investigate how the porosity of SiCOH films affects plasma-induced damage, two plasma-enhanced chemical vapor deposition (PECVD) deposited low-k SiCOH films with porosities of ~7% (dense) and ~25% (porous) were studied.

8.2 Experimental Section

8.2.1 Materials

SiCOH films were deposited on Si(100) substrates using PECVD. Details about the PECVD deposition parameters can be found elsewhere.[14] Plasma treatment was performed by exposing SiCOH films to oxygen plasma for 5 s using a plasma cleaning system (Plasma Etch PE-50). Hydrogenated 1,2-dipalmitoyl(d62)-sn-glycero-3-phosphoglycerol (DPPG) was purchased from Avanti Polar Lipids Inc. (Alabaster, AL). DPPG monolayers were deposited on silicon (100) wafers which had a ~90 nm thermal oxide layer using a Langmuir–Blodgett method that has been previously described in detail.[15]

8.2.2 Raman Spectroscopy

Raman spectra were acquired from low-k films in a backscattering geometry without polarizing optics using a Renishaw inVia Raman microscope. The Raman microscope was equipped with a Nd:YAG 532 nm laser with a 150 mW illuminating power, an Olympus

LMPIanFLN 100× objective (numerical aperture = 0.8), a 1800 lines/mm grating, a 65 μm slit, and a RenCam CCD detector. Raman spectra were collected using the extended scan mode in the 1100–3600 cm^{-1} range with a 10 s exposure time, and all spectra represent the average of five scans. All Raman spectra were collected under ambient conditions. Raman spectra acquired from a bare region of silicon (100) substrates were used as a background and were subtracted from all presented Raman spectra. Raman signal in the 1000–1100 cm^{-1} range was not analyzed due to spectral interference from the silicon substrate.

8.2.3 Sum Frequency Generation Spectroscopy

SFG has been recently developed into an analytical technique that provides characterization of molecular structures at surfaces and buried interface in situ.[16-21] SFG spectra were acquired in the SSP and PPP polarization combinations from silicon-supported SiCOH films in a face-up geometry (Figure 8.1) using a commercial SFG spectrometer purchased from EKSPLA. Descriptions of the SFG spectrometer can be found in chapter 1.[22] The input visible and infrared input angles were 60 ° and 54 °, respectively. The pulse energies of the visible and infrared beams were ~9 and ~90 μJ, respectively. Beyond chapter 1, more detailed descriptions of SFG theory and applications can be found elsewhere.[23-36]

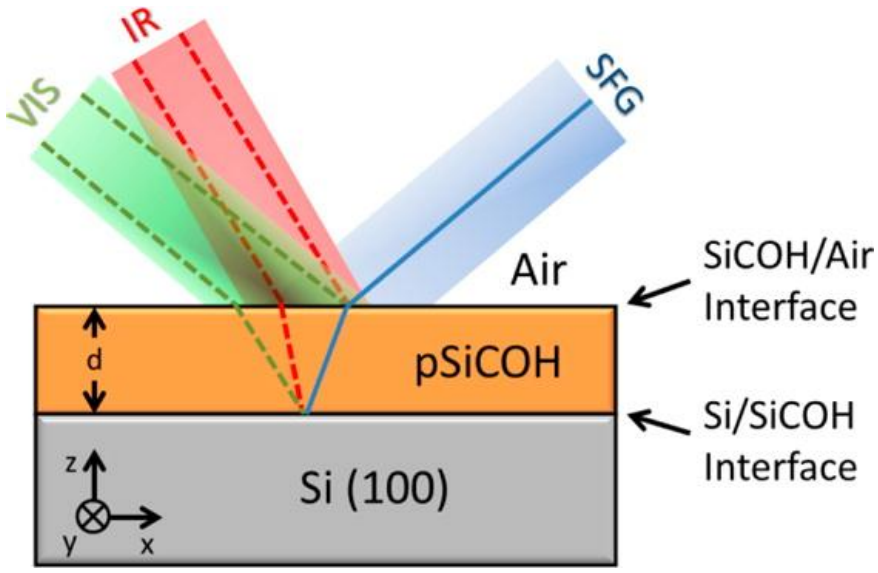

Figure 8.1. Schematic diagram of the face-up SFG experimental geometry.

8.3 Results and Discussion

8.3.1 Characterization of the Dense SiCOH Bulk

PECVD deposited low-k films, which are commonly referred to as SiCOH films, have a similar molecular structure as poly(methylsilsesquioxane).[37] However, the SiCOH skeleton does not contain silsesquioxane cages but is primarily composed of three SiO bond structures: SiO cage, SiO network, and suboxide bonds.[38] Detailed descriptions of the bond structure of bulk pSiCOH films can be found elsewhere.[38,39] Two SiCOH films with different porosities were investigated. First, a SiCOH film which was deposited without added porogon was studied. This film had an intrinsic porosity of ~7% and was considered a relatively dense film. A SiCOH film that was deposited using porogen which had ~25% porosity was then utilized as a porous film for comparison to the dense film. Descriptions of the mechanical, optical, and electrical properties of similar dense and porous SiCOH films can be found elsewhere.[1]

We first investigated how the bulk molecular structure of a dense SiCOH film was altered by a short oxygen plasma treatment using Raman spectroscopy. Features were detected near 2970, 2910, 2240, 1430, and 1000 cm^{-1} in the Raman spectra collected from pristine and oxygen plasma treated dense SiCOH films (Figure 8.2) which can be assigned to the methyl C–H asymmetric stretch, methyl C–H symmetric stretch, Si–H stretch, methyl bending, and Si–O–Si vibrational modes, respectively.[40-42] The peaks near 1000 cm^{-1} (not displayed) were not used for analysis due to interference from Raman signal generated from the silicon wafer substrate in the same spectral region. The intensities of the peaks near 2970 and 2910 cm^{-1} were relatively constant before and after oxygen plasma treatment. One weak feature was observed in the Raman difference spectrum between the plasma-treated and the pristine SiCOH film. The weak feature in the difference spectrum suggests that there were fewer methyl groups present in the plasma-treated film relative to the pristine dense film. Oxygen plasma treatment of SiCOH films has been reported to oxidize surface methyl groups,[43] which is consistent with the slight decrease in the methyl Raman peak intensity after plasma treatment. However, no substantial features were detected in the Raman difference spectrum which indicates that oxygen plasma treatment did not lead to substantial oxidation of the methyl groups in the bulk of the dense SiCOH film. Therefore, the Raman spectra indicate that short plasma treatment did not substantially alter the bulk molecular structure of the dense SiCOH film.

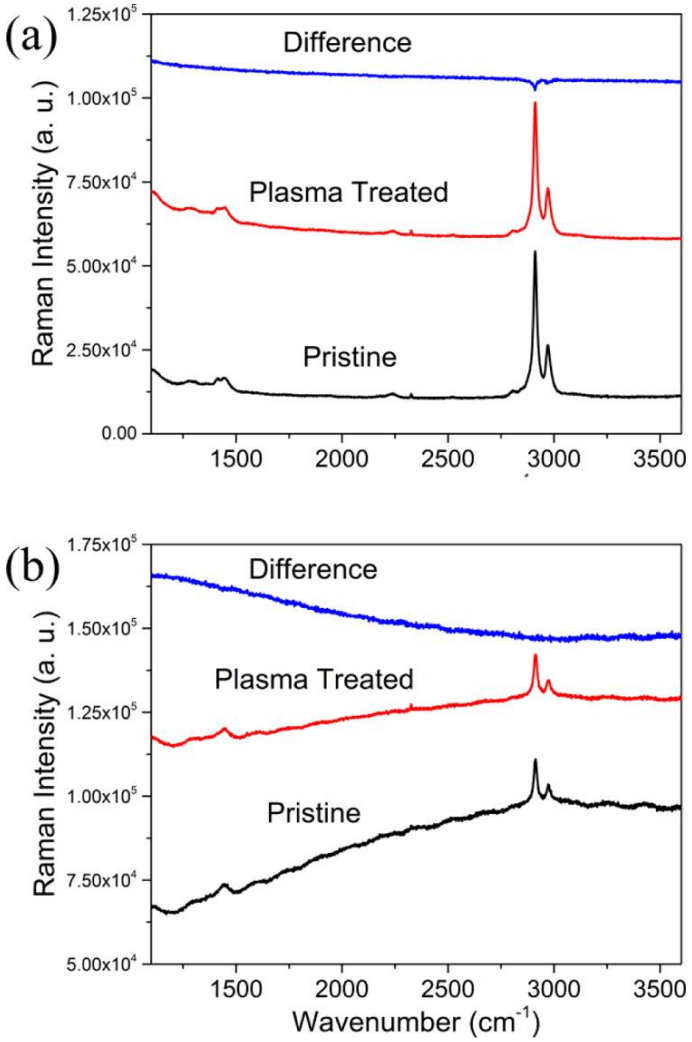

Figure 8.2. Raman spectra collected from (a) dense and (b) porous SiCOH films before and after plasma treatment.

8.3.2 Characterization of the Dense SiCOH/Air Interface

After characterizing the effect of plasma treatment on the bulk molecular structure of a dense SiCOH film, the effect of plasma treatment on the molecular structure at the dense SiCOH/air and Si/dense SiCOH interfaces was investigated using SFG. In the previous chapter we showed that SFG signal acquired in the SSP polarization combination from ~100 nm thick low-k films deposited on silicon wafer substrates would selectively probe the low-k/air interface

with negligible contribution from the Si/SiO_2/low-k buried interface.[13] Two features near 2925 and 2975 cm^{-1} were detected in the SFG SSP spectrum acquired from a dense SiCOH film (Figure 8.3) which can be assigned to the $Si–CH_3$ C–H symmetric and asymmetric stretching vibrational modes, respectively.[44] The detection of features contributed by $Si–CH_3$ groups in the SFG SSP spectrum indicates that $Si–CH_3$ groups were ordered at the low-k/air interface. The $Si–CH_3$ symmetric feature appeared as a dip while the asymmetric appeared as a peak due to the interference between the resonant signal and the nonresonant background.[45] The strong symmetric peak intensity indicates that the ordered $Si–CH_3$ groups were oriented near the surface normal.[13,46]

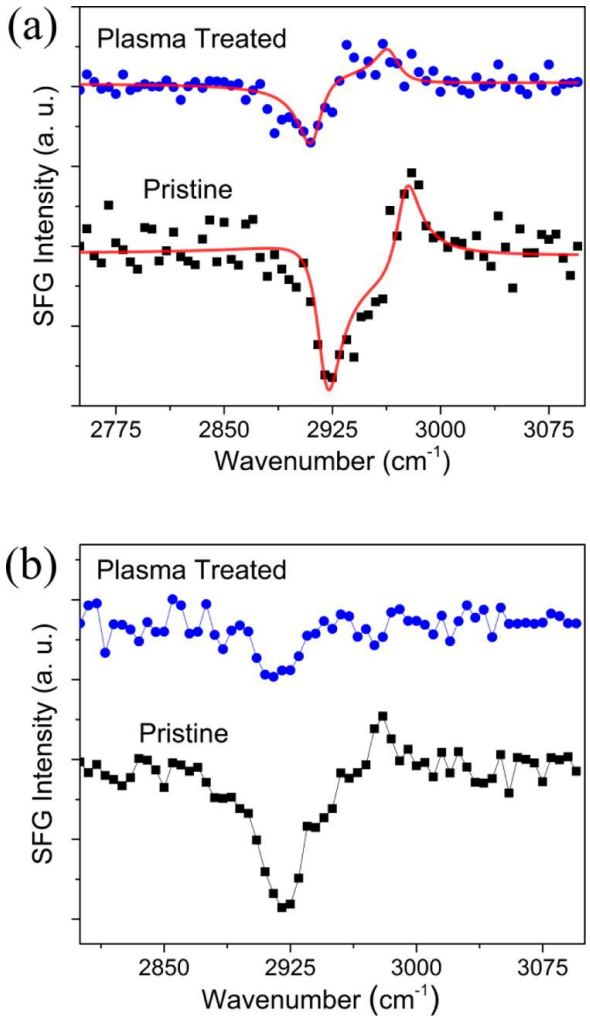

Figure 8.3. SFG (a) SSP and (b) PPP spectra acquired from a dense SiCOH film before and after oxygen plasma treatment.

The orientation of the Si–CH_3 groups at the dense SiCOH/air interface was deduced by comparing experimentally determined methyl $\chi_{yyz,as}/\chi_{yyz,ss}$ ratios to theoretical $\chi_{yyz,as}/\chi_{yyz,ss}$ values (Figure 8.4, Table 8.1). The experimental $\chi_{yyz,as}/\chi_{yyz,ss}$ ratio suggests that the Si–CH_3 groups at the pristine dense SiCOH/air interface were oriented at ~48 °relative to the surface normal.

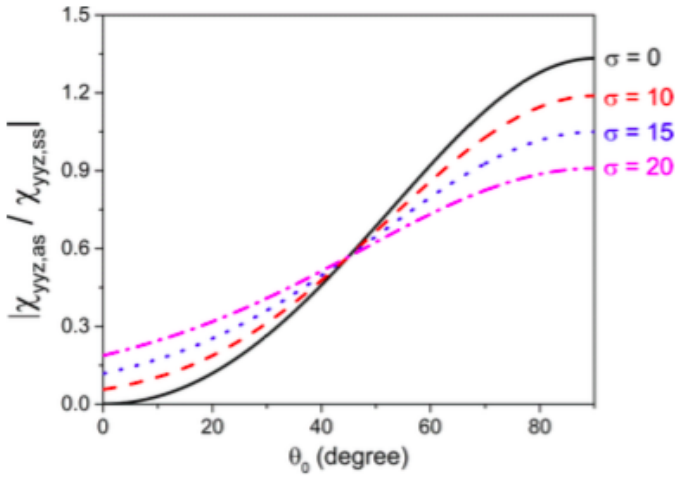

Figure 8.4. Methyl $\chi_{yyz,as}/\chi_{yyz,ss}$ ratio plotted as a function of methyl tilt angle.

Dense SiCOH SFG Fitting Results

ω_q (cm^{-1})	$A_{q,ssp}$	Γ_q (cm^{-1})	χ_{NR}	Φ
Pristine				
2920	4.5 ± 0.6	10.0 ± 2.0	8.0 ± 0.1	-2.1 ± 0.1
2975	-2.8 ± 0.5	10.0 ± 2.1		
Plasma Damaged				
2912	2.1 ± 0.4	10.0 ± 2.1	8.0 ± 0.1	-1.1 ± 0.1
2965	-1.0 ± 0.5	10.0 ± 3.9		

Table 8.1. Fitting results for SFG SSP spectra acquired from pristine and plasma treated dense SiCOH films.

SFG SSP spectrum was then collected from a dense SiCOH film which had been plasma treated. Two features near 2920 and 2970 cm^{-1} were detected in the SFG SSP spectrum collected from a plasma-treated dense SiCOH film (Figure 8.3). However, the feature intensities were lower than the corresponding intensities in the SFG spectrum acquired from the pristine film. In addition, the C–H symmetric stretching feature appeared as a dip while the asymmetric peak appeared as a peak. The peak shapes observed in the SFG SSP spectra acquired from pristine and plasma-treated SiCOH films will be discussed later. After plasma treatment, the orientation of methyl groups at the dense SiCOH/air interface was ~41 °. The different methyl group orientations at the dense SiCOH/air interface before and after oxygen plasma treatment may be due to oxidization of the SiCOH surface. Previous studies reported that oxygen plasma treatment of low-k films produced a silica-like layer near the film surface.[47,48] Si–CH_3 groups, which are bonded to oxygen atoms in the SiCOH network, may be locked into different configurations in the oxidized silica-like network relative to the pristine SiCOH surface.

Although the dense SiCOH surface was likely oxidized to a silica-like layer, the detection of features contributed by methyl groups in the SFG spectra acquired from the plasma-treated dense SiCOH/air interface indicate that methyl groups were still present at the dense SiCOH/air interface after plasma treatment. To estimate the effects of the plasma treatment on the surface coverage of methyl groups at the dense SiCOH/air interface, experimentally measured $\chi_{yyz,ss}$ values (obtained by spectral fitting) before and after plasma treatment were compared. The orientations of the methyl groups at the dense SiCOH/air interface before and after plasma treatment were already deduced; therefore, the ratio of the methyl number density at the surface after plasma treatment to the methyl density at the surface before plasma treatment ($N_{s,I,after}/N_{s,I,\ before}$) could then be determined by assuming a delta distribution for the methyl

orientation at the surface (equation 8.1). Values for cosθ and $\cos^3\theta$ were solved for by using the experimentally determined methyl average orientation as input values. The left side of equation 8.1 was solved for using the experimental fitting results. We believe that a delta distribution can be used to describe the average methyl orientation angle and therefore enables characterization of the average molecular structure of the surface before and after plasma treatment. The $N_{s,I,after}/N_{s,I,\ before}$ ratio for the dense SiCOH film surface was 0.36, which indicates that the methyl surface coverage after plasma treatment was ~36% of the surface coverage at the pristine dense SiCOH/air interface. Decreased methyl surface coverage is consistent with previous studies that reported that oxygen plasma treatment substantially depleted methyl groups at low-k/air interfaces.[49]

$$\frac{\chi^{(2)}_{yyz,ss,after}}{\chi^{(2)}_{yyz,ss,before}} = \frac{\frac{1}{2}\langle N_{s,1,after}\rangle\beta^{(2)}_{ccc}[\langle cos\theta\rangle(1+R)-\langle cos^3\theta\rangle(1-R)]}{\frac{1}{2}\langle N_{s,1,before}\rangle\beta^{(2)}_{ccc}[\langle cos\theta\rangle(1+R)-\langle cos^3\theta\rangle(1-R)]} \quad (8.1)$$

The similar peak shapes in the SFG spectrum acquired from plasma damaged dense SiCOH films relative to the SFG SSP spectrum acquired from pristine dense SiCOH films suggest that the sign of the methyl resonant susceptibility at the dense SiCOH/air interface ($\chi^{(2)}_{yyz}$) had not switched after plasma treatment.[50] Therefore, plasma treatment resulted in ordered methyl groups at the plasma treated dense SiCOH/air interface that had the same absolute orientation relative to methyl groups at the pristine dense SiCOH/air interface.[50] The absolute orientation of the methyl groups at the low-k/air interface before and after plasma treatment was then deduced by calibrating the phase difference between resonant signal from oriented methyl groups and a nonresonant signal from a silicon (100) substrate. The phase difference was calibrated by depositing a monolayer of DPPG on a silicon (100) wafer that had a ~90 nm surface thermal oxide. The methyl group of a DPPG monolayer should be directed away from

the silicon wafer toward the air.[51] The distance between SFG signal generated at the silicon and at the DPPG monolayer, which is approximately the same distance between the nonresonant SFG signal generated from a silicon wafer and the resonant signal generated at the dense SiCOH/air interface, was fixed by the thermal oxide thickness.

Three features were detected in the SFG SSP spectrum collected from the DPPG monolayer (Figure 8.5) near 2890, 2940, and 2965 cm^{-1} which can be assigned to the methyl symmetric stretching, methyl Fermi resonance, and methyl asymmetric stretching vibrational modes, respectively.[45] DPPG molecules have one methyl group at the end of an alkyl chain which indicates that the methyl features detected in the SFG spectrum were contributed by the terminal methyl group of DPPG. The methyl symmetric stretching and Fermi resonance, which are assumed to share the same symmetry,[52] both appeared as dips in the spectra while the asymmetric feature appeared as a peak. The feature shapes in the SFG spectrum collected from the DPPG monolayer indicate that SFG signal contributed by symmetric stretching vibrational modes of methyl groups that are located ~100 nm away from the silicon and are oriented "pointing away" from the silicon bulk will appear as a dip in SFG spectra and the asymmetric stretching mode will appear as a peak. The methyl symmetric stretch feature appeared as a dip in the SFG spectrum acquired from a dense SiCOH film while the asymmetric feature appeared as a peak, which indicates that methyl groups at the dense SiCOH/air interface were oriented "pointing away" from the silicon substrate, toward the air.

In summary, the orientation of methyl groups at the dense SiCOH/air interface before and after plasma treatment was ~48 ° and ~41 °, respectively. The methyl surface coverage decreased by ~64% after plasma treatment. The absolute orientation of methyl groups at the dense SiCOH/air interface was "pointing away" before and after plasma treatment.

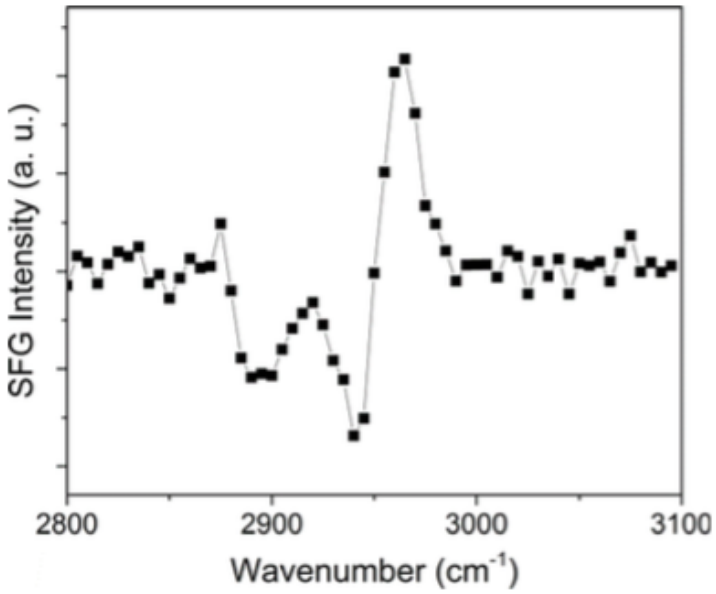

Figure 8.5. SFG SSP spectrum acquired from a DPPG monolayer deposited on a silicon wafer that had a ~90 nm thick thermal oxide layer.

8.3.3 Characterization of the Buried Si/Dense SiCOH Interface

SFG PPP spectra were then collected from a dense SiCOH film to characterize the Si/dense SiCOH buried interface. Unlike SFG spectra collected in the SSP polarization combination, SFG PPP spectra collected from silicon-supported low-k films will have contributions from both the low-k/air and Si/low-k interfaces. Two features near 2920 and 2980 cm^{-1} were detected in the SFG PPP spectrum acquired from a dense SiCOH film (Figure 8.3). The Si–CH_3 C–H symmetric stretch feature appeared as a dip while the asymmetric feature appeared as a peak in the SFG PPP spectrum. SFG PPP spectrum was then collected from a dense SiCOH film that had been plasma treated. One feature near 2920 cm^{-1} that appeared as a dip was detected in the SFG PPP spectrum acquired from a plasma-treated dense SiCOH film (Figure 8.3).

To investigate the interference between the surface and buried interface SFG signals in the SFG PPP spectra acquired from a dense SiCOH film, SFG PPP spectra were simulated before and after plasma treatment for the dense SiCOH films.[13] Details about the determination of Fresnel coefficients in similar multilayer systems can be found in chapter 1.[52-56] SFG spectra were simulated after plasma treatment by adjusting the orientation and N_s parameters for methyl groups at the dense SiCOH/air interface. The methyl group orientation after plasma treatment was set as 41 °, and the surface methyl depletion was taken into account by setting $N_{s,I,after} = 0.36*N_{s,I,before}$. Short oxygen plasma treatment of SiCOH films has been reported to oxidize the surface of low-k dielectric films. However, short oxygen plasma treatment is not expected to substantially alter the bulk SiCOH structure, so $N_{s,II}$ was assumed to be constant before and after plasma treatment.

SFG spectra were first simulated by varying the nonresonant signal until the peak shapes in the simulated spectra approximately matched the peak shapes detected in the experimentally observed spectra. The simulated SFG spectrum that resembled the experimentally observed spectrum was then optimized by varying the methyl tilt angle parameter at the buried Si/dense SiCOH interface. The simulated SFG spectrum that most closely resembled the experimentally observed SFG spectrum was then selected. After the simulated SFG spectrum that best fit the experimentally observed SFG spectrum was selected, the contributions from the dense SiCOH/air and dense SiCOH/Si interfaces to the detected SFG spectrum were simulated to elucidate the molecular structure at each interface. To characterize the buried Si/dense SiCOH interface, plasma-treated films were simulated first because the buried interface will contribute more to the SFG signal relative to the contribution of the buried interface to the SFG signal

generated from a pristine film due to the lower methyl number density at the plasma treated SiCOH film surface.

Two features near 2920 and 2965 cm^{-1} were present in the simulated SFG spectra from a plasma-treated dense SiCOH film (Figure 8.6b). Figure 8.6b shows that the intensity of the asymmetric feature changed as the methyl orientation angle at the buried interface varied from 10 ° to 80 °. For example, the asymmetric feature intensity was strong when the buried methyl groups were oriented at ~40 °–50 °, and the feature intensity was weak when the buried methyl groups were oriented at ~80 ° (Figures 8.6b,d). However, the intensity of the symmetric feature was relatively constant at different methyl tilt angles at the buried interface. The similarity between the simulated SFG spectra with a methyl orientation of ~80 ° or ~20 ° at the dense SiCOH/Si interface and the experimentally observed SFG spectrum acquired from plasma treated dense SiCOH films suggests that methyl groups at the buried Si/PMSQ interface had a very low or very high tilt angle (Figure 8.6a). A previous study indicated that methyl groups at the PMSQ/Si interface were oriented with a very high tilt angle.[13] Furthermore, methyl groups at buried metal/polymer interfaces have been reported to be oriented at very high tilt angles.[56] Based on the similar molecular structures of PMSQ and SiCOH and that methyl groups tend to be oriented with very high tilt angles at buried metal/polymer interfaces, the orientation of methyl groups at the dense SiCOH/Si interface was likely ~80 ° rather than ~20 °.

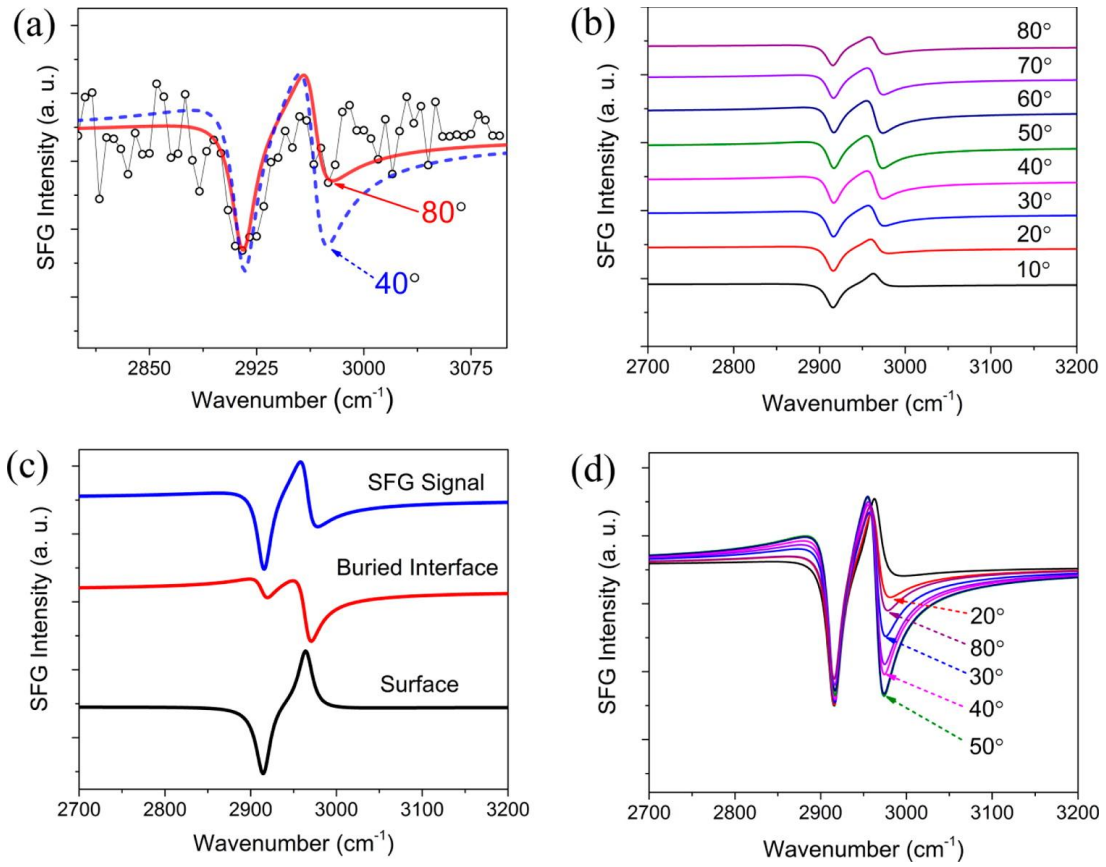

Figure 8.6. (a) Experimental and simulated SFG PPP spectra acquired from a dense SiCOH film after oxygen plasma treatment. The unfilled circles display the experimental data points, and the solid curves display the simulated SFG spectra when the buried methyl tilt angle was set at 40 °or 80 °. (b) Simulated SFG PPP spectra from a plasma-treated dense SiCOH film where the methyl group orientation at the buried interface was varied between 10 ° and 90 °. The curves were offset successively for clarity. (c) Simulated SFG PPP spectrum from a plasma-treated dense SiCOH film together with the surface and buried interface components of the simulated SFG signal. (d) Simulated SFG PPP spectra from a plasma-treated dense SiCOH film where the methyl group orientation at the buried interface was varied between 10 °and 90 °. The curves were not offset for comparison to (b).

After the SFG spectra from a plasma-treated dense SiCOH film was simulated, the contributions from the surface and buried interface were plotted (Figure 8.6c). The SFG signal contributed from the buried interface was dominated by a methyl asymmetric feature that appeared as a dip which is consistent with the high methyl tilt angle at the buried interface. The SFG signal contributed from the surface had two features of similar intensity contributed by the

methyl symmetric and asymmetric stretches. The strong symmetric feature in the SFG signal contributed from the plasma-treated surface is consistent with the relatively low methyl tilt angle observed at the dense SiCOH film surface. Although both the surface and buried interface signal had features contributed by the methyl asymmetric stretch, only a methyl symmetric stretch feature was detected in the experimentally observed SFG spectrum acquired from a plasma-treated dense SiCOH film. The opposite peak shapes of the asymmetric feature in the SFG spectra contributed from the surface and buried interface, respectively, suggest that destructive interference weakened the asymmetric feature in the detected SFG signal.

After the molecular structure of the buried interface at the plasma-treated dense SiCOH/Si interface was characterized, a similar analysis was performed to characterize the molecular structure at the pristine dense SiCOH/Si interface. As indicated above, the dense SiCOH/air interface contributed substantially more to the SFG signal relative to the plasma-treated dense SiCOH/air interface due to a higher methyl density at the pristine surface. Consequently, different methyl tilt angles only slightly affected the simulated SFG spectra from a pristine dense SiCOH film (Figure 8.7b). Figure 8.7b displays the experimentally detected SFG PPP spectrum acquired from a pristine dense SiCOH film and simulated SFG PPP spectra from a pristine dense SiCOH film where the buried methyl tilt angle parameter was set at 50 ° or 80 °.

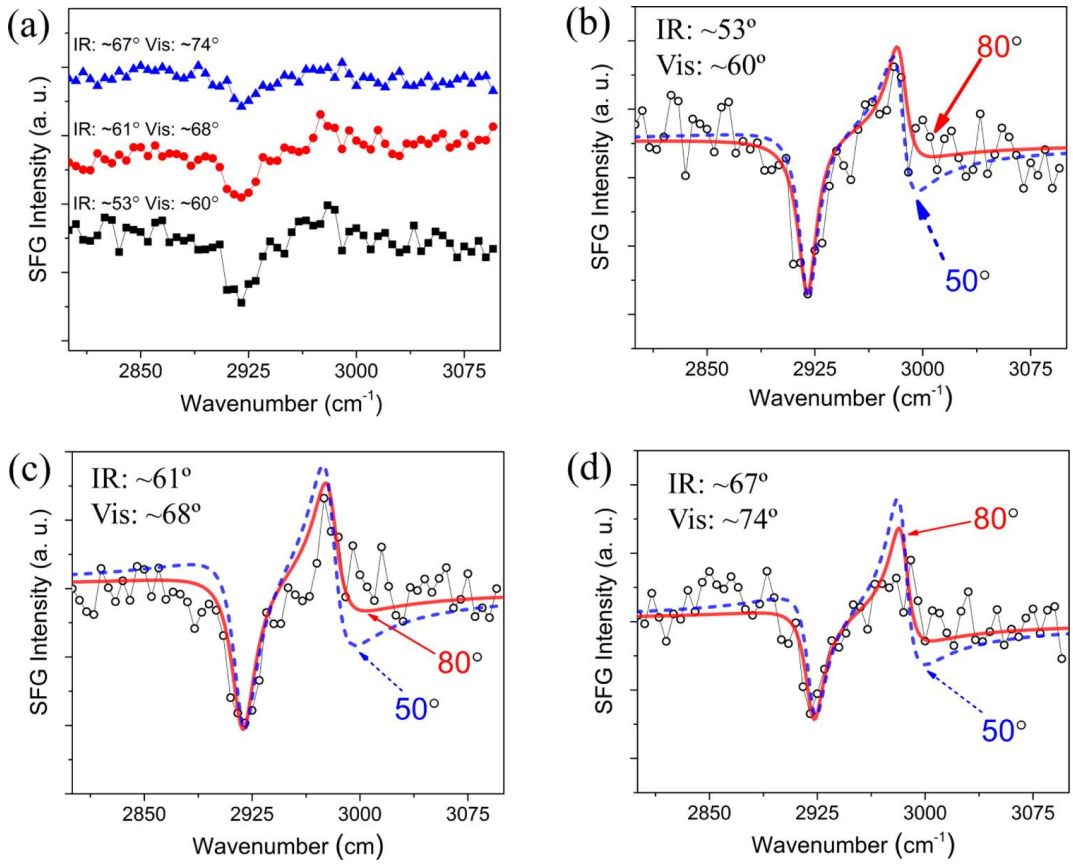

Figure 8.7. (a) Experimental SFG PPP spectra acquired from a pristine dense SiCOH film at different laser input angles. (b) Experimental and simulated SFG PPP spectra acquired from a pristine dense SiCOH film when the input visible and infrared angles were 60 ° and 53 °, respectively. (c) Experimental and simulated SFG PPP spectra acquired from a pristine dense SiCOH film when the input visible and infrared angles were 68 ° and 61 °, respectively. (d) Experimental and simulated SFG PPP spectra acquired from a pristine dense SiCOH film when the input visible and infrared angles were 74 ° and 67 °, respectively. The unfilled circles display the experimental data points and the solid curves display the simulated SFG spectra when the buried methyl tilt angle was set at 50 ° or 80 °.

When the buried methyl tilt angle was ~80 °, two features which appeared as a dip and a peak, respectively, were present in the simulated SFG PPP spectrum, and the simulated spectrum closely matched the experimentally detected SFG PPP spectrum acquired from a dense SiCOH film. When the buried methyl tilt angle was ~50 °, the simulated SFG PPP spectrum also matched the experimentally observed spectrum; however, the asymmetric feature appeared as a derivative

shaped peak. The similar methyl asymmetric peak shapes in the experimentally detected SFG PPP spectrum acquired from a dense SiCOH film and the corresponding simulated SFG PPP spectrum where the buried methyl tilt angle was ~80 ° suggest that the buried methyl tilt angle was ~80 ° at the pristine dense SiCOH/Si interface.

To further investigate the molecular structure at the pristine dense SiCOH/Si interface, SFG PPP spectra were collected from the same dense film with two additional sets of input angles for the input visible and infrared beams. Different input angles will change the Fresnel factors at the SiCOH/air and SiCOH/Si interfaces and will therefore alter the contributions of each interface to the overall signal. SFG spectra of dense SiCOH films were simulated at different input angles by maintaining the same film thickness and molecular structure parameters at the surface and buried interface while the Fresnel factors at the surface and buried interface were adjusted. Fresnel factors were determined at each set of input angles as described in chapter 1.[13]

Simulated SFG PPP spectra from dense SiCOH films were then matched to experimentally detected SFG spectra acquired at different input laser angles following the discussion above about matching simulated SFG spectra to experimentally detected SFG spectra. Figure 8.7a displays the experimentally detected SFG PPP spectra acquired from pristine dense SiCOH films where the input visible and infrared angles were varied between 60 °–74 ° and 53 °–67 °, respectively. Two methyl features were detected near 2920 and 2970 cm^{-1} in the SFG PPP spectrum acquired from a dense SiCOH film at input visible and infrared angles of 68 ° and 61 °, respectively (Figure 8.7c). However, when the input visible and infrared angles were 74 ° and 67 °, respectively, only one feature near 2920 cm^{-1} was detected in the SFG spectrum acquired from a dense pristine SiCOH film (Figure 8.7d).

Following the SFG simulation results discussed above, SFG spectra were first simulated to match the experimentally detected peak shapes, and then the methyl orientation at the buried interface was varied. Figure 8.7c displays simulated SFG spectra from a pristine dense SiCOH film where the buried methyl tilt angle parameter was set at 50 ° or 80 °. Two features that appeared as a dip and peak, respectively, were present in the simulated SFG spectra in Figure 8.7c. When the methyl tilt angle at the buried interface was set at 50 ° or 80 °, the asymmetric feature appeared as a derivative shaped peak or as a peak, respectively, which is similar to the behavior of the asymmetric feature in the simulated SFG spectra displayed in Figure 8.7b. Figure 8.7d displays simulated SFG spectra from a pristine dense SiCOH film where the input visible and infrared angles were 74 ° and 67 °, respectively. As discussed above, only one feature near 2920 cm^{-1} was detected in the experimental SFG PPP spectrum. The asymmetric feature appeared as a peak or as a derivative shaped peak in the simulated SFG PPP spectra where the buried methyl tilt angle parameter was set at 80 ° or 50 °, respectively. A methyl asymmetric feature was not detected in the experimental SFG PPP spectrum which suggests that the simulated SFG spectra with the weakest asymmetric feature more closely matched the experimental spectrum. When the methyl tilt angle at the buried interface was 80 °, the asymmetric feature was weaker than when the methyl tilt angle was 50 °, which suggests that the buried methyl groups were oriented at a high tilt angle. The cumulative input angle studies therefore suggest that Si–CH_3 groups at the pristine dense SiCOH/Si interface were oriented at a high tilt angle before plasma treatment.

In summary, the molecular structure at the dense SiCOH/Si interface was elucidated by simulating SFG PPP spectra using known surface molecular structure parameters that were

deduced from experimental SFG measurements. By varying the methyl orientation at the buried dense SiCOH/Si interface, the simulated SFG spectra could be optimized to match experimentally detected SFG spectra. The cumulative SFG results from plasma treatment and input angles studies suggest that Si–CH_3 groups at the dense SiCOH/Si interface were oriented at a very high tilt angle before and after plasma treatment. The similar molecular structure at the buried interface before and after plamsa treatment is consistent with the similar Raman spectra acquired from dense SiCOH films before and after plasma treatment. The SFG and Raman results therefore indicate that the molecular structure at the buried dense SiCOH/Si interface was not substantially altered by the plasma treatment.

8.3.4 Characterization of Porous SiCOH Films

After characterizing the effect of plasma treatment on the interfacial and bulk molecular structures of a dense SiCOH film, a similar investigation was performed on a porous SiCOH film. First, the bulk molecular structure of the porous SiCOH film was characterized using Raman spectroscopy. The Raman spectrum acquired from a pristine porous SiCOH film (Figure 8.2) displayed peaks near 2915 and 2975 cm^{-1} that can be assigned to the methyl symmetric and asymmetric stretching vibrational modes, respectively. A broad background was present in the Raman spectrum which may have been contributed by fluorescence from porogen residues present in the SiCOH bulk.[57] Unlike the Raman spectrum acquired from a dense SiCOH film, however, no peaks contributed from Si–H or methyl bending vibrational modes were detected in the Raman spectrum acquired from a porous SiCOH film. In addition, the intensities of the methyl features in the Raman spectrum acquired from the porous SiCOH film were lower than the corresponding intensities in the Raman spectrum acquired from the dense SiCOH film. The low intensities of the methyl features in the Raman spectrum acquired from the porous SiCOH

film indicate that less methyl groups were present in the film, which is consistent with the high porosity of the film. After plasma treatment, no substantial features were detected in the difference spectrum between the Raman spectra acquired from pristine and plasma-treated films which indicates that the bulk molecular structure of the plasma-treated films was not substantially different after plasma treatment.

Next, the surface molecular structure of a porous SiCOH film was investigated using SFG. The SFG SSP spectrum collected from a porous SiCOH film is displayed in Figure 8.8a. Two features were detected near 2920 and 2975 cm^{-1} that appeared as a dip and a peak, respectively. Following the methyl group orientation analysis discussed above, the orientation of methyl groups at the porous SiCOH film/air interface was ~38 °.

Porous SiCOH SFG Fitting Results

ω_q (cm^{-1})	$A_{q,ssp}$	Γ_q (cm^{-1})	χ_{NR}	Φ
Pristine				
2923	4.0 ± 0.5	8.0 ± 1.2	8.0 ± 1.7	-7.6 ± 0.1
2978	-1.7 ± 0.4	8.0 ± 1.6		
Plasma Damaged				
2920	1.6 ± 0.4	8.0 ± 2.1	8.0 ± 0.1	1.5 ± 0.1
2977	-1.3 ± 0.4	8.0 ± 2.8		

Table 8.2. SFG fitting results for SFG SSP spectra acquired from pristine and plasma treated dense SiCOH films.

After plasma treatment, two features were detected near 2920 and 2975 cm^{-1} that appeared as a peak and a dip, respectively (Figure 8.8a). Unlike the dense SiCOH/air interface, the reversed peak shape after plasma treatment indicates that the $Si–CH_3$ groups at the porous SiCOH/air interface switched absolute orientation after plasma treatment from a “pointing up” to

a “pointing down” (into the SiCOH bulk) orientation. The orientation and surface density of methyl groups after plasma treatment were 55 ° and ~60%, respectively. The higher surface density at the porous SiCOH/air interface after plasma treatment relative to the dense SiCOH/air interface may be due to a slight etching effect of the plasma treatment that exposed a new layer of film and thus exposed more $Si–CH_3$ groups at the porous SiCOH/air interface. After plasma treatment, the tilt angle of methyl groups at the porous SiCOH/air interface was higher than the corresponding tilt angle at the pristine surface. As discussed above, the tilt angle of methyl groups at the dense SiCOH/air interface decreased from ~48 ° to 41 ° after plasma treatment. The effects of plasma treatment on dense and porous SiCOH films will be compared later.

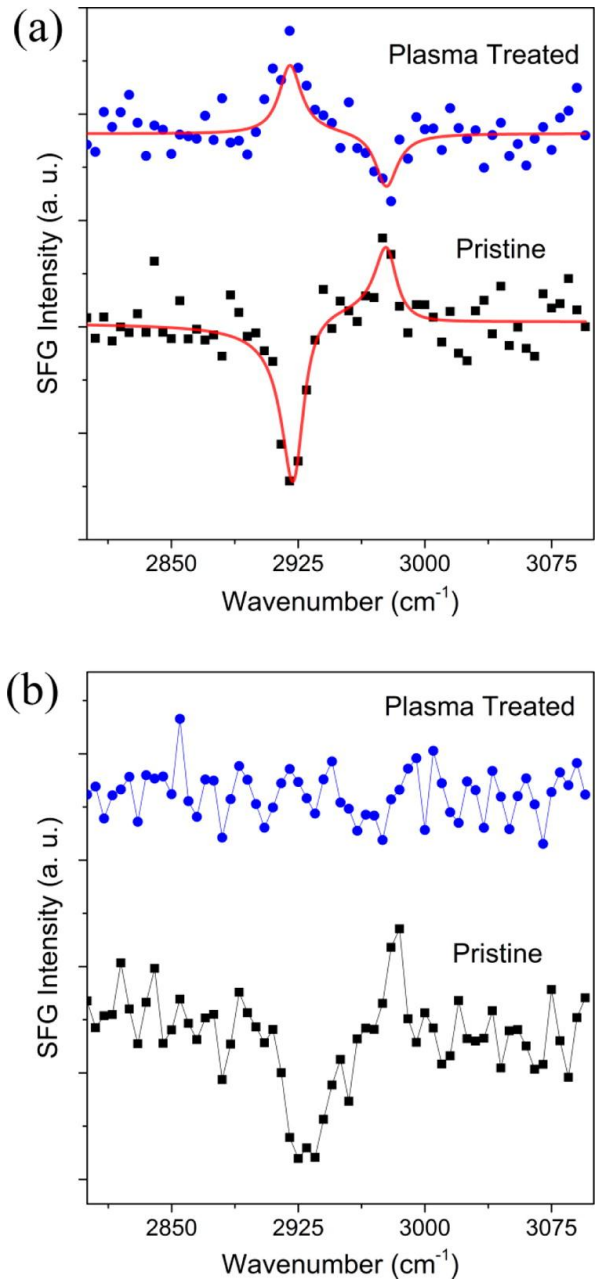

Figure 8.8. SFG (a) SSP and (b) PPP spectra acquired from a porous SiCOH film before and after oxygen plasma treatment.

After the effects of plasma treatment on the molecular structure at the porous SiCOH/air interface were investigated, SFG PPP spectra were collected from the porous SiCOH film to

investigate the porous SiCOH/Si interface. The SFG PPP spectra collected from a porous SiCOH are displayed in Figure 8.8b. Two features were detected near 2920 and 2975 cm^{-1} in the SFG spectrum acquired from a pristine porous SiCOH film that appeared as a dip and a peak, respectively. One very weak feature near 2970 cm^{-1} was detected in the SFG PPP spectrum acquired from a plasma-treated porous SiCOH film (Figure 8.8b). To deduce the molecular structure of the porous SiCOH/Si interface, SFG spectra from porous SiCOH films were simulated following the SFG simulation methodology used to deduce the molecular structure at the dense SiCOH/Si interface. Plasma-treated porous SiCOH films were simulated by setting the surface methyl group orientation after plasma treatment to 65 °, and the surface methyl depletion was taken into account by setting $N_{s,I,after} = 0.5*N_{s,I,before}$. In addition, different Fresnel factors were used to simulate SFG spectra from porous SiCOH films relative to dense SiCOH films. Refractive index values for porous SiCOH films have been reported and are generally lower than corresponding refractive index values of dense SiCOH films due to the lower densities of the porous films.[58] The molecular structure at the plasma treated porous SiCOH/Si interface was investigated first due to the lower contribution from the plasma-treated surface to the overall SFG signal.

Figure 8.9a displays simulated and experimental SFG PPP spectra acquired from a plasma-treated porous SiCOH film. Two methyl features were detected near 2920 and 2975 cm^{-1} that appeared as a derivative shaped peak and a dip, respectively, in the simulated SFG PPP spectra (Figure 8.9a). Although both the surface and buried interface components of the SFG PPP signal had features contributed by the methyl symmetric stretch (Figure 8.9c), only a weak methyl asymmetric stretch feature was detected in the experimentally observed SFG spectrum acquired from a plasma-treated porous SiCOH film. The opposite peak shapes of the symmetric

feature in the SFG spectra contributed from the surface and buried interface suggest that destructive interference weakened the symmetric feature in the detected SFG signal (Figure 8.9a).

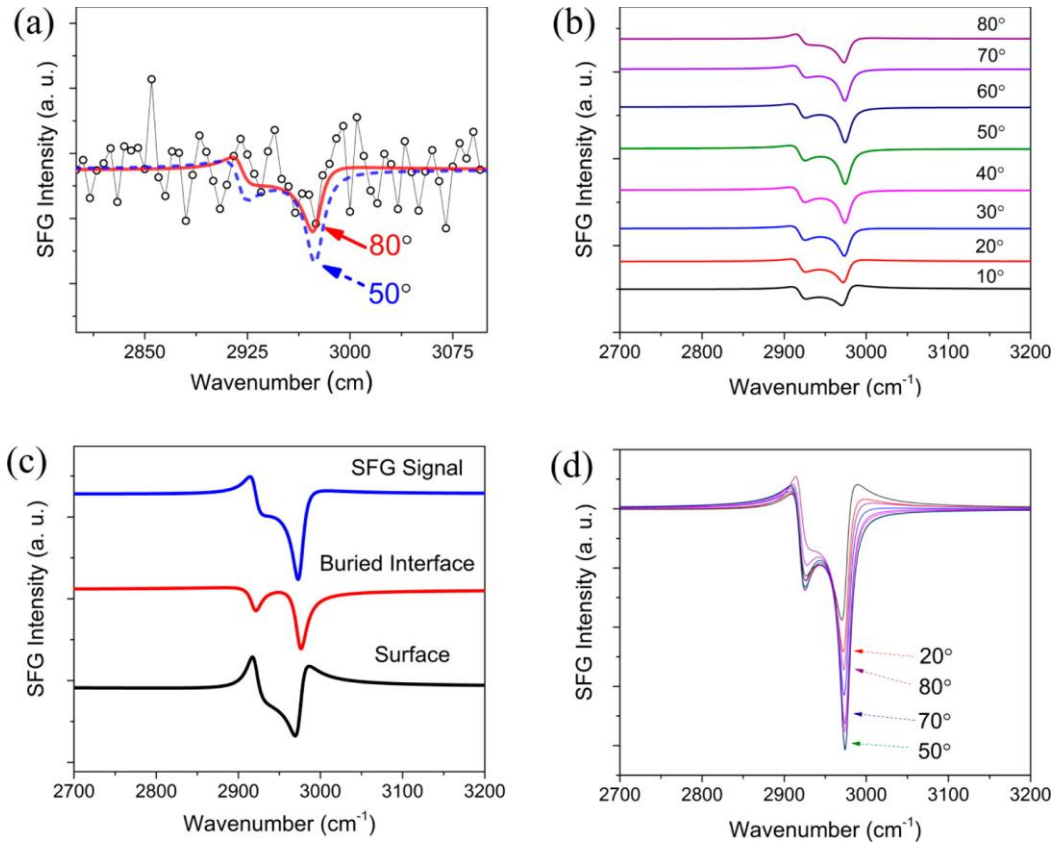

Figure 8.9. (a) Experimental and simulated SFG PPP spectra acquired from a porous SiCOH film after oxygen plasma treatment. The unfilled circles display the experimental data points, and the solid curves display the simulated SFG spectra when the buried methyl tilt angle was set at 50 ° or 80 °. (b) Simulated SFG PPP spectra from a plasma-treated dense SiCOH film where the methyl group orientation at the buried interface was varied between 10 ° and 90 °. The curves were offset successively for clarity. (c) Simulated SFG PPP spectra from a plasma-treated porous SiCOH film together with the surface and buried interface components of the simulated SFG signal. (d) Simulated SFG PPP spectra from a plasma-treated porous SiCOH film where the methyl group orientation at the buried interface was varied between 10 ° and 90 °. The curves were not offset for comparison to (b).

When the methyl tilt angle at the plasma-treated porous SiCOH/Si interface was varied between 10 ° and 90 °, the asymmetric feature intensity continuously changed in the simulated

SFG spectra (Figure 8.9b). The strongest asymmetric feature intensity occurred when the buried methyl tilt angle was ~50 ° while the weakest feature intensity occurred when the buried methyl tilt angle was ~80 ° or ~10 ° (Figures 8.9b,d). The very weak feature near 2970 cm^{-1} in the experimental SFG spectrum acquired from a plasma-treated porous SiCOH film suggests that the closest match between simulated and experimental SFG spectra occurs when the tilt angle of methyl groups at the buried porous SiCOH/Si interface was very high or very low. Therefore, the methyl groups at the porous SiCOH/Si interface were likely oriented at a high tilt angle following the discussion above about the methyl tilt angle at the buried dense SiCOH/Si interface.

The molecular structure at the pristine porous SiCOH/Si interface was then investigated by acquiring SFG PPP spectra from a porous SiCOH film using two additional sets of input angles for the input visible and infrared beams (Figure 8.10a). Figure 8.10b displays the experimental SFG PPP spectrum acquired from a porous SiCOH film where the input visible and infrared angles were 60 ° and 53 °, respectively. Two methyl features near 2920 and 2975 cm^{-1} with similar intensities were observed in the experimental SFG PPP spectrum acquired from a pristine porous SiCOH film (Figure 8.10b). SFG PPP spectra from a porous SiCOH film were then simulated by varying the methyl tilt angle parameter at the buried porous SiCOH/interface (Figure 8.10b). When the methyl tilt angle parameter was set at 80 °, two features with similar intensities were observed in the simulated SFG PPP spectrum. However, when the methyl tilt angle parameter was set at 50 °, the asymmetric feature had a higher intensity than the symmetric feature. Based on the similar symmetric and asymmetric feature intensities in the experimental SFG PPP spectrum acquired from porous SiCOH films, the simulated SFG PPP spectra suggest that the methyl tilt angle at the pristine porous SiCOH/Si interface was ~80 °.

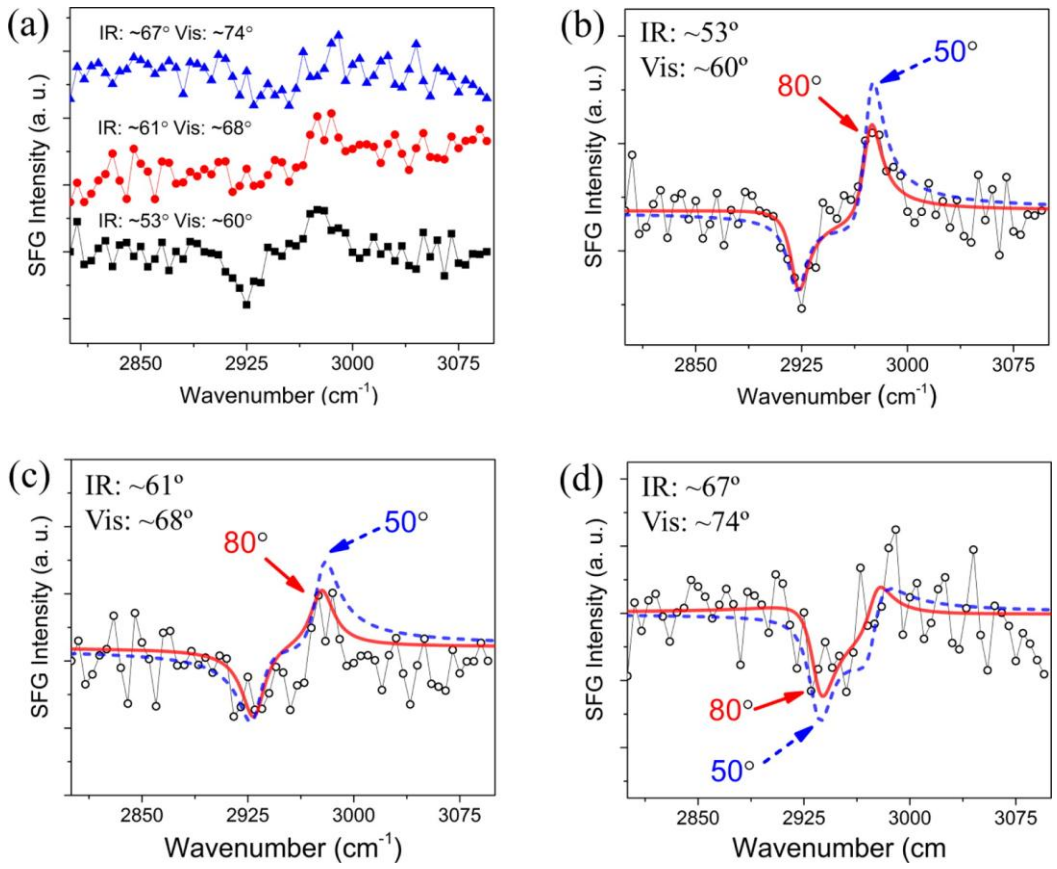

Figure 8.10. (a) Experimental SFG PPP spectra acquired from a pristine porous SiCOH film at different laser input angles. (b) Experimental and simulated SFG PPP spectra acquired from a pristine porous SiCOH film when the input visible and infrared angles were 60 ° and 53 °, respectively. (c) Experimental and simulated SFG PPP spectra acquired from a pristine porous SiCOH film when the input visible and infrared angles were 68 ° and 61 °, respectively. (d) Experimental and simulated SFG PPP spectra acquired from a pristine porous SiCOH film when the input visible and infrared angles were 74 ° and 67 °, respectively. The unfilled circles display the experimental data points and the solid curves display the simulated SFG spectra when the buried methyl tilt angle was set at 50 ° or 80 °.

Figure 8.10c displays the experimental SFG PPP spectrum acquired from a porous SiCOH film where the input visible and infrared angles were 68 ° and 61 °, respectively. Two weak methyl features near 2925 and 2975 cm^{-1} that appeared as a dip and a peak, respectively, were detected

that had similar intensities. Figure 6.10c displays the simulated SFG PPP spectra from a porous SiCOH film when the buried methyl tilt angle parameter was set at 50 ° or 80 °. Similar to Figure 8.10b, when the buried methyl tilt angle was set at 80 °, the two methyl features had similar intensities in the simulated SFG PPP spectrum. However, when the buried methyl tilt angle was set at 50 °, the methyl asymmetric feature had a higher intensity than the symmetric feature. The similar feature intensities in the simulated SFG PPP spectrum where the buried methyl tilt angle was set to 80 ° suggest that the methyl tilt angle at the buried porous SiCOH/Si interface was ~80 °. Figure 8.10d displays the experimental SFG PPP spectrum acquired from a porous SiCOH film where the input visible and infrared angles were 74 ° and 67 °, respectively. One feature near 2920 cm^{-1} was observed in the experimental SFG PPP spectrum (Figure 8.10d). Only a very weak methyl symmetric feature was detected in the experimental SFG PPP spectrum which suggests that the simulated SFG spectrum with the weakest symmetric feature more closely matched the experimental spectrum. Figure 8.10d displays that the symmetric feature intensity was weak when the buried methyl tilt angle was 80 ° and was relatively higher when the buried methyl tilt angle was 50 °. The cumulative SFG input angle studies therefore suggest that the methyl tilt angle at the pristine porous SiCOH/Si interface was very high. The SFG plasma treatment and input angle results together with the Raman results therefore indicate that the short-term plasma treatment of the porous SiCOH film did not substantially alter the molecular structure at the buried porous SiCOH/Si interface.

8.3.5 Comparison between Plasma Treatment Effects on Dense and Porous SiCOH Film Interfaces

The molecular structures at the surface and buried interface of dense and porous SiCOH films were compared before and after plasma treatment to determine how the film porosity influenced the effects of the plasma treatment. The methyl group surface density was lower after plasma treatment at both the dense and porous film surfaces. Plasma treatment resulted in the absolute orientation of the surface methyl groups at the porous film switching from a "pointing up" to a "pointing down" orientation. However, the absolute orientation of surface methyl groups at the dense film surface did not switch after plasma treatment. The constant absolute orientation of methyl groups at the dense film surface before and after plasma treatment suggests that the molecular structure at the dense film surface was more resistant to the plasma damage compared to the molecular structure at the porous film surface. However, the buried SiCOH/Si interface was not substantially altered after plasma treatment at the dense or porous SiCOH/Si interface. The similar molecular structure at the buried interface before and after plasma treatment is consistent with the limited penetration depth of short oxygen plasma treatments.

Pores at the surface and in the bulk of the porous SiCOH film may have resulted in a relatively larger penetration depth of oxygen into the film compared to the dense film.[43] Furthermore, the porous film would have more exposed surface area where reactions could take place between the SiCOH film and the plasma. The large surface area and the greater oxygen penetration depth may have resulted in more oxidization of the porous SiCOH surface molecular structure during the oxygen plasma treatment compared to the dense film. The larger extent of oxidation may have altered the network structure at the porous SiCOH/air interface more substantially than at the surface of the dense SiCOH film. The switch in absolute orientation at

the porous SiCOH/air interface after plasma treatment may be due to Si–CH_3 groups that were physically moved as the SiCOH network at the SiCOH/air interface was altered. Another possibility is that a very thin silica layer formed at the SiCOH/air interface such that all of the Si–CH_3 groups that were initially "pointing up" were oxidized by the plasma. A portion of Si–CH_3 that were located slightly below the surface and had a "pointing down" orientation and were not oxidized by the plasma may have then contributed to the detected SFG signal.

8.4 Conclusion

The effects of plasma treatment on the molecular structures of SiCOH/air and Si/SiCOH interfaces were investigated using SFG and Raman spectroscopy. The orientation of methyl groups at the dense SiCOH/air interface before and after plasma treatment was ~48 ° and ~41 °, respectively. The methyl surface coverage decreased by ~64% after plasma treatment and the absolute orientation of methyl groups at the dense SiCOH/air interface was "pointing away" before and after plasma treatment. These results indicate that plasma treatment substantially altered the surface molecular structure. At the porous low-k surface, the methyl orientation changed from 38 ° to 55 ° after plasma treatment. The surface density of methyl groups was ~60%, respectively, relative to the pristine porous surface. The collective data indicate that both the network structure and porosity of low-k SiCOH films influence the effects of oxygen plasma treatment on the molecular structures at low-k SiCOH film surfaces. Simulated and experimental SFG spectra before and after plasma treatment together with SFG spectra acquired from the same SiCOH film using different sets of input angles enabled nondestructive characterization of molecular structures at the buried Si/SiCOH interface. The methodology developed in this study demonstrates that SFG can be used to nondestructively characterize the molecular structure of low-k SiCOH film surfaces and buried interfaces before and after plasma

8.5 Impact

Understanding the molecular structure of surfaces is important to rationally design future processing and deposition steps. For example, inorganic silica capping layers deposited on low-k surfaces have been shown to improve the adhesion, mechanical integrity, and dielectric properties of low-k films located in damascene-structured multilayer stacks during chemical mechanical polishing (CMP) and CMP cleaning processes[59,60]. Low-k films could withstand CMP processing without delamination from an underlying capping layer when the interfacial adhesion strength between the low-k film and the silica was increased by plasma treating the low-k surface before silica deposition. However, the parameters for the plasma treatment were found by trial and error approaches rather than rationally designed.

The studies in this chapter provide a nondestructive way to characterize the effects of processing steps on low-k dielectric surfaces. Therefore, possible contamination from sample preparation or damage from analysis will not largely affect the SFG results. Such methodology can be used in combination with surface property studies to elucidate surface structure property relationships. Knowledge about which functional groups are present at plasma treated low-k surfaces as well as the orientation of surface functional groups can be directly correlated to the adhesion and quality of films deposited on the low-k surfaces in microelectronic packages. Such structure-property relationships can then be used to guide plasma processing rather than using trial and error approaches.

In this chapter, SFG was also demonstrated to be capable of probing buried interfaces of commercial low-k materials for the first time. Simultaneously characterizing the surface and buried interface of commercial films *in situ* is an important step in the development of SFG into

a metrology tool for nondestructive characterization of polymer interfaces. For both dense and porous films, the SFG results indicate that plasma treatment did not alter the buried interface. More generally, for the first time, nondestructive metrology was used to experimentally show that plasma treatment of a thin film did not alter the molecular structure of a buried interface.

Characterization of low-k dielectric interfacial molecular structures using SFG together with characterization of the morphology, elemental composition, and molecular composition of low-k dielectric surfaces using conventional surface analytical techniques should provide a more complete understanding of the effects of plasma treatment on low-k dielectric interfaces. Furthermore, the developed methodology is general and can be extended to nondestructively characterize the effects of many different plasma treatments, wet chemical treatments, and surface repair treatments on the molecular structures at the surface and buried interface of many thin organic layers or polymer films.

8.6 References

(1) Grill, A.; Gates, S. M.; Ryan, T. E.; Nguyen, S. V.; Priyadarshini, D. Progress in the Development and Understanding of Advanced Low K and Ultralow K Dielectrics for Very Large-Scale Integrated interconnects—State of the Art. *Appl. Phys. Rev.* **2014**, *1* (1), 011306.

(2) Grill, A.; Edelstein, D.; Lane, M.; Patel, V.; Gates, S.; Restaino, D.; Molis, S. Interface Engineering for High Interfacial Strength between SiCOH and Porous SiCOH Interconnect Dielectrics and Diffusion Caps. *J. Appl. Phys.* **2008**, *103* (5), 054104.

(3) Chen, F.; Shinosky, M. A. Electron Fluence Driven, Cu Catalyzed, Interface Breakdown Mechanism for BEOL Low-K Time Dependent Dielectric Breakdown. *Microelectron. Reliab.* **2014**, *54* (3), 529–540.

(4) Guo, X.; Jakes, J. E.; Nichols, M. T.; Banna, S.; Nishi, Y.; Shohet, J. L. The Effect of Water Uptake on the Mechanical Properties of Low-K Organosilicate Glass. *J. Appl. Phys.* **2013**, *114* (8), 084103.

(5) Dauskardt, R. H. with Taek-Soo Kim. Integration Challenges of Nanoporous Low Dielectric Constant Materials. *IEEE Trans. Device Mater. Reliab.* **2009**, *9* (4), 509–515.

(6) Tan, T. L.; Gan, C. L.; Du, A. Y.; Tan, Y. C.; Ng, C. M. Delamination-Induced Dielectric Breakdown in Cu/low- K Interconnects. *J. Mater. Res.* **2008**, *23* (06), 1802–1808.

(7) Lin, Y.; Tsui, T. Y.; Vlassak, J. J. Water Diffusion and Fracture in Organosilicate Glass Film Stacks. *Acta Mater.* **2007**, *55* (7), 2455–2464.

(8) Baklanov, M. R.; de Marneffe, J.-F.; Shamiryan, D.; Urbanowicz, A. M.; Shi, H.; Rakhimova, T. V.; Huang, H.; Ho, P. S. Plasma Processing of Low-K Dielectrics. *J. Appl. Phys.* **2013**, *113* (4), 041101.

(9) King, S. W. Dielectric Barrier, Etch Stop, and Metal Capping Materials for State of the Art and beyond Metal Interconnects. *ECS J. Solid State Sci. Technol.* **2014**, *4* (1), N3029–N3047.

(10) Chen, Z. Investigating Buried Polymer Interfaces Using Sum Frequency Generation Vibrational Spectroscopy. *Prog. Polym. Sci.* **2010**, *35* (11), 1376–1402.

(11) Chen, Z.; Shen, Y. R.; Somorjai, G. A. Studies of Polymer Surfaces by Sum Frequency Generation Vibrational Spectroscopy. *Annu. Rev. Phys. Chem.* **2002**, *53* (1), 437–465.

(12) Zhang, X.; Myers, J. N.; Bielefeld, J. D.; Lin, Q.; Chen, Z. In Situ Observation of Water Behavior at the Surface and Buried Interface of a Low-K Dielectric Film. *ACS Appl. Mater. Interfaces* **2014**, *6* (21), 18951–18961.

(13) Myers, J. N.; Zhang, X.; Bielefeld, J. D.; Lin, Q.; Chen, Z. Nondestructive in Situ Characterization of Molecular Structures at the Surface and Buried Interface of Silicon-Supported Low-K Dielectric Films. *J. Phys. Chem. B* **2015**, *119*, 1736–1746.

(14) King, S. W.; Gradner, J. A. Intrinsic Stress Fracture Energy Measurements for PECVD Thin Films in the SiOxCyNz:H System. *Microelectron. Reliab.* **2009**, *49* (7), 721–726.

(15) Nguyen, K. T.; Le Clair, S. V.; Ye, S.; Chen, Z. Molecular Interactions between Magainin 2 and Model Membranes in Situ. *J. Phys. Chem. B* **2009**, *113* (36), 12358–12363.

(16) Shen, Y. R. Surface Properties Probed by Second-Harmonic and Sum-Frequency Generation. *Nature* **1989**, *337* (6207), 519–525.

(17) Eisenthal, K. B. Liquid Interfaces Probed by Second-Harmonic and Sum-Frequency Spectroscopy. *Chem. Rev.* **1996**, *96* (4), 1343–1360.

(18) Richmond, G. L. Molecular Bonding and Interactions at Aqueous Surfaces as Probed by Vibrational Sum Frequency Spectroscopy. *Chem. Rev.* **2002**, *102* (8), 2693–2724.

(19) Kim, J.; Somorjai, G. A. Molecular Packing of Lysozyme, Fibrinogen, and Bovine Serum Albumin on Hydrophilic and Hydrophobic Surfaces Studied by Infrared−Visible Sum Frequency Generation and Fluorescence Microscopy. *J. Am. Chem. Soc.* **2003**, *125* (10), 3150–3158.

(20) Geiger, F. M. Second Harmonic Generation, Sum Frequency Generation, and $X^{(3)}$: Dissecting Environmental Interfaces with a Nonlinear Optical Swiss Army Knife. *Annu. Rev. Phys. Chem.* **2009**, *60* (1), 61–83.

(21) Walter, S. R.; Geiger, F. M. DNA on Stage: Showcasing Oligonucleotides at Surfaces and Interfaces with Second Harmonic and Vibrational Sum Frequency Generation. *J. Phys. Chem. Lett.* **2010**, *1* (1), 9–15.

(22) Wang, J.; Chen, C.; Buck, S. M.; Chen, Z. Molecular Chemical Structure on Poly(methyl Methacrylate) (PMMA) Surface Studied by Sum Frequency Generation (SFG) Vibrational Spectroscopy. *J. Phys. Chem. B* **2001**, *105* (48), 12118–12125.

(23) Ye, H.; Huang, J.; Park, J.-R.; Katz, H. E.; Gracias, D. H. Correlations between SFG Spectra and Electrical Properties of Organic Field Effect Transistors. *J. Phys. Chem. C* **2007**, *111* (35), 13250–13255.

(24) Ye, H.; Abu-Akeel, A.; Huang, J.; Katz, H. E.; Gracias, D. H. Probing Organic Field Effect Transistors In Situ during Operation Using SFG. *J. Am. Chem. Soc.* **2006**, *128* (20), 6528–6529.

(25) Ye, S.; Tong, Y.; Ge, A.; Qiao, L.; Davies, P. B. Interfacial Structure of Soft Matter Probed by SFG Spectroscopy: Interfacial Structure of Soft Matter by SFG Spectroscopy. *Chem. Rec.* **2014**, *14* (5), 791–805.

(26) Ge, A.; Peng, Q.; Qiao, L.; Yepuri, N. R.; Darwish, T. A.; Matsusaki, M.; Akashi, M.; Ye, S. Molecular Orientation of Organic Thin Films on Dielectric Solid Substrates: A Phase-Sensitive Vibrational SFG Study. *Phys Chem Chem Phys* **2015**, *17* (27), 18072–18078.

(27) Yan, E. C. Y.; Fu, L.; Wang, Z.; Liu, W. Biological Macromolecules at Interfaces Probed by Chiral Vibrational Sum Frequency Generation Spectroscopy. *Chem. Rev.* **2014**, *114* (17), 8471–8498.

(28) Fu, L.; Wang, Z.; Psciuk, B. T.; Xiao, D.; Batista, V. S.; Yan, E. C. Y. Characterization of Parallel B-Sheets at Interfaces by Chiral Sum Frequency Generation Spectroscopy. *J. Phys. Chem. Lett.* **2015**, *6* (8), 1310–1315.

(29) Shih, J.-Y.; Huang, W.-C.; Ko, C.-T.; Yang, Z.; Hu, S.-H.; Leu, J.; Chou, K. C.; Chen, K.-N. Adhesion Investigation Between Metal and Benzocyclobutene (BCB) Polymer Dielectric Materials in 3-D Integration Applications. *IEEE Trans. Device Mater. Reliab.* **2014**, *14* (3), 914–920.

(30) Yang, Z.; Nikakhtari, H.; Wolf, S.; Hu, D.; Gray, M. R.; Chou, K. C. Binary Solvents with Ethanol for Effective Bitumen Displacement at Solvent/Mineral Interfaces. *Energy Fuels* **2015**, 150702131148000.

(31) FitzGerald, W. R.; Jena, K. C.; Hore, D. K. Effects of Single-Source Multiple Beam Interference in Vibrational Sum Frequency Generation Spectroscopy. *J. Mol. Struct.* **2015**, *1084*, 368–373.

(32) Covert, P. A.; Hore, D. K. Assessing the Gold Standard: The Complex Vibrational Nonlinear Susceptibility of Metals. *J. Phys. Chem. C* **2015**, *119* (1), 271–276.

(33) Lu, X.; Myers, J. N.; Chen, Z. Molecular Ordering of Phenyl Groups at the Buried Polystyrene/Metal Interface. *Langmuir* **2014**, *30* (31), 9418–9422.

(34) Myers, J. N.; Chen, Z. Surface Plasma Treatment Effects on the Molecular Structure at Polyimide/air and Buried Polyimide/epoxy Interfaces. *Chin. Chem. Lett.* **2015**, *26* (4), 449–454.

(35) Hankett, J. M.; Liu, Y.; Zhang, X.; Zhang, C.; Chen, Z. Molecular Level Studies of Polymer Behaviors at the Water Interface Using Sum Frequency Generation Vibrational Spectroscopy. *J. Polym. Sci. Part B Polym. Phys.* **2013**, *51* (5), 311–328.

(36) Zhang, C.; Myers, J. N.; Chen, Z. Elucidation of Molecular Structures at Buried Polymer Interfaces and Biological Interfaces Using Sum Frequency Generation Vibrational Spectroscopy. *Soft Matter* **2013**, *9* (19), 4738.

(37) Volksen, W.; Miller, R. D.; Dubois, G. Low Dielectric Constant Materials. *Chem. Rev.* **2010**, *110* (1), 56–110.

(38) Grill, A. Porous pSiCOH Ultralow- *k* Dielectrics for Chip Interconnects Prepared by PECVD. *Annu. Rev. Mater. Res.* **2009**, *39* (1), 49–69.

(39) Grill, A.; Neumayer, D. A. Structure of Low Dielectric Constant to Extreme Low Dielectric Constant SiCOH Films: Fourier Transform Infrared Spectroscopy Characterization. *J. Appl. Phys.* **2003**, *94* (10), 6697.

(40) Lam, J. C. K.; Huang, M. Y. M.; Tan, H.; Mo, Z.; Mai, Z.; Pei Wong, C.; Sun, H.; Shen, Z. Vibrational Spectroscopy of Low-K/ultra-Low-K Dielectric Materials on Patterned Wafers. *J. Vac. Sci. Technol. Vac. Surf. Films* **2011**, *29* (5), 051513.

(41) Doux, C.; Aw, K. C.; Niewoudt, M.; Gao, W. Analysis of HSG-7000 Silsesquioxane-Based Low-K Dielectric Hot Plate Curing Using Raman Spectroscopy. *Microelectron. Eng.* **2006**, *83* (2), 387–391.

(42) Lam, J. C. K.; Huang, M. Y. M.; Hau Ng, T.; Khalid Bin Dawood, M.; Zhang, F.; Du, A.; Sun, H.; Shen, Z.; Mai, Z. Evidence of Ultra-Low-K Dielectric Material Degradation and Nanostructure Alteration of the Cu/ultra-Low-K Interconnects in Time-Dependent Dielectric Breakdown Failure. *Appl. Phys. Lett.* **2013**, *102* (2), 022908.

(43) Goldman, M. A.; Graves, D. B.; Antonelli, G. A.; Behera, S. P.; Kelber, J. A. Oxygen Radical and Plasma Damage of Low-K Organosilicate Glass Materials: Diffusion-Controlled Mechanism for Carbon Depletion. *J. Appl. Phys.* **2009**, *106* (1), 013311.

(44) Zhang, D.; Ward, R. S.; Shen, Y. R.; Somorjai, G. A. Environment-Induced Surface Structural Changes of a Polymer: An *in Situ* IR + Visible Sum-Frequency Spectroscopic Study. *J. Phys. Chem. B* **1997**, *101* (44), 9060–9064.

(45) Lambert, A. G.; Davies, P. B.; Neivandt, D. J. Implementing the Theory of Sum Frequency Generation Vibrational Spectroscopy: A Tutorial Review. *Appl. Spectrosc. Rev.* **2005**, *40* (2), 103–145.

(46) Chen, C.; Wang, J.; Chen, Z. Surface Restructuring Behavior of Various Types of Poly(dimethylsiloxane) in Water Detected by SFG. *Langmuir* **2004**, *20* (23), 10186–10193.

(47) Ryan, E. T.; Gates, S. M.; Grill, A.; Molis, S.; Flaitz, P.; Arnold, J.; Sankarapandian, M.; Cohen, S. A.; Ostrovski, Y.; Dimitrakopoulos, C. Property Modifications of Nanoporous pSiCOH Dielectrics to Enhance Resistance to Plasma-Induced Damage. *J. Appl. Phys.* **2008**, *104* (9), 094109.

(48) Shamiryan, D.; Baklanov, M. R.; Vanhaelemeersch, S.; Maex, K. Comparative Study of SiOCH Low-K Films with Varied Porosity Interacting with Etching and Cleaning Plasma. *J. Vac. Sci. Technol. B Microelectron. Nanometer Struct.* **2002**, *20* (5), 1923.

(49) Bao, J.; Shi, H.; Liu, J.; Huang, H.; Ho, P. S.; Goodner, M. D.; Moinpour, M.; Kloster, G. M. Mechanistic Study of Plasma Damage of Low K Dielectric Surfaces. *J. Vac. Sci. Technol. B Microelectron. Nanometer Struct.* **2008**, *26* (1), 219.

(50) Ward, R. N.; Davies, P. B.; Bain, C. D. Orientation of Surfactants Adsorbed on a Hydrophobic Surface. *J. Phys. Chem.* **1993**, *97* (28), 7141–7143.

(51) Sung, W.; Seok, S.; Kim, D.; Tian, C. S.; Shen, Y. R. Sum-Frequency Spectroscopic Study of Langmuir Monolayers of Lipids Having Oppositely Charged Headgroups. *Langmuir* **2010**, *26* (23), 18266–18272.

(52) Lambert, A. G.; Neivandt, D. J.; Briggs, A. M.; Usadi, E. W.; Davies, P. B. Interference Effects in Sum Frequency Spectra from Monolayers on Composite Dielectric/Metal Substrates. *J. Phys. Chem. B* **2002**, *106* (21), 5461–5469.

(53) Wilson, P. T.; Briggman, K. A.; Wallace, W. E.; Stephenson, J. C.; Richter, L. J. Selective Study of Polymer/dielectric Interfaces with Vibrationally Resonant Sum Frequency Generation via Thin-Film Interference. *Appl. Phys. Lett.* **2002**, *80* (17), 3084.

(54) Tong, Y.; Zhao, Y.; Li, N.; Osawa, M.; Davies, P. B.; Ye, S. Interference Effects in the Sum Frequency Generation Spectra of Thin Organic Films. I. Theoretical Modeling and Simulation. *J. Chem. Phys.* **2010**, *133* (3), 034704.

(55) Backus, E. H. G.; Garcia-Araez, N.; Bonn, M.; Bakker, H. J. On the Role of Fresnel Factors in Sum-Frequency Generation Spectroscopy of Metal–Water and Metal-Oxide–Water Interfaces. *J. Phys. Chem. C* **2012**, *116* (44), 23351–23361.

(56) Lu, X.; Li, B.; Zhu, P.; Xue, G.; Li, D. Illustrating Consistency of Different Experimental Approaches to Probe the Buried Polymer/metal Interface Using Sum Frequency Generation Vibrational Spectroscopy. *Soft Matter* **2014**, *10* (29), 5390.

(57) Marsik, P.; Verdonck, P.; De Roest, D.; Baklanov, M. R. Porogen Residues Detection in Optical Properties of Low-K Dielectrics Cured by Ultraviolet Radiation. *Thin Solid Films* **2010**, *518* (15), 4266–4272.

(58) Zhou, W.; Bailey, S.; Sooryakumar, R.; King, S.; Xu, G.; Mays, E.; Ege, C.; Bielefeld, J. Elastic Properties of Porous Low-K Dielectric Nano-Films. *J. Appl. Phys.* **2011**, *110* (4), 043520.

(59) Heo, K.; Ree, B. J.; Choi, K. K.; Ree, M. Structural reliability evaluation of low-k nanoporous dielectric interlayers integrated into microelectronic devices. *RSC Advances* **2015**, *5*, 87084-87089.

(60) Choi, K. K.; Cho, I. H.; Park, S. J.; Lim, J. E.; Jung, O. J.; Park, J. H.; Min, B. S.; Hwang, S. B.; Ko, M. J.; Lee, J. G. Characterization and integration of new porous low-k dielectric ($k < 2.3$) for 65 nm technology and beyond. *Thin Solid Films* **2007**, *515*, 5025–5030.

Chapter 9

SFG ANALYSIS OF THE MOLECULAR STRUCTURES AT THE SURFACES AND BURIED INTERFACES OF PECVD ULTRALOW-DIELECTRIC CONSTANT PSICOH

9.1 Introduction

As we discussed above, low dielectric constant SiCOH and ultralow-k porous SiCOH (pSiCOH) materials prepared by plasma-enhanced chemical vapor deposition (PECVD) have been successfully integrated into advanced interconnects to replace silicon dioxide as insulators to decrease RC delay since the 90 nm technology node.[1–7] In the previous chapter, we utilized SFG to characterize the molecular structure at the low-k/air and Si/SiO_2/low-k interfaces of silicon-supported low-k SiCOH films with different porosities (provided by Intel) before and after plasma treatment. The effects of plasma treatment on the molecular structures at the interfaces were compared to the bulk damage by comparing SFG and Raman spectra collected from the films before and after plasma damage. In this chapter, we will present our SFG studies on the molecular structural changes at the ultralow-k/air surface and SiCNH/pSiCOH interfaces of PECVD films provided by IBM before and after plasma treatment and after repairing the damaged samples using a commercial repair reagent. Here, ammonia plasma was selected to simulate the plasma damage to pSiCOH material during the pre-clean process before the deposition of a dielectric cap.

As presented above in this dissertation, methodologies have been developed in our group to nondestructively probe the molecular structure of low-k materials deposited on fused silica

substrate and Si wafer surface respectively.[8,9] In particular, molecular structures at the surface and interface of Si-supported low-k material were obtained by separating contributions from the low-*k*/air surface and the Si/low-*k* interface to SFG spectra.[8] It is suggested that the SFG spectrum collected from a Si supported low-k material with certain thickness using the ssp polarization combination is dominated by the contribution from the low-k/air surface, while the SFG spectrum collected using the ppp polarization combination is contributed from both the low-k/air surface and the low-k/Si interface.

Here, a similar method was used to elucidate the molecular structures at the ultralow-k/air surface of a pSiCOH film before and after plasma treatment and after repair by using ssp SFG measurements. X-ray photoelectron spectroscopy (XPS) was implemented as a supplemental tool to further study the structural changes at the pSiCOH/air surface before and after plasma treatment and after repair. Then ppp SFG measurements were also performed. As mentioned above, the ppp spectrum is contributed by both the surface and the buried interface. Since the surface structure was already known from the ssp study above, the buried interface structure can be deduced from the ppp measurement. To verify the obtained interfacial structure, different angles of the input laser beams were used in the ppp measurements to collect different ppp spectra. More details about how to obtain and confirm the molecular structures at the SiCNH/pSiCOH interface will be presented below. This research successfully determined the molecular structures of the ultralow-k/air surface and the buried SiCNH/ultralow-k interface of the pristine sample, the sample after ammonia plasma treatment, and the sample after repairing. This research was collaboratively performed with Dr. Xiaoxian Zhang in our group.

9.2 Experimental section

The Si/SiCNH (15 nm)/pSiCOH (100 nm) film structures were fabricated using commercial 300 mm PECVD tools. Subsequently, the pSiCOH film was exposed to a NH_3 plasma in a 300 mm commercial PECVD tool for 18 s, at 350 °C, and 550 W of rf power, to simulate the pre-clean plasma used during chip fabrication. Additionally, proprietary commercial repair reagents were used to restore the hydrophobicity of the pSiCOH film after it was damaged by the NH_3 plasma. The silylation repair was performed under UV irradiation at 250 °C for 1 min. SiCOH film fabrication, plasma treatment, and repair were performed at IBM. A commercial SFG spectrometer (EKSPLA) was used to measure the SFG spectra of the Si/SiCNH/pSiCOH structure. A face up geometry was used in this study, as shown in Figure 9.1. More detailed descriptions the SFG spectrometer were described in chapter 1.

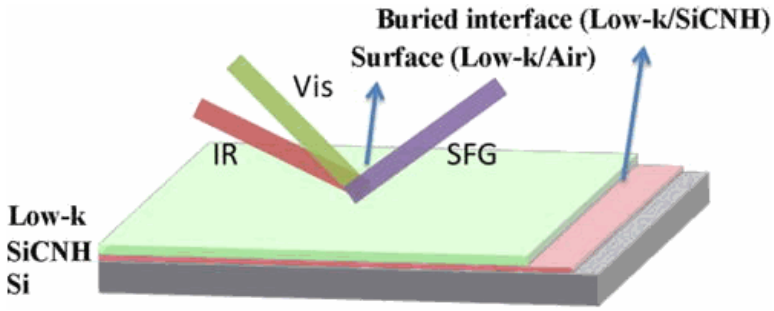

Figure 9.1. Schematic of the SFG experimental geometry used in chapter 9.

9.3 Results and discussion

9.3.1 Characterization of the pSiCOH/air surface

First, SFG was utilized to characterize the molecular structures at the pSiCOH/air surface. Then the effects of NH_3 plasma treatment and repair on the molecular structures at the pSiCOH/air surface were investigated. Our previous studies demonstrated that ssp SFG signal generated from the ultralow-k films with ~100 nm thickness deposited on silicon wafer would selectively probe the ultralow-k/air surface and the influence of the signals generated from the

Si/ultralow-k buried interface could be ignored.[8] Therefore, ~100 nm pSiCOH films were selected here and SFG measurements using the ssp polarization combination were carried out first to selectively probe the SFG signal generated from the pSiCOH/air surface. The molecular structures at the pSiCOH/air surface were compared before and after exposing the pSiCOH film to NH_3 plasma and after subsequent repair. The spectrum of the pSiCOH film deposited on top of an ultrathin SiCNH film is shown in Figure 9.2(a). Two pronounced peaks with peak centers at ~2920 and ~2975 cm^{-1} were detected in the ssp SFG spectrum, which can be assigned to the Si-CH_3 C-H symmetric and asymmetric stretching vibrational modes, respectively.[9] The observation of Si-CH_3 features in the ssp SFG spectrum suggests that the pSiCOH/air surface was covered by ordered CH_3 groups. Different from the SFG spectrum collected previously from a low-k film with similar structure deposited on fused SiO_2 prism,[9] the Si-CH_3 symmetric stretching feature appeared as a negative peak while the asymmetric stretching signal appeared as a positive peak which has been attributed to the interference between the resonant signal and the non-resonant background.[8] In order to deduce the average orientation of methyl groups at the pSiCOH/air surface, the ssp SFG spectrum shown in Figure 9.2(a) was fit using equation 1.23 and the derived fitting parameters (Table 9.1) were compared to theoretical $\chi_{yyz,as}/\chi_{yyz,ss}$ values shown in Figure 9.3. Here, the experimentally measured $\chi_{yyz,as}/\chi_{yyz,ss}$ ratio indicated that the Si-CH_3 groups at the as deposited pSiCOH/air surface were oriented at ~47 ° relative to the surface normal. Likely not all the methyl groups adopt the same orientation. Ideally to describe the accurate orientation information of the methyl groups, it is necessary to deduce the entire orientation distribution. Due to the limited measurable parameters we have from SFG, we can only determine the average orientation of the methyl groups. We believe that such average orientation is important for us to understand molecular structures of surfaces and buried

interfaces which we studied here. Also, such structural information at the buried interface which will be discussed below can only be acquired by SFG experiments.

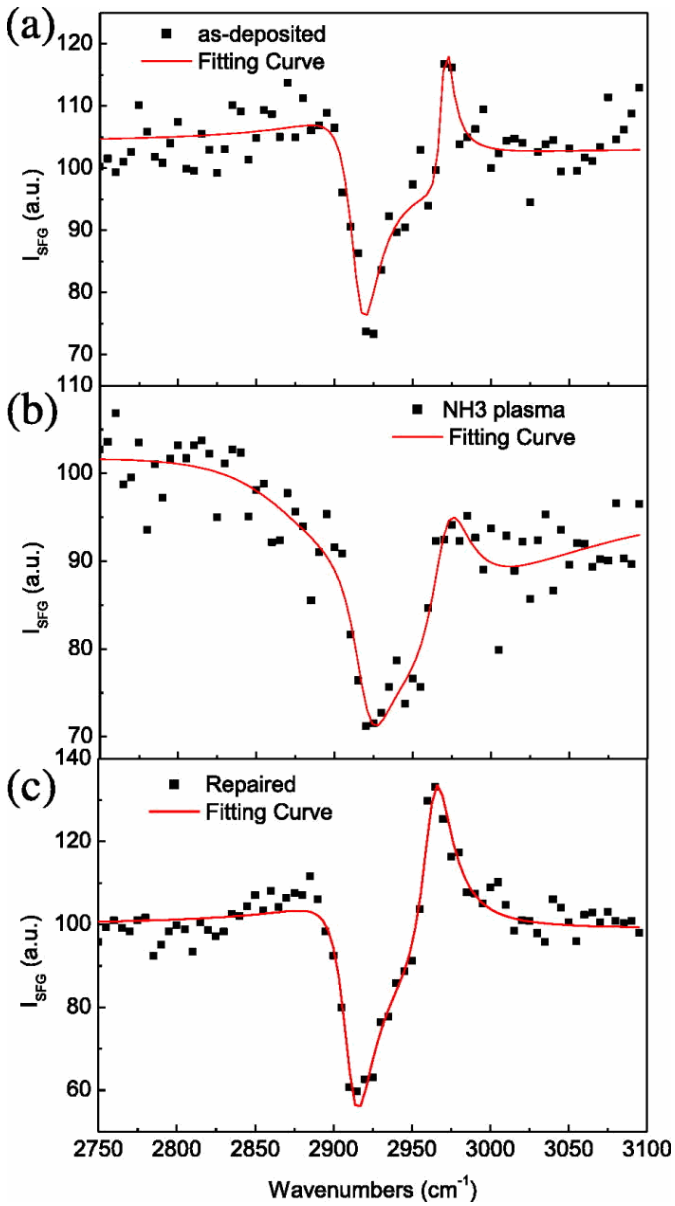

Figure 9.2. ssp SFG spectra and the corresponding fitting curves of a pSiCOH film (a) as-deposited, (b) after NH_3 plasma treatment, and then (c) after repairing the plasma-damaged film.

	As-deposited		NH_3 plasma 18 s		Repaired	
Peak (cm^{-1})	A	Γ	A	Γ	A	Γ
2920	−17.7	10.9	−10.4	15.0	79.7	12.8
2975	5.1	4.7	10.3	15.0	−34.4	12.0
$\chi^{(2)}_{as}$	1.1		0.7		−2.7	
$\chi^{(2)}_{ss}$	−1.6		−0.7		6.2	

Table 9.1. Fitting parameters for the SFG ssp spectra shown in Figure 9.2.

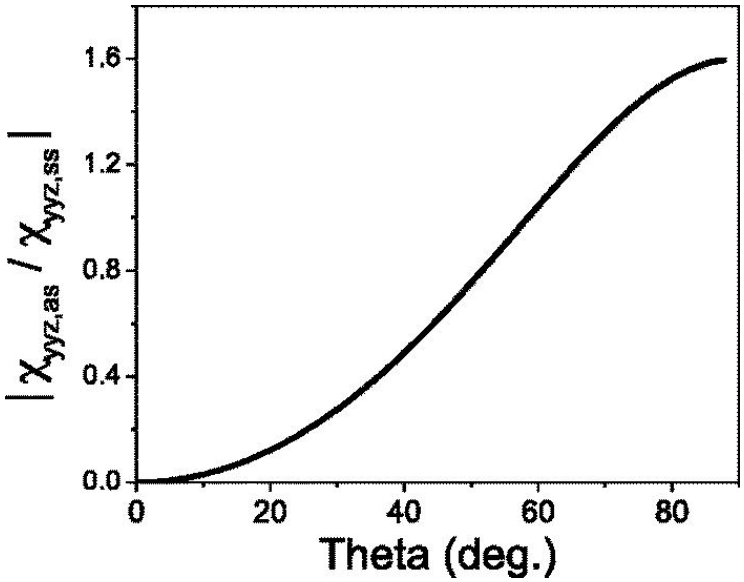

Figure 9.3. Methyl $\chi_{yyz,as}/\chi_{yyz,ss}$ ratio plotted as a function of tilt angle.

Subsequently, similar SFG measurements were carried out to examine the effect of NH_3 plasma treatment and subsequent repair. Figures 9.2(b) and 9.2(c) display the ssp SFG spectra collected from a pSiCOH film which had been plasma treated and then repaired. Similar to the as-deposited sample, two pronounced peaks located near 2920 and 2975 cm^{-1} were detected in the SFG ssp spectra collected from the NH_3 plasma treated pSiCOH film. The symmetric Si-CH_3 C-H stretching signal appeared as a negative peak while the asymmetric stretching appeared as a positive peak. The detection of strong Si-CH_3 features at the pSiCOH/air surface from the NH_3 plasma damaged film shows that the pSiCOH/air surface was still covered by ordered Si-CH_3 groups. However, the spectral features differed from those collected from the as-deposited sample shown in Figure 9.2(a). After fitting the spectra (Table 9.1), the average orientation of methyl groups at the pSiCOH/air surface after NH_3 plasma treatment was determined to be ~58 °, which means that the methyl groups on the surface lay down more towards the surface after exposure to NH_3 plasma. After repairing the plasma-damaged sample, the average orientation of methyl groups at the surface was reduced to 38 °, indicating the methyl groups on the plasma-damaged surface tilted up again after repair. Our measurements were capable of providing more quantitative results about the status of functional groups at the surface, as presented below (Table 9.2).

Sample	Orientation of CH_3 groups (deg.)	Surface coverage (%)
As-deposited	47	100.0
After NH_3 plasma treatment	58	59.1
After repair	38	133.1

Table 9.2. The deduced methyl average orientation and surface coverage of pSiCOH thin film before and after NH_3 plasma treatment and repair.

To evaluate the influence of the plasma treatment and the effectiveness of repair on the damaged surface, the change of the surface coverage of methyl groups at the pSiCOH/air surface was determined by comparing the experimentally measured $\chi_{yyz,ss}$ values before and after plasma treatment and after repair. Since the average orientations of the methyl groups at the pSiCOH/air surface before and after plasma treatment and after repair were deduced before, the ratios of the CH_3 molecular number at the pSiCOH/air surface after NH_3 plasma treatment and restoration of plasma-damaged pSiCOH film to the CH_3 molecular number at the untreated surface could thus be deduced as described in chapter 8. A delta angle distribution was assumed here for the methyl orientation on the surface and at the buried interface to characterize the average orientation of the methyl groups. The ratio of methyl molecular number densities after NH_3 plasma treatment to that before plasma treatment was 0.59, indicating that the surface coverage of CH_3 groups after plasma treatment was ~59% of that of untreated pSiCOH/air surface. That is, about 41% of methyl groups were removed from the untreated pSiCOH/air surface by the exposure to the NH_3 plasma. The reduction of surface coverage of methyl groups is consistent with previous results which reported the removal of methyl groups and the formation of a non-porous nitride surface layer on porous dielectric film by NH_3 plasma treatment.[10,11] In addition, the surface coverage

change of methyl groups after repairing the plasma-damaged pSiCOH/air surface was determined using a similar method, and the ratio of molecular number densities at the pSiCOH/air surface after repairing the NH_3 plasma damaged sample to that before plasma treatment was 1.33, indicating that the surface coverage of CH_3 groups after repair was ~133% of that of untreated pSiCOH/air surface. Next, XPS measurements were applied to provide more information about the elemental compositions and chemical bonding of the pSiCOH film surface before and after NH_3 plasma treatment and repair.

9.3.2 Characterization of the pSiCOH films by XPS

In order to obtain overall elemental composition changes before and after treatment, XPS survey spectra were collected from the untreated, plasma-damaged, and repaired pSiCOH films, respectively.

	C 1s at. %	O 1s at. %	Si 2p at. %	N 1s at. %
Untreated	41.4	34.1	24.4	/
NH_3 plasma	14.3	54.5	24.0	7.2
Repaired	15.4	41.2	26.5	16.9

Table 9.3. Fitting results of XPS survey spectra.

The C 1s content decreased from 41.4% to 14.3% after the plasma treatment, and then increased to 15.4% after repair (Table 9.3), whose trend is similar to the corresponding SFG surface results shown above. However, SFG ssp spectra collected from the pSiCOH/air surfaces suggested that about 40% methyl groups were removed from pSiCOH surface after NH_3 plasma treatment, while XPS results indicated that carbon content reduced more compared to the SFG results. For the repaired film, ssp SFG results indicated that a 33.1% increase in methyl groups (compared to the original sample) occurred at the pSiCOH/air surface after repairing the NH_3

plasma-damaged surface, while XPS measurement indicated that carbon content increased only from 14.3% to 15.4% after repair. This discrepancy is most likely due to the fact that XPS signal is collected from ~10 nm thick top layers of the samples, while SFG provides information from only approximately monolayer/submonolayer from the surface.

Therefore, from the combined XPS and SFG data, it is concluded that the carbon content from the ~10 nm top layer near the surface (or surface region) of a pSiCOH film decreased from 41.4% to 14.3% after NH_3 plasma treatment, while 40% methyl groups at the pSiCOH/air surface (or the top surface layer) were removed by the plasma treatment. After repairing the plasma-damaged pSiCOHfilm, more methyl groups were detected at the pSiCOH/air surface compared to the as-deposited film, however, carbon content collected from the ~10 nm top layer of the pSiCOH film increased only from 14.3% to 15.4%, indicating that the repair method used here is very superficial and may only repair the very few top layers of the damaged pSiCOH but not to the depth probed by XPS.

Figure 9.4 displays the high-resolution C 1s XPS spectra collected from the untreated, plasma-damaged, and repaired pSiCOH films. That is, a typical C 1s envelope was used to provide local binding information about carbon. More quantitative information about various carbon binding changes, including C-C/C-H, C-O, C = O, were obtained by deconvoluting all high-resolution C 1s XPS spectra shown in Figure 9.4, and the fitting results are listed in Table 9.4. Figure 9.4 and Table 9.4 show that for as-deposited pSiCOH film, the carbon near the surface is solely in the form of C-C/C-H bonds. However, NH_3 plasma treatment damaged the film, leading to a decrease in the percentage of the C-C/C-H bonds from 100% to 59.3%, and to the formation of C-O and C = O bonds. This might be a result of the interaction of dangling C bonds formed by the exposure to the NH_3 plasma and the reaction with oxygen from the

environment. After repairing the plasma damaged sample, the percentage of C-O bonds decreased and no C = O signal was detected, while the C-C/C-H bonds increased from 59.3% to 87.2%, indicating that the repaired surface is dominated by C-C/C-H bonds again, similar to the as-deposited sample. Combining all the XPS and SFG results, we can conclude that the repair method used here can effectively recover the plasma damaged surface of the pSiCOH film.

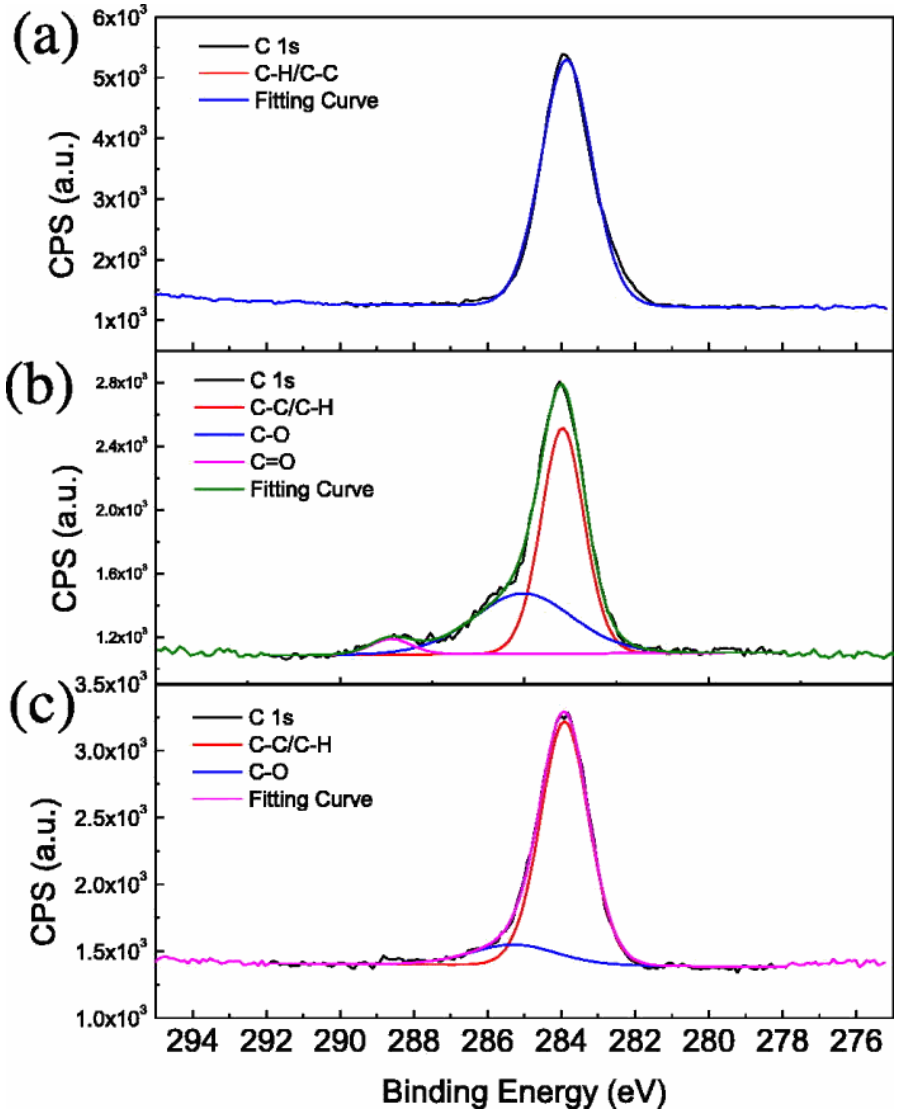

Figure 9.4. C 1s high resolution XPS spectra collected from (a) untreated pSiCOH thin film; (b) pSiCOH thin film after NH_3 plasma treatment for 18 s; (c) pSiCOH thin film after NH_3 plasma treatment for 18 s then repaired.

Sample	C-C/C-H	C-O	C=O
As-deposited	100%	/	/
NH_3 18 s	59.3	36.7	3.9
NH_3 + repaired	87.2	12.9	/

Table 9.4. Fitting results of the C 1s high resolution XPS spectra.

9.3.3 Characterization of the buried SiCNH/pSiCOH interface

As discussed above, from ssp SFG and XPS measurements, we can clearly understand the molecular structures of the pSiCOH/air surface. Subsequently, ppp SFG spectra were acquired from the three pSiCOH films to achieve molecular level understanding of the buried interface. We want to detect whether the plasma treatment and the repair can affect the molecular structure at the SiCNH/pSiCOH buried interface or not. Our previous SFG studies (chapter 7) suggested that different from the ssp spectra, the ppp spectra collected from a low-k film on Si are contributed from both the low-k/air surface and the Si/low-k interface.

Here we adopted a similar approach to the one reported in the last chapter used to study pSiCOH samples provided by Intel. First, the surface structure was deduced. Next, SFG spectra were simulated using known surface structures to deduce the molecular structure at the buried interface. Simulated SFG spectra were then matched to experimental SFG spectra collected at different input angles. First, ppp SFG spectra were collected from the untreated pSiCOH film using different input angles. One negative peak around 2920 cm^{-1} ($Si-CH_3$ C-H symmetric stretch) and one positive peak around 2975 cm^{-1} ($Si-CH_3$ C-H asymmetric stretch) were observed in all three ppp SFG spectra of the untreated pSiCOH film (Figure 9.5(a)), which is very similar to the ssp SFG spectra shown before.

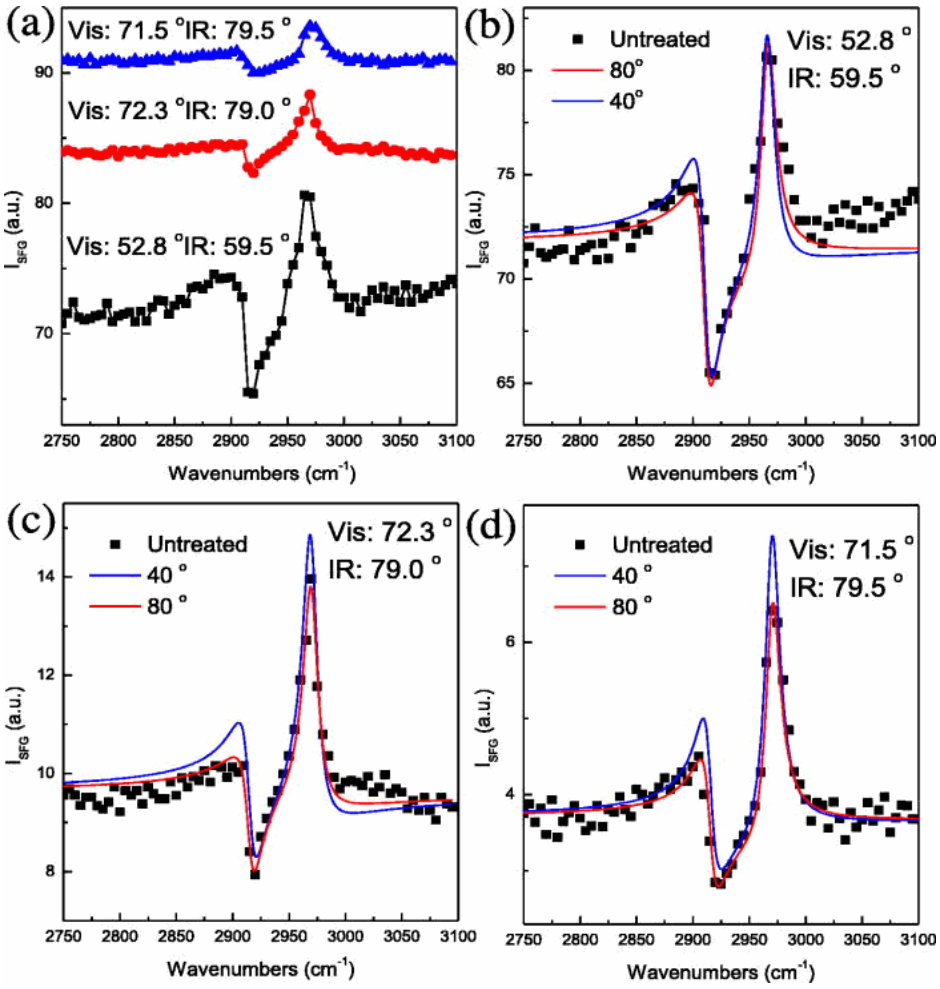

Figure 9.5. (a) Experimental SFG ppp spectra acquired from an untreated pSiCOH film deposited on top of an ultrathin SiCNH film at different input laser angles. (b)–(d) Experimental and simulated ppp SFG spectra for different visible and IR beams input angles. The simulations were based on the tilt angles of the methyl groups at the buried interface of 40 (blue line) and 80 (red line) degrees.

Then SFG spectra were simulated by varying the parameters including phase difference between non-resonant signal and SFG signals, and molecular structural parameters at the buried interface (such as orientation, molecular number, and coverage of methyl groups). To be specific, the peak shapes in the simulated spectra were firstly altered by tuning the phase difference between non-resonant background signal and SFG signal to match the peak shapes detected experimentally in the ppp SFG spectrum.

Subsequently, the simulated SFG spectrum was further optimized by varying molecular structural parameters at the buried interface as mentioned above. The contributions from the pSiCOH/air surface and SiCNH/pSiCOH interface were simulated to clarify the molecular structure at each interface. Figures 9.5(b)–9.5(d) show the optimized simulated SFG spectra at different laser input angles. Figure 9.6 shows the detailed simulated ppp SFG spectra as the average orientation of methyl groups at the buried interface varied from $0°$ to $90°$. In addition, the optimized simulated ppp SFG spectra as well as the corresponding components from surface and buried interface at different input laser angles of the visible and IR beams are displayed. For the smallest input angles used here (visible beam: $52.8°$ and IR beam: $59.5°$), we can clearly see from Figure 9.6(a) that the asymmetric peak changed substantially while the symmetric peak was almost unchanged as the average orientation of methyl groups at the SiCNH/pSiCOH buried interface varied from $0°$ to $90°$ for the untreated sample. As compared with the corresponding experimentally collected ppp SFG spectrum, it is clear that the simulated spectrum with the methyl orientation angle at the buried interface of $80°$ matched the experimental spectrum best (Figure 9.5(b)). The contributions from the surface and the buried interface were simulated (by using $80°$ as the most likely methyl orientation at the buried interface) and shown in Figure 9.6(b). Interestingly, the pSiCOH/air surface contributes much more to the overall SFG signal

relative to the contribution from the SiCNH/pSiCOH buried interface, which is due to the difference of Fresnel factors at the surface and buried interface.

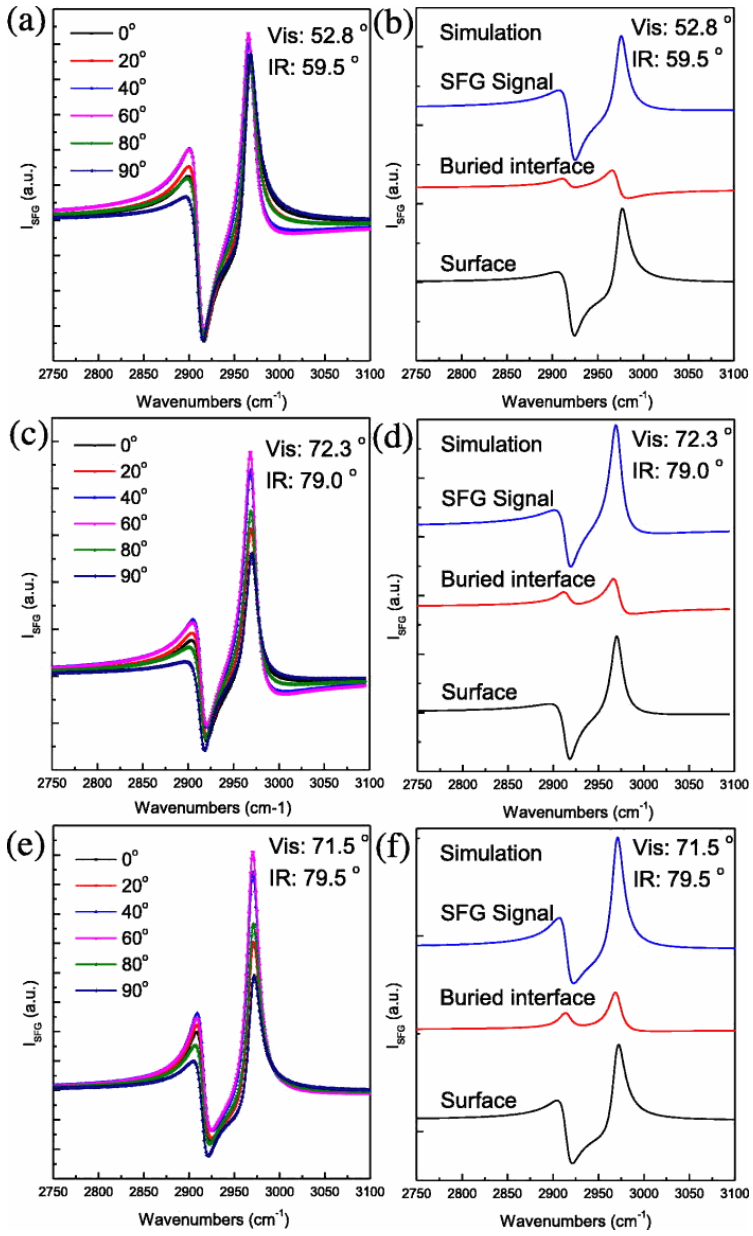

Figure 9.6. (a), (c), and (e) Simulated ppp SFG spectra as a function of the methyl orientation at the untreated SiCNH/pSiCOH buried interface for different visible and IR beams input angles. (b), (d), and (f) Simulated ppp SFG spectra from the untreated pSiCOH film together with the surface and buried interface components of the simulated SFG signal for different visible and IR beam input angles.

Therefore, in order to collect two additional sets of data to further confirm this result, higher laser input angles were selected because the ratio of Fresnel factors at the buried interface to the Fresnel factors at the surface changed. However, both Fresnel factors decreased as the input angles increased. The decrease of Fresnel factors directly induced the overall SFG signals to decrease as the input angles increased, which can be clearly observed in Figure 9.5(a). By altering the input laser angles, ppp SFG spectral features remained similar and only the peak intensities became smaller as the input laser angles increased. Similar simulation processes were subsequently applied to obtain the possible average orientation of methyl groups at the buried interface for the untreated pSiCOH films. Different from the case of low input laser angles (Figure 9.6(a)), here both symmetric and asymmetric peaks altered as the orientation of CH_3 at the SiCNH/pSiCOH buried interface varied from 0 ° to 90 °. Therefore, it is easy to conclude that the simulated ppp SFG spectra with the methyl average orientation of 80 ° at the buried interface are the closest ones for the two cases measured with high input laser angles, as shown in Figures 9.5(c) and 9.5(d). Combining the low input laser angle result, our SFG studies show that the orientation of methyl groups at the buried interface is around 80 ° vs. the surface normal for the untreated film. That is to say, methyl groups almost lie down at the buried interface, which is quite different from the top surface but quite similar to our previous study where the tilt angle of methyl groups at the buried interface is high for model low-k films.

Next, a similar method was used to determine the molecular structural changes at the SiCNH/pSiCOH buried interface after the structure was exposed to NH_3 plasma. Figure 9.7(a) presents the ppp SFG spectra collected from the plasma treated Si/SiCNH/pSiCOH film structure at various laser input angles. Only the ppp spectrum collected at the input angles of the visible and IR beams at about 71.5 ° and 79.5 °, respectively, showed relatively strong SFG signal.

Similar to the untreated sample case, one negative peak around 2920 cm^{-1} ($Si\text{-}CH_3$ C-H symmetric stretch) and one positive peak around 2975 cm^{-1} ($Si\text{-}CH_3$ C-H asymmetric stretch) were observed in the corresponding ppp SFG spectrum (Figure 9.7(a)), which is also very similar to the ssp SFG spectra shown before (Figure 9.2(b)). For the other two spectra (collected at the input angles of the visible and IR beams at about 52.8 °and 59.5 °, as well as 72.3 °and 79.0 °), the SFG signals are very weak and the spectral signatures are not clear enough. While the calculations indicated higher Fresnel factors at lower input angles, lower SFG signal was observed here, which may be due to the interference between the non-resonant background signal and SFG contributions from the surface and interface. Therefore, we decided that only the ppp SFG spectrum with the strong signal should be analyzed. The other two sets of data from which we could not obtain the unique conclusion about the methyl orientation at the buried interface will not be used for data analysis.

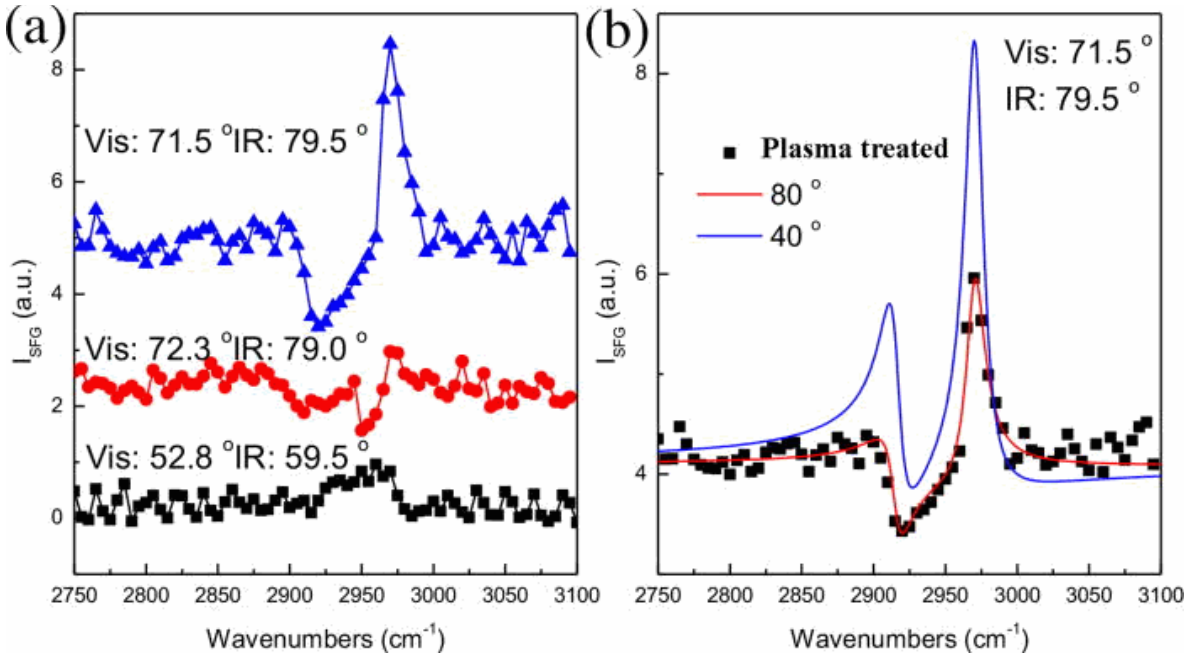

Figure 9.7. (a) Experimental ppp SFG spectra from a plasma-treated Si/SiCNH/pSiCOH structure for different input laser angles. (b) Experimental and simulated ppp SFG spectrum acquired from the structure in film (a) for the input angles of the visible and IR beams of 71.5 ° and 79.5 °, respectively.

To simulate the ppp SFG spectrum of the pSiCOH film after NH_3 plasma treatment, several simulation parameters need to be reconsidered compared to the untreated sample. We already knew from the ssp SFG results that the methyl group average orientation after plasma treatment was ~58 ° and about 41% methyl groups were removed from pSiCOH/air surface compared to that of the untreated sample. The comparison between the experimental ppp SFG spectrum and two simulated spectra with two different average orientations of methyl groups at the buried interface was shown in Figure 9.7(b). More detailed simulation results as the average orientation of methyl groups at the buried interface varied from 0 ° to 90 ° were displayed in Figure 9.8(a). Similar to the untreated case at the same input laser angles, both symmetric and asymmetric C-H stretching peaks were altered as the methyl orientation at the buried interface changed (Figure 9.8(a)). Therefore, it is clearly observed that the 80 ° case fits the experimental spectrum best, which is the same as the untreated case. This result indicates that the 18 s NH_3

plasma treatment only altered the surface structures but did not affect the molecular structures at the buried interface, as might be expected from a short plasma treatment.

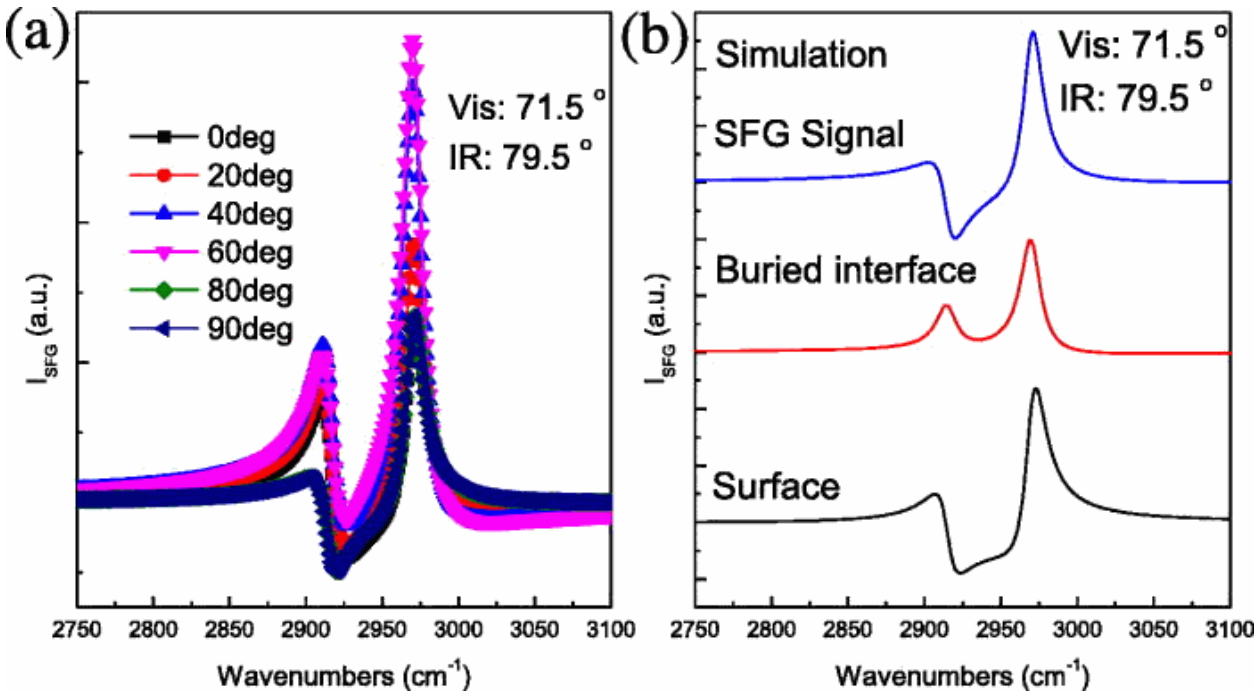

Figure 9.8. (a) Simulated ppp SFG spectra as the orientation of methyl groups at the plasma-treated SiCNH/pSiCOH buried interface varied from 0 ° to 90 ° and the input laser angles of visible and IR beams are 71.5 ° and 79.5 °, respectively. (b) Simulated ppp SFG spectra from a plasma-treated pSiCOH film together with the surface and buried interface components of the simulated SFG signal as the input angles of visible and IR beams are 71.5 ° and 79.5 °, respectively.

Furthermore, similar steps were also used to examine the possible structural changes at the SiCNH/pSiCOH buried interface of plasma-damaged structure after repair. From our above discussions on the surface structural changes observed by combining ssp SFG and XPS measurements, it can be expected that the repair method can repair only the very few layers from the top of the pSiCOH film instead of the whole plasma-damaged region. Therefore, the molecular coverage of methyl groups at the buried interface was believed to be constant

compared to the untreated one. SFG measurements were applied firstly here to collect ppp SFG spectra from the repaired pSiCOH film using different input laser angles (Figure 9.9(a)). The spectral signatures of these three spectra are similar, which are all dominated by two significant peaks, one negative peak around 2920 cm^{-1} (Si-CH_3 C-H symmetric stretch) and one positive peak around 2975 cm^{-1} (Si-CH_3 C-H asymmetric stretch). This spectral feature is very similar to the ssp SFG spectrum collected from the repaired pSiCOH film shown before (Figure 9.2(c)). The intensities of these two peaks decreased as the input laser angles decreased, whose trend is very similar to the untreated case. After obtaining the various ppp SFG spectra of repaired sample at different input laser angles, simulation was carried out to determine the possible average orientation of methyl groups at the buried interface. Figure 9.9(b) gives the direct comparison between the experimental ppp SFG spectrum and two simulated spectra with two different average orientations of methyl groups at the buried interface with the input angles of the visible and IR beams at 52.8 ° and 59.5 ° respectively. Figure 9.10(a) shows the simulation results as the average orientation of methyl groups at the buried interface varied from 0 ° to 90 °. Only the shape of the symmetric peak and the intensity of the asymmetric peak were changed as the methyl orientation at the buried interface changed (Figure 9.9(b)). Based on this simulation, it is thus suggested that the average orientation of CH_3 groups at the buried interface is around 80 °, which is the same as the untreated and plasma-damaged cases. To make this result more reliable, simulation was also applied to two additional sets of data obtained by tuning the input laser angles (Figures 9.9(c), 9.9(d), and 9.10(c)–9.10(f)). Clearly, as the methyl orientation at the buried interface varied from 0 ° to 90 °, both symmetric and asymmetric peaks were altered, which supports the determined result. And similarly, the 80 ° simulated spectrum matched the ppp experimental spectrum most closely at both sets of high input laser angles. The cumulative

data suggest that the orientation of methyl groups at the buried interface was not changed after repair, showing that the repair process does not affect the buried interface structure in this study.

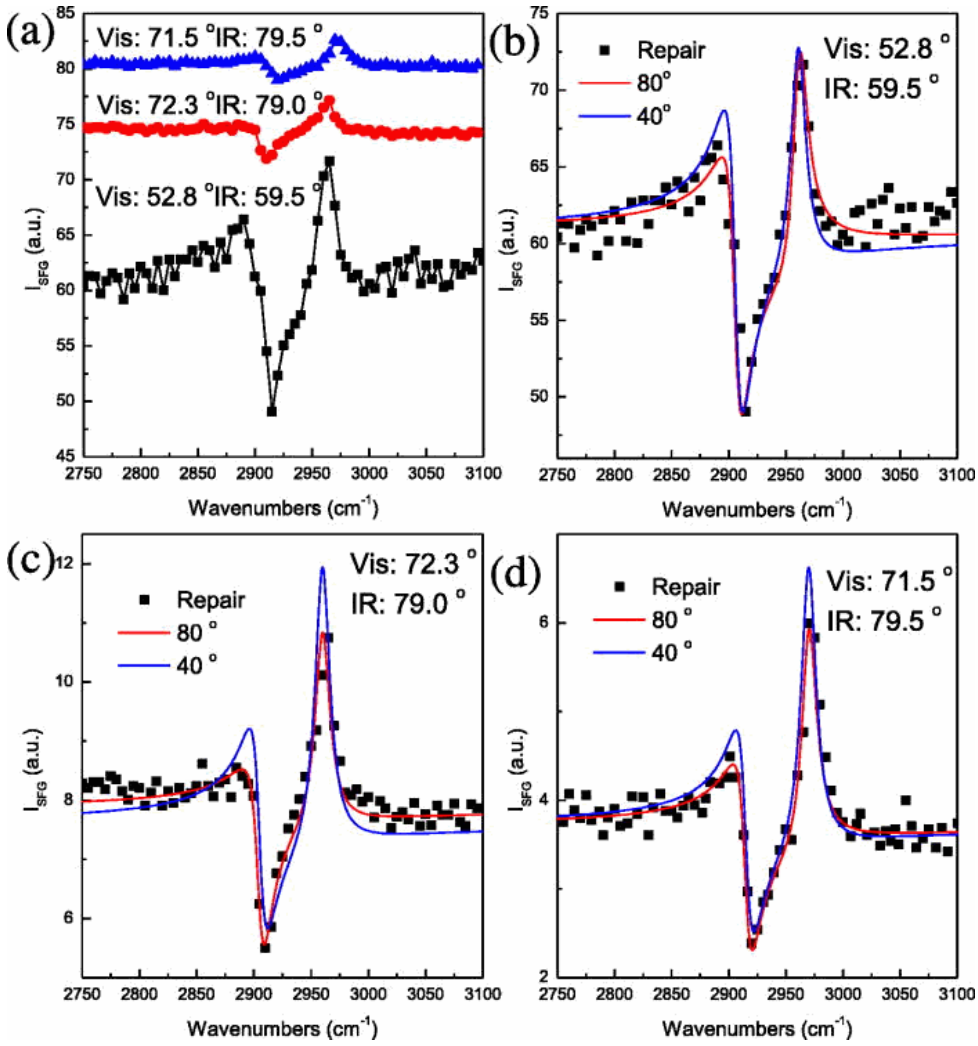

Figure 9.9. (a) Experimentally collected SFG ppp spectra from a repaired pSiCOH/SiCNH film at different input laser angles. Experimentally collected and simulated SFG ppp spectra with the input angles of visible and IR beams at (b) 52.8 ° and 59.5 °, (c) 72.3 ° and 79.0 °, and (d) 71.5 ° and 79.5 °, respectively.

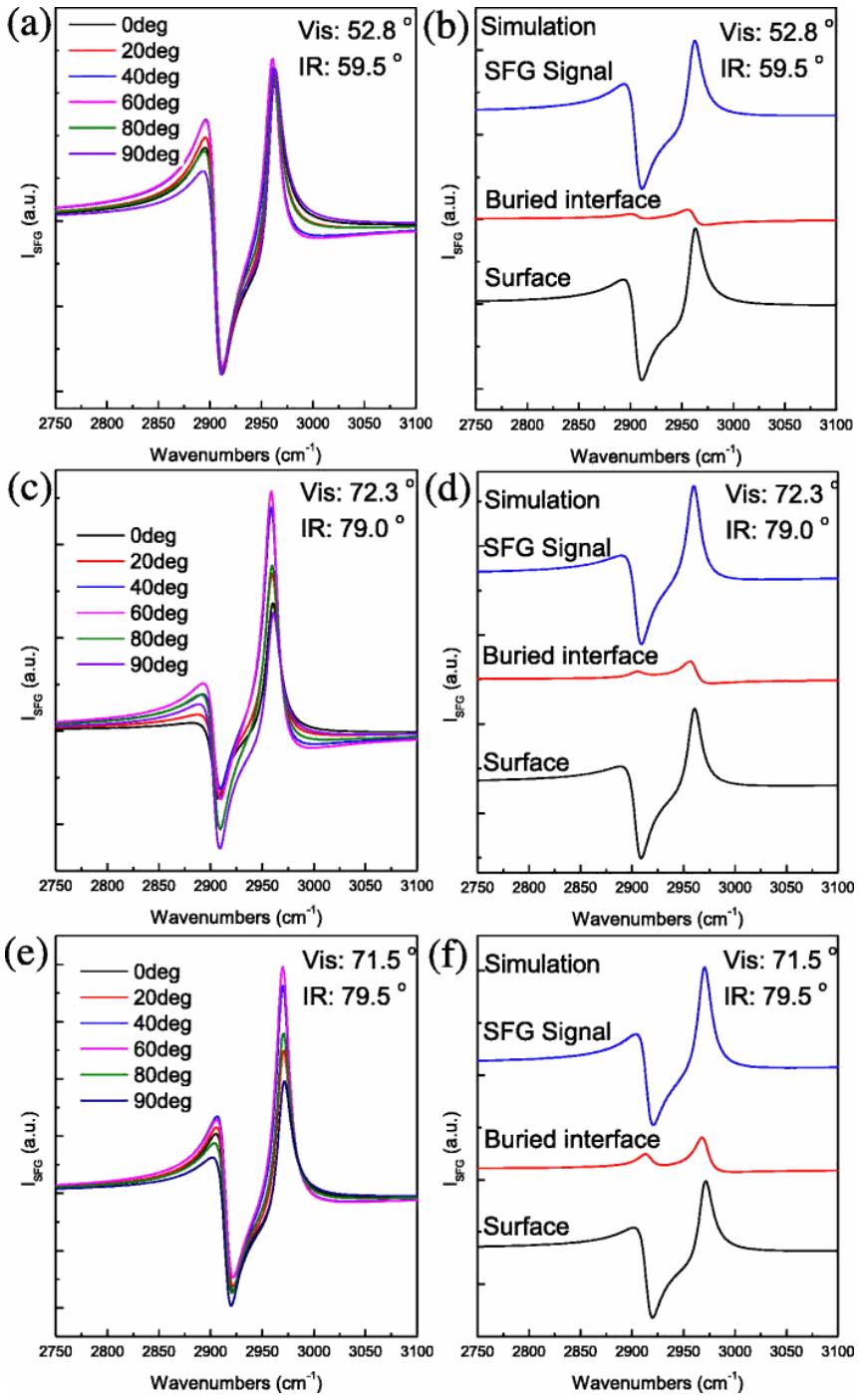

Figure 9.10. Simulated ppp SFG spectra from the pSiCOH film on SiCNH as the orientation of the methyl groups at the repaired SiCNH/pSiCOH buried interface varied from 0 ° to 90 ° at different input angles of the visible and IR beams: (a) 52.8 ° and 59.5 °, (c) 72.3 ° and 79.0 °, and (e) 71.5 ° and 79.5 °, respectively. Simulated ppp SFG spectra from the repaired pSiCOH film together with the surface and buried interface components of the simulated SFG signal at the input angles of visible and IR beams: (b) 52.8 ° and 59.5 °, (d) 72.3 ° and 79.0 °, and (f) 71.5 ° and 79.5 °, respectively.

9.4 Effects of reactive ion etching (RIE) and repair on pSiCOH interfaces

Following the study on the effect of ammonia plasma treatment and dielectric repair on SiCOH interfaces, we then applied the same methodology to study how reactive ion etching (RIE) and dielectric repair affect SiCOH interfaces. As discussed above, ammonia plasma was selected to simulate the plasma damage to pSiCOH during the pre-clean process before the deposition of a dielectric cap. Here, pSiCOH films were treated with RIE and then repaired using silylation to study how real processing steps (rather than simulated steps) currently used at IBM during microelectronic package fabrication affect SiCOH surfaces and buried interfaces. The first goal was to compare how SiCOH interfaces are damaged by ammonia plasma treatment and RIE. The second goal was to characterize how different plasma damaged surfaces were repaired by the same silylation process. The same experimental parameters used in the NH_3 plasma study were used. Here, two sets of input angles were used: In the 'flat' samples, the input visible and infrared angles were 60 ° and 53 °, respectively. In the 'tilted' samples, the input visible and infrared angles were 68 ° and 61 °, respectively.

Two features were detected in the SFG spectrum collected from the RIE treated surface near 2850 and 2940 cm^{-1}. The feature near 2850 cm^{-1} can be assigned to methylene groups, possibly from Si-CH_2-Si components in the structure. One possibility is that the –CH_2- links in the bulk were exposed on the surface after the RIE etched the topmost surface layers away. The feature near 2940 can be fit using two peaks centered at 2920 and 2960 cm^{-1} which indicates that Si-CH_3 groups were still present at the surface after RIE treatment. The orientation of Si-CH_3 groups at the RIE treated surface was determined to be ~40°. For comparison, after NH_3 treatment, the groups were oriented at 58°. The number density of Si-CH_3 groups at the RIE treated surface divided by the number density of Si-CH_3 groups at the repaired surface was ~0.12

(N_{RIE}/N_{repair} = 0.12). The number density decrease after RIE was greater than after ammonia treatment which suggests that RIE oxidized more methyl groups on the surface.

The SSP polarization combination was used to probe the repaired SiCOH surface, shown in Figure 7.11. Two derivative-shaped peaks were detected with peak centers near 2912 and 2965 cm^{-1} which can be assigned to the Si-CH_3 C-H symmetric and asymmetric stretches, respectively. This indicates that the repaired surface was dominated by Si-CH_3 groups, which is similar to the repaired SiCOH surface from NH_3 plasma treated samples. The orientation of the methyl groups at the repaired surface was ~55°, different than their orientation at the repaired surface after NH_3 treatment (38°).

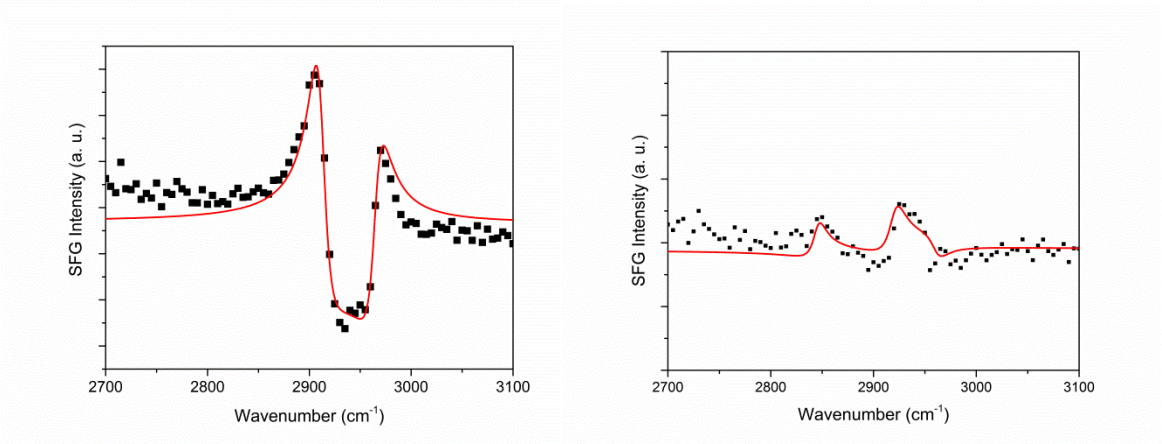

Figure 9.11 SSP spectrum from repaired (left) and RIE treated (right) SiCOH films.

We also acquired SFG spectra in the 3000-3600 cm^{-1} range to check if adsorbed water was present at the surface (Figure 9.12). At the RIE treated surface, a broad peak was observed from ~3150 to 3600 cm^{-1}. However, at the repaired surface, a similar broad peak appeared around 3250 to 3600 cm^{-1}. This broad feature can be assigned to adsorbed surface water that was

either strongly (peak center ~3200 cm^{-1}) or weakly hydrogen bonded (peak center ~3400 cm^{-1}) at the surface.

The stronger peak intensity of the water feature in the spectrum collected from the RIE treated surface indicates that more water was adsorbed at the surface or that the water was more ordered, relative to the repaired surface. In addition, the feature had a stronger component near 3200 cm^{-1} which indicates that more strongly hydrogen bonded water was present at the RIE treated surface. At the repaired surface, the water feature was weaker and was dominated by weakly hydrogen bonded water.

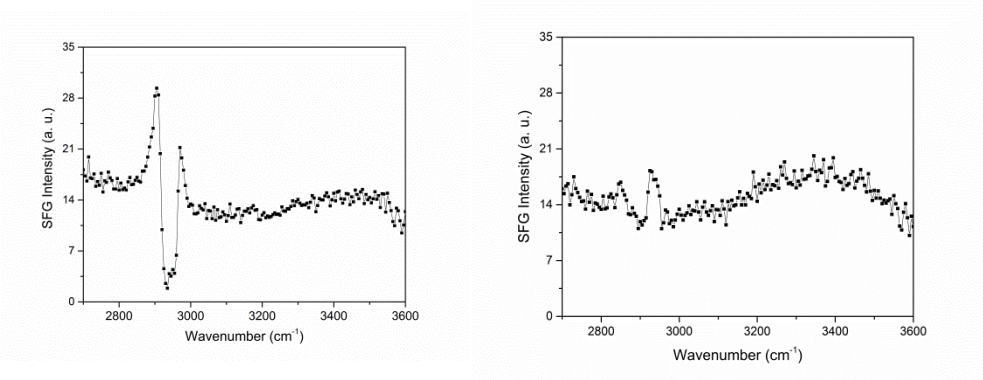

Figure 9.12. SSP spectrum from repaired (left) and RIE treated (right) SiCOH films.

The buried SiCNH/SiCOH interfaces at RIE damaged and repaired films were then characterized by collecting SFG PPP spectra from the SiCOH films (Figure 9.13). Two weak features near 2920 and 2965 cm^{-1} were detected in the SFG PPP spectrum collected from the RIE treated film. To simulate SFG spectra, the depletion of methyl groups due to the RIE treatment was accounted for by reducing the number density by ~80-90% following the surface results and the surface orientation was set at 40°. Simulated SFG spectra matched experimental spectra when the buried Si-CH_3 groups were oriented at 80°. Combined with our previous results, these results indicate that the buried interface was not substantially altered by RIE treatment or repair.

Two features near 2920 and 2965 cm^{-1} were detected in the SFG PPP spectrum collected from the repaired film. No new features were detected in the PPP spectrum, which indicates that the buried interface was also dominated by Si-CH_3 groups. Following our previously methodology, we simulated SFG PPP spectra where the surface contributions were known to deduce the buried interface structure. Similar to our previous finding, simulated SFG spectra matched experimental spectra when the buried Si-CH_3 groups were oriented at 80° (using a surface orientation of 55°).

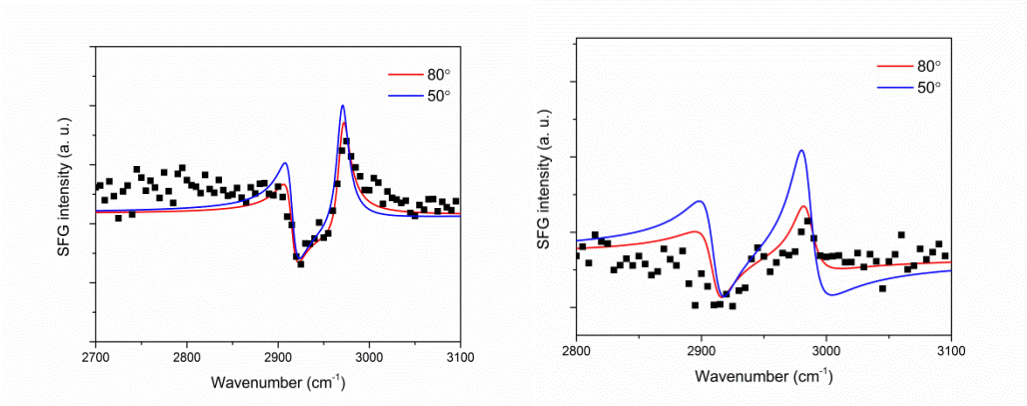

Figure 9.13. SFG PPP spectrum 'flat' samples repaired (left) and RIE treated (right).

To support the SFG studies on the 'flat' samples, we also collected SFG PPP spectra from RIE treated and repaired SiCOH films using a different set of input angles following our previous methodology (Figure 9.14). The molecular structure at the SiCOH interfaces is constant, but features in the SFG spectra may change shape at different input angles as discussed previously. Two features near 2915 and 2965 cm^{-1} were detected in the SFG PPP spectrum collected from the repaired sample using the 'tilted' sample geometry. Consistent with the previous results, simulated SFG spectra matched experimental spectra when the buried Si-CH_3 groups were oriented at 80°

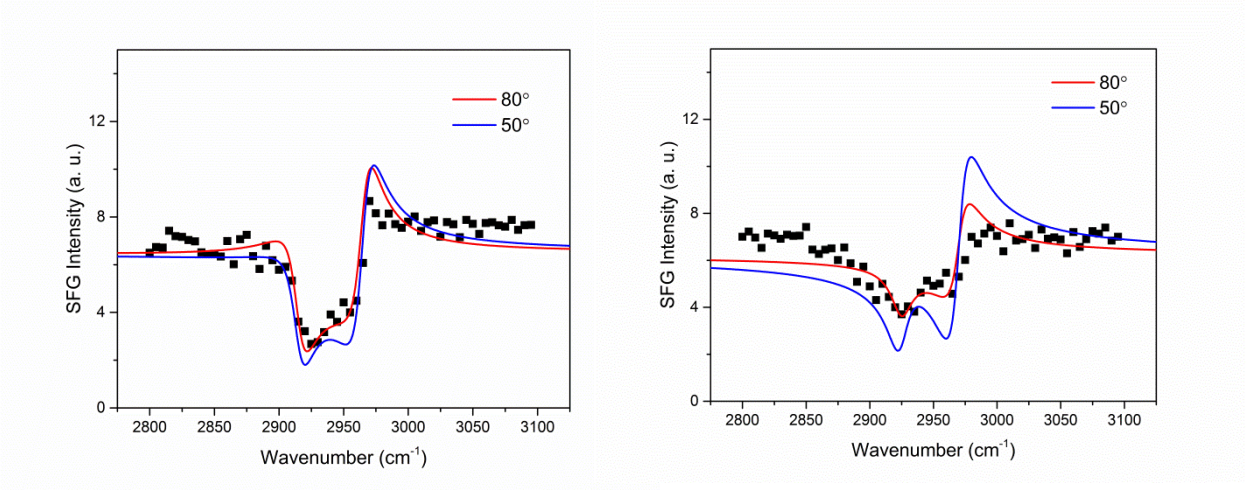

Figure 9.14. SFG PPP spectrum 'tilted' samples repaired (left) and RIE treated (right).

In summary, this study shows that both repair and RIE treatment changed the surface structure, but not the buried interfacial structure.

9.5 Conclusion

The main advantage SFG has over many commonly used surface analytical techniques such as XPS and ATR-FTIR is that it can be used to quantitatively characterize molecular structures at buried interfaces in situ selectively without contributions from the bulk material in terms of what functional groups are present at the interface, the orientation of the functional groups, and surface coverage.

The effects of NH_3 plasma treatment, RIE, and dielectric repair on the molecular structures at the pSiCOH/air surface and SiCNH/pSiCOH interface were investigated. Combining ssp SFG and XPS measurements, it is concluded that the surface coverage and orientation of Si-CH_3 groups at the pSiCOH surface were altered after exposure to NH_3 plasma for 18 s, but the damage was limited to the surface. After RIE, methylene groups were detected at

the pSiCOH surface and the surface coverage and orientation of Si-CH_3 groups at the pSiCOH surface were changed. RIE may have had a greater etching effect than ammonia plasma which exposed bulk –CH_2- groups to the surface. Comparing both the ammonia plasma and the RIE studies, these results demonstrate that etched layers at pSiCOH surfaces resulting from plasma treatment have different molecular structures than corresponding pristine surfaces. Consequently, the molecular structure at etched surfaces should be characterized in tandem with surface energy and surface elemental composition to elucidate the effects of various plasma treatments.

The repair method used in this study can effectively repair the surface structures after ammonia plasma treatment but will not recover completely the entire plasma-damaged layer. Simulated SFG spectra with various average orientations of methyl groups at the buried interface were compared with experimental ppp SFG spectra using different sets of input laser angles to determine the molecular structural information at the buried interface after exposure to NH_3 plasma, RIE, and repair of the plasma-damaged pSiCOH film. The average orientation and coverage of methyl groups at the buried interface were found to be unchanged after NH_3 plasma treatment, RIE, and repair. This study clearly demonstrated that SFG is a powerful tool to elucidate surface and buried interface structures of ultralow-k dielectrics. We believe that this technique is general and can be extended to provide *in-situ* molecular level studies of many other thin film systems in tandem with traditional studies using surface analytical techniques to elucidate the effects of film surface damage or modification.

9.6 Impact

The method developed in this chapter is general and demonstrates that SFG measurements can be used to characterize real industry samples and the effects of industrial microfabrication processing steps on molecular structures at silicon-supported thin film

interfaces. By analyzing the SiCOH films on silicon wafers, RIE and silylation repair were performed using manufacturing scale tools at IBM. In our previous studies on pSiCOH films provided by Intel, real industry samples were characterized, but a model plasma treatment was used. Here, real industry samples were characterized in addition to real industry processing steps. By combining such SFG studies with other surface characterization techniques and interfacial property measurements, structure-function relationships at interfaces can be directly elucidated and used in the design of new materials with optimized properties. For example, the molecular structure of pSiCOH (or other) film surfaces can be correlated to effectiveness of downstream processing steps such as the deposition of an inorganic film on a surface modified pSiCOH (or other) films.

9.7. References

(1) Grill, A.; Gates, S. M.; Ryan, T. E.; Nguyen, S. V.; Priyadarshini, D. Progress in the Development and Understanding of Advanced Low K and Ultralow K Dielectrics for Very Large-Scale Integrated interconnects—State of the Art. *Appl. Phys. Rev.* **2014**, *1* (1), 011306.

(2) Grill, A.; Neumayer, D. A. Structure of Low Dielectric Constant to Extreme Low Dielectric Constant SiCOH Films: Fourier Transform Infrared Spectroscopy Characterization. *J. Appl. Phys.* **2003**, *94* (10), 6697.

(3) Grill, A.; Patel, V. Low dielectric constant films prepared by plasma-enhanced chemical vapor deposition from tetramethylsilane. *J. Appl. Phys.* **1999**, *85*, 3314.

(4) Grill, A.; Patel, V. Ultralow- dielectrics prepared by plasma-enhanced chemical vapor deposition. *Appl. Phys. Lett.* **2001**, *79*, 803.

(5) Grill, A.; Edelstein, D.; Lane, M.; Patel, V.; Gates, S.; Restaino, D.; Molis, S. Interface engineering for high interfacial strength between SiCOH and porous SiCOH interconnect dielectrics and diffusion caps. *J. Appl. Phys.* **2008** 103, 054104.

(6) Hoofman, R.; Verheijden, G.; Michelon, J.; Iacopi, F.; Travaly, Y.; Baklanov, M.; Tőkei, Z.; Beyer, G. Challenges in the implementation of low-k dielectrics in the back-end of line. *Microelectron. Eng.* **2005**, *80*, 337.

(7) Baklanov, M.R.; Marneffe, J.; Shamiryan, D.; Urbanowicz, A. M.; Shi, H.; Rakhimova, T.V.; Huang, H.; Ho, P. Plasma processing of low-k dielectrics. *J. Appl. Phys.* **2013**, *113*, 041101.

(8) Myers, J. N.; Zhang, X.; Bielefeld, J. D.; Lin, Q.; Chen, Z. Nondestructive in Situ Characterization of Molecular Structures at the Surface and Buried Interface of Silicon-Supported Low-K Dielectric Films. *The Journal of Physical Chemistry B* **2015**, *119*, 1736–1746.

(9) Zhang, X.; Myers, J. N; Bielefeld, J. D.; Lin, Q.; Chen, Z. In Situ Observation of Water Behavior at the Surface and Buried Interface of a Low-K Dielectric Film. *ACS Appl. Mater. Interfaces* **2014**, *6*, 18951.

(10) Liu, P.; Chang, T.; Yang, Y.; Cheng, Y.; Sze, S. Effects of NH_3-plasma nitridation on the electrical characterizations of low-k hydrogen silsesquioxane with copper interconnects. *IEEE Trans. Electron Dev.* **2000**, *47*, 1733.

(11) Chang, T.; Mor, Y.; Liu, P.; Tsai, T.; Chen, C.; Mei, Y.; Sze, S. The effect of ammonia plasma treatment on low-k methyl-hybrido-silsesquioxane against photoresist stripping damage. *Thin Solid Films* **2001**, *398*, 632.

Chapter 10

Conclusion and Outlook

The overall goal of this thesis was to develop instrumental and data analysis methodologies that can be used to nondestructively characterize interfacial molecular structures at buried polymer interfaces in microelectronic devices and elucidate the relationship between buried molecular structures and interfacial properties. In this thesis, several advances were presented in the development of SFG vibrational spectroscopy into a metrology tool for nondestructive characterization of molecular structures at buried polymer/polymer, metal/polymer and semiconductor/polymer interfaces *in situ*. In particular, three advances in using SFG as a metrology tool were presented: #1) Buried polymer/epoxy interfaces were characterized before and after microelectronic processing steps and accelerated stress testing to directly relate molecular structural changes at buried adhesive interfaces to changes in adhesion properties; #2) Nondestructive characterization of buried copper/epoxy interfaces using SFG was combined with destructive characterization of fractured surfaces of the delaminated interface for comprehensive locus of failure analysis at the molecular level; and #3) Quantitative data analysis methodology was developed to simultaneously characterize the surface and buried interface of silicon-supported thin low-k polymer films nondestructively before and after microelectronic processing steps which provided a molecular level understanding of the effects of the processing.

In chapter 2, the surface molecular structure of spin cast homopolymers which contain phenyl groups was found to be influenced by the solvent aromaticity. The surface molecular

structure of spin cast homopolymers which contain phenyl groups was found to be influenced by the solvent aromaticity. When phenyl groups were located in a linear polymer backbone, spin casting with aromatic solvents enhanced the phenyl SFG signal relative to when a non-aromatic solvent was used which suggests that the aromatic solvent induced the surface phenyl groups to be more ordered and/or to lie more perpendicular to the film surface. In addition, when alkyl structures were believed to be present at the solvent/air interface, alkyl structures were observed at the film/air interface which suggests that molecular structure at the solvent/air interface was carried to the film surface. The effects of solvent aromaticity on phenyl ordering at spin cast film surfaces were explained by different molecular structures of polymer chains at solvent/air interfaces, preferential solvation of functional groups during evaporation, and re-orientation of bulky side groups at the polymer film/air interface.

Designing polymer films with desired surface structures is difficult. Using the knowledge obtained from this study, we may be able to control and design surface structures of polymer films with tunable properties using spin coating by choosing proper solvents. Better understanding of the relationship between coating solvent and the resulting spin cast film surface will aid in the rational design of polymer surface properties for applications in microelectronic packaging, solar cells, and biomedical devices.

In chapter 3, the effects of polyimide surface plasma treatment on the molecular structures at corresponding polyimide/air and buried polyimide/epoxy interfaces were investigated *in situ* using SFG vibrational spectroscopy. SFG results showed that the polyimide backbone molecular structure was different at polyimide/air and polyimide/epoxy interfaces before and after plasma treatment. The different molecular structures at each interface indicate that structural reordering of the polyimide backbone occurred as a result of plasma treatment and

contact with the epoxy adhesive. Furthermore, quantitative orientation analysis indicated that plasma treatment of polyimide surfaces altered the twist angle of the polyimide backbone at corresponding buried polyimide/epoxy interfaces. These results provide insight on the molecular level effects of plasma treatment on adhesion strength and the lack of clear correlation between surface energy calculations and interfacial adhesion strength measurements.

Delamination at polyimide/epoxy interfaces due to weak interfacial adhesion continues to be reliability concern in microelectronic packaging. Plasma treatment is widely used to increase the adhesion strength of polyimide to epoxy underfills, however the adhesion mechanism is not well understood. This research suggests that buried interfacial molecule structures can be affected by plasma treatment on the surfaces used to prepare the interfaces, which should be considered in adhesion mechanisms and such structures should be correlated to adhesion strength measurements. Relationships between adhesion strength and interfacial molecular structures at buried adhesive interfaces can then be used to design interfacial structures with predicted adhesion properties in microelectronic packages that can withstand harsh qualification tests.

In chapter 4, SFG and ATR-FTIR were used to study molecular structures at buried epoxy interfaces during hygrothermal aging to relate molecular structural changes at buried interfaces to decreases in macroscopic adhesion strength. SFG peaks associated with strongly hydrogen bonded water were detected at hydrophilic material/epoxy interfaces. Ordered interfacial water was also correlated to large decreases in interfacial adhesion strength that occurred as a result of hygrothermal aging, which suggests that water diffused to the interface and replaced original hydrogen bond networks. No water peaks were observed at hydrophobic material/epoxy interfaces, which was correlated with a much smaller decrease in adhesion strength from the same aging process. ATR-FTIR water signals observed in the epoxy bulk were

mainly contributed by relatively weakly hydrogen bonded water molecules, which suggests that the bulk and interfacial water structure was different. Changes in interfacial methyl structures were observed regardless of the interfacial hydrophobicity which could be due to water acting as a plasticizer that restructured both the bulk and interfacial molecular structure. This research demonstrated that SFG studies of molecular structural changes at buried epoxy interfaces during hygrothermal aging can contribute to the understanding of moisture-induced failure mechanisms in electronic packages that contain organic adhesives. Importantly, hygrothermal treatment was found to influence hydrophobic interfaces less, showing that hydrophobic materials can better resist qualification testing in high heat humidity environments. The work in this chapter suggests that the interfacial adhesion strength at organic adhesive interfaces in microelectronic packages may be improved during hygrothermal aging qualification testing by using polymers with hydrophobic surface structures, polymers with surfaces modified to be more hydrophobic, or buried interfaces engineered to be more hydrophobic.

In chapter 5, methodology was developed to nondestructively characterize the molecular structure at buried copper/epoxy interfaces in situ using SFG vibrational spectroscopy. The methodology was applied to elucidate the relationship between molecular structure at the buried copper/epoxy interface and delamination behavior by correlating molecular structure with the locus of failure analysis. SFG and locus of failure analysis suggested that molecular ordering and silane behavior at the copper interface both contribute to a gradient in network structure and mechanical properties near the copper interface. Silanes adhesion promoters were directly detected at buried copper/epoxy interfaces and delamination was found to occur in the epoxy about 10 nm from the interface rather than at the copper/epoxy interface. This work suggests that an adhesive transition layer should be used between copper and epoxy that has high cohesive

strength, strong adhesion to copper and copper oxides, and sufficient thickness and composition to allow diffusion of the epoxy components into the layer such that sharp gradients in cohesive strength are not present in the layer. The combined destructive and nondestructive characterization methodology developed is general and can be directly applied to selectively characterize relationships between molecular structure at buried metal/polymer interfaces and interfacial properties such as adhesion, delamination, and interfacial moisture transport during Joint Electron Device Engineering Council qualification testing.

In chapter 6, methodology was developed to achieve in situ observation of water structure and water-induced structure changes at the poly(methyl silsesquioxane) (PMSQ) surface and the PMSQ/solid buried interface at the molecular level by combining SFG vibrational and FTIR spectroscopic studies. First, in situ SFG investigations of water uptake were performed to provide direct evidence that water diffuses predominantly along the PMSQ/solid interface rather than through the bulk. Furthermore, SFG experiments were conducted at the PMSQ/water interface to simulate water behavior at the pore inner surfaces for porous low-k materials. Water molecules were found to form strong hydrogen bonds at the PMSQ surface, while weak hydrogen bonding was observed in the bulk. However, both strongly and weakly hydrogen bonded water components were detected at the PMSQ/SiO_2 buried interface. This suggests that the water structures at PMSQ/solid buried interfaces are also affected by the nature of solid substrate. Moreover, the orientation of the Si-CH_3 groups at the buried interface was permanently changed by water adsorption, which might due to low flexibility of Si-CH_3 groups at the buried interface. This study provides direct evidence that water molecules tend to strongly bond (chemisorbed) with low-k dielectric at pore inner surfaces and at the low-k/solid interface of porous low-k dielectrics. Therefore, water components at the surfaces, rather than the bulk, are

likely more responsible for chemisorbed water related degradation of the interconnection layer. This finding suggests that the structure of low-k pore surfaces and film surfaces should be modified to prevent chemisorbed water.

In chapter 7, in situ nondestructive methodology to characterize the molecular structure at the surface and buried interface of silicon-supported low-k dielectric thin films using SFG was described. Film thickness-dependent reflected SFG signals were observed, which were explained by multiple reflections of the input and SFG beams within the low-k film. The effect of multiple reflections on the SFG signal was determined by incorporating thin-film interference into the local field factors at the low-k/air and Si/low-k interfaces. Simulated thickness-dependent SFG spectra were then used to deduce the relative contributions of the low-k/air and low-k/Si interfaces to the detected SFG signal. The nonlinear susceptibilities at each interface, which are directly related to the interfacial molecular structure, were then deduced from the isolated interfacial contributions to the detected SFG signal. The method developed is general and demonstrates that SFG measurements can be integrated into other modern analytical and microfabrication methods that utilize silicon-based substrates. Therefore, the molecular structure at the surface and buried interface of thin polymer or organic films deposited on silicon substrates can be measured in the same experimental geometry used to measure many optical, electrical, and mechanical properties and the developed methodology can be directly incorporated into microelectronic packaging metrology.

In chapter 8, the effects of oxygen plasma treatment on molecular structures at the surfaces and buried interfaces of low-k organosilicate (SiCOH) films provided by Intel were investigated using SFG vibrational spectroscopy and Raman spectroscopy. SFG and Raman spectra were acquired from pristine and plasma-treated low-k SiCOH films to characterize the

interfacial and bulk molecular structures of the films before and after plasma treatment. Two SiCOH films with similar molecular structures but different porosities were investigated to correlate the effects of plasma treatment to the porosity of low-k films. SFG spectra indicated that the surface molecular structure of dense SiCOH films was more resistant to plasma damage than the surface molecular structure of porous SiCOH films. Furthermore, the ratio of SFG peak intensities before and after plasma treatment enabled quantification of methyl depletion at the surface of SiCOH films after plasma treatment. The molecular structure at buried Si/SiCOH interfaces was characterized by simulating SFG spectra from pristine and plasma-treated SiCOH films. SFG spectra from plasma-treated low-k films were simulated by adjusting the methyl orientation and number density parameters at the low-k/air interface to match experimental results. Simulated SFG spectra indicated that methyl groups at the buried interface of both dense and porous SiCOH films were oriented with a high tilt angle before and after plasma treatment. The developed methodology is general and can be extended to characterize the effects of many different plasma treatments, wet chemical treatments, and surface repair treatments on the interfacial molecular structures of many polymer or organic films. Simultaneously characterizing the surface and buried interface of commercial films *in situ* is an important step in the development of SFG into a metrology tool for nondestructive characterization of polymer interfaces.

In chapter 9, the effects of NH_3 plasma treatment and the effectiveness of the dielectric repair on molecular structures at the surface and buried interface of a pSiCOH film deposited on top of a SiCNH film on a Si wafer were fully characterized using SFG, supplemented by X-ray photoelectron spectroscopy. After exposure to NH_3 plasma for 18 s, about 40% of the methyl groups were removed from the pSiCOH surface, and the average orientation of surface methyl

groups tilted more towards the surface. The repair method used here effectively repaired the molecular structures at the pSiCOH surface but did not totally recover the entire plasma-damaged layer. Additionally, simulated SFG spectra with various average orientations of methyl groups at the SiCNH/pSiCOH buried interface were compared with the experimental SFG spectra collected using three different laser input angles to determine the molecular structural information at the SiCNH/pSiCOH buried interface after NH3plasma treatment and repair. The molecular structures including the coverage and the average orientation of methyl groups at the buried interface were found to be unchanged by NH_3 plasma treatment and repair. Taken together with chapter 8, this chapter further demonstrates SFG as a powerful metrology tool capable of nondestructive characterization of real industry samples and real industry processing steps.

The general nature of the methodology developed in this thesis enables it to be directly utilized by the growing number of research groups worldwide that use SFG for interface characterization. Furthermore, by correlating interfacial molecular structure to interfacial properties, we have elucidated general interfacial structure-property relationships. Accurately predicting interfacial properties in microelectronic packages based on structure-property relationships developed in this fundamental scientific research will help overcome many barriers in rational interface engineering currently faced by the microelectronics industry and will accelerate the development, implementation, and commercialization of future integrated circuits and semiconductor devices. Furthermore, the structure-property relationships elucidated in this research are general and can be applied in many scientific and engineering research areas where polymer/solid interfaces play an important role, such as polymer composites, optical fibres, paints, and anti-corrosion coatings.

There are several ways to extend the work presented in this research. The work in chapter 2 can be extended by correlating the molecular structure of polymer chains at the solvent/air interface determined using molecular dynamics simulations to that obtained from SFG studies to gain further insight into how solvent/air molecular structures are correlated to the surface molecular structure of spin cast films. Further studies should focus on the effect of polymer chain molecular weight on the surface structure of spin cast films as well as the consequences and applications of different polymer film surface structures induced by spin casting in aromatic and non-aromatic solvents. The ultimate goal of this research will be the design of polymer films with desired and controlled surface structures using spin coating with certain solvents.

The work in chapter 3 can be extended by directly correlating different molecular structures at buried polyimide/epoxy interfaces to adhesion strength measurements. The general methodology can also be used to study interfaces between commercial passivation layer materials (polyimide or other) and various packaging materials developed by our collaborators in the semiconductor industry.

The work in chapter 5 can be extended by characterizing the effects of flux residues at metal surfaces and buried metal/epoxy interfaces. Flux treatment is a widely used processing step during soldering in microelectronic packaging. Organic flux residues have been hypothesized to weaken interfacial adhesion at copper/epoxy interfaces, but the components of the flux that lead to weakened adhesion aren't known. SFG studies could be used to elucidate what components of fluxes remain after reflow and what components are present at buried adhesive interfaces. Such knowledge could be used to aide in the design of new fluxes that won't weaken adhesion at copper/epoxy interfaces.

The work in chapters 7, 8, and 9 can be extended by directly correlating molecular structures at low-k interfaces to adhesion strength measurements, dielectric breakdown behavior, and the structure of metal or inorganic layers deposited on treated low-k surfaces using atomic layer deposition. In addition, SFG studies could be used to characterize how wet chemical etching alters low-k surface molecular structures. Such knowledge could then be used to design new etching conditions for air-gap interconnects that require precise etching of low-k materials.